PLASTIC COLLAPSE OF CIRCUMFERENTIAL SURFACE DEFECTS IN PIPELINE MATERIALS

by

Jae-Boong Choi

A thesis
presented to the University of Waterloo
in fulfillment of the
thesis requirement for the degree of
Doctor of Philosophy
in
Mechanical Engineering

Waterloo, Ontario, Canada, 1997

The University of Waterloo requires the signatures of all persons using or photocopying this thesis. Please sign below, and give address and date.

ABSTRACT

Fitness for purpose techniques for the evaluation of defects in pipeline girth welds as described in Appendix K of the CSA Z662 have proven to be overly conservative for high applied strains. Conventional limit loads, including CSA Z662, were not consistent in assessing the plastic collapse of surface defects. The effect of crack geometry was not successfully accounted for using available limit loads.

The full pipe subject to remote bending was simplified to obtain a better understanding of plastic collapse behaviour. An extensive program combining analytical, experimental and numerical study was performed for all simplified geometries. As a result of detailed finite element analyses, a plastic collapse solution was introduced and compared with available experimental data.

The ligament failure criteria, which was introduced for tensile and single edge notch tension (SENT) specimen analyses, provided good agreement with experimental data for wide plate specimens and full pipes. In general, it was observed that geometries with shallow surface cracks produced high plastic collapse loads even when the cracks were long. Deep and long cracks produced much lower plastic collapse loads, and the occurred by ligament necking. A plastic collapse solution for surface defects in pipeline girth welds was proposed and showed significant improvement over existing solutions for assessing such surface defects.

The proposed plastic collapse solutions for wide plates and full pipes provided better, more consistent agreement with experimental data than available conventional limit load solutions, and, above all, these solutions reflect the physical behaviour of pipeline defects. This method should be used to investigate defect interactions and embedded cracks.

Acknowledgements

I would like to express my sincere appreciation to my supervisor, Professor Steve Lambert, for his encouragement, guidance, patience and kindness. He has shown to me what a true supervisor should be.

The present research was funded through a contract with NOVA Gas Transmission Ltd. I would like to thank Dr. Alan Glover for his patient help. I also would like to thank Professor Roy Pick and his family for their guidance and kindness.

Throughout of this work, Steve Hitchman has provided technical computing support. The ready and kind assistance of Ernst Huber is greatly acknowledged. Young-Kyu Song's kind assistance in preparing specimens and photos is appreciated.

Also, I would like to acknowledge my indebtedness to my follow graduate students for their encouragement and support. In particular, I would like to thank Xin Wang for his great help.

I would like extend my appreciation to Eun-Sung Cho for his friendly and patient support. I also would like to thank all Korean fellows, Graduate students, Arirang Hoops and Arirang Spiders, in Waterloo for their warm care.

Last but not least, I would like to express my sincere gratitude to my country, *Korea* and to this beautiful country, *Canada*.

My parents gave me unconditional support and encouragement, and have been a source of strength for me through my many years of study. This thesis belongs to them.

I would like to share this thesis with my wife, Mi-Yeon Kee Choi, as we did for entire Canadian life. Thanks for your love and support. You deserve all my heart.

Table of Contents

List of Tables

List of Figures

Chapter 1

Introduction

Pipelines are one of the most convenient and cost effective ways of transporting natural energy resources, such as gases and oils, over long distances. In North America, Western Europe, Australia and Asia, large diameter high pressure pipelines are in operation and under construction to convey hydrocarbon energy many thousands of kilometres. The Alaskan Natural Gas Transportation System (ANGTS) alone operates more than 6400 *km* of line pipe of diameters from 1067 to 1422 *mm* and largely of X70 grade steel (Hale, 1980). The Polar Gas and Arctic Islands systems in Canada are of similar scale. In Europe, the pipelines from the Yamal peninsula in northern Russia to Germany and Austria are close to 5000 *km* and predominantly 1422 *mm* in diameter. In Australia, pipelines conveying natural gas from the Northwest Shelf to Western Australia cover 1470 *km* with a diameter of from 660 to 813 *mm*.

Since the mid-1950s, large scale natural gas development in western Canada induced the construction of the TransCanada Pipeline system and Alberta Gas Trunk Line system for transporting natural gas from Alberta. The pipeline systems of these and other transmission companies have continued to expand as reserves and markets have grown. Furthermore,

recent exploration has proven large natural gas reserves in the Arctic regions and off the east coast. These frontier regions are under investigation, and future Canadian natural gas exploration and development are likely to be concentrated in these areas. The size of proven natural gas reserves in conventional areas and the potential of arctic areas will result in a continuing high level of gas pipeline construction activity in Canada.

With an increasing number of pipelines required for the energy transportation industry, it becomes increasingly critical to operate them with minimal maintenance over long periods to justify the high capital cost. The failure of linepipe can result in damage to the environment and the public as well as high repair costs. Detection, characterisation and assessment of flaws in pipeline girth welds are required to prevent the failure of linepipe. The assessment of the integrity of pipelines has been pursued over the last decade, and has resulted in a number of standards specifying failure prevention criteria. This research is intended to refine existing flaw assessment procedures for underground pipelines.

Assessment of cracked components is made both at the design stage and during service. A structure may be considered to contain hypothetical crack-like defects during the design stage, or may be found to have real cracks during non-destructive examination while in service. In both situations, the crack resistance of the component has to be evaluated. A number of methods have been established for the assessment of defects. In 1980, the publication of BSI-PD6493:1980, *Guidance on some methods for the derivation of acceptable levels of defects in fusion welded joints*, made it possible to undertake an engineering critical assessment of defects in welds. The method was based on a fracture mechanics methodology with an independent plastic collapse criterion based on defect recategorization. This method has been widely accepted as a conservative assessment (Denys, 1992, Scott, 1993).

The recategorization rules of BSI PD6493:1980 were found to be overly conservative for pipeline geometries. For this reason, an experimental program was undertaken to develop procedures for assessing defects in line pipe girth welds at the University of Waterloo (Pick et al., 1980) and the Welding Institute of Canada (Glover et al., 1981; Glover and Coote, 1983). Together they conducted an extensive series of full-scale pipe bending tests. As a result, an alternative girth weld acceptance standard based on these empirical results was developed and incorporated in Appendix K of CSA-Z184 (1986). Appendix K provides empirical adjustments to BSI PD6493:1980 for fracture to achieve a consistent level of conservatism and replaces the recategorization rules with an empirical plastic collapse criteria. Appendix K, however, remains overly conservative for high levels of longitudinal strain (Scott, 1993, Denys, 1993). A refined analysis of defect behaviour in pipelines will provide a greater understanding of failure mechanisms, and allow modification of the failure criterion to fit pipeline geometry more accurately.

The failure mode of a cracked structure can be a combination of fracture and plastic collapse. If a material is brittle, then failure of a cracked structure is dominated by fracture. As the material toughness increases, the failure mode changes to plastic flow controlled, that is, plastic collapse. In deriving tolerable sizes of defects to prevent failure, consideration must be given to both fracture and plastic collapse.

Most standards used to measure fracture toughness have been established on the basis of bending loading, which gives the most severe condition. For example, ASTM E813 (1987) recommends the use of a single edge notch bending (SENB) specimen or a compact tension (CT) specimen to measure fracture properties. While a pipeline may be subject to global bending, the local loading on a defect can be considered uniaxial tension if the defect is small. A crack subjected to uniaxial tension is less severe than that subjected to bending, and will withstand a higher load before fracture. Therefore, a fracture criterion based on

bending may be overly conservative for small defects in pipelines. This effect has been observed and interpreted (O'Dowd and Shih, 1992) in terms of constraint. The efforts to improve fracture prevention standards by considering the effects of constraint have resulted in the development of several methodologies for quantification of constraint, i.e., the *J-T* analysis and the *J-Q* analysis, for fracture assessment. However, no consideration has been given to a revised plastic collapse criterion for pipeline failure assessment.

Constraint can be defined as the deformation conditions applied to a defect in a structure, for example, loading and local geometry. The constraint in a fracture test specimen (Figure 1.1) can be discussed in terms of in-plane constraint (radial or thickness direction) and out-of-plane constraint (circumferential or width direction). Out-of-plane constraint is dependent on the width of the specimen, and two extremes are represented by plane strain and plane stress. Since the defect in an actual pipeline can be considered to be in a plane strain situation, fracture toughness specimens must satisfy the plane strain condition. In-plane constraint depends on the loading condition, strain hardening and geometry. Bending loads provide a higher hydrostatic stress at the crack-tip than tensile loading, that is, higher in-plane constraint. A deeply cracked specimen also provides higher in-plane constraint compared to a shallow cracked specimen. From the view point of continuum mechanics, fracture is promoted by higher levels of hydrostatic stress at the crack-tip (higher constraint) which results in crack tearing, while plastic collapse is governed by the deviatoric stress and the amount of crack ligament yielding. For plastic collapse, failure occurs through plastic flow without any significant crack tearing. Since the level of in-plane constraint is important in interpreting the failure mechanisms of a cracked structure, an investigation of constraint effects in assessing defects must be performed for both fracture and plastic collapse modes of failure.

Constraint effects on fracture assessment have been studied by several researchers and have been successfully quantified. These results were reviewed and studied in association with pipeline geometries by the author (1993). The author's (1993) investigation of out-of-plane constraint for fracture assessment involved three-dimensional finite element analyses for various widths of single edge notch bending or tension specimens. Several parameters were reviewed for the quantification of width effects. The author (1993) obtained the size requirements to satisfy plane strain conditions for X70 pipeline material. The quantification of in-plane constraint for fracture control was obtained by undertaking two-dimensional plane strain finite element analyses for various crack depths of single edge notch tension and single edge notch bending specimens. When a geometry has sufficient constraint, the crack tip stress fields can be described by a single parameter expression, based on the J-integral, over a suitable range near the crack tip. In cases where this is not possible, a second parameter can be introduced to provide an improved description of crack tip stress fields. Two parameters that have been used with some success are the elastic T-stress and the Q-stress. These parameters have been quantified for some test geometries as a function of crack geometry. Since the J-T analysis is based on an elastic T-stress, the validity is confined to small-scale yielding. O'Dowd and Shih (1991) have suggested that the J-Q analysis can be extended to quantify in-plane constraint for large-scale yielding.

Investigations of in-plane constraint in pipeline defects have been performed by Martin (1991) and the author (1993, 1997) by conducting two-dimensional finite element analyses to predict the J-integral and the crack tip stress fields using the finite element program ABAQUS (HKS, 1996). Martin (1991) used the modified J-T analysis (J-F_T analysis) for the quantification of in-plane constraint, and thereby extended the J-T analysis to large-scale yielding. Martin tabulated the T-stress and expressions for the stress field based on F_T as a function of crack geometry for tension and bending specimens. The author (1993) performed a J-Q analysis for the same geometry, and also tabulated Q values as a function

of crack geometry and load. The author (1993) also provided a fracture assessment method using Q by modifying the failure assessment diagram.

The effect of constraint on plastic collapse has only been studied qualitatively on the basis of a physical interpretation (Brocks et al., 1989). However, it has been revealed that deeply cracked SENB specimens (higher in-plane constraint) withstand higher maximum loads (Zhang and Lin, 1990). The same trend was also observed in double edge notched tension (DENT) specimens (Kussmaul et al., 1992). Brocks and Schmitt (1993) conducted finite element calculations for various specimens to obtain the limit load. They concluded that high-constraint specimens (i.e., CT, DENT specimens) gave higher limit loads compared to conventional limit loads. The same trend has also been observed experimentally for single edge notched tension (SENT) specimens (Lambert et al., 1993). With increasing crack depth, the maximum net-section stress at failure tends to increase. From these results, it is evident that the local crack-tip constraint affects the global plastic flow behaviour. However, the effects of constraint on plastic collapse due to crack geometry have not been clearly defined for a surface crack in a pipeline structure.

One of the most popular steel grades used for natural gas conveying pipeline systems is CSA Grade 483 or API 5L Grade X70, a low alloy carbon steel. This is a weldable structural steel with a minimum yield strength of 483 MPa and a minimum ultimate strength of 565 MPa. Grade 483 line pipe is manufactured from a controlled rolled flat skelp. The rolling process of pipeline steel plate results in an anisotropic structure, and the difference in cooling rate between the surface and the mid-section produces an inhomogeneous structure through the thickness. In most assessment procedures currently available, these inhomogeneous and anisotropic characteristics have not been considered.

As computers have become faster, cheaper, more powerful and more widely available, the number of problems addressed numerically has grown exponentially. The finite element method (FEM) is the most widely employed numerical method for the solution of fracture mechanics problems and can be employed in the standard manner or modified to account for the singular nature of the near crack-tip fields. In spite of difficulties in designing an optimal mesh for accurate results, the FEM has been widely used and implemented commercially (ADINA, NASTRAN, ABAQUS, etc.), and has been widely used for the solution of non-linear fracture problems. Problems involving material inhomogeneity, anisotropy and large deformation, can be addressed accurately using the FEM. Therefore, the FEM has been used extensively to solve specific fracture problems.

It is the intent of this thesis to study the effect of crack-tip constraint on plastic flow behaviour for a circumferential surface crack in a pipeline. The microstructural characteristics of the pipeline steel have been thoroughly investigated in terms of the volume fraction of the constituents, grain sizes and microhardness measurements. The parameters obtained were employed in the FEM analyses.

FEM analyses have been conducted on various geometries simulating a pipeline containing a surface crack. As shown in Figure 1.2, a full pipe containing a circumferential surface crack which is subject to remote bending can be modelled as a wide plate subject to local uniaxial tension. The failure behaviour of the ligament of a surface crack can be modelled using an SENT specimen. The research initiated with SENT specimens involved both numerical and experimental analyses of their behaviour. The numerical analyses for SENT specimens were intended to develop a method for the quantification of in-plane constraint for the prediction of plastic collapse. Material properties obtained from microstructural investigation and tensile tests have been applied to the FEM analyses. The methods developed based on SENT specimens to assess constraint and microstructural effects have been adapted to wide

plates, and compared to experimental results. Lambert (1992, 1993) conducted a series of tests on fracture toughness specimens (SENT and SENB) and mini wide plates. The results of these tests have been used in the present thesis to validate the finite element analysis. With further numerical analyses of line pipe, the method has been employed to modify the plastic collapse criteria for pipeline failure assessment. A fitness-for-purpose type failure criterion for a cracked pipeline has been presented on the basis of the FEM analyses resolving the effects of crack geometry.

Scope of the Thesis

In the following chapters, the results from this research will be presented. Chapter 2 discusses the current assessment procedures used to evaluate pipeline defects. The chapter reviews plastic collapse solutions for SENT specimens, wide plates and full pipes. Current solutions are compared to experimental data produced by Lambert (1991, 1993). Limitations of these defect assessment guidelines are highlighted.

In Chapter 3, microscopic observations of Grade 483 (X70) pipeline steel are presented along with tensile test results. Specimens were prepared from two linepipe steels (thickness of 8.4 mm and 13.4 mm) provided by NOVA Gas Transmission Ltd. Microstructural parameters including grain size, microhardness numbers and second phase volume fraction are presented for both pipes. Tensile testing was used to assess the inhomogeneity of pipeline steel in the thickness direction. Also, anisotropic parameters were measured in conjunction with the tensile properties. Microstructural parameters presented in this chapter were used in the microstructure based finite element analyses conducted in this thesis.

Chapter 4 covers the plastic collapse behaviour of SENT specimens in terms of both numerical and experimental analyses. Conventional finite element analyses conducted with material parameters obtained from Chapter 3 are presented along with test data.

The plastic collapse behaviour of wide plates is presented in Chapter 5. FEM analyses performed for various crack geometries are presented in comparison to test results (Lambert, 1993). A plastic collapse criterion based on ligament necking is introduced. The effect of crack geometry on plastic collapse in wide plates has been presented in terms of a geometry correction factor based on extensive finite element analyses.

Chapter 6 presents FEM analyses results for full pipes subject to remote bending along with full pipe test results by Coote et al (1981). A plastic collapse solution based on extensive finite element analyses is introduced. The effect of crack geometry on plastic collapse is presented in comparison with currently available plastic collapse solutions.

The thesis is concluded in Chapter 7. A summary, major conclusions of the present work and recommendations for future research are presented.

Chapter 2

Background

The present research is focused on circumferential defects in base metal in linepipes under remote bending. In service, bending moments placed on the cross section of a linepipe result in a local tensile stress. A wide plate subjected to tension can simulate the load on a cracked area of pipeline as shown in Figure 1.2. The wide plate containing a surface crack can in turn be simplified to an SENT specimen loaded in tension. Lambert (1991, 1993) performed an extensive experimental program to help establish design criteria for girth weld defects in natural gas pipelines to serve as a guideline for defect acceptability. The test program was carried out for SENB, SENT and mini wide plate specimens. The present research includes numerical analyses simulating these SENT specimens and wide plates. The results are used to build a plastic collapse database for circumferential surface defects in pipelines.

In this chapter, plastic collapse solutions for test specimens (SENB and SENT), wide plates and full-scale pipeline structures are reviewed. Comparisons between current solutions and test results will be made in the following Chapters.

If a cracked specimen of adequate toughness is subjected to tension, plasticity will develop at the crack tip and spread through the specimen. The maximum load carrying capacity will be reached when continuous plastic flow occurs without further increase in load. This failure behaviour is defined as plastic collapse.

For simplicity, most plastic collapse solutions assume rigid-perfectly plastic material behaviour. To be conservative, any strain hardening can be ignored, and the material yield stress can be used in this model. Alternatively, a higher 'flow' stress may be used to approximately account for strain hardening. Generally, the flow stress is a function of both the geometry and the material. In practice, however, the flow stress is assumed to be a material property. Most standards recommend a specific definition for flow stress.

The proper selection of flow stress is crucial in determining the plastic collapse load of a structure. For ferritic steels, the flow stress is usually taken as the average of the yield and tensile strength of the material. For pipeline applications, flow stress of $\sigma_y + 68.7\ MPa\ (10\ ksi)$ is usually used; this was determined based on full scale pipe experiments (Wilkowski and Eiber, 1978). Erdogan (1982) suggests a flow stress of $\sigma_y + 0.8\ (\sigma_{us} - \sigma_y)$ for pipeline steels without welds. This definition could lead to non-conservative estimates for materials with a high yield to tensile ratio.

Continuum Mechanics Approach to Plastic Collapse

Commonly, limit analysis is used to define a lower bound and an upper bound solution for plastic collapse. A lower bound limit load is obtained from a statically admissible stress field satisfying equilibrium, and an upper bound is obtained from a kinematically admissible strain field satisfying compatibility and the flow rule. Usually, the lower bound limit load is used as a conservative

estimate of the load carrying capacity of a structure. The review by Miller (1988) provides a large number of lower bound limit load solutions.

For a geometry which is too complicated for the calculation of a plastic limit load, such as a plate with an eccentric embedded crack under in-plane bending, an elastically calculated stress in a generalised plate model can be used. By undertaking an elastic analysis of the defect-free structure, the tensile, bending and shear stress resultants at the cross-section containing the flaw are obtained. Combining these stress resultants with plastic limit load solutions for cracked plates, a limit solution for a structure, which is generalised as a two-dimensional plate, can be obtained. Miller (1988) summarises a wide range of such plate solutions for both plane stress and plane strain.

One of the most popular methods to calculate upper bound plastic limit loads makes use of slip line field theory. If the maximum shear stress (Tresca) failure theory is used for a rigid non-hardening plastic material, deformation will occur along discrete lines at 45° to the direction of the principal stress; these are called slip lines. The material between the slip lines remains rigid and moves as a solid block. The solution can be obtained by calculating the load at which stresses along the slip lines reach the shear yield stress and a kinematically admissible stress field is created.

Finite element analysis is also a useful method to calculate limit loads. A lower bound limit load is calculated by applying small displacement theory with an elastic- (or rigid-) perfectly plastic material model. The limit load is obtained from the point at which yielding spreads across the uncracked ligament. An upper bound limit load can also be calculated by considering the true behaviour of the structure calculating the elastic-plastic material deformation, including strain hardening, and incorporating large changes to the geometry.

Empirical Approach

The plastic collapse solutions can also be obtained by testing scale models of the flawed structure. This method gives solutions involving empirical constants representing test results. By the nature of this method, these solutions are considered to be the most accurate, but the range of variables can be limited and testing can be expensive. Scale effects must also be considered.

Plastic collapse solutions currently in use for cracked pipelines subject to remote bending are derived from limit load analyses (PD6493, 1991, CEGB/R6, 1988), or derived from empirical results (Willoughby, 1982; CSA Z622, 1994). In the following sections, plastic collapse solutions for test specimens, wide plates and pipeline structures will be presented.

2.1 Limit Analysis

There are two basic assumptions in deriving the limit load for structures: the material is assumed to be perfectly plastic without strain hardening or softening, and the structure is assumed to obey small deformation theory, that is, changes in geometry during deformation are assumed negligible.

Under these assumptions, there are three basic relations that must be satisfied for the deformation of a structure. They are equilibrium, the constitutive relation and compatibility. While the lower bound solution is based on the equilibrium equations and the chosen yield criterion, the upper bound solution is based on the compatibility equations and the flow rule associated with the yield criterion. The complete or exact solution must satisfy all three requirements: equilibrium, compatibility, and the constitutive relations.

2.2 The Lower and Upper Bound Theorems

The Lower Bound Theorem

Since small deformation is assumed, the virtual work principal can be used. For a body of volume V and total surface area S (Figure 2.1), the principle of virtual work can be stated as follows:

$$\int_S T_i du_i \cdot dS = \int_V \sigma_{ij} d\varepsilon_{ij} \cdot dV \tag{2.1}$$

The left hand side of this equation represents the work done by the surface or external forces, and the right hand side is the plastic work dissipated to create an increment of plastic strain. In this equation, T_i represents the surface tractions, u_i, the corresponding displacement, and σ_{ij} and ε_{ij} represent the internal stresses and strains. This equation can be rewritten using T_i^*, the fictitious surface stresses acting on the surface of the real body, and, σ_{ij}^* the matching fictitious stress field satisfying equilibrium,

$$\int_S T_i^* du_i \cdot dS = \int_V \sigma_{ij}^* d\varepsilon_{ij} \cdot dV \tag{2.2}$$

Equation (2.2) can now be divided into two surfaces as follows:

$$\int_S T_i^* du_i \cdot dS = \int_{S_u} T_i^* du_i \cdot dS + \int_{S_T} T_i^* du_i \cdot dS = \int_{S_u} T_i^* du_i \cdot dS + \int_{S_T} T_i du_i \cdot dS \tag{2.3}$$
$$(\because T_i = T_i^* \quad \text{on} \quad S_T)$$

where S represents the total surface area, S_U the surface subject to displacement and S_T the surface subject to tractions. Equation (2.11) can also be rewritten as

$$\int_{S_U} T_i du_i \cdot dS + \int_{S_T} T_i du_i \cdot dS = \int_V \sigma_{ij} d\varepsilon_{ij} dV \tag{2.4}$$

Combining equation (2.12) and (2.13) gives

$$\int_{S_U} T_i^* du_i \cdot dS + \int_{S_T} T_i du_i \cdot dS = \int_V \sigma_{ij}^* d\varepsilon_{ij} dV \tag{2.5}$$

Subtracting equation (2.4) from (2.5) results in

$$\int_{S_U} (T_i - T_i^*) du_i \cdot dS = \int_V (\sigma'_{ij} - \sigma_{ij}^*) d\varepsilon_{ij} dV \tag{2.6}$$

According to the maximum principle work, the right hand side must be greater or equal to zero. Therefore, equation (2.6) becomes

$$\int_{S_U} T_i du_i \cdot dS \geq \int_{S_U} T_i^* du_i \cdot dS \tag{2.7}$$

Equation (2.7) represents the lower bound theorem. This equation states that if a body satisfies the yielding condition and has small displacements, the work done by the actual forces or surface tractions on S_U is greater than, or equal to, the work done by the surface tractions that satisfy the statically admissible stress field.

The Upper Bound Theorem

The virtual work principle can be written in terms of a kinematically admissible displacement increment field dv^* and the actual stress field du_i (Figure 2.2):

$$\int_S T_i du_i \cdot dS = \int_V \sigma_{ij} d\varepsilon_{ij}^* \cdot dV + \Sigma \int_{S_D} q \left| dv^* \right| \cdot dS_D^* \tag{2.8}$$

where $d\varepsilon_{ij}^*$ is the assumed plastic strain increment, dv^* denotes the tangential displacement increment discontinuity on a surface S_D^*, and q is the shearing stress component of σ_{ij} in the direction of the displacement increment discontinuity.

From the maximum work principle,

$$\int_V (\sigma_{ij}^* - \sigma_{ij}) d\varepsilon_{ij}^* \cdot dV \geq 0 \tag{2.9}$$

Applying equation (2.9) to (2.8):

$$\int_S T_i du_i \cdot dS \leq \int_V \sigma_{ij}^* d\varepsilon_{ij}^* \cdot dV + \Sigma \int_{S_D} k \left| dv^* \right| \cdot dS_D^* \tag{2.10}$$

where k is the yield stress and $k > q$. The surface area can be divided into two areas, S_U and S_T. This gives

$$\int_S T_i du_i^* \cdot dS = \int_{S_U} T_i du_i \cdot dS + \int_{S_T} T_i du_i^* \cdot dS \tag{2.11}$$

Therefore, equation (2.10) becomes

$$\int_{S_U} T_i du_i \cdot dS_U \le \int_V \sigma_{ij}^* d\varepsilon_{ij}^* \cdot dV + \Sigma \int_{S_D} k\left|dv^*\right| \cdot dS_D^* - \int_{S_T} T_i du_i^* \cdot dS_T \qquad (2.12)$$

Equation (2.12) is generally known as the upper bound theorem. It states that the rate of work done by the unknown surface tractions on S_U is less than or equal to the rate of internal energy dissipated in the kinematically admissible velocity field.

2.3 Slip-Line Field Theory

Slip-line field theory is based on the assumption of non-homogeneous plane strain deformation of a rigid perfectly plastic isotropic material. While these assumptions do not exactly match industrial materials, this theory gives a good approximation to the maximum load carrying capacity of structures. Since the slip-line field solution is determined by considering the kinematically admissible velocity field, it is usually considered an upper-bound limit load.

The non-zero strains for a model of plane strain rigid plastic body are given by

$$\begin{aligned}
\varepsilon_x &= \varepsilon_x(x,y) \\
\varepsilon_y &= \varepsilon_y(x,y) \\
\varepsilon_{xy} &= \varepsilon_{xy}(x,y) \\
\sigma_x &= \sigma_x(x,y) \\
\sigma_y &= \sigma_y(x,y) \\
\sigma_z &= \sigma_z(x,y) \\
\tau_{xy} &= \tau_{xy}(x,y)
\end{aligned} \qquad (2.13)$$

From the Levy-Mises relations (Levy, 1871, Mises, 1913), the stress-strain relations can be written as

$$\begin{aligned} d\varepsilon_x &= \tfrac{2}{3}d\lambda\left[\sigma_x - \tfrac{1}{2}(\sigma_y + \sigma_z)\right] \\ d\varepsilon_y &= \tfrac{2}{3}d\lambda\left[\sigma_y - \tfrac{1}{2}(\sigma_x + \sigma_z)\right] \\ d\varepsilon_z &= \tfrac{2}{3}d\lambda\left[\sigma_z - \tfrac{1}{2}(\sigma_x + \sigma_y)\right] \\ d\varepsilon_{xy} &= d\lambda\tau_{xy} \end{aligned} \tag{2.14}$$

where $d\lambda$ is a scalar measuring the plastic flow rate. Since $d\varepsilon_z = 0$, the third line of equation (2.14) yields

$$\sigma_z = \tfrac{1}{2}(\sigma_x + \sigma_y) \tag{2.15}$$

With this condition, the von Mises yield criterion becomes

$$\tfrac{1}{4}(\sigma_x - \sigma_y)^2 + \tau_{xy} = k^2 \tag{2.16}$$

where τ_{xy} is the applied shear stress and k is the shear yield stress. The equilibrium equations are

$$\begin{aligned} \frac{\partial \sigma_x}{\partial x} + \frac{\partial \tau_{xy}}{\partial y} &= 0 \\ \frac{\partial \sigma_y}{\partial y} + \frac{\partial \tau_{xy}}{\partial x} &= 0 \end{aligned} \tag{2.17}$$

These three equations (equations (2.16) and (2.17)) can provide the solutions for three unknowns, σ_x, σ_y and τ_{xy}. These three equations are sufficient to give the stress distribution

in cases where the boundary conditions are given only in terms of stresses. Such problems are known as *statically determinate*. However, if the boundary conditions are specified in terms of displacements or velocities, the stress-strain relations must also be used to solve the problem.

The state of stress at any point may be represented in the form of Mohr's circle diagram as shown in Figure 2.3. The corresponding Mohr circle diagram for the strain-rates is shown in Figure 2.4. The directions of maximum shear stress, indicated by points A and B in Figure 2.3, coincide with the directions of maximum shear strain-rate (A and B of Figure 2.4). Such directions are free of extension or compression. These directions form two orthogonal families of curves which are known as slip-lines.

A schematic illustration of these slip lines is shown in Figure 2.5 for a small curvilinear element. The slip-line field solution can be obtained by drawing the two families of slip-lines (α and β) and calculating the state of stresses.

One of the simplest ways of deriving the slip-lines is based on the equations of equilibrium (equation (2.17)). From the Mohr circle diagram (Figure 2.3), the stress components of equation (2.17) can be expressed in terms of the mean (or hydrostatic) stress, p, and the yield shear stress, k, as

$$\begin{aligned} \sigma_x &= -p - k\sin 2\phi \\ \sigma_y &= -p + k\sin 2\phi \\ \tau_{xy} &= k\cos 2\phi \end{aligned} \tag{2.18}$$

Differentiating and substituting equation (2.18) into (2.17), the equilibrium conditions become

$$
\begin{aligned}
-\frac{\partial p}{\partial x} - 2k\cos 2\phi \frac{\partial \phi}{\partial x} - 2k\sin 2\phi \frac{\partial \phi}{\partial y} = 0 \\
-2k\sin 2\phi \frac{\partial \phi}{\partial x} - \frac{\partial p}{\partial y} + 2k\cos 2\phi \frac{\partial \phi}{\partial y} = 0
\end{aligned}
\tag{2.19}
$$

Since the axes can be taken to represent any arbitrary direction, equation (2.19) can be simplified by taking $\phi = 0$, giving:

$$
\begin{aligned}
-\frac{\partial p}{\partial x} - 2k\frac{\partial \phi}{\partial x} = 0 \\
-\frac{\partial p}{\partial y} + 2k\frac{\partial \phi}{\partial y} = 0
\end{aligned}
\tag{2.20}
$$

Upon integration, equation (2.20) finally becomes

$$
\begin{aligned}
p + 2k\phi = C_1 \qquad & \text{i.e., constant along an } \alpha\text{ - line} \\
p - 2k\phi = C_2 \qquad & \text{i.e., constant along a } \beta\text{ - line}
\end{aligned}
\tag{2.21}
$$

Equations (2.21) are known as the Hencky (1923) equations, and are equivalent to the equilibrium equations for a plane strain fully plastic body.

These equations, however, are not sufficient to solve a problem when the boundary conditions are described by displacements or velocities, Supplementary velocity equations are required. Since the principal axes of stress and of plastic strain increment coincide, the maximum shear velocity lines and the velocity slip-lines are the same as the maximum shear stress lines and the stress slip-lines. From Figure 2.6, the velocities in the slip directions can be written as

$$u_x = u\cos\phi - v\sin\phi$$
$$u_y = u\sin\phi + v\cos\phi \tag{2.22}$$

Taking the x axis to be $\phi = 0$, equation (2.22) yields

$$\left(\frac{\partial u_x}{\partial x}\right)_{\phi=0} = \frac{\partial u}{\partial x} - v\frac{\partial \phi}{\partial x} \tag{2.23}$$

Since the normal strain rates are zero along the slip-lines,

$$\frac{\partial u}{\partial x} - v\frac{\partial \phi}{\partial x} = 0 \quad \text{or} \quad du - vd\phi = 0 \quad \text{along an } \alpha\text{ - line} \tag{2.24}$$

and similarly,

$$\frac{\partial v}{\partial y} + u\frac{\partial \phi}{\partial y} = 0 \quad \text{or} \quad dv + ud\phi = 0 \quad \text{along a } \beta\text{ - line} \tag{2.25}$$

Equations (2.24) and (2.25) are known as the compatibility equations for the velocities due to Geiringer (1930).

2.4 Plastic Collapse Solutions for Test Specimens

The test specimens to be considered in this section are single edge notched bending (SENB) and tension specimens (SENT) tested with fixed grips (Figure 2.7).

2.4.1 SENB Specimen

For SENB specimens, the limit load, P_L, can be expressed as (Miller, 1988)

$$P_L = \alpha B b^2 \sigma_o / S \tag{2.26}$$

where σ_o is the flow stress, and B, b and S are given in Figure 2.7. Green and Hundry (1956) derived an α value of 1.21 for $a/t > 0.18$ for plane stress using the Tresca yield criterion. For plane strain, von Mises will give 1.155 times the Tresca limit load (Miller, 1988) using slip-line field theory. The EPRI handbook (Kumar et al., 1981) proposes an α value of 1.456 for plane strain and 1.072 for plane stress. Miller (1988) recommends α = 1.41 for plane strain for use in CEGB/R6 (1988).

Chen et al. (1978) proposed an analytical solution for P_L based on slip line field theory for deeply notched specimens ($a/t > 0.5$). Chell and Spink (1977) performed tests to verify the proposed equation by Chen et al. (1978) and suggested an empirical equation to correct this solution. Zhang and Lin (1990) investigated the equation for shallow cracks ($a/t < 0.5$) by conducting experimental and numerical analyses, and found that Chen et al.'s equation was not valid for shallow cracks. They proposed an empirical equation to calculate α for shallow cracks ($0.05 \leq a/t \leq 0.5$) which was given by

$$\alpha = \left[0.9534 + 1.309(a/t) - 0.8157(a/t)^2\right] \tag{2.27}$$

Wu et al. (1990) also proposed empirical equations on the basis of test results for both shallow and deep cracks:

$$\alpha = [1.199 + 0.096(a/t)] \qquad for \quad a/t > 0.172$$

$$\alpha = \left[1.125 + 0.3892(a/t) - 2.238(a/t)^2\right] \quad for \quad 0.021 < a/t < 0.172 \tag{2.28}$$

Zhang and Lin (1990), Kumar et al. (1981) and Miller's (1988) α values are plotted and compared in Figure 2.8.

Faucher et al. (1992) performed an experimental investigation of the effect of specimen geometry (crack depth and the effect of side grooves) on the fracture toughness of the same line pipe steel used in the present program, Grade 483 (X70). The maximum load results were compared with available limit load solutions. It was observed that the geometries bearing higher out-of-plane constraint (i.e, side-grooved specimens) gave a higher maximum load carrying capacity. Most specimens failed near, or over the limit load suggested by Miller (1988). The results are presented in Table 2.1 and Figure 2.8. Lambert (1993) also carried out a series of tests with SENB specimens made from the same *X70* line pipe. The test results are summarized in Table 2.2 and Figure 2.8 along with Faucher et al.'s (1992) results.

2.4.2 SENT - Fixed Grips

Lower-Bound Load

Since both ends of the SENT specimen are restrained not to rotate due to the fixed grips, no bending effect is present. If neither the stress concentration due to the crack-tip nor the strain hardening of the material are considered, the lower bound load for an SENT specimen can be determined from stress equilibrium as:

$$P_L = \sigma_o \cdot (t-a)B \tag{2.29}$$

where σ_o is the material yield stress. In equation (2.29), the Tresca yield condition was adopted. For von Mises plane strain, P_L should be multiplied by 1.155. A schematic illustration of the lower-bound solution is given in Figure 2.9.

Upper-Bound Load

In order to determine the upper-bound limit load, a deformation failure mode must be assumed that satisfies the compatibility condition. An SENT specimen can be divided into three rigid parts, *a*, *b* and *c* (Figure 2.10). At failure, part *c* moves toward the crack front side, and results in necking. If the relative velocity along the sliding planes *AB* and *AC* is, $\dot{\delta}$, the rate of separation of part *a* and *c* is $2\dot{\delta}\ sin\alpha$ as shown in Figure 2.10. Applying the upper-bound theorem in terms of energy,

$$P_U \cdot 2\dot{\delta} \sin\alpha = \frac{2k\dot{\delta} \cdot (t-a)B}{\cos\alpha} \tag{2.30}$$

where *k* is the shear yield stress. The left hand side of equation (2.20) is the rate of external energy applied due to P_U and the right hand side of equation (2.30) is the rate of internal energy dissipation over the two sliding surfaces *AB* and *AC*. Equation (2.30) can be rewritten:

$$P_U = \frac{2k(t-a)B}{\sin 2\alpha} \tag{2.31}$$

In equation (2.31), P_U has a maximum value when $\alpha = 45°$. Then,

$$P_U = 2k \cdot (t-a)B = \sigma_o (t-a)B \tag{2.32}$$

based on the Tresca yield criterion.

Note that equation (2.32), the upper bound load, is equal to the lower bound load given by equation (2.29). Thus, the derived solution is the complete limit load for an SENT specimen.

For SENT specimens with fixed grips, Miller (1988) suggested the limit load using equation (2.32) for Tresca plane stress. The plane strain Mises solution is 1.155 times the Tresca solution.

2.5 Wide Plates in Tension

In the case of a small defect in a pipeline, the local loading can be considered to be remote tension. Thus, surface cracked wide plates in tension having a surface crack can be used to predict the local failure of a pipeline. For this reason, the investigation of failure behaviour on wide plates has been widely studied.

Connors and Hellen (1983) performed tests on mild steel (Grade 40, σ_y = 293 MPa, σ_{ult} = 420 MPa) plates containing surface defects of either rectangular, or part-circular shape which were produced by spark erosion machining. They concluded that the maximum net-section stress, at ligament fracture, which was preceded by significant plastic deformation of the plate, was greater than the material yield stress. It has been observed that with increasing ligament thickness, the ligament failure load approached the plastic collapse load based on ultimate stress. This

behaviour has been explained in terms of strain hardening. While the tendency of increasing maximum net-section stress with decreasing crack size was evident for rectangular defects, it was not observed for semi-circular defects. In their analysis, the test results were interpreted in terms of global parameters, e.g., maximum nominal or net-section stress. The stress or strain distribution across the ligament was not considered.

Denys (1992) undertook wide plate tests to determine the failure behaviour of surface breaking weld metal root cracks in thick-walled large diameter pipelines. Twelve tensile-loaded, fatigue pre-cracked, 450 *mm* wide curved specimens were tested. Surface cracks were introduced in the middle of the welds. The failure mode of the wide plates was characterised by three regimes; elastic-plastic fracture, net-section yielding and gross-section yielding. Six test specimens containing surface cracks in the slightly overmatched welds failed by either elastic-plastic fracture (nominal stress at failure < yield stress) or net-section yielding (net-section failure stress > yield stress, and gross-sectional failure stress < yield stress). He observed that the failure mode of the welded wide plates was very sensitive to microstructure, crack size (in particular crack depth), and the relative difference between weld and pipe metal yield strength. He concluded that the dominant factor causing elastic-plastic fracture was the very low toughness of the root pass. Fracture initiation was not from the deepest point of the crack but from the low toughness root pass. Therefore, he recommended consideration of the variation in weld toughness through the thickness based on the microstructure. However, no consideration of the crack ligament was given.

Lambert (1993) tested a number of wide plates containing various sizes of surface cracks under tensile loading in *X70* pipeline steel. The configuration of these mini-wide-plate specimens is given in Figure 2.11 (Lecsek, 1992). A surface defect was introduced using a jewellers slitting saw and pre-fatigued under four-point bending. No evidence of ductile tearing was observed from any specimen tested.

There are several plastic collapse solutions currently in use for surface cracked wide plates in tension.

PD 6493:1981

The PD 6493:1981 analysis of plastic collapse conservatively assumes an infinitely long surface defect and that collapse occurs when the net stress on the ligament beneath the defect reaches the flow stress. For tension loads, the PD6493:1980 plastic collapse solution can be expressed as

$$a_{max} = t(1 - \frac{\sigma_{pc}}{\sigma_f}) \tag{2.33}$$

or

$$\sigma_{pc} = \sigma_f(1 - \frac{a}{t}) \tag{2.34}$$

where

t	=	*plate wall thickness*
a	=	*height or depth of the crack*
σ_{pc}	=	*nominal applied stress at failure*
σ_f	=	*flow stress*

Since the PD6493:1980 plastic collapse solution does not use the load carrying capacity of the uncracked side ligaments, equation (2.34) is very conservative for short surface defects. In 1991, PD 6493:1991 implemented a revised plastic collapse solution using net-section yielding.

The Net-section Yielding Solution (PD6493:1991)

The net-section yielding solution (PD6493:1991) assumes that the crack ligament area can sustain a load corresponding to the point of material plastic flow (conservatively this point can be assumed as a yielding stress, or practically assumed as a material flow stress). This assumption is acceptable if the material is sufficiently tough, and if there are negligible bending effects in the loading (i.e., rigid restraint). Plastic collapse will occur when tensile loading leads to a net-section stress equal to the material flow stress.

For a semi-elliptical surface crack in a wide plate, the net-section yielding solution is given by

$$\sigma_{pc} = \sigma_f \left[1 - \frac{\pi c a}{2 t W_d} \right] \tag{2.35}$$

where W_d is the plate width. Since this solution fully utilises the crack ligament area as defect-free without any correction for crack-tip plasticity, the prediction may not be conservative.

CEGB/R6

The plastic collapse solutions in the R6 procedure provide an allowance for the uncracked ligaments on either side of short surface cracks or defects. The R6 method assumes that the defect is semi-elliptical in shape and that the stresses on the defect are redistributed over a length equal to the defect length, c, plus the wall thickness, t. The plastic collapse solution is given by (Miller, 1988):

$$\sigma_{pc} = \sigma_f \left[1 - \frac{\pi c a}{2t(2c+t)} \right] \tag{2.36}$$

It should be noted that this solution is valid for $a/2c > 0.1$ and rigid restraint of the ends of the specimen is assumed.

2.6 Pipeline Structures Subject to Remote Bending

The following are plastic collapse solutions for pipeline structures currently in use.

Net-Section Collapse Solution (Miller, 1988)

Miller (1988) presents the limit load for a partial circumferential crack in a pipe as shown in Figure 2.12. The global plastic collapse solution in terms of applied bending moment is:

$$\sigma_{pc} = \frac{M_{pc}}{4R^2 t} = \sigma_f \left[\cos\frac{(1-\eta)\beta}{2} - \frac{(1-\eta)\sin\beta}{2} \right] \tag{2.37}$$

This equation assumes that the defect is at the most critical position (12 o'clock), and that the neutral axis does not intersect the flaw. This net-section collapse solution assumes that the crack ligament area can sustain a load corresponding to the material flow stress. Both CEGB/R6 (1988) and PD6493:1991 recommend the use of this net-section collapse solution.

The Willoughby Plastic Collapse Solution

The Willoughby plastic collapse solution is given by (Willoughby, 1982):

$$\sigma_{pc} = \sigma_f \left[1 - 0.8 \frac{ca}{tR} \right] \tag{2.38}$$

Equation (2.38) has a similar form to the net-section yielding solution (equation (2.35)). The constant, *0.8* in equation (2.38), has been derived from experimental data (Willoughby, 1982) using a lower bound to test results. This value gives an approximate safety factor of 2 on defect length or depth for high toughness materials. The application of equation (2.38) is limited to $a/t < 0.8$.

The CSA Z662 Plastic Collapse Solution

The University of Waterloo (Pick et al, 1980) and the Welding Institute of Canada (Glover et al, 1981) performed a series of full scale tests to investigate the behaviour of interior surface defects in girth welds of large diameter gas line pipe. Erdogan (1982) and Wilkowski and Eiber (1980) conducted similar testing. Coote et al. (1986) summarized the results of all these tests.

Wilkowski and Eiber (1980) proposed that failure of pipelines in bending can be considered in three regimes: brittle fracture, elastic-plastic fracture and net-section plastic collapse. Material that is sufficiently tough to avoid fracture will fail by net-section collapse. Wilkowski et al. (1987) proposed an empirical screening criterion to determine whether the failure mode of a component will be by net-section collapse. According to this criterion, net-section collapse occurs only when the plastic zone starting from the end of a crack reaches the neutral axis of the pipe. For larger diameter pipes containing a crack smaller than 10% of the circumference, it is unlikely that net-section collapse will occur based on this criterion.

The majority of failures of full scale pipe tests show elastic-plastic fracture with large degrees of plasticity. Worswick et al. (1981) proposed a ligament instability model predicting failure when

the ligament below the defect becomes fully plastic. Worswick (1981) modified the ligament instability model by applying a correction in terms of crack length to reduce the scatter in experimental results. CSA Z184 (1986) adopted an alternative ligament instability model. This model can be found in the renumbered CSA Standard CSA Z622, Appendix K. In this approach, failure is assumed to occur when plasticity in the section extends to 10% of the pipe circumference. In order to achieve a minimum factor of safety of 1.5 based on stress, a factor of 2.0 was applied on defect depth and 2.5 on defect length. The maximum depth of the defect was also restricted to 50% of the wall pipe thickness and the length to 10% of the circumference. These limitations were imposed due to the limits on the test data used to develop the model.

The CSA Z622 (1994) plastic collapse solution provides a simple equation to calculate a maximum allowable crack length:

$$C_{max} = 2\pi R[1.03 - \frac{\sigma_{pc}}{\sigma_Y}] / [18\frac{a}{t}] \tag{2.39}$$

where σ_Y is the specified minimum yield strength (SMYS). This equation can be inverted to obtain the maximum allowable stress (plastic collapse solution) as a function of defect size,

$$\sigma_{pc} = \sigma_Y\left[1.03 - \frac{18ca}{2\pi Rt}\right] \tag{2.40}$$

Note that equation (2.40) contains σ_Y instead of σ_f.

Chapter 3

Material Properties

All specimens were cut from parent material obtained from two short pipe sections of 8.4 or 13.4 mm thickness 762 mm diameter pipe supplied by NOVA Gas Transmission Ltd. The pipe was produced by Stelpipe using double arc submerged longitudinal seam welding of a controlled rolled skelp. The low alloy carbon steel pipe material corresponded to CAN3-Z245.1 Grade 483 or API 5L Grade X70. CAN3-Z245.1 Grade 483 line pipe is used principally for conveying natural gas, including gas transmission in Arctic areas.

Pipes for gas transport made to CAN3-Z245.1 (or API X70) specifications are mostly made as controlled rolled low alloy carbon steels with a special treatment to produce a fine ferrite grain size. Grade 483 line pipe, therefore, provides strength, toughness and weldability which are crucial to natural gas transportation pipeline systems. The mechanical property requirements for the CSA and API standards are given in Table 3.1.

The chemical composition limits for CSA and API are shown in Table 3.2. Linepipes can be classified by the manufacturing process. Manufacturing processes used for line pipe include forming steel plate in the U-O process followed by expansion, and rolling steel strip on

continuous mills into spiral pipe. The microstructure of linepipe is influenced by the addition of alloying elements and by the manufacturing process.

3.1 Microstructural Observations

Microstructural observations were made of samples taken from both pipes (8.4 and 13.4 mm thickness). Specimens were polished and etched to observe the microstructure in three orientations. Microhardness measurements were used to determine the through-thickness hardness variation.

3.1.1 Specimen Preparation

Samples used for the investigation of the microstructure were taken from both 8.4 mm and 13.4 mm thickness pipes. In order to make observations of the three orthogonal planes, three samples were cut from each pipe as shown in Figure 3.1. A low-speed band saw was used to cut samples using cutting fluid to prevent excessive heating during sectioning (ASM,1990a). All samples were mounted in bakelite and a series of grinding steps using successively finer grit silicon carbide papers were carried out on the mounted samples. The ground samples were polished using 1.0-μm Al_2O_3 and 0.3-μm Al_2O_3 consecutively on a medium-nap cloth using a low-speed polishing wheel. The specimens were etched immediately after final polishing. To reveal the ferrite grains, 2% Nital (2% HNO_3 in ethanol) was used as the etchant (ASM handbook, 1990a). The etching time was 15 seconds, and specimens were immediately washed with methanol to prevent excessive reaction between the etchant and the surface.

3.1.2 General Observations

A photomicrograph taken from a typical specimen is given in Figure 3.2. The microstructure consists of recrystalized ferrite (a), accicular ferrite (b) and carbon rich microconstituents (b). The ferrite grains were very small (4-6 μm) and equiaxed. Accicular ferrite, which looks like torn white rags, was found inside the dark carbon rich region. The carbon rich microconstituents were either upper bainite or lower pearlite. It was not possible to resolve those microconstituents using the optical microscope alone. This microstructure is typical of control-rolled low alloy carbon steel Grade 483 (X70) plate (Sage, 1981; Warren et al., 1981).

Since the controlled rolling process takes time and occurs over a wide temperature range, the microstructures developed in the final product are always heterogeneous and complex (Warren et al., 1981). The microstructures observed from the **T**, **R** and **C** planes are given in Figures 3.3 to 3.5. The microstructure observed on the **T** plane (Figure 3.3) shows no directional segregation of the carbon rich microconstituents. However, the microstructure observed on the **C** plane (Figure 3.4) and **R** plane show a banded segregation of the carbon rich microconstituents, which strings out in the rolling direction (longitudianl direction). This banded segregation of carbon rich microconstituents is typical of a rolled steel plate.

As shown in Figures 3.4 and 3.5, banding by severe segregation of the second phase at the center of the plate is observed from both pipes on the **C** and **R** planes. This carbon-rich centerline is typical of hot-rolled plate, and is usually a result of segregation in the ingot (ASM Handbook, 1991a).

The grain size was measured for both pipes using the Java system (JAVA, 1991). The results are summarised in Table 3.3. The ferrite grain size at the surface (within 1 mm of each surface) was slightly smaller than that at the mid-section for both pipes. The density of the carbon rich microconstituents at the surface was also higher than at the mid-section. This seems to be a result of the difference in cooling rate between the surface and the mid-section. Woodhead (1981) reported this effect of cooling rate on ferrite grain size for X70 pipeline steels, and noted that slow cooling resulted in ferrite grain growth. The well known Hall-Petch (Hall, 1951; Petch, 1953) relationship gives an inverse relationship between the material yield strength and grain size. The difference in yield strength between the surface and mid-section will be discussed later based on tensile tests and micro-hardness measurements.

The volume fraction of carbon rich microconstituents was measured manually using the JAVA system. This was close to 10% for both the mid-section and the surfaces as summarized in Table 3.4. While the number of carbon rich microconstituents at the mid-section was lower, the size of carbon rich microconstituents at the mid-section was larger than that at the surface, and thus the volume fraction was similar in the two areas.

3.2 Microhardness Testing

Since the geometry considered in this research involves a circumferential crack, the microstructural inhomogeneity in the thickness direction must be addressed. For plastic collapse analyses, material tensile properties are required, i.e., the stress-strain curve. Therefore, inhomogeniety was investigated in terms of the tensile properties.

It is well known that hardness testing is a convenient way to obtain approximate ultimate tensile properties for metallic materials. There are well-established relations between tensile

properties and hardness values for low-alloy carbon steels (ASM Handbook, 1991b). To examine the effect of microstructural differences in the thickness direction, Vickers microhardness testing was used. A Shimadzu HMV-2000 micro hardness tester, which is equipped with a microprocessor-controlled, digital read-out display that automatically converted from filar units to hardness values, was used for these measurements. The load was set to 200 *gf* as recommended for low-alloy carbon steels in the ASM Handbook (1991b).

The Vickers hardness values in the thickness direction were measured at least 3 times for both 8.4 and 13.4 mm thickness samples. Hardness measurements were taken from the surface to the center using 0.2 mm intervals, large enough to avoid any effect of residual stresses due to previous indentations. Figures 3.6 and 3.7 show the hardness values through the thickness for 8.4 and 13.4 mm specimens, respectively.

Figure 3.6 shows the variation in the hardness values for a 8.4 mm thickness specimen. The distance, r, from the surface was non-dimensionalized by dividing by the thickness, t. Since the variation in hardness near the outside surface was of major concern in this program, five more sets of measurements were made from the outside surface to the mid-section. The hardness measurements close to the outside surface (within 20% of the thickness from the surface) gave higher values compared to those measured near the mid-section. The hardness gradually decreased and became uniform through the mid-section, then was slightly elevated near the inside surface. Results for for both surfaces and mid-section are presented in Tables 3.5 and 3.6.

These hardness results are consistent with earlier observations of the grain size variation through the thickness. With decreasing grain size, the strength of the material increases. Therefore, the gradual decrease in hardness with increasing distance from the surface is

likely caused by the difference in ferrite grain size produced by different cooling rates between the surface and mid-section.

Figure 3.7 shows the hardness measurements from the 13.4 mm thick specimen. The decrease in hardness was more obvious than for the 8.4 mm specimen. The variation in cooling rate in the through-thickness direction for the thick specimen is likely less severe.

Figures 3.8 and 3.9 show the estimated tensile strength from the hardness measurements using the conversion table for low-alloy carbon steel (ASM Handbook, 1991b). Average tensile strengths were 702 and 673 MPa for 8.4 and 13.4 mm thickness specimens, respectively, which gives 4% higher strength for 8.4 mm pipe. Results for for both surfaces and mid-section are presented in Tables 3.7 and 3.8. Average values obtained within 5%, 10% and 20% of the thickness from the surface are given along with values from the corresponding mid-section. The results will be discussed in the following section along with the tensile test results.

3.3 Tensile Tests

Based on the observed inhomogeneity in the thickness direction from the microhardness testing (Section 3.2), tensile tests were designed to quantify the difference in tensile strength between the surfaces and the mid-section. Two sets of tensile test specimens were prepared, one each for 8.4 mm and 13.4 mm thickness pipes. All specimens were machined with a 60 mm gage length in the pipe axial direction (rolling direction) to accommodate a 2 inch (50.8 mm) extensometer for strain measurement. A set of tensile test specimens consisted of full-thickness specimens (circular and/or rectangular cross-section), mid-section specimens (circular and rectangular cross-section), and inside and outside surface specimens. The thickness of the surface specimens was restricted to no less than 20% of the thickness due

to machining difficulties. Five to six specimens were machined for each specimen type to assess repeatability. The specimen dimensions are given in Figures 3.10 and 3.11 for 8.4 and 13.4 mm thickness pipes, respectively.

A hydraulic Instron (model 4206) testing machine was used for all tests. The strain rate was 0.001/sec. A PC-based program was used to collect stress-strain data using a 2 inch extensometer (Instron) and a built in load cell. Figure 3.12 shows the test specimen under test.

3.3.1 Tensile Test Results

The yield stress was obtained using a 0.2% strain offset line, and the tensile strength was measured from the point of maximum load. Average tensile properties for each specimen configuration based on at least 5 samples in each case are presented in Tables 3.9 and 3.10 for 8.4 and 13.4 mm thick material, respectively.

True stresses, σ, were calculated using the following relation:

$$\sigma = \sigma_{eng}(\varepsilon_{eng} + 1) \tag{3.1}$$

where

$$\sigma_{eng} = \frac{P}{A_0}$$
$$\varepsilon_{eng} = \frac{l - l_0}{l_0} \tag{3.2}$$

P and A_0 are the applied load and initial cross section area, and l and l_0 are the current and initial gauge lengths, respectively. True strain was obtained from the relationship:

$$\varepsilon = ln\frac{l}{l_0} = ln(1+\varepsilon_{eng}) \tag{3.3}$$

Equations (3.2) and (3.3) are based on a constant volume assumption during deformation, and are valid until necking occurs.

The true stress-strain relationship was fit to the Ramberg-Osgood relation:

$$\varepsilon = \frac{\sigma}{E} + \alpha\left(\frac{\sigma}{\sigma_o}\right)^n \tag{3.4}$$

where α and n are curve fitting parameters.

8.4 mm thickness pipe

Full-thickness specimen (8 *mm* x 8 *mm* cross-section area) tensile tests gave a yield strength of 540 MPa and a 670 MPa tensile strength, with a modulus of elasticity of 210 GPa. The actual results are shown in Figure 3.13. Faucher et al. (1992) tested the same 8.4 *mm* thickness Grade 483 pipeline steel, and obtained yield and tensile strengths of 537 and 640 MPa, respectively, which are in good agreement with the present results. Since the specified minimum yield strength and tensile strength for Grade 483 pipeline steel (API X70) are 483 MPa and 565 MPa, respectively (ASM Metals Handbook, 1992a, CAN3-Z245.1, 1992), both yield and tensile strengths are well above this minimum requirement.

Two types of specimens were prepared to obtain the stress-strain curve from the mid-section, one with a rectangular (5 mm x 5 mm) and the other with a circular (D = 5 mm) cross-section. The stress-strain curves from these tests are shown in Figures 3.14 and 3.15 in comparison with the corresponding full-thickness specimen results. Stress-strain curves rectangular tensile specimens (5 mm x 5 mm) were slightly lower (about 2% between 1 and 3 % strain) than the full-thickness specimens test results. This result is consistent with the microhardness test results given in Section 3.2.

Figure 3.16 shows stress-strain curves for the outside surface test specimens (outer 20% of the thickness). The average stress was about 8% higher than the full-thickness test results. This tendency is consistent with the results from the microhardness measurements. Stress-strain curves obtained from the inside surface test specimens (inner 20% of the thickness, Figure 3.17) were also slightly higher (2.5%) than the full-thickness test results as expected from the microhardness measurements.

13.4 mm Thickness Pipe

Tensile tests with full-thickness specimens (13.4 mm x 8 mm rectangular cross-section) gave an average yield strength of 500 MPa and an average tensile strength of 640 MPa, with an elastic modulus of 210 GPa. Figure 3.18 shows the true stress – true strain curves obtained from these tests. The average yield strength is 8% lower than for the 8.4 mm thickness pipe. The 13.4 mm thickness pipe consists of coarser ferrite than the 8.4 mm thickness pipe. This difference in ferrite grain size is likely responsible for the lower strength in the 13.4 mm thickness pipe. Warren et al. (1981) investigated X70 pipeline steels made of 0.45% V steel with two different plate thicknesses (13 mm and 20 mm), and observed that the thicker plate, which contained coarser ferrite, had lower yield and tensile strengths. In the present case, both yield and tensile strengths were above the minimum requirement

specified by API and CSA standards (ASM Metals Handbook, 1992a, CAN3-Z245.1, 1992).

True stress – true strain curves obtained from mid-section specimen testing are shown in Figures 3.19 and 3.20 for rectangular (8 mm x 8 mm cross-section) and circular (D = 8 mm) specimens, respectively. The average stress was slightly lower (2%) than the full-thickness test results as expected from the microhardness measurements.

Figures 3.21 and 3.22 show true stress – true stain curves for outside surface specimens (outer 20% of the thickness) and inside surface specimens (inner 20% of the thickness), respectively. The average true stress from the outside surface specimens was about 6% higher than for the full-thickness specimens. The inside surface specimen results were about 2% higher. These results are consistent with the microhardness measurements.

In subsequent FEM analyses, the true stress – true strain curves shown in Figures 3.23 and 3.24 for the 8.4 and 13.4 mm specimens, respectively, were used.

3.4 Orthotropic Characteristics

Rolled steel plate usually produces orthotropic characteristics. That is, the material possesses symmetry about three orthogonal planes which are oriented at 90° to each other. While the von-Mises stress function is used universally for isotropic materials, Hill's stress function is widely accepted for use in anisotropic (and orthotropic) material analyses.

3.4.1 Hill's Stress Potentials for Anisotropic Metal Plasticity

Hill's stress function is an extension of the Mises stress function. The function includes 6 parameters which accommodate anisotropic behaviour. The function is given by

$$f(\sigma)=\sqrt{F(\sigma_{22}-\sigma_{33})^2+G(\sigma_{33}-\sigma_{11})^2+H(\sigma_{11}-\sigma_{22})^2+2L\tau_{23}{}^2+2M\tau_{31}{}^2+2N\tau_{12}{}^2} \quad (3.5)$$

in terms of rectangular (Cartesian) stress components, where F, G, H, L, M, N are Hill's stress potentials which are constants to be obtained from tensile tests in different orientations. They are defined using

$$\begin{aligned}
F &= \frac{\sigma_0^2}{2}\left(\frac{1}{\bar{\sigma}_{22}^2}+\frac{1}{\bar{\sigma}_{33}^2}-\frac{1}{\bar{\sigma}_{11}^2}\right)=\frac{1}{2}\left(\frac{1}{R_{22}^2}+\frac{1}{R_{33}^2}-\frac{1}{R_{11}^2}\right),\\
G &= \frac{\sigma_0^2}{2}\left(\frac{1}{\bar{\sigma}_{33}^2}+\frac{1}{\bar{\sigma}_{11}^2}-\frac{1}{\bar{\sigma}_{22}^2}\right)=\frac{1}{2}\left(\frac{1}{R_{33}^2}+\frac{1}{R_{11}^2}-\frac{1}{R_{22}^2}\right),\\
H &= \frac{\sigma_0^2}{2}\left(\frac{1}{\bar{\sigma}_{11}^2}+\frac{1}{\bar{\sigma}_{22}^2}-\frac{1}{\bar{\sigma}_{33}^2}\right)=\frac{1}{2}\left(\frac{1}{R_{11}^2}+\frac{1}{R_{22}^2}-\frac{1}{R_{33}^2}\right),
\end{aligned} \quad (3.6)$$

$$\begin{aligned}
L &= \frac{3}{2}\left(\frac{\tau_0}{\bar{\tau}_{23}}\right)^2=\frac{3}{2R_{23}^2},\\
M &= \frac{3}{2}\left(\frac{\tau_0}{\bar{\tau}_{13}}\right)^2=\frac{3}{2R_{13}^2},\\
N &= \frac{3}{2}\left(\frac{\tau_0}{\bar{\tau}_{12}}\right)^2=\frac{3}{2R_{12}^2}
\end{aligned}$$

where σ_0 is the reference yield stress obtained from a tensile test in one direction, and $\tau_0 = \frac{\sigma_0}{\sqrt{3}}$. Direct, $\overline{\sigma}_{11}$, $\overline{\sigma}_{22}$, $\overline{\sigma}_{33}$, and shear, $\overline{\tau}_{12}$, $\overline{\tau}_{23}$, $\overline{\tau}_{13}$ yield strengths are obtained in the three orthogonal directions. R_{11}, R_{22}, R_{33}, R_{23}, R_{13}, R_{12} are anisotropic yield ratios ($R_{11} = \frac{\sigma_{11}}{\sigma_0}, R_{22} = \frac{\sigma_{22}}{\sigma_0}$, etc.).

Using the above stress potentials, the flow rule becomes

$$d\varepsilon^{pl} = d\lambda \frac{\partial f}{\partial \sigma} = \frac{d\lambda}{f} b, \tag{3.7}$$

where, from the definition of f above,

$$b = \begin{bmatrix} -G(\sigma_{33} - \sigma_{11}) + H(\sigma_{11} - \sigma_{22}) \\ F(\sigma_{22} - \sigma_{33}) - H(\sigma_{11} - \sigma_{22}) \\ -F(\sigma_{22} - \sigma_{33}) + G(\sigma_{33} - \sigma_{11}) \\ 2N\sigma_{12} \\ 2M\sigma_{31} \\ 2L\sigma_{23} \end{bmatrix} \tag{3.8}$$

Assuming that the elastic strain rates are small compared to the plastic strain rates, the plastic incompressibility condition gives

$$d\varepsilon_{11} + d\varepsilon_{22} + d\varepsilon_{33} = 0 \tag{3.9}$$

Therefore, it is possible to obtain the 6 stress function parameters (potentials) in terms of strains which are available from tensile testing.

3.4.2 Transverse Anisotropy in Rolled Steel Plate

In the manufacture of rolled steel plate, an anisotropic microstructure is usually expected. Consider 1 and 2 to be the rolling and cross directions in the plane of the steel plate and 3 the thickness direction. The rolling process, as observed for the Grade 483 pipeline steel, usually produces an isotropic structure in terms of strength in the 1-2 plane but has a different strength in the thickness (3) direction. This is normally referred to as *transverse anisotropy.*

This anisotropic structure can be considered as orthotropic, having three orthogonal axes which correspond to the rolling direction, the cross direction and the thickness direction. For such orthotropic structures, material constants required for Hill's stress function can be derived by performing tensile tests only in the rolling and cross directions.

For a tensile test performed in the rolling direction, the flow rule given by equations (3.7) and (3.9) gives the following relationship between the incremental strain ratios:

$$d\varepsilon_{11} : d\varepsilon_{22} : d\varepsilon_{33} = G + H : -H : -G \tag{3.10}$$

on the assumption of relatively small elastic strains. Then, the so-called r-value, the ratio of width (cross direction) to thickness strain, is defined by

$$r_1 = \frac{d\varepsilon_{22}}{d\varepsilon_{33}} = \frac{H}{G} \tag{3.11}$$

For a tensile test performed in the cross direction, the incremental strain ratios can be derived in a similar way.

$$d\varepsilon_{11} : d\varepsilon_{22} : d\varepsilon_{33} = -H : F + H : -F \tag{3.12}$$

and

$$r_2 = \frac{d\varepsilon_{11}}{d\varepsilon_{33}} = \frac{H}{F} \tag{3.13}$$

By using r_1 and r_2, which can be measured from tensile tests, the parameters required for Hill's stress function can be obtained.

A transverse anisotropic material gives $r_1 = r_2$. And from equation (3.6),

$$R_{11} = R_{22} = 1 \tag{3.14}$$

and by relating equations (3.11) and (3.6)

$$R_{33} = \sqrt{\frac{r_1 + 1}{2}} \tag{3.15}$$

After assuming $R_{12} = R_{23} = R_{31} = 1$. As a result, $L = M = N = 1.5$.

3.4.3 Results

Since the microstructures in the rolling and cross directions were observed to be similar, all parameters were calculated on the basis of transverse anisotropy. The values for r_1 were calculated using the strains measured from both the uniformly deformed region and the necked region during a post mortem examination of the tensile test specimens used in

Section 3.3. R_{33} values were derived from the tensile test data in the rolling direction using equation (3.15). All of the results are summarized in Tables 3.11 and 3.12 along with average strain measured from tensile specimens. A significant difference in the thickness direction was observed, indicated here by R_{33} values different from 1.

The anisotropic parameters are very sensitive to the measured strains. It was difficult to obtain an accurate measurement of strain in the uniformly deformed cross-section because the amount of strain was so small. As a result, the parameters show considerable scatter. However, the measurements from the necked area were more consistent since this area experienced much higher strain. It is thus recommended to use parameters obtained from the necked area. For the purposes of subsequent FEM analysis, an average value for R_{33} of 0.93 was used for the 8.4 mm thick material, and 0.87 for the 13.4 mm thick material.

3.5 Tensile Test Simulation

A tensile specimen represents a simple geometry which permits a direct comparison between finite element analysis and experimental results. By simulating the tensile test with the finite element method, suitable numerical methods and options for plastic collapse analysis can be obtained. The results of numerical analysis of an elastic-plastic component are influenced by mesh design, plasticity theory, and the algorithm used to obtain the non-linear solution. In these tensile test simulations, plasticity theories and numerical methods for plastic collapse were investigated for application to subsequent finite element analyses of cracked specimens and components.

Material true stress – true strain data used for the finite element analyses were taken from the data presented in section 3.3.1, Figures 3.29 and 3.30.

3.5.1 Modelling a Tensile Specimen

Two typical tensile test specimens having rectangular cross sections, an 8 mm x 8 mm full-thickness specimen (8.4 mm thickness material) and an 8 mm x 13 mm full-thickness specimen (13.4 mm thickness material), were chosen from the tensile test matrix. Half of a tensile specimen was modelled with 160, 20-node quadratic iso-parametric brick elements which use a reduced Gaussian integration scheme (C3D20R), as shown in Figure 3.25. The full thickness of the specimen was modelled to accommodate inhomogeneity in the thickness direction. Since the purpose of the analysis was to simulate plastic collapse including necking, the mesh was designed with 160 elements, enough to accommodate local deformation. The grip was modelled using fixed boundary conditions at the top of specimen, and displacement control was applied to simulate the actual tensile test. Due to this loading condition, necking was expected at the bottom surface of the specimen (Figure 3.25), which bears the least constraint. The size of the elements was reduced at the bottom of the specimen to allow for more significant geometry changes in the area where necking was expected. Since the material behaviour was elastic-plastic, a non-linear static analysis was chosen. ABAQUS uses Newton's method to solve the non-linear equilibrium equations.

Plastic collapse is an instability problem, where the load (or stress) may decrease with increasing displacement (or strain) after the point of necking. The modified Riks method (Crisfield, 1981) is an algorithm which allows an effective solution in such cases. ABAQUS (HKS, 1996) provides the modified Riks algorithm for solving non-linear static problems as an option. This option was used for the following plastic collapse analyses.

ABAQUS provides true stresses and strains at each integration point in each element, and reaction forces and displacements at each node. In order to compare the finite element analysis results directly with the actual tensile test, the engineering stress was calculated by

dividing the vertical components of the reaction forces acting at the bottom of the model with the initial net-section area. The engineering strain was obtained using the displacement for the node matching the actual extensometer location. Then, the true stress and true strain were obtained from the relation given by equations (3.1) and (3.3).

All analyses were performed using the incremental theory of plasticity coupled with large displacement deformation and the modified Riks algorithm.

3.5.2 Point of Instability

The tensile test simulation predicted a point of instability where the maximum load was reached as shown in Figure 3.26. After this point, the engineering stress decreased with increasing displacement (the unloading process), representing negative stiffness due to the non-linear change in geometry. The load applied at this point can then be considered as a numerically determined maximum load carrying capacity, that is, the plastic collapse load. After instability occurs, specimen deformation becomes localised with increasing displacement. The deformed mesh after necking is shown in Figure 3.27. As shown in Figure 3.27, localisation at the bottom of the specimen, which represents *necking*, is obvious after the point of instability. Therefore, the instability point can be considered an initiation point for numerically determined necking.

In a numerical analysis of a tensile specimen, the condition for necking can be derived based on continuum mechanics. The load applied to a tensile specimen, P, is related to the true stress, σ, and instantaneous area, A, through

$$P = \sigma A \tag{3.16}$$

Therefore

$$dP = \sigma dA + A d\sigma \tag{3.17}$$

Necking occurs at the maximum load, where $dP = 0$. Equation (3.17) becomes

$$\frac{d\sigma}{\sigma} = -\frac{dA}{A} = \frac{dl}{l} = d\varepsilon \tag{3.18}$$

Therefore, the true stress at maximum load is

$$\sigma = \frac{d\sigma}{d\varepsilon} \tag{3.19}$$

This condition can be applied to the Ramberg-Osgood relationship. For example, from equation (3.4),

$$\frac{\sigma}{\sigma_0} = \alpha^{-\frac{1}{n}} (\varepsilon_{pl})^{\frac{1}{n}} \tag{3.20}$$

where $\varepsilon_{pl} = \varepsilon - \varepsilon_{el}$ is the plastic strain. Taking the derivative of equation (3.20) with respect to strain gives

$$\frac{d(\frac{\sigma}{\sigma_0})}{d\varepsilon} = \frac{1}{n} \cdot \alpha^{-\frac{1}{n}} (\varepsilon_{pl})^{\frac{1}{n}-1} \tag{3.21}$$

Equating (3.20) and (3.21),

$$\alpha^{\frac{1}{n}}(\varepsilon_{pl})^{\frac{1}{n}} = \frac{1}{n}\cdot\alpha^{\frac{1}{n}}(\varepsilon_{pl})^{\frac{1}{n}-1} \tag{3.22}$$

Gives the following condition which must be satisfied at the onset of necking for a Ramberg-Osgood material:

$$\varepsilon_{pl} = \frac{1}{n} \tag{3.23}$$

That is, the true plastic strain at the point of necking is numerically equal to the inverse of the strain hardening exponent, n, for a Ramberg-Osgood material. For our 8.4 mm thick material, n = 11.1, giving a true plastic strain at necking of 0.0897, and 0.093 for n = 10.9 for our 13.4 mm thick material. These values were the same as these obtained in the finite element analyses.

The finite element analysis results for 8.4 and 13.4 mm thickness specimens are shown in Figures 3.28 and 3.29, respectively along with the tensile test results. The finite element analysis for the 8.4 mm thickness specimen predicts the necking at a true strain of 0.09 (true stress of 714 MPa), and is in good agreement with the test results. The finite element analysis for the 13.4 mm thickness specimen gives the point of instability at a true strain of 0.093 (true stress of 670 MPa). The tensile test gave a true strain of approximately 0.105 (true stress of 680 MPa) at the initiation of necking. The difference between the two results was not significant.

In order to verify the numerical plastic collapse solution given by equation (3.23), materials with three different n values of 5, 20 and ∞ and a yield stress of 540 MPa were used with a the 8.4 mm thickness mesh. The engineering stress – strain curves are shown in Figure 3.30.

The engineering stress was used to check the maximum load point clearly. The maximum load occurred at a true strain of *1/n* for all cases as shown in Figure 3.30. The predicted true stress at maximum load for all cases was the same as the input true stress corresponding to a true strain of *1/n*. It is thus clear that plastic collapse is predicted based on equation (3.23).

3.5.3 Plane Stress versus Plane Strain

The incremental theory of plasticity, based on the Levy-Mises equations, defines the flow rule as

$$d\varepsilon_{ij} = \frac{\partial f(\sigma_{ij})}{\partial \sigma_{ij}}(d\lambda) \tag{3.24}$$

where $f(\sigma_{ij})$ is the isotropic yield function, and $d\lambda$ is the plastic compliance. For the von Mises criterion, equation (3.24) becomes

$$\left(d\varepsilon_{ij}\right)_p = S_{ij}d\lambda \tag{3.25}$$

where S_{ij} represents the deviatoric stress components. This implies that the ratio of the current incremental plastic strain to the current deviatoric stress is constant. An alternate form of equation (3.25), in which σ is expressed in terms of the three principal stress components, is

$$\begin{aligned} d\varepsilon_1 &= d\lambda[\sigma_1 - \tfrac{1}{2}(\sigma_2 + \sigma_3)] \\ d\varepsilon_2 &= d\lambda[\sigma_2 - \tfrac{1}{2}(\sigma_1 + \sigma_3)] \\ d\varepsilon_3 &= d\lambda[\sigma_3 - \tfrac{1}{2}(\sigma_1 + \sigma_2)] \end{aligned} \tag{3.26}$$

It can be shown that in terms of the effective stress, σ_e, and effective strain, ε_e, $d\lambda = d\varepsilon_e/\sigma_e$. By applying this relation, equation (3.26) becomes

$$\begin{aligned} d\varepsilon_1 &= \frac{d\varepsilon_e}{\sigma_e}[\sigma_1 - \tfrac{1}{2}(\sigma_2 + \sigma_3)] \\ d\varepsilon_2 &= \frac{d\varepsilon_e}{\sigma_e}[\sigma_2 - \tfrac{1}{2}(\sigma_1 + \sigma_3)] \\ d\varepsilon_3 &= \frac{d\varepsilon_e}{\sigma_e}[\sigma_3 - \tfrac{1}{2}(\sigma_1 + \sigma_2)] \end{aligned} \tag{3.27}$$

For a plane stress analysis, $\sigma_1 = \sigma_3 = 0$, and $\sigma_e = \sigma_2$. Therefore, the σ_2 and ε_2 must be equivalent to σ_e and ε_e, respectively. A plane stress analysis will produce the same true stress - true strain curve as the input σ_e and ε_e data.

For plane strain conditions, $\varepsilon_3 = 0$, and thus $\sigma_3 = 0.5\sigma_2$, and $d\varepsilon_2 = -d\varepsilon_3$ from equation (3.27). The von Mises effective stress in terms of the three principal stresses is given by

$$\sigma_e = \frac{1}{\sqrt{2}}\sqrt{((\sigma_2 - \sigma_1)^2 + (\sigma_3 - \sigma_1)^2 + (\sigma_2 - \sigma_3)^2)} \tag{3.28}$$

Using $\sigma_1 = 0$, $\sigma_3 = 0.5\ \sigma_2$ in equation (3.28) gives $\sigma_2 = 1.155\ \sigma_e$. By applying these conditions to equation (3.27), $d\varepsilon_2$ becomes

$$d\varepsilon_2 = \frac{d\varepsilon_e}{\sigma_e}[0.75\sigma_2] = 0.75(\frac{\sigma_2}{\sigma_e})d\varepsilon_e = 0.86 \cdot d\varepsilon_e \qquad (3.29)$$

Since the measured strain is ε_2, the resulting true strain in the plane strain case must be 14% less than the equivalent strain. At the same time, the measured true stress (σ_2) will be 1.155 times higher than for plane stress. For a Ramberg-Osgood material, this decrease of true strain (ε_2) requires $1/(0.86)^{1/n}$ times higher true stress (σ_2) to produce the same effective stress compared to the plane stress analysis. Combining these two effects, the true stress measured (σ_2) from the plane strain analysis will be 1.17 times higher than that (σ_2) of plane stress analysis for 8.4 mm thick material (n = 11.15). The factor is also approximately 1.17 for 13.4 mm thick material. The plane strain analysis resulted in 1.17 times higher true stress - true strain curves than those of the plane stress analyses as shown in Figures 3.31 and 3.32.

For 8.4 mm thick material, the plane stress analysis showed the maximum load instability at a true strain of 0.089, the same values as was observed in the tensile test analysis. The plane strain analysis resulted in the maximum load at a true strain of 0.077, 13.4% less than the plane stress analysis. This is consistent with the arguments presented above.

While both the plane stress and the plane strain meshes have the same constraint throughout the width (the 1-direction in Figure 3.25), the tensile test specimen mesh made of 3-D solid elements has different constraint at the surface and the centre. This difference results in localised deformation after instability has occurred. The equivalent plastic strain contours at maximum stress are plotted for both the plane strain and the plane stress analyses (8.4 mm thickness material) in Figure 3.33. Plastic strain was close to 0.089 through the width for both cases. The 3-D analysis showed a difference in the plastic strains between the center and the surface after the instability had occurred (Figure 3.34). For all cases, the

instability occurred when the plastic strain reached 0.089 in the width direction as predicted analytically. Exactly the same behaviour was observed for the 13.4 mm thick material analysis.

In order to investigate the effect of strain hardening, three different n values of 5, 20 and ∞ (perfect plastic) were applied in both the plane strain and plane stress analyses. The resulting engineering stress – strain curves are shown in Figure 3.35 along with the results for $n = 11.1$. The perfect plastic material resulted in a 1.155 times higher engineering stress at the point of instability for the plane strain analysis, which is consistent with the von-Mises material analysis mentioned above. The materials with n values of 5 or 20 resulted in a 19 % or 16 % difference, respectively, which are also consistent with the relationship given by equation (3.29). These results will be plotted as limiting values as the crack depth becomes zero for SENT results to be presented in Chapter 4.

3.5.4 Finite Element Analyses based on Microstructural Characteristics

In the previous sections, microstructural analyses revealed inhomogeniety in the thickness direction, and also the orthotropic characteristics of the material. These results were used in finite element analyses using ABAQUS. The same 3-D mesh which was used for the isotropic material analysis was modified to account for different material properties at the surface and mid-section. This mesh is shown in Figure 3.36. Based on the micro-hardness measurements and tensile tests, the thickness was divided into surface regions (20% of the thickness) and the mid-section (60% of the thickness). The true stress – true strain curves for the mid-section, inside and outside surfaces were obtained from Figures 3.23 and 3.24 for the 8.4 and the 13.4 mm thick materials, respectively.

As discussed in Section 3.4.1, the orthotropic behaviour of pipeline steel plate can be modeled in terms of Hill's stress function, which is an option in ABAQUS. R_{33} values obtained from the tensile tests (0.93 for the 8.4 mm thickness material and 0.87 for the 13.4 mm thickness material) were applied in the present analysis.

Figures 3.37 and 3.38 show the true stress – true strain curves resulting from the microstructure based finite element analysis along with the isotropic analysis results. The true stress – true strain curves from the microstructure based analysis exactly coincide with the isotropic material analysis results and test results. This implies that the true stress – true strain curves measured at the mid-section, inside and outside surface are reasonable.

The point of instability was also at the same point as observed from the isotropic analysis. Since the tensile test specimen only produces a uniaxial state of stress, the resulting true stress – true strain curve is independent of the R_{33} value until deformation becomes localised. After the formation of necking produces stresses in all three directions, the deformed section produced more strain in the 1 direction than that for the isotropic analysis as shown in Figure 3.39. These same options were used in the microstructure based finite element analysis for SENT specimens.

3.6 Summary

Based on microstructural investigations of Grade 483 pipeline steel, the following observation can be made:

- The rolled steel plate used herein had transverse anisotropy. This implies that the strength properties are the same in the rolling and cross (circumferential) directions, but

different in the thickness direction. Quantification of these anisotropic characteristics was achieved in terms of Hill's stress function. The anisotropic parameters measured from the tensile test specimens (Tables 3.11 and 3.12) were applied in the finite element analyses to be discussed in subsequent chapters.

- The inhomogeniety in the thickness direction was quantified by conducting micro-hardness tests and a series of tensile tests for both 8.4 and 13.4 mm thickness pipe. The results from both microhardness testing and tensile testing were in good agreement, and gave higher strengths at the outside and inside surfaces. The stress-strain curves resulting from these tensile tests, as shown in Figures 3.23 and 3.24 for both 8.4 and 13.4 mm thickness pipes, were used in the finite element analyses to be discussed in subsequent chapters.

- A finite element analysis was performed on tensile test specimens to predict the plastic collapse behaviour. Necking was observed at a true strain of $1/n$. The numerically determined point of necking was very close to the test results. Microstructure based finite element analyses were performed by applying inhomogeneity and orthotropic characteristics. The finite element results were consistent with the corresponding tests.

Chapter 4

SENT Specimens

An SENT specimen with fixed grips simulates a surface crack without considering the effect of crack surface length or shape. An investigation of plastic collapse in SENT specimens was carried out as a first step in the analysis of the plastic collapse behaviour of a surface crack in a pipe.

Lambert (1995) performed a series of SENT fracture tests, and found that high-constraint specimens (i.e., deep crack SENT) resulted in higher limit loads compared to low-constraint specimens (i.e., shallow crack SENT). With increasing crack depth, the maximum net-section stress was observed to increase. From these results, it is clear that local crack-tip constraint affects global plastic flow behaviour.

In this chapter, the constraint effects on plastic collapse for SENT specimens will be discussed based on experimental and finite element analysis results. Extensive finite element analyses have been completed with material properties obtained from tensile tests and microstructural observations discussed in Chapter 3.

4.1 Experimental Results

SENT testing (Lambert, 1992, 1993) was conducted in two phases. In the first phase, three different configurations as illustrated in Figure 4.1 (12.5 mm wide (a), 25 mm wide (b), or 25 mm wide with severe side grooves to produce a 12.5 mm wide net-section (c)) were designed to reveal the proper width satisfying plane strain out-of-plane constraint. As a result of first phase testing, all second phase specimens were made 25 mm wide without side-grooves as illustrated in Figure 4.1 (b). Specimens were cut from both 8.4 and 13.4 *mm* thickness pipes, and their axes were aligned with the longitudinal axis of the pipe, so that the cracks were in the L-S orientation.

The test matrix, giving the actual specimen dimensions, the maximum nominal stress (load divided by uncracked area) and the corresponding net-section stress (load divided by ligament net-section area), is given in Tables 4.1 and 4.2 for phase I and phase II tests, respectively. The failure mode for almost all specimens was rupture or plastic collapse preceded by severe necking at the net-section. A small amount of ductile tearing prior to necking was observed in only two specimens, E3 and E6. However, the amount of crack growth was insignificant, and both specimens failed after a significant amount of plastic deformation led to necking at the ligament without further crack growth. These experimental results demonstrated that the failure of SENT specimens made of Grade 483 steels was dominated by plastic collapse rather than fracture.

4.1.1 Failure Mechanism

The failure mechanism observed in most SENT specimens is illustrated in Figure 4.2. The specimen, loaded in tension, has insufficient hydrostatic stress at the crack-tip to cause a

crack to tear through the ligament. With increasing load, therefore, the crack-tip blunts (rather than propagates) due to shear deformation along the direction of maximum shear stress (Figure 4.2 (b)). The plastic strain increases without crack propagation. At maximum load, the increase in net-section stress caused by strain hardening is just offset by the decrease in load-carrying area located between the two slip lines; this is referred to as geometric softening (Honeycombe, 1984). At this maximum load, necking occurs at the backside of the specimen (Figure 4.2 (c)); that is, deformation becomes localised. Since a region with high hydrostatic stress delays plastic flow, cracked specimens in which the crack-tip region produces a significant hydrostatic stress field support a higher maximum net-section stress unless plastic behaviour is interrupted by crack propagation.

After the initiation of necking, rapid ligament contraction from the backside of the specimen, between the two symmetrical maximum shear stress planes, occurs without further increase in load (Figure 4.2 (d)). The reduced area experiences increasing strain, and higher net-section stresses. The stress concentration on the reduced area increases the hydrostatic stress at the crack-tip. The increased hydrostatic stress at the crack-tip, combined with high strain, allows voids to nucleate, grow, and finally coalesce to produce tearing through the contracted ligament (Figure 4.2 (e)). This tearing process is accompanied by continuous ligament area contraction from the back side, and the final failure shape is at an angle rather than parallel to the fatigue pre-crack plane as shown in Figure 4.2 (f).

As illustrated schematically in Figure 4.2 (f), the fracture surface plane deviated from the pre-crack plane by about 30-35°. The % reduction in area of the fracture surface was close to 70%. No difference was observed between shallow and deep cracked specimens. For most specimens, the fracture surface was flat and smooth which implies that the fracture occurred by a ductile tearing process. Figures 4.3 and 4.4 show details near the cracktip for

the fractured specimens with $a/t = 0.25$ (J10) or 0.77 (J3). Only a small amount of crack-tip blunting was observed prior to ductile tearing. No significant ductile crack growth which would lead to ductile fracture prior to necking was observed from either shallow or deep crack specimens. This implies that the maximum load was obtained at the point of necking, which occurred prior to the ductile tearing process.

Figure 4.5 shows the deformed microstructure in the thickness direction of fractured specimen J10 with $a/t = 0.25$. The microstructure in the ligament is at an angle to the loading line, perpendicular to the fractured surface. The region which experienced high strain thus produced a significant amount of net-section reduction prior to ductile tearing.

A deeply cracked specimen, J6, showed a different failure mechanism: failure by shear slip along the maximum shear stress plane with no tearing. The net-section stress increased until shear bands formed along the symmetrical maximum shear planes, and the specimen failed through one of these shear bands. The resulting failure line between the two broken parts was not symmetrical. This is similar to the shearing off zone (cup and cone fracture process) observed from uniaxial tensile test specimens. In this case, while yielding in the ligament area was suppressed by high hydrostatic stresses, the material was tough enough to withstand failure until voids grew and coalesced. Final failure occurred with a sudden shearing off through the shear band. These specimens carried higher net-section stresses due to the suppression of plastic flow.

Several shallow cracked specimens, e.g., J1 and J2, failed at unusually high loads. They had unusual features on their fracture surfaces, such as material inhomogeneity that interrupted fatigue pre-cracking or irregular fatigue pre-cracks that made net-section calculations difficult.

4.1.2 Maximum Net-section Stress and Constraint

Major design codes define the plastic collapse solution for SENT specimens as the point where the net-section stress reaches the material flow stress. For an SENT specimen, the net-section stress, σ_{NS} is defined by

$$\sigma_{NS} = \frac{P}{W(t-a)} \tag{4.1}$$

where P is the applied load, t is the thickness, a is the crack depth, and W is the width out of the plane. PD 6493:1991 recommends the average of the yield and tensile strength for the flow stress. For pipeline steels, it is common to use the yield stress plus 69 MPa (10 ksi). The measured yield and tensile strengths for 8.4 mm thickness pipe were 540 and 660 MPa, respectively, which gives an average of 600 MPa. For 13.4 mm thickness pipe, yield and tensile strengths of 500 and 640 MPa, giving an average of 570 MPa. In the present analysis, the flow stress was defined using the yield strength plus 69 MPa, giving 609 or 569 MPa for 8.4 or 13.4 mm thick pipes, respectively.

The maximum net-section stresses, normalized by the appropriate flow stress for each SENT specimens, are presented in Figure 4.6. All specimens failed at a higher maximum net-section stress than predicted using the conventional limit load. The normalized failure stress generally increases with normalized crack depth. Those points which deviated from this increasing trend were exceptional. Specimens G6, G10 and J9 had load-displacement curves which displayed excessive scatter due to equipment problems, and produced lower maximum net-section stresses than the others. Specimens J1 and J2 had irregular crack fronts as mentioned earlier, which resulted in higher maximum net-section stresses compared to the others. These specimens were excluded from subsequent analyses.

All side-grooved specimens resulted in an opposite tendency. That is, the maximum net-section stresses for low *a/t* specimens were higher than those for high *a/t* specimens. The severely side-grooved specimens used here exhibit much higher constraint. Since this excessive constraint is unrealistic, side-grooved specimens were not included in the subsequent analyses.

The differences in maximum net-section stresses as a function of *a/t* ratio were analyzed in terms of the material inhomogeneity discussed in Chapter 3. As observed from both micro-hardness and tensile tests, the material mid-section was softer than the surface (outer 20 % of thickness). This difference in the thickness direction was considered by applying a different material flow stress to the mid-section and surface. Flow stresses for each section were obtained by adding 69 MPa to the yield stresses listed in Tables 3.9 and 3.10. The ligament area was divided into sections as appropriate and the flow stresses for the ligament were obtained from the section flow stresses and the rule of mixtures. The results are presented in Figure 4.7. This calculation invariably produced an increased material flow stress in the ligament area, which reduced the failure ratio for deep cracked specimens slightly and produced marginally better results. The maximum net-section stress still shows an increasing tendency with increasing *a/t* ratio. Note that the biggest apparent reduction in scatter in this figure is due to the elimination of side-grooved and other specimens.

The length of the crack front, which is the specimen width for an SENT specimen, is an important factor in characterizing the out-of-plane constraint. A longer crack front more closely simulates a plane strain condition in the middle. The length of the crack ligament is also an important factor, because the shear lips at the crack surfaces are influenced by the ligament length. In this case, a smaller ligament produces smaller shear lips, and results in higher constraint for the geometry. The ligament length also has an inverse relation to in-

plane constraint. Therefore, a constraint parameter, C_{cp}, is herein defined as the specimen width, W, divided by the specimen ligament, b,

$$C_{cp} = \frac{W}{b} \tag{4.2}$$

The distribution of maximum net-section stresses as a function of this constraint parameter is given in Figure 4.8. The maximum net-section stresses were normalized by dividing by the material ultimate stress. The ultimate stress was used so that the resulting curve fit would pass through unity at $W/b = 0$ since this can be considered representative of an uncracked tensile specimen. The maximum net-section stress increases with increasing C_{cp} in an approximately linear manner. The straight line shown in the Figure 4.8 was obtained using linear regression and had an R^2 value of 0.91.

An empirical plastic collapse solution for SENT specimens was derived as a function of the constraint parameter defined in equation (4.2). Test results for 12.5 and 25 *mm*-wide specimens were used. Based on the linear regression line in Figure 4.8, the empirical plastic collapse solution (based on the nominal stress) is given by

$$\sigma_{pc} = \sigma_f \left(0.02573 \cdot \frac{W}{b} + 1 \right) \cdot \frac{A_{net}}{A_o} \tag{4.3}$$

where $A_O = tB$, and $A_{net} = (t-a)B$ (net-section area). The term involving W/b in the above equation is an empirical correction for the in-plane and the out-of-plane constraint. Equation (4.3) provides a narrower band for the SENT test results compared to the conventional method as shown in Figure 4.9. While the conventional method is not capable

of reflecting the effect of constraint observed from the SENT test, this empirical solution provides good agreement with the test results.

4.2 Finite Element Analyses

In order to investigate constraint effects on plastic collapse for SENT specimens in terms of continuum mechanics, finite element analyses were performed using the finite element program ABAQUS, version 5.5 (HKS, 1996).

In order to investigate constraint effects, two and three-dimensional finite element analyses were performed. Large displacement analyses using incremental plasticity were used based on the previous tensile test simulations. The net-section stress and the load line displacement (the displacement over a 55 mm gage length), were used to compare the global deformation of specimens and to facilitate comparison with experimental results.

4.2.1 Two-dimensional Analyses

Two-dimensional plane stress or plane strain finite element analyses were performed on four crack geometries with crack depths, a/t, of 0.2, 0.4, 0.6 or 0.8, to investigate in-plane constraint effects on plastic collapse. The basic mesh design was adapted from the fracture analysis conducted as a part of the numerical program on the same SENT specimens by the author (Choi, 1993). A detailed of the mesh for a crack depth, a/t, of 0.2 is shown in Figure 4.10. Three other crack depths are shown in Figure 4.11. Because of symmetry, only the upper-half plane was modelled.

The model was designed to use eight node iso-parametric quadrilateral elements with reduced integration. A reduced integration scheme was used because it usually yields more accurate results and reduces running time (HKS, 1996; Barlow, 1976). Reduced integration also removes one degree of constraint, therefore preventing locking associated with fully developed plastic flow. When the purpose of the analysis is to analyze crack tip stresses and strains, a very high level of mesh refinement is required (McMeeking and Parks, 1979). However, a plastic collapse analysis should be performed with larger crack tip elements compared to a fracture analysis in order to allow more deformation on the way to plastic collapse. The fan mesh around the crack-tip (Figure 4.10) was designed with 16 x 8 elements in this case. Since it is advisable to begin with a finite radius at the crack-tip when the crack-tip is subject to high plasticity, the mesh was designed with an initial blunt notch radius to ligament length ratio of 0.01. During loading, the crack tips blunted to maximum openings between 10 and 15 times their undeformed openings so that the initial notch radius had no effect on the results.

Traction free boundary conditions were applied on the free surfaces and the initially blunted crack surface, while the node at the crack tip was restrained to remain on the line of symmetry along with all other nodes through the crack ligament. An evenly distributed displacement was applied at the edge of the specimen to model fixed grip loading conditions, which does not allow the specimen to rotate. A schematic illustration of the boundary conditions is given in Figure 4.12.

Out-of-plane Constraint Effects - Plane Strain vs Plane Stress

Results for 2-D plane strain and plane stress analyses are shown in Figures 4.13 and 4.14 for 8.4 mm and 13.4 mm thickness specimens ($a/t = 0.25$), respectively. Resulting maximum net-section stresses are summarized in Tables 4.3 and 4.4.

The maximum net-section stress obtained from the plane stress analysis for the 8.4 mm thick material was 29% less than that of the plane strain analysis. The 13.4 mm thick material produced a 28% difference between plane strain and plane stress analyses.

The maximum net-section stress based on the plane stress analysis was 12% less than that of the 2-D plane stress bar analysis (658 MPa, Section 4.1) for the 8.4 mm thick material. This difference was caused by the stress concentration at the crack-tip. Since the plane stress model cannot produce a hydrostatic state of stress, which delays plastic flow with increasing net-section stress, the concentrated stress at the crack-tip area accelerates plasticity development from the crack-tip area toward the back side of the specimen. Therefore, the specimen initiated necking under a lower net-section stress compared to the bar analysis.

In-plane Constraint Effects

The effect of in-plane constraint was investigated in terms of the maximum net-section stress. In order to extend the investigation of in-plane constraint, two more crack geometries, a/t = 0.1 and 0.9, were added to the set of 8.4 mm thickness specimens analyzed. The maximum net-section stress was normalized by dividing by the yield strength, and is plotted versus a/t in Figure 4.15 for both plane strain and plane stress analyses. The results for uncracked tensile specimens are plotted using a/t = 0. No significant effect of crack depth was observed for a/t from 0.2 to 0.8.

For plane strain analyses, the average maximum net-section stress obtained from 8.4 mm thickness specimens (818 MPa) was slightly (6%) higher than the maximum net-section (engineering) stress obtained from the 2-D plane strain tensile specimen analysis (771 MPa, Section 4.2). This difference was caused by the crack-tip which creates a severe stress concentration. As observed from the plane strain tensile specimen analysis, the presence of a

tensile hydrostatic stress suppresses the development of plastic strain, and results in a higher net-section stress. However, the difference was only 6% for this situation.

As reported based on the fracture analysis of SENT specimens (Choi, 1993), there is a significant in-plane constraint effect on the stress field around the crack-tip. A shallow crack SENT specimen, e.g., $a/t = 0.2$, produces a lower crack-tip stress field compared with a deeply cracked SENT specimen, e.g., $a/t = 0.8$. The difference is caused by the lack of in-plane constraint observed for a shallow crack, which results in less hydrostatic stress around the crack-tip. However, the difference in hydrostatic stress becomes negligible with increasing plasticity. Under the same net-section stress which creates a small amount of plasticity at the crack tip, the deeply cracked specimen (a/t = 0.8) produces a higher hydrostatic stress field than the shallow cracked specimen (a/t = 0.2) as seen by Figures 4.16 and 4.17. With increasing plasticity, however, the difference becomes insignificant as shown in Figures 4.18 and 4.19. Therefore, the maximum net-section stress, which was measured after plasticity fully developed through the net-section, was not influenced by the difference in in-plane constraint. The contour plots of equivalent plastic strain at the maximum net-section stress for, $a/t = 0.2$, 0.4, 0.6 and 0.8, are shown in Figures 4.20, 4.21, 4.22 and 4.23 respectively. For all four cases, the contour line of 0.089 has reached the back side of the specimen, that is, plasticity is fully developed through the net-section. After this point, the net-section produced more plastic strain without increasing net-section stress, and necking initiated from the back side of specimen as shown in Figure 4.23. The results are consistent with the tensile specimen using plane strain and plane stress analyses. The 2-D finite element analysis based on von-Mises material behaviour did not show any effect on the maximum net-section stress with a/t ranges varying from 0.2 to 0.8.

The Strain Hardening Effect – Plane Strain vs Plane Stress

Three different materials with n values of 5, 20 and ∞ were used with the same mesh (8.4 mm thickness specimen) to investigate the strain hardening effect on the maximum net-section stress. The true stress – true strain curves were produced using the Ramberg-Osgood equation with a yield strength of 540 MPa for all cases. The resulting maximum net-section stresses are given by Figure 4.24 as a function of a/t.

For plane strain, no in-plane constraint effect on the maximum net-section stresses was observed for a/t ranging from 0.1 to 0.9. While the perfect plastic material gave the same maximum net-section stress as the tensile specimen analysis, the three other materials showed a small difference (5 - 6%) between the tensile specimen plane strain analyses and the SENT plane strain analyses. The presence of the crack-tip created a 5 - 6% higher maximum net-section stress than for a plane strain tensile specimen analysis using a strain hardening material, but the strain hardening rate had no effect on this difference.

The failure mechanism of the plane stress SENT specimen was different from the plane strain specimen. Figures 4.25 – 4.28 present von-Mises stress contour plots at the maximum net-section stress for all cases. For the perfectly plastic material (Figure 4.25) the maximum net-section stress occurred when the plastic zone covered the ligament line starting at the crack-tip. The crack-tip created a stress concentration which produced plastic strain; this developed along the ligament line with increasing load. The maximum net-section stress (466 MPa) was 14 % less than for a plane stress tensile specimen (540 MPa) due to this crack-tip effect. For a material with n = 5, however, a more highly concentrated Mises stress was evident around the crack-tip. Since the material hardens with increasing load, the crack-tip area produced more plastic strain with no spreading of the plastic zone along the

ligament line. As observed from the deformed mesh (Figure 4.28), the crack-tip saw a very large strain which stretched the structure in the loading direction. The stress required to satisfy equilibrium with the applied load was produced primarily in the crack-tip area. The applied load reached the maximum value when the plastic strain in the crack-tip area became equivalent to the strain necessary for the load increment.

Comparing Figures 4.25 – 4.28, the amount of strain at the crack-tip increased with decreasing n value. The material with $n = 5$ continuously hardens with increasing strain, and thus produced more strain than for a material with a higher n value. For this reason, long and thin crack-tip elements were required to accommodate the large strains in the loading direction. Deep crack geometries (a/t = 0.6 and 0.8) with relatively small size elements at the crack-tip resulted in slightly higher maximum net-section stresses. However, the real 3-D structure will produce strain in the 3-direction resulting in shear-lips rather than stretching as observed from the plane stress analysis. Therefore, the increasing tendency observed from deep cracks using a material with $n = 5$ was ignored.

A decreasing maximum net-section stress with increasing a/t was clearly observed for plane stress analyses for a/t ranging from 0 to 0.2. As mentioned above, the crack-tip initiates plastic strain development for the plane stress SENT specimen. However, the area governed by the high stress concentration for a shallow cracked specimen (i.e., $a/t = 0.1$) is relatively small compared with a deeply cracked specimens, and thus the structure produced higher net-section stresses at the point of instability. The difference between $a/t = 0$ and $a/t = 0.1$ increases with decreasing n value. According to this failure mechanism, a high strain hardening material requires more plastic strain before it develops along the ligament line. Therefore, the presence of the crack-tip easily lowered the load carrying capacity of the ligament area. This tendency was consistent for all cases.

4.2.2 Three-dimensional Analyses

In order to simulate the deformation of SENT specimens, three-dimensional finite element analyses were performed with four crack geometries, a/t = 0.2, 0.4, 0.6 and 0.8. The width of the specimen was set to 25 *mm*. A quarter of the specimen was modelled using four layers of 3-D elements based on the 2-D SENT specimen mesh shown in Figure 4.29. The number of elements in the 1-2 plane was reduced to minimise this problem size. The minimum number of elements was chosen based on a preliminary analysis to verify the optimal number of elements without compromising accuracy. The mesh consisted of 20-node quadratic iso-parametric brick elements with reduced Gaussian integration (C3D20R). The crack-tip was initially blunted to allow free movement of the crack-tip with increasing strain similar to the 2-D analysis. Numerical methods and material properties were adapted from the 2-D SENT analysis. The loading and boundary conditions were consistent with the 2-D analyses and the experiments (fixed grip displacement control).

The relation between net-section stress and load-line displacement for a 8.4 mm thickness specimen with a/t = 0.8 is shown in Figure 4.30 along with plane strain and plane stress analyses results. The maximum net-section stresses are summarized in Tables 4.3 and 4.4 for the 8.4 and 13.4 mm thick specimens.

The maximum net-section stresses are presented in Figure 4.31 versus a/t. The results are bounded by the plane strain and plane stress analyses results, and were closer to the plane strain analysis as expected since the specimen width was selected to simulate plane strain conditions. Shallow cracked specimens (a/t = 0.2 and 0.4) produced lower maximum net-section stresses due to a reduction in out-of-plane constraint. With increasing a/t ratio, the maximum net-section stresses approached the plane strain condition.

While the 2-D plane strain analysis produced almost the same maximum net-section stresses for all four crack geometries, the 3-D analysis showed an increasing maximum net-section stress with increasing a/t ratio as mentioned above. The difference is likely related to the size of the shear lips observed at the surface of the crack-tip. Contour plots of equivalent plastic strain at the point of instability are given in Figures 4.32 and 4.33 for a/t = 0.2 and a/t = 0.8, respectively for 8.4 mm thickness specimens. For a/t = 0.2, the plastic strain spreads widely over the crack-tip surface area. For a/t = 0.8, however, the area affected by the plane stress condition is smaller.

The Out-of-plane Constraint

The effect of out-of-plane constraint was investigated by modelling various widths. Widths of 12.5, 6.25 or 50 mm were used for an 8.4 thickness specimen, and a width of 12.5 mm was used for a 13.4 mm thickness specimen. Resulting maximum net-section stresses, normalized by dividing by the ultimate stress, are plotted versus W/b in Figure 4.34. Specimens with a high value of W/b produced maximum net-section stresses closer to the plane strain analysis, while specimens with a low value of W/b had maximum net-section stresses approaching the plane stress analysis. Decreasing the width of the specimen will result in maximum net-section stresses close to the plane stress analysis which by definition has no out-of-plane constraint.

Only two points, for widths of 25 and 50 mm and a/t = 0.2, deviated from this trend. As shown in Figure 4.35, the SENT specimen with a/t = 0.2 produced a significant amount of strain in the width direction (ε_{33}) as it approached maximum load. As expected, ε_{33} developed where the hydrostatic stress was absent. The resulting ε_{33}, which is zero in a plane strain analysis, lowers the maximum load by releasing extra strain to satisfy stress equilibrium. SENT specimens with a/t = 0.8 produced little strain in the 3 direction as

shown in Figure 4.36, and thus gave maximum net-section stresses close to the plane strain analysis.

The effect of out-of-plane constraint was examined based on strain hardening behaviour. Two additional values for n, 5 and ∞, were used with the 8.4 mm thickness specimen for two different widths: 25 and 12.5 mm. The results are shown in Figure 4.37. The material with more strain hardening gave higher maximum net-section stresses with increasing W/b. For the elastic-perfectly plastic material ($n = \infty$), maximum net-section stresses were close to the plane strain analysis. As mentioned in the discussion of the 2-D SENT analysis, the plane stress condition produced high plastic strain emanating from the crack-tip due to the stress concentration. For a material with $n = \infty$, as soon as the crack-tip area yielded, the plastic strain started to spread along the ligament line without any resistance until it reached the back side of the specimen. This behaviour is not realistic unless the structure is vanishingly thin. Widths of 12.5 or 25 mm were thus sufficient to simulate plane strain conditions for $n = \infty$. The strain hardening material generated more plastic strain at the crack-tip area before the plastic strain spread along the ligament line. The structure produced more strain in the 3-direction near the crack-tip surface area, that is, larger shear lips, and thus the maximum net-section stress deviated from the plane strain analysis as shown in Figure 4.37.

4.2.3 Microstructure Based Finite Element Analysis

Microstructural characteristics of our material observed in Chapter 3 were applied in the SENT analyses. The same meshes as were used for the isotropic analysis were used here. Microstructure based finite element analyses were performed in three stages. First, inhomogeniety in the thickness direction was modelled using different true stress – true strain curves for the surface and the mid-section. Second, orthotropic characteristics

observed in the tensile tests were modelled using Hill's anisotropic yield function. Last, the two models were combined.

Three different true stress – true strain curves (Figures 3.23 and 3.24), obtained from tensile testing, were used for the mid-section, inside surface and outside surface. The thickness of the surfaces was set to 20% of the specimen thickness in accordance with the tensile test configurations. The crack was placed on the outside surface to remain consistent with the SENT experiments. The 3-D mesh used for this analysis is given in Figure 4.38. The resulting maximum net-section stresses are plotted in Figure 4.39 for both 8.4 and 13.4 mm thickness specimens along with isotropic analysis results. Since the mid-section material had a lower strength than the surface in the ligament area, the maximum net-section stresses from deep crack specimens were higher than those from isotropic analyses.

On the basis of previous analyses, orthotropic characteristics of the material were modelled using Hill's stress function with an R_{33} value of 0.93 for the 8.4 mm thickness specimen and 0.87 for the 13.4 mm thickness specimen. Due to the change in the orientation of the Cartesian co-ordinates, this R value was assigned to the 1 direction (Figure 4.38). The results are shown in Figure 4.40 compared with the isotropic analysis results. Since there is a weakness in the 1 direction, the presence of σ_{11} reduced the maximum net-section stresses for all crack geometries. Deep cracked geometries produced lower maximum net-section stresses, because the area governed by σ_{11} was relatively large compared with shallow cracked specimens.

The microstructure based analysis was completed by combining the inhomogeniety and orthotropic characteristics. The resulting maximum net-section stresses are given in Figure 4.41. For 8.4 mm thickness specimens, the resulting maximum stresses from all four crack geometries were slightly lower than the 3-D isotropic analyses. Even the deepest crack

geometry (a/t = 0.8), which has a higher tensile strength over the ligament than the full-thickness material, produced a 2% lower maximum net-section stress than the 3-D isotropic analysis due to the orthotropic characteristics. For 13.4 mm thickness specimens, the same trend was observed. The deepest crack geometry (a/t = 0.8) produced a 5% lower maximum net-section stress than the corresponding 3-D isotropic analysis. Slightly lower (3 -5%) maximum net-section stresses were observed for all crack geometries.

The variation of net-section stress with load line displacement based on a 55 mm extensometer is plotted in Figures 4.42 (8.4 mm thickness) and 4.43 (13.4 mm thickness) for various crack geometries. Maximum net-section stresses resulting from the microstructure based finite element analyses gave increasing maximum net-section stress with increasing a/t, but this effect was less significant than the experiments.

4.2.4 Comparison with Experimental Results

In order to verify the finite element analysis, the results were compared with the test data. Two and 3-D finite element analysis results are compared with experimental results in Figures 4.44 for a 8.4 mm thickness specimen with a/t = 0.6. The net-section stress is plotted versus 55 mm displacement. Experimental data with extraordinary scatter were excluded as previously discussed.

Figure 4.45 shows finite element analysis results for a/t = 0.8 for the 8.4 mm thickness specimen in comparison with test results with a/t values higher than 0.7. Both specimens resulted in higher net-section stresses than the plane strain analysis. The curve for E3 (a/t = 0.732) was close to the curve from the plane strain analysis with lower a/t ratios. E6 (a/t = 0.778) showed higher net-section stresses than those of the plane strain analysis.

Maximum net-section stresses from the SENT experiments are plotted versus *W/b* in Figure 4.46 along with finite element analysis results. Both the isotropic and microstructure-based finite element analyses are presented. The maximum net-section stress was non-dimensionalized by dividing by the ultimate stress for each material. The *a/t* ratio is indicated above each data point. The experimental data show an obvious increasing tendency of maximum net-section stress with increasing *W/b*. Most test data produced for *a/t* ranging from 0.2 to 0.6 were close to the microstructure based finite element analysis results. Most data points from shallow crack specimens are below the 2-D plane strain analysis, while deep cracked specimens ($a/t \geq 0.6$) produced much higher maximum net-section stresses. This implies that the deep cracked specimen, which has high in-plane constraint, produced higher maximum net-section stresses with a mechanism which was not modelled with the present finite element analysis.

4.3 Summary

On the basis of the SENT analyses, the followings observations were made.

- Based on the experimental results, the traditional limit load derived from the analytical solution was too conservative for all crack configurations, especially for deep crack specimens with *a/t* over 0.6.

- The experimentally determined maximum net-section stress increased with increasing *a/t*. Three-dimensional finite element analyses were used to assess the role of strength differences (higher strength at the surface) and orthotropic characteristics on this behaviour. In spite of higher strength material in the ligament area, the 3-D microstructural based finite element analyses produced lower maximum net-section stresses than those of 3-D isotropic analyses due to the weakness in the thickness

direction. While these microstructural based analyses were in good agreement with test results for shallow crack geometries (a/t less than 0.6), they gave lower results than the experiments for deeply cracked geometries. This suggests that the change in in-plane constraint affects the plastic collapse load for SENT specimens in a manner which can not be simulated with a von Mises yield criteria.

Chapter 5

Wide Plates

The plastic collapse of wide plates with various crack configurations was analysed both numerically and experimentally. An extensive series of wide plate specimens cut from Grade 483 linepipe material were tested by Lambert (1993), and used herein to investigate plastic collapse behaviour. Based on the crack configurations for these wide plate specimens, extensive finite element analyses were completed. The finite element analyses used both isotropic and microstructural based material models.

5.1 Test Results

A series of wide plate specimens subjected to tension with fixed end grips were tested by Lambert (1993). Table 5.1 summarises the configurations of the wide plates tested. Specimens were cut from both 8.4 and 13.4 mm thick pipe. Lambert (1993) tested specimens from both parent plate and welded specimens, but only specimens cut from parent plate were used in the present analysis. For the 8.4 mm thickness specimens, widths of 150 or 280 mm were used. Figure 2.11 illustrates these wide plate specimen configurations. For the 13.4 mm thickness specimens, only 150 mm wide specimens were tested due to capacity limitations of the test rig.

For all specimens, artificial surface defects were introduced into the outside surface using a slitting saw. The initial defects were extended to a semi-elliptic shape under fatigue loading. All cracks were introduced in the circumferential direction of the pipe, and the tensile load was applied along the longitudinal axis of the pipe. These configurations were consistent with the SENT specimens discussed in chapter 4.

Loading was applied under displacement control using an LVDT mounted directly to the specimen grips. Two clip gages were used. A 3 mm clip gage was mounted across the crack mouth to monitor the crack mouth opening displacement, and a 52 mm clip gage was mounted on the opposite side (inside the pipe) to measure local displacement.

5.1.1 General Observations

No significant stable crack growth prior to the global plastic collapse was observed in any of the specimens. That is, none of the specimens failed by ductile fracture before plastic collapse occurred. Even with a long and deep crack (XP3), which has the highest constraint, the maximum net-section stress was greater than the flow stress. For most of the specimens tested, breakthrough of the surface crack occurred after the specimen reached maximum load. Only WP3 showed ligament breakthrough before global plastic collapse occurred. However, the difference in net-section stresses for ligament breakthrough and plastic collapse was less than 0.2%. Before global plastic collapse, local necking from the back side of the ligament occurred in a manner similar to the SENT specimens. Local necking was restricted to the ligament, prior to the point at which global necking initiated. Like the SENT specimens, the fractured surfaces at the crack ligament were smooth and at an angle. The test results are summarised in Tables 5.1 and 5.2.

The net-section stress at failure ranged from 601 to 708 MPa for the 8.4 mm thick specimens, and 601 to 689 MPa for the 13.4 mm thick specimens, resulting in about a 23% variation for each case. Except for WPQ3, which had a long, deep crack, the maximum net-section stresses exceeded the corresponding flow stresses, which were 609 and 569 MPa for 8.4 and 13.4 mm thick materials, respectively. This further indicates that the mode of failure was by plastic collapse.

5.1.2 Comparisons with Standard Solutions

The test results were compared with three standard plastic collapse solutions, PD6493:1980, CEGB/R6 and net-section yielding (PD6493:1991), in Figures 5.1 and 5.2 in terms of the safety factor. The safety factor was calculated by dividing the experimental results by the corresponding plastic collapse solutions based on the flow stress. The results are plotted versus a/t and c/W in Figures 5.1 and 5.2, respectively. The PD 6493:1980 solution is overly-conservative and inconsistent. The safety factor ranges from 1.59 to 4.27 (mean of 2.36 and standard deviation of 0.747). This gives a maximum relative difference of 168%. This solution gives excessively high safety factors for deep cracked specimens as shown in Figure 5.1. The CEGB/R6 (1988) solution provides less scatter with the safety factor ranging from 1.30 to 1.72 (mean of 1.47 and standard deviation of 0.13) with a maximum relative difference of 32%. Higher safety factors were observed for larger cracks, i.e., specimens WP3, WP4 and XP3. The net-section yielding solution (PD 6493:1991) gives the best prediction. The safety factor ranges between 0.99 and 1.21 (mean of 1.08 and standard deviation of 0.057), giving a 23 % maximum difference.

The maximum safety factor for the WP series was for WP8, which contained the smallest crack. This trend was obvious for most of the WP series results. The same trend was observed with the XP series except for specimen XP1. Specimen XP1 contained a comparatively short (width) and deep crack, and gave a very high safety factor. Since the net-section yielding solution has

proven to be the best for these tests, the results will be discussed in terms of the net-section stress in the following.

5.1.3 Maximum Net-section Stress and Constraint

The 23% difference in maximum net-section stresses for various crack geometries can be explained in terms of constraint at the ligament. Figures 5.3 and 5.4 show the resulting maximum net-section stresses versus *a/t* or *c/W*, respectively. Increasing either *a/t* or *c/W* decreases the maximum net-section stress. This implies that the maximum net-section stress is inversely related to constraint at the ligament.

For the SENT specimens, the opposite effect was observed. This different trend is expected as the behaviour of an edge crack is different from a surface crack. Increasing the crack depth for an SENT specimen linearly increases the net-section stress on the ligament under remote tension. However, increasing the crack depth for a small surface crack does not provide a linear increase in the net-section stress at the ligament. Since the crack is small compared to the full plate width, the increase in crack depth changes the overall net-section area by only a small amount. However, the local crack ligament experiences a larger increase in net-section stress due to the stress concentration. For this reason, wide plate specimens with a high constraint crack reach ligament instability at a lower net-section stress than for a low constraint crack. In order to investigate the effect of crack geometry on plastic collapse, extensive finite element analyses were performed.

5.2 Finite Element Analyses

Three-dimensional finite element analyses were performed to provide a comparison with experiments. All specimens tested were modelled for direct comparison. A quarter of a wide plate specimen containing a semi-elliptic surface crack was modelled using 20-noded isoparametric 3-D solid elements with reduced integration as shown in Figure 5.5. The crack tip was modelled in a similar way to the SENT specimen and transformed along the crack line as shown in Figure 5.6. A fixed end grip condition was applied with displacement loading. The same program options as used for the 3-D SENT analyses were used.

5.2.1 Comparison to Test Results

The resulting maximum net-section stresses for all specimens are plotted versus a/t and c/W in Figures 5.7 and 5.8 along with the test results. The maximum net-section stress was normalised by dividing by the ultimate stress, since this model assumes ligament necking as the plastic collapse criterion. Except for long cracks, i.e., WQP3 and WQP4, the maximum net-section stresses were higher than the ultimate stress. The predicted maximum net-section stresses were close to the test results for most short crack specimens ($c/W < 0.2$). The results for long and deep crack specimens were higher than the test results.

Figure 5.9 shows contour plots of equivalent plastic strain at the maximum load for WP8, which had the smallest crack. Plastic strain was well developed along the entire net-section. This global plastic strain reached 0.09, which was the value used as the plastic collapse criteria in both tensile and SENT specimen analyses. This implies that the maximum load was obtained at global plastic collapse. As compared in Figures 5.10 and 5.11, the plastic strain in the crack ligament was not very different from the global plastic strain. The

resulting maximum net-section stress was slightly higher than the ultimate stress due to the hydrostatic stress at the ligament. The same trend was observed for WP7, WP10, WP5 and WP9.

Figure 5.12 shows contour plots of equivalent plastic strain for WP4, which had a short and deep crack. The plastic strain along the maximum shear stress plane was less than 0.09 at maximum load, and the strain was concentrated in the crack ligament. The plastic strain produced in the ligament was very high and elements along the crack front were excessively deformed as shown in Figure 5.12. In this case, the applied load was offset by plastic strain around the crack-tip, and the maximum load was obtained before the plastic strain along the maximum shear stress plane reached 0.09. The maximum net-section stress was slightly higher than the ultimate stress. However, deformation in the ligament area at that load was unrealistically high, indicating possible ligament collapse.

For long crack specimens, i.e., WQ3, the same failure mechanism as WP4 was observed. The plastic strain in the crack-tip area was very high and failure occurred before the global plastic strain reached 0.09. The resulting maximum net-section stress was less than the ultimate stress due to the extensive plastic strain along the long crack ligament. However, plastic strain in the ligament at maximum load was excessively high. Due to the excessive plastic strain in the ligament area at maximum load, failure was considered to have occurred prior to global collapse. For this reason, a ligament necking condition was introduced as the failure criteria. Failure was assumed when the plastic strain at the deepest point of the crack ligament reached 0.09, as in the SENT analysis. This assumption is consistent, since the failure mode in the crack ligament of wide plate specimens was similar to that in SENT specimens.

Figures 5.11, 5.12 and 5.13 present contour plots of equivalent plastic strain at ligament necking for WP8, WP4 and WQP3, respectively. The most highly constrained specimen, WQP3, produced the smallest amount of global plastic strain when the ligament reached the point of necking. The resulting net-section stresses at ligament necking are plotted versus *a/t* and *c/W* in Figures 5.14 and 5.15, respectively, along with the test results. The maximum net-section stresses using the ligament necking failure criteria were much closer to the test results than were global plastic collapse. The difference between global plastic collapse and ligament necking was smaller for shallow and short crack geometries. The difference was larger for more highly constrained specimens. Except for XP1, which resulted in an extraordinarily high maximum net-section stress in the test, resulting ligament necking stresses were very close to the test results, including long crack geometries. For short cracks, the ligament necking stresses were slightly lower than test results. While specimens WP7 and WP8 showed increasing maximum net-section stress with decreasing crack length from the tests, both ligament necking and global plastic collapse predictions from finite element analyses approached the ultimate stress. It is expected that the finite element analyses will predict failure at the ultimate stress when the crack size approaches zero. Excluding XP1, a maximum difference of 6% between the test and the ligament necking prediction was observed from WP8. The average ratio between the test results and ligament necking prediction was 1.008 with standard deviation of 0.02. The maximum value was 1.057 and the minimum value was 0.99.

5.2.2 Microstructure Based Finite Element Analyses

A microstructure based finite element analysis was performed. Differences in strength in the thickness direction were modelled using different true stress – true strain curves for the mid-section and the surfaces. The mesh was designed with two layers of 3-D solid elements at each surface, which covers 20% of whole thickness at each side, to accommodate the

different material properties in the thickness direction. The same R values as were used in the SENT analyses were applied in the thickness direction to model the orthotropic characteristics. These two analyses were combined to produce a microstructure based analysis. The same program options used for the SENT analyses were used.

The resulting maximum net-section stresses are plotted versus a/t in Figure 5.16. The maximum net-section stresses were slightly lower than those for isotropic, homogeneous analyses for all WP and XP series. However, the difference was less than 2%. The ligament necking stress is given in Figure 5.17. The results were also slightly lower than the isotropic homogeneous analysis results, with a difference of 1-2%. The maximum difference was observed in long and deep crack geometries, i.e., WPQ3 and WPQ4, as expected.

Since there was no significant difference between the microstructure based analyses and the isotropic homogeneous analyses, subsequent finite element analyses were performed based on isotropic homogeneous material model.

5.3 Plastic Collapse Solution for Wide Plates

Based on a successful comparison with experiment, the ligament necking criterion was used in the analysis of a wide range of crack geometries in order to develop a plastic collapse solution for wide plates. The analysis matrix is summarised in Table 5.3.

Based on these finite element analyses, a plastic collapse solution for surface cracked wide plates is proposed in the following form:

$$\sigma_{PC} = \sigma_{ult} \cdot f_g^{WP} \tag{5.1}$$

where σ_{ult} is material ultimate strength and f_g^{WP} is a crack geometry correction factor. Equation (5.1) gives the plastic collapse solution in terms of the nominal stress. This geometry correction factor represents the effect of crack geometry on ligament necking, and is a function of three parameters, *a/t*, *c/W* and *W/t*. Therefore, it is more general than the CEGB/R6 solution which considers only the immediate crack area.

The geometry correction factors for three different W/t values are shown in Figures 5.18 to 5.20. The equivalent geometry correction factors obtained from the CEGB/R6 plastic collapse solution are presented using open symbols. The plastic collapse solution is sensitive to all three parameters: *a/t*, *c/W* and *W/t*. The CEGB/R6 solution, by comparison, was not as sensitive to the specific crack geometry.

Figure 5.21 shows safety factors obtained for the test data. Safety factors were calculated by dividing the maximum stresses from the test by the corresponding plastic collapse predictions. The solid circles represent the proposed plastic collapse solution represented by equation (5.1). In calculating the geometry correction factor for a given geometry, linear interpolation was used between available finite element analysis data. For the validation of equation (5.1), the corresponding solutions for each geometry were not used. The results show very good agreement with the experimental data and significant improvement over the CEGB/R6 analysis. Since the ligament necking instability model was successful in the prediction of plastic collapse of surface defects, the same procedures were used in the analysis of pipes as discussed in the next chapter.

5.4 Summary

As a result of extensive experiments and finite element analyses on wide plate specimens, the followings conclusions can be drawn:

- A series of wide plate experiments showed a strong dependency of failure load on crack geometry. Short and shallow crack geometries produced higher maximum net-section stresses, while long and deep crack geometries resulted in lower maximum net-section stresses.

- The maximum net-section stresses at failure predicted using isotropic homogeneous finite element analyses were close to the material ultimate stress with no significant dependence on crack geometry. However, the ligament necking stress, developed as the plastic collapse criterion from SENT analyses, provided better agreement with test results for wide plates.

- Microstructure based finite element analyses resulted in insignificant differences compared with isotropic homogeneous analyses.

- A plastic collapse solution for wide plates was introduced in terms of a geometry correction factor based on extensive finite element analyses. This plastic collapse solution gives higher net-section stresses for short crack geometries, and lower net-section stresses for long and deep crack geometries compared to currently available net-section yielding solutions. This solution also predicts higher net-section stresses for long and shallow crack geometries. The geometry factor in the present plastic collapse solution reflects the effect of crack geometry on ligament necking, and is a function of

a/t, *c/W* and *W/t*. This solution provided the best prediction in comparison with experimental data a with maximum difference of 6%. The net-section yielding solution, which gives the best prediction among currently available plastic collapse solutions, produced a maximum difference of 23%.

- The ligament necking criterion, having been validated using wide plate specimens, will be applied to full pipes in the next chapter.

Chapter 6

Pipelines

The plastic collapse of pipelines subject to remote bending was investigated by performing extensive finite element analyses. This resulted in a plastic collapse solution for surface defects in full pipes which was verified using full pipe test data (Coote et al., 1981).

6.1 Review of Full Pipe Test Results

The full pipe test results summarized by Coote et al. (1981) were reviewed using current plastic collapse solutions presented in Chapter 2 to produce Table 6.1. For each solution, the safety factor was calculated by dividing the failure stress by the corresponding plastic collapse solution. In order to investigate the effect of constraint, safety factors obtained from each solution based on the material flow stress were plotted against a/t and $2c/(\pi D)$ in Figures 6.1 through 6.8. At each data point, the material flow stress and the second parameter (a/t or $2c/(\pi D)$) are shown. In these analyses, through crack geometries were excluded.

Both PD6493: 1991 and CEGB/R6 (1988) recommend the net-section collapse solution (Miller, 1988). The net-section collapse solution (Chapter 2) gives safety factors ranging from 0.76 to

1.28 (mean = 1.03, standard deviation = 0.150). As shown in Figure 6.1, no clear dependency on a/t was observed. Figure 6.2 shows a weak dependency on $2c/(\pi D)$. Short cracks (small c) provided higher safety factors and long cracks produced slightly lower safety factors. Short crack geometries produced safety factors over 1.0 for most cases. Long and deep crack geometries resulted in much lower safety factors than for all short crack geometries.

Willoughby's (1982) solution gives similar scatter, with safety factors ranging from 0.903 to 1.343 (mean = 1.143, standard deviation = 0.128) as shown in Figures 6.3 and 6.4. The results show a slight increase in safety factor with increasing a/t. Short, deep cracks provided higher safety factors compared with long, deep cracks. Long, shallow cracks produced safety factors greater than 1.0.

Application of CSA Z622 (1994) was conservative for all cases as shown in Figure 6.5 and 6.6. This is expected since this procedure was developed using this data set and has a built-in factor of 2.0 on defect depth and 2.5 on defect length. The safety factor increases slightly as both a/t and $2c/(\pi D)$ increase (mean = 1.411, standard deviation = 0.194). Predictions with the actual crack dimensions and with the internal factors of safety removed are presented in Figures 6.7 and 6.8. The resulting safety factors range from 0.917 to 1.444 (mean = 1.214, standard deviation = 0.156). This solution shows a similar trend as the two previous solutions. Higher safety factors were observed for most shorter cracks and long, shallow cracks compared with long, deep cracks.

6.2 Finite Element Analyses

A pipe subject to remote bending was modelled with 3-D solid elements as shown in Figure 6.9. Due to symmetry, a quarter of the specimen was used. The crack-tip area (Figure 6.10) was modelled in a similar manner to the 3-D wide plate mesh. The mesh was designed with 987 to

1485 3-D solid elements. The boundary conditions are illustrated in Figure 6.11. Remote bending at the end opposite to the crack was displacement controlled. At the line of symmetry, on the side opposite the crack, one half of the pipe circumference were fixed to approximate the experimental support conditions. The same program options that used for 3-D wide plate analyses were used here. Based on the results of the wide plate analyses, three parameters, a/t, $2c/(\pi R)$ and R/t, were considered in the analysis matrix. Since the bending moment produces tension stress on the upper half of the pipe, $2c/(\pi R)$ was chosen. Finite element analyses were performed for total of 60 various crack geometries as summarised in Table 6.2.

Plastic collapse behaviour was observed to follow two different mechanisms. For shallow cracks (small a), plastic collapse occurred on the compression side prior to ligament necking. The resulting maximum stress was much higher than the ultimate stress. Deeper cracks produced high strain in the ligament, and ligament necking occurred before the pipe reached compression failure. In these cases, stress at ligament necking was lower than for shallow cracks.

6.2.1 A Plastic Collapse Solution for Pipeline Circumferential Surface Defects

Based on extensive finite element analyses, a plastic collapse solution for pipeline circumferential surface defects is introduced in the following form:

$$\sigma_{PC} = \sigma_{ult} \cdot f_g^{FP} \tag{6.1}$$

where σ_{ult} is the material ultimate strength and f_g^{FP} is a geometry correction factor for pipes. Equation (6.1) gives the plastic collapse solution in terms of nominal stress for a plain pipe with the geometry correction factor reflecting the effect of crack geometry on plastic

collapse. While the geometry correction factor for the CEGB/R6 plastic collapse solution is known to be unconservative, this geometry correction factor fully reflects the physical behaviour of pipeline defects. This solution is similar in form to the wide plate plastic collapse solution presented in chapter 5 (equation (5.1)).

The resulting geometry correction factors for four different R/t values are shown in Figures 6.12 to 6.15 along with the equivalent CEGB/R6 geometry factors (open symbols). As can be seen from the figures, the geometry correction factor is not sensitive to crack length for some shallow crack geometries. However, with increasing crack depth, long cracks produced much lower values. The geometry correction factor was consistently high for all short crack geometries. The effect of the three different parameters is significant as shown in Figures 6.12 to 6.15. Geometries with R/t = 90.71 showed no sign of ligament necking, and all failed at the maximum load. Geometries with R/t = 11.34 failed by ligament necking for most cases except for the smallest cracks. The equivalent geometry correction factors for CEGB/R6 were inconsistent. They were lower for short cracks and higher for deep and long cracks than the proposed solution.

6.2.2 Comparison with Test Results

The proposed plastic collapse solution was applied to the full pipe test data presented by Coote et al. (1981). The safety factors are shown in Figure 6.16, compared with CEGB/R6 and CSA Z622 solutions. Since the material ultimate strength was not available for the tested material, the ultimate strength in equation (6.1) was replaced with the material flow stress. The geometry correction factors were calculated by using linear interpolation between available finite element data. The present solution resulted in a mean safety factor of 0.96 with a standard deviation of 0.148, better than both the CEGB/R6 and the CSA

Z622 solutions which had mean values of 1.022 and 1.216, and standard deviations of 0.166 and 0.162, respectively.

While the safety factors for most short cracks were higher than 1, those for long crack geometries were lower than 1 for most cases. The reason for such low safety factors for long cracks may be due to welds in all test specimens. Since the present plastic collapse solution assumes ligament necking when the strain at the ligament back face reached the necking strain of the parent material, it may be unconservative for weld material which is usually less ductile than the parent material. This, however, does not explain why only long cracks are a problem.

6.2.3 A Plastic Collapse Solution for Pipeline Girth Weld Defects

The present solution was not conservative in assessing long cracks. For this reason, an empirical correction was applied to the crack depth by multiplying the depth by 2. The material flow stress was also replaced with the material yield strength. The resulting safety factors are shown in Figure 6.17 along with the CSA Z622 and the CEGB/R6 solutions. The CSA Z622 plastic collapse solution uses a factor of safety of 2 for crack depth and 2.5 for crack length.

The result shows a significant improvement for long crack geometries without a corresponding increase in safety factor for short cracks. The resulting safety factor was therefore consistent for all crack geometries. The present solution reflects the physical behaviour of surface defects in full pipes, but more work is required to determine why this correction to depth was necessary.

6.3 Summary

The following observations can be made based on the full pipe analyses:

- Full pipe test data (Coote et. al., 1981) showed a strong dependency on crack geometry. Short, shallow cracks produced higher failure stresses than long, deep cracks. Long, shallow cracks resulted in higher failure stresses than long, deep cracks. A similar trend was observed in previous wide plates analyses.

- A plastic collapse solution for a pipeline surface defect was introduced with a geometry correction factor based on extensive 3-D full pipe finite element analyses. A Total of 60 cases were analysed, and corresponding geometry correction factors were tabulated as a function of a/t, $2c/(\pi R)$ and R/t.

- A plastic collapse solution for pipeline girth weld defects was proposed by applying a factor of 2 to the crack depth. The results showed a consistent level of conservatism for all crack geometries. The present solution provides good agreement with the full pipe test data by Coote et al. (1981), and reflects the physical behaviour of surface defects.

Chapter 7

Conclusions and Recommendations

This work was undertaken to gain on understanding of plastic collapse behaviour of circumferential defects in pipes in bending. An extensive program combining analytical, experimental and numerical study was performed. Tensile specimens, single edge notch tension specimens, wide plate specimens and full pipes were thoroughly investigated.

Conclusions

- A ligament failure criterion was developed based on the necking mechanism in a tensile specimen. This method was consistent for cracked specimens and component geometries and offered improvements over available procedures.

- An extensive microstructural investigation was performed on typical Grade 483 pipeline steels. The difference in strength between the surfaces and the mid-section was

observed, and quantified in terms of corresponding stress-strain curves for different sections. Also, orthotropic characteristics due to the rolling process were analysed by applying Hill's stress function. While the inhomogeneity in the thickness direction resulted in higher plastic collapse loads than for isotropic homogeneous analyses, the orthotropic characteristics lowered plastic collapse loads due to the weakness involved in the thickness direction. The combined microstructural based analyses produced slightly lower plastic collapse loads for SENT and wide plate specimens. However, the difference was not significant for wide plates.

- Two different failure modes were observed in wide plate specimens, net-section collapse and ligament collapse. Net-section collapse was observed for wide plates having a small crack, and ligament collapse was observed for relatively larger cracks. For the geometries involved in the current finite element analyses, net-section collapse was observed for $a/t \leq 0.25$ and $c/W \leq 0.125$.

- The ligament failure criteria provide excellent predictions of ligament collapse for wide plate specimens. The predictions were within 7% of available experimental data. The best available plastic collapse solution was net-section yielding, which gave estimates within 23% of the same experimental results. Therefore, extensive finite element analyses of wide plates were performed to produce a plastic collapse solution which was presented in terms of an empirical geometry correction factor.

- Three-dimensional full pipe finite element analyses with various crack geometries were performed with remote bending boundary conditions. For shallow or short crack geometries, plastic collapse was observed from the compressed section indicating global collapse due to compression. Ligament failure was observed for long and deep crack geometries prior to global collapse. A total of 60 different geometries were

analysed to produce a plastic collapse solution which was similar to the plastic collapse solution proposed for wide plates.

- A modified plastic collapse solution for pipeline girthweld defects was proposed by applying a factor of 2 to the crack depth. The results showed good agreement with experimental data and provided a consistent level of conservatism for all crack geometries.

Recommendations

- The proposed plastic collapse solution in welds showed good agreement with the full pipe experimental data (Coote et al., 1981). However, it is necessary to examine the effect of weld metal properties, especially weld mismatch.

- The finite element analyses for full pipes were restricted to 60 geometries with a single stress - strain curve. A database of the geometry correction factors for various crack geometries and various material properties is required.

- This research has dealt exclusively with surface cracks. Conventional limit load analyses give similar results for embedded defects, but experimental evidence suggests they are much better. This effect should be examined with the proposed method.

- The proposed method is applicable to examine interaction effects for adjacent defects which are difficult to assess by conventional limit loads. This should be done.

References

ASM, 1990a, Metals Handbook – Tenth edition, Volume 1, p. 226 –

ASM, 1990a, Metals Handbook – Tenth edition, Volume 1, p. 327 –

ASM, 1985a, Metals Handbook – Ninth edition, Volume 9, p. 165 –

ASM, 1985b, Metals Handbook – Ninth edition, Volume 8, p. 90 –

Barlow, J., 1976, *Optimal Stress Locations in Finite Element Models,* International Journal of Numerical Methods in Engineering, Vol. 10, pp. 243-251

Brocks, W., Künecke, G., Noack, H.-D. and Veith, H.,1989, *On the Transferability of Fracture Mechanics Parameters from Specimens to Structures Using FEM,* Nuclear Engineering and Design, Vol.112, pp.1-14.

Brocks, W. and Schmitt, W., 1993, *Quantitative Assessment of the Role of Crack Tip Constraint on Ductile Tearing,* ASTM STP1171, Constraint Effects in Fracture pp. 64-78.

CAN3-Z245.1, 1992, *Pipeline Systems and Materials*, Canadian Standards Association, Rexdale, Ontario

CEGB/R6, 1988, *Background to and Validation of Report of CEGB Report R/H/R6 – Revision 3*, International Journal of Pressure Vessel and Piping, Vol. 32, pp. 105 - 196

Chell, G.G., and Spink, G.M., 1977, A Yield Fracture Mechanics Analysis of Three-point Bend Specimens and Its Implications to Fracture Toughness Testing. Engineering Fracture Mech.9, 101-121.

Chen, C., et al., 1978, Proceedings on Metal Fracture Research. Metallurgical Industry Publishing House.

Choi, J.B., 1993, *Investigation of Constraint Effects in Pipeline Fracture Specimens*, MASc Thesis, Dept. of Mechanical Engineering, University of Waterloo

Choi, J.B. and Lambert S.B., Pick, R.J., Glover, A., 1993, *Analysis of Constraint in Single Edge Notch Tension Specimens*, Proceedings of the 1997 ASME PVP Conference, Orlando, Florida, Fatigue and Fracture, PVP-Vol. 346, ASME, pp. 301 – 307

Connors, D.C. and Hellen, R.A.J., 1983, *Observations of the Ductile Fracture of Plates with Surface Defects*, CEGB Technology Planning and Research Division Report, TPRD/B/01992/N83.

Coote, R.I., Glover, A.G., Pick, R.J. and Burns, D.J., 1981, *Alternative Girth Weld Acceptance Standards in the Canadian Gas Pipeline Code,* Welding and Performance of Pipelines, The Welding Institute, London, paper 21.

Coote, R.I., Glover, A.G., Pick, R.J. and Burns, D.J., 1986, *Alternative Girth Weld Acceptance Standards in the Canadian Gas Pipeline Code,* Welding and Performance of Pipelines, The Welding Institute.

Crisfield, M.A., 1981, *Ivanov's Yield Criterion for Thin Plates and Shells using Finite Elements,* TRRL Lab. Report 919, Crowthorne.

CSA Z184 - M86, 1986, Canadian Standards Association, Gas Pipeline Systems.

CSA Z662 - Appendix K, 1994, Canadian Standards Association, *Standards of Acceptability for Circumferential Pipe Butt Welds Based on Fracture Mechanics Principles,* Oil and Gas Pipeline Systems.

Denys, R.M., 1992, *The Effect of Weld Metal Matching on Girth Weld Performance, Volume 1: A General Literature Review,* Report to the Welding Supervision Committee, Pipeline Research Committee, of the American Gas Association.

Denys, R.M., 1993, *The European Pipeline Research Group's Guidelines on Acceptable Girth Weld Defect in Transition Pipelines,* Proc. 8th Symposium on Pipeline Research, American Gas Association, Paper 37, Houston.

Erdogan, F., 1982, Th*eoretical and Experimental Study of Fracture in Pipelines Containing Circumferential Flaw,* U.S. Department of Transportation Report DOT-RSPA-DMA-50/83/3, N.T.I.S.

Faucher, B., Roy, G. and Tyson W.R., 1992, *Interpretation of Toughness Tests Using the Failure Avoidance Diagram for a Pipeline Steel,* Proceedings of CANMET Pipeline Conference, VIII-7-1-VIII-7-13.

Glover, A.G., Coote, R.I., 1983, *Full Scale Fracture Tests of Pipeline Girth Welds,* Proceedings for the Conference for the 4th National Congress on Pressure Vessels and Piping Technology, ASME, pp. 107 – 121.

Glover, A.G., Coote, R.I., and Pick, R.J., 1981, *Engineering Critical Assessment of Pipeline Girth Welds,* Proceeding of Fitness for Purpose Validation of Welded Construction Conference, The Welding Institute, paper 30.

Green, A.P. and Hundry, B.B., 1956, *Initial Plastic Yielding in Notch Bend Tests,* Journal of the mechanics and Physics of Solids, Vol.4, pp.128-144.

Hale, D., *Alaskan Gas Breakthrough Neraing*, Pipeline Gas Journal, Sept. 1980.

Hall, E.O., 1951, Proc. Phys. Soc., B64, pp. 747.

Hencky, Z. Angew, 1923, Math. Mech. Vol.4, pp.323

HKS, 1996, ABAQUS *Users Manual,* Hibbit, Karlsson, and Sorenson, Providence, R.I.

Honeycombe, R.W.K., 1984, *The Plastic Deformation of Metals*, Edward Arnold, p. 26.

Kumar, V., German, M.D., and Shih, C.F., 1981, *An Engineering Approach for Elastic-plastic Fracture Analysis*, EPRI NP-1931, Electric Power Research Institute, Palo Alto, USA.

Kussmaul, K., Roos, E., Eisele, U., Silcher, H. and Restemeyer, D., *1992, Influence of Specimen Thickness on The Deformation and Fracture Behaviour of Wide Plates*, Engineering Fracture Mechanics Vol.41, No.2, pp.169-176.

Lambert, S.B., 1995, *Fracture of Girth Weld Defects Subject to High Longitudinal Strains*, Report for NOVA Corporation of Alberta, Dept. of Mechanical Engineering, University of Waterloo.

Lambert, S.B., 1992, 1993, *private communications*

Lambert, S.B. and Martin, J.T., 1991, *High Strain Fracture Numerical Research Program: Phase I Final Report*, Report for NOVA Corporation of Alberta, Dept. of Mechanical Engineering, University of Waterloo.

Lecsek, R., 1991, *Mini-wide Plate Tensile Testing of Natural Gas Pipeline*, Work term report, Dept. of Mechanical Engineering, University of Waterloo.

Levy, M, 1871, *Memoire sur les Equations Generales des Mouvements Interieurs des Corps Solides Ductiles au dela des Limites ou Elasticite Pourrait les Ramener a leur Premier Etat*, C. Rend., Paris, Vol.70, pp. 1323

Martin, J.T., 1991, *Constraint Effects in Pipeline Fracture Specimens*, MASc thesis, Dept. of Mechanical Engineering, University of Waterloo.

McMeeking and Parks, 1979, *On Criteria for J-Dominance of Crack-Tip Fields in Large Scale Yielding*, Elastic-Plastic Fracture, ASTM STP 668, pp. 175 – 194.

Miller, A.G., 1988, *Review of Limit Loads of Structures Containing Defects*, International Journal of Pressure Vessels and Piping, Vol. 32, pp197-327.

Mises, R., 1913, Gottinger Nachr. Math.-Phys. Kl., pp.582

O'Dowd, N.P. and Shih, C.F., 1991, *Family of Crack-Tip Fields Characterized by A Triaxiality Parameter - I. Structure of Fields*, Journal of Mechanics and Physics of Solids, Vol. 39, No.8, pp. 989-1015

O'Dowd, N.P. and Shih, C.F., 1992, *Family of Crack-Tip Fields Characterized by A Triaxiality Parameter - II. Fracture Applications*, Journal of Mechanics and Physics of Solids, Vol. 40, No.5, pp. 939-963

PD 6493:1980, *Guidance on Some Methods for the Derivation of Acceptance Levels for Defects in Fusion Welded Joints*, British Standards Institute.

PD 6493:1991, *Guidance on Some Methods for Assessing the Acceptability of Flaws in Fusion Welded Structures*, British Standards Institute.

Petch, N.J., 1953, J. of Iron Steel Inst., Vol. 173, pp. 25.

Pick R.J. Glover, A.G. and Coote, R.I., 1980 *Full Scale Testing of Large Diameter Pipelines,* Proceedings of Pipeline and Energy Plant Piping Conference, pp.357-366, Pergamon Press, Oxford.

Sage, A.M., 1981, *A Review of the Physical Metallurgy of High Strength, Low Alloy Line Pipe and Pipe Fitting Steels,* Proceedings of an International Conference Sponsored by the Metals Society, in association with The Welding Institute, London, pp. 39-50.

Scott, P.M., 1993, *Interpretive study of Published and Recent Research on the Applicability and Limitations of Current Fracture Prediction Models for Girth Welds,* Canadian Metallurgical Quarterly, Vol.32, No.3, pp.223-238

Warren A., Ubihi, H.S. and Jack, D.H., 1981, *Relationship between Processing, Microstructure and Properties in 0.45% V Steel for X70 Pipelines,* Proceedings of an International Conference Sponsored by The Metals Society, in association with The Welding Institute, London, pp. 96-103.

Willoughby, A.A., 1982, *A Survey of Plastic Collapse Solutions Used in the Failure Assessment of Part Wall Perfects,* Welding Institute Report, Cambridge TWI Research Report 191.

Wilkowski, G.M. and Eiber R.J., 1978, *Review of Fracture Mechanics Approaches to Defining Critical Defect Size Girth Weld Discontinuities,* Welding Research Bulletin 329.

Wilkowski, G., Ahmed, I., Barnes, D., Brust, F., Gjadialo,N., Guerrieri,D., Kiefner, J., Kramer, G., Landow, M., Marschall, C., Maxey, W., Nakagaki, M., Papaspyropoulos, V., Pasupathi, V. and Scott, P., 1987, Nuclear Engineering Design, Vol. 98, pp195

Wilkowski, G. and Eiber, R.J., 1980, *Evaluation of Tensile Failure of Girth Weld Repair Grooves Subjected to Offshore Laying Stresses*, Energy Sources Technology Conference, New Orleans.

Woodhead, J.H., 1981, *Some Effects of Cooling Rate on Structure and Properties of Vanadium and Niobium Structural Steels*, Proceedings of an International Conference Sponsored by the Metals Society in association with The Welding Institute, London, pp. 237 - 241.

Worswick, M.J., Coote, R.I., Pick, R.J. and Burns, D.J., 1981, *Investigation of Plastic Collapse Criteria for Defects in Line Pipe Girth Welds During Bending*, Welding and Performance of Pipelines, The Welding Institute, London, Paper 30.

Wu, S.X., Mai, Y.W. and Cotterell, B., 1990, *Plastic -η factor (η_p) of Fracture Specimens with Deep and Shallow Cracks*, International Journal of Fracture, Vol. 45, pp.1-18.

Zhang, D.Z. and Lin, J. 1990, *A General Formula for Three-Point Bend Specimen J-integral Calculation*, Engineering Fracture Mechanics, Vol. 36, No.5, pp.789-793.

Tables

$$Q = a_0 + a_1\dot{L} + a_2\dot{L}^2 + a_3\dot{L}^3$$

CCP

a/t	a_0	a_1	a_2	a_3
0.25	3.9406	7.9036	3.7352	0.5270
0.5	6.6302	11.2936	5.0883	0.7022
0.75	6.1555	11.4064	5.5502	0.8208

SENT

a/t	a_0	a_1	a_2	a_3
0.25	-0.5960	1.4177	1.0393	0.1732
0.375	-0.6529	1.5506	1.2188	0.2145
0.5	-1.3369	0.9285	1.0644	0.2055
0.625	-7.0947	-7.5954	-2.8865	-0.3800
0.75	-7.4264	-7.5495	-2.6614	-0.3217

SENB

a/t	a_0	a_1	a_2	a_3
0.25	-4.8860	-5.4387	-2.2500	-0.3245
0.375	-0.5838	-0.5060	0.5711	0.1123
0.5	-2.8658	-2.4212	-0.6282	-0.0480
0.625	-4.3086	-4.9971	-1.9367	-0.2503
0.75	-0.8434	-4.3827	-1.6582	-0.2115

Table 2.1 SENB test results by Faucher et al. (1992).

Span (S) = 53.200 (mm) Sy = 500 (MPa)
nu = 0.3 E = 210000 (MPa)
rp = 0.44

Spec.	W (mm)	B (mm)	ao (mm)	a/W	Pmax (N)
S1	13.34	13.34	7.400	0.555	8441.242
S3	13.30	13.30	6.853	0.515	9514.030
S4	13.30	13.30	7.648	0.575	7257.237
S5	13.18	13.18	6.496	0.493	10192.778
S6	13.28	13.28	7.258	0.547	8679.364
S8	13.33	13.33	7.319	0.549	8156.062
S10	13.30	13.30	6.836	0.514	9691.000
S11	13.30	13.30	6.822	0.513	9001.342
S12	13.39	13.39	6.913	0.516	9757.000

Span (S) = 53.360 (mm) Sy = 500 (MPa)
nu = 0.3 E = 210000 (MPa)
rp = 0.44

Spec.	W (mm)	B (mm)	ao (mm)	a/W	Pmax (N)
W1	13.08	13.70	6.63	0.51	13463.000
W2	12.40	14.15	6.09	0.49	7619.671
W3	13.34	13.74	6.87	0.51	7379.705
W4	12.90	13.59	6.64	0.51	9035.980
W5	13.39	13.58	6.60	0.49	8055.930
W9	11.17	13.67	5.70	0.51	5276.780

Span (S) = 40.720 (mm) Sy = 383 (MPa)
nu = 0.3 E = 200000 (MPa)
rp = 0.44

Spec.	W (mm)	B (mm)	ao (mm)	a/W	Pmax (N)
X1	10.18	10.35	5.36	0.53	5256.716
X2	10.11	10.11	5.32	0.53	4672.085
X3	10.13	10.38	5.49	0.54	4386.793

Table 2.2 SENB test results by Lambert (1993).

	Grade, Class	Yield Strength (MPa)	Tensile Strength (MPa)
CAN3-Z245.1	483	483	565
API 5L	X70	482	565
Test	483	510	640

Table 3.1 Minimum tensile properties for Grade 483 (X70) pipeline steel (ASM Handbook, 1990b).

Specification	Grade	Composition, %									
		C	Mn	P	S	Si	Cr	Ni	Mo	Cu	Others
CAN3-Z245.1	483	0.26	(a)	0.03	0.035	0.5	(a)	(a)	(a)	(a)	(b)
API 5L	X70	0.23	1.6	0.04	0.05						(c)

(a) Maximum content maybe subject to agreement by purchaser and manufacturer.

(b) Maximums are 0.11% Nb, 0.11% V, 0.06% Ti, 0.001% B, and 0.020% (product analysis only) Ce.

(c) 0.005% min Nb, 0.02% min V, or a combination thereof shall be used at the discretion of the manufacturer.

Table 3.2 Compositions of Grade 483 pipeline steel (ASM Handbook, 1990b).

	Mid-section	Surface
8.4 mm thickness pipe	5.0 μm	3.5 μm
13.4 mm thickness pipe	5.7 μm	4.0 μm

Table 3.3 Grain size measured from the Grade 483 pipeline steel (intercept method).

	Mid-section	Surface (0.1t)	Surface (0.025t)
8.4 mm thickness pipe	0.110	0.103	0.107
13.4 mm thickness pipe	0.126	0.096	0.102

Table 3.4 Volume fraction of second phase measured from the Grade 483 pipeline steel.

	HARDNESS NUMBER			
AREA	Outside 5%	Middle 90%	Inside-5%	Over-all
Average	243.3	219.1	225.2	220.9
Deviation	19.2	13.2	11.8	14.0
/MID	1.11	1.00	1.03	1.01
AREA	Outside 10%	Middle 80%	Inside-10%	Over-all
Average	235.9	218.0	225.4	220.9
Deviation	17.5	12.8	13.0	14.0
/MID	1.08	1.00	1.03	1.01
AREA	Outside 20%	Middle 60%	Inside-20%	Over-all
Average	228.8	217.6	221.0	220.9
Deviation	16.3	12.3	13.6	14.0
/MID	1.05	1.00	1.02	1.02

Table 3.5 Hardness numbers measured from 8.4 mm thickness pipe.

	HARDNESS NUMBER			
AREA	Outside 5%	Middle 90%	Inside-5%	Over-all
Average	232.9	210.3	232.2	212.8
Deviation	7.4	7.8	6.6	9.2
/MID	1.11	1.00	1.10	1.01
AREA	Outside 10%	Middle 80%	Inside-10%	Over-all
Average	227.7	208.8	228.7	212.8
Deviation	6.8	7.2	6.3	9.2
/MID	1.09	1.00	1.10	1.02
AREA	Outside 20%	Middle 60%	Inside-20%	Over-all
Average	222.4	205.8	223.5	212.8
Deviation	6.3	6.1	6.3	9.2
/MID	1.08	1.00	1.09	1.03

Table 3.6 Hardness numbers measured from 13.4 mm thickness pipe.

	TENSILE STRENGTH (MPa)			
AREA	Outside 5%	Middle 90%	Inside-5%	Over-all
Average	771.8	696.2	717.1	701.7
Deviation	60.6	40.6	34.5	43.7
/MID	1.11	1.00	1.03	1.01
AREA	Outside 10%	Middle 80%	Inside-10%	Over-all
Average	750.2	692.3	716.6	701.7
Deviation	55.3	38.9	40.3	43.7
/MID	1.08	1.00	1.04	1.01
AREA	Outside 20%	Middle 60%	Inside-20%	Over-all
Average	727.1	691.2	701.8	701.7
Deviation	52.0	37.4	42.5	43.7
/MID	1.05	1.00	1.02	1.02

Table 3.7 Converted tensile strength for 8.4 mm thickness pipe.

	TENSILE STRENGTH (MPa)			
AREA	Outside 5%	Middle 90%	Inside-5%	Over-all
Average	740.0	668.4	670.0	672.8
Deviation	24.5	23.8	121.8	31.6
/MID	1.11	1.00	1.00	1.01
AREA	Outside 10%	Middle 80%	Inside-10%	Over-all
Average	721.6	664.0	687.3	672.8
Deviation	23.9	22.6	72.8	31.6
/MID	1.09	1.00	1.04	1.01
AREA	Outside 20%	Middle 60%	Inside-20%	Over-all
Average	705.6	654.9	690.2	672.8
Deviation	20.5	20.4	41.1	31.6
/MID	1.08	1.00	1.05	1.03

Table 3.8 Converted tensile strength for 13.4 mm thickness pipe.

Index	Width (mm)	Thickness (mm)	YS (MPa)	TS (MPa)
8x8 mm	7.6	8.5	540	660
5x5 mm	5.0	5.0	528	645
D=5 mm	5.0	5.0	528	645
outside	5.0	2.0	583	713
inside	5.0	2.0	554	677

Table 3.9 Tensile properties for 8.4 mm thickness pipe.

Index	width (mm)	thickness(mm)	YS (MPa)	TS (MPa)
13.4x8 mm	6.8	13.5	500	640
8x8 mm	8.3	8.4	490	627
D=8mm	8.3	8.3	490	627
outside	5.4	2.7	530	678
inside	5.3	2.7	510	653

Table 3.10 Tensile properties for 13.4 mm thickness pipe.

Index	ε_w	ε_t	R_{33}	F	G	H	L	M	N
8x8 mm	-0.036	-0.052	0.930	0.422	0.578	0.578	1.500	1.500	1.500
5x5 mm	-0.041	-0.048	0.960	0.457	0.543	0.543	1.500	1.500	1.500
D=5 mm	-0.042	-0.045	0.990	0.490	0.510	0.510	1.500	1.500	1.500

(a) Under uniform strain.

Index	ε_w	ε_t	R_{33}	F	G	H	L	M	N
8x8 mm	-0.456	-0.622	0.933	0.426	0.574	0.574	1.500	1.500	1.500
5x5 mm	-0.411	-0.546	0.935	0.428	0.572	0.572	1.500	1.500	1.500
D=5 mm	-0.404	-0.627	0.907	0.392	0.608	0.608	1.500	1.500	1.500

(b) Necked area

Table 3.11 Hill's stress function parameters for 8.4 mm thickness pipe.

Index	ε_w	ε_t	R_{33}	F	G	H	L	M	N
13.4x8	-0.024	-0.051	0.855	0.316	0.684	0.684	1.500	1.500	1.500
8x8	-0.025	-0.058	0.846	0.301	0.699	0.699	1.500	1.500	1.500
D=8	N/A	N/A	N/A	N/A	N/A	N/A	N/A	N/A	N/A

(a) Under uniform strain.

Index	ε_w	ε_t	R_{33}	F	G	H	L	M	N
13.4x8	-0.347	-0.600	0.886	0.363	0.637	0.637	1.500	1.500	1.500
8x8	-0.360	-0.683	0.874	0.345	0.655	0.655	1.500	1.500	1.500
D=8	-0.380	-0.787	0.861	0.326	0.674	0.674	1.500	1.500	1.500

(b) Necked area.

Table 3.12 Hill's stress function parameters for 13.4 mm thickness pipe.

Specimen	Thickness (mm)	Width (mm)	*a/t*	S_{net} (MPa)
B3	8.4	12.5	0.558	746.0
B4	8.4	12.5	0.779	755.1
B6	8.4	12.5	0.242	688.2
B7	8.4	12.5	0.267	646.2
B8	8.4	12.5	0.735	672.4
B9	8.4	12.5	0.520	679.2
E1	8.4	25.0	0.239	685.8
E2	8.4	25.0	0.474	697.9
E3	8.4	25.0	0.732	835.1
E4	8.4	25.0	0.287	737.8
E5	8.4	25.0	0.507	756.7
E6	8.4	25.0	0.778	922.0
F1 (SG)	8.4	12.5	0.250	824.0
F2 (SG)	8.4	12.5	0.500	776.0
F3 (SG)	8.4	12.5	0.750	836.0
A1	13.4	12.5	0.265	638.3
A2	13.4	12.5	0.536	654.5
A3	13.4	12.5	0.752	709.3
C7	13.4	12.5	0.305	655.0
C8	13.4	12.5	0.532	655.7
C9	13.4	12.5	0.757	686.7
D1	13.4	25.0	0.383	690.0
D2	13.4	25.0	0.542	714.6
D3	13.4	25.0	0.764	781.0
D4	13.4	25.0	0.330	728.7
D5	13.4	25.0	0.532	700.6
D6	13.4	25.0	0.774	799.1
D7 (SG)	13.4	12.5	0.250	836.0
D8 (SG)	13.4	12.5	0.500	782.0
D9 (SG)	13.4	12.5	0.750	780.0

(SG): Side-Grooved specimen

Table 4.1 SENT results for Grade 483 parent plate material (Phase I).

Specimen	Thickness (mm)	Width (mm)	*a/t*	S_{net} (MPa)
G1	8.4	25.0	0.274	722.5
G2	8.4	25.0	0.649	860.0
G3	8.4	25.0	0.660	840.8
G4	8.4	25.0	0.262	757.8
G6	8.4	25.0	0.625	701.5
G8	8.4	25.0	0.596	760.5
G10	8.4	25.0	0.379	789.5
G11	8.4	25.0	0.593	749.5
J1	13.4	25.0	0.436	785.7
J2	13.4	25.0	0.411	732.9
J3	13.4	25.0	0.787	814.2
J5	13.4	25.0	0.347	668.3
J6	13.4	25.0	0.796	842.4
J9	13.4	25.0	0.810	745.0
J10	13.4	25.0	0.245	627.5

Table 4.2 SENT results for Grade 483 parent plate material (Phase II).

Specimen t = 8.4 mm	a/t	S_{net} (MPa)
2-D Plane Strain	0.2	820
	0.4	813
	0.6	813
	0.8	823
2-D Plane Stress	0.2	583
	0.4	573
	0.6	581
	0.8	625
3-D Isotropic Analysis	0.2	763
	0.4	789
	0.6	802
	0.8	814
3-D Microstructure Based Analysis	0.2	745
	0.4	766
	0.6	776
	0.8	798

Table 4.3 The maximum net-section stresses resulted from finite element analyses for 8.4 mm thickness specimens.

Specimen t = 13.4 mm	a/t	S_{net} **(MPa)**
2-D Plane Strain	0.2	772
	0.4	765
	0.6	766
	0.8	770
2-D Plane Stress	0.2	548
	0.4	573
	0.6	560
	0.8	592
3-D Isotropic Analysis	0.2	705
	0.4	720
	0.6	739
	0.8	755
3-D Microstructure Based Analysis	0.2	684
	0.4	693
	0.6	706
	0.8	720

Table 4.4 The maximum net-section stresses resulted from finite element analyses for 13.4 mm thickness specimens.

Spec.	Outer Radius Ro	Thick. t	Gauge Length 2b	Crack Depth a	Crack Width 2c	a/t	Pmax	CS. Area No Crack	CS. Area Crack	Snom (MAX)	Snet (MAX)
	(mm)	(mm)	(mm)	(mm)	(mm)		(kN)	(mm^2)	(mm^2)	(MPa)	(MPa)
WP1	381.0	8.4	152.40	4.78	9.87	0.57	788.10	1289.05	1251.99	611.38	629.48
WP3	381.0	8.4	152.10	5.80	23.38	0.69	744.32	1286.47	1179.97	578.58	630.80
WP4	381.0	8.4	152.55	5.65	22.40	0.67	781.00	1290.33	1190.93	605.27	655.79
WP5	381.0	8.4	151.20	4.05	15.34	0.48	817.67	1278.76	1229.96	639.42	664.79
WP7	381.0	8.4	151.35	3.66	14.72	0.44	854.35	1280.04	1237.73	667.44	690.26
WP8	381.0	8.4	150.70	2.40	12.82	0.29	885.05	1274.47	1250.30	694.45	707.87
WP9	381.0	8.4	151.75	3.50	27.68	0.42	810.69	1283.47	1207.38	631.64	671.45
WP10	381.0	8.4	151.40	2.80	28.30	0.33	828.08	1280.47	1218.24	646.70	679.73
XP1	381	13.4	152.2	7.64	28.52	0.57	1296.50	2053.74	1882.61	631.29	688.67
XP2	381	13.4	152.10	6.350	38.95	0.47	1137.10	2052.35	1858.09	554.05	611.97
XP3	381	13.4	152.15	11.080	65.93	0.83	862.70	2053.04	1479.31	420.21	583.18
XP4	381	13.4	151.82	4.860	28.33	0.36	1224.40	2048.53	1940.39	597.70	631.01
XP5	381	13.4	152.25	8.310	32.86	0.62	1105.10	2054.44	1839.97	537.91	600.61
WQP3	381	8.4	279.02	6.200	90.25	0.74	1178.78	2400.88	1961.41	490.98	600.99
WQP4	381	8.4	279.53	4.900	93.5	0.58	1281.48	2405.48	2045.65	532.73	626.44

Yield stress = 510 (MPa)
Ultimate Stress = 720 (MPa)
Flow Stress = 579 (MPa)
Elastic Modulus = 210 (GPa)
Poisson's ratio = 0.3

Table 5.1 Summary of wide plate test results (Lambert, 1993).

Spec.	Outer Radius Ro [mm]	Thick. t [mm]	Plate Width 2b [mm]	Crack Depth a [mm]	Crack Width 2c [mm]	PD 6493 -1981 Safety Factor	CEGB R6	Net Section Yielding	Ligament Necking Solution	Maximum Net-section Stress
WP1	381	8.4	152.4	4.78	19.74	2.329512	1.462395	1.065144	0.994897	0.95674473
WP3	381	8.4	152.1	5.8	23.38	3.069366	1.580663	1.035792	0.994949	0.94148862
WP4	381	8.4	152.55	5.65	22.4	3.035845	1.613959	1.076831	1.03274	0.97733235
WP5	381	8.4	151.2	4.05	15.34	2.027504	1.390095	1.091611	1.008788	0.97619819
WP7	381	8.4	151.35	3.66	14.72	1.942209	1.401264	1.133428	1.034869	1.01508455
WP8	381	8.4	150.7	2.4	12.82	1.596427	1.319141	1.162344	1.056518	1.0502483
WP9	381	8.4	151.75	3.5	27.68	1.778013	1.384857	1.102537	1.014268	0.98452394
WP10	381	8.4	151.4	2.8	28.3	1.592857	1.330504	1.116153	1.011514	0.99231746
WQP3	381	8.4	279.02	6.2	90.25	3.078234	1.716561	0.986841	0.993365	0.95092703
WQP4	381	8.4	279.53	4.9	93.5	2.099443	1.509214	1.02864	0.991205	0.96822492
XP1	381	13.4	152.2	7.64	28.52	2.581054	1.595562	1.210321	1.1	1.08
XP2	381	13.4	152.1	6.35	38.95	1.850762	1.346625	1.07552	0.98705	0.94732306
XP3	381	13.4	152.15	11.08	65.93	4.26547	1.604465	1.024921	1.000309	0.90696731
XP4	381	13.4	151.82	4.86	28.33	1.648222	1.302272	1.108974	0.98749	0.97527935
XP5	381	13.4	152.25	8.31	32.86	2.488759	1.445451	1.055547	1.004358	0.93406892

Table 5.2 Summary of wide plate analyses results.

Spec.	Outer Radius Ro [mm]	Thick. t [mm]	Plate Width 2W [mm]	Crack Depth a [mm]	Crack Width 2c [mm]	a/t	c/W	2W/t	Sy [MPa]	Sult [MPa]	Geometry Correction Factor	CEGB/R6 Correction factor
wja1	381	8.4	598.4734	2.1	29.92	0.25	0.050	71.25	540	658	1.1216	0.8467
wja2	381	8.4	598.4734	2.1	59.86	0.25	0.100	71.25	540	658	1.1003	0.8278
wja3	381	8.4	598.4734	2.1	89.78	0.25	0.150	71.25	540	658	1.0927	0.8204
wja4	381	8.4	598.4734	2.1	119.8	0.25	0.200	71.25	540	658	1.0866	0.8165
wja5	381	8.4	598.4734	2.1	148.62	0.25	0.250	71.25	540	658	1.0866	0.8142
wja6	381	8.4	598.4734	2.1	297.24	0.25	0.500	71.25	540	658	1.0547	0.8090
wjb1	381	8.4	598.4734	4.2	29.92	0.5	0.050	71.25	540	658	1.0699	0.6934
wjb2	381	8.4	598.4734	4.2	59.86	0.5	0.100	71.25	540	658	1.0365	0.6556
wjb3	381	8.4	598.4734	4.2	89.78	0.5	0.150	71.25	540	658	1.0289	0.6409
wjb4	381	8.4	598.4734	4.2	119.8	0.5	0.200	71.25	540	658	1.0243	0.6330
wjb5	381	8.4	598.4734	4.2	148.62	0.5	0.250	71.25	540	658	1.0334	0.6283
wib6	381	8.4	598.4734	4.2	297.24	0.5	0.500	71.25	540	658	0.9650	0.6181
wjc1	381	8.4	598.4734	6.3	29.92	0.75	0.050	71.25	540	658	0.9863	0.5401
wjc2	381	8.4	598.4734	6.3	59.86	0.75	0.100	71.25	540	658	0.9650	0.4834
wjc3	381	8.4	598.4734	6.3	89.78	0.75	0.150	71.25	540	658	0.9468	0.4613
wjc4	381	8.4	598.4734	6.3	119.8	0.75	0.200	71.25	540	658	0.9195	0.4495
wjc5	381	8.4	598.4734	6.3	148.62	0.75	0.250	71.25	540	658	0.8830	0.4425
wjc6	381	8.4	598.4734	6.3	297.24	0.75	0.500	71.25	540	658	0.6884	0.4271
wka1	381	8.4	1196.9468	2.1	59.84	0.25	0.050	142.49	540	658	1.1003	0.8278
wka2	381	8.4	1196.9468	2.1	119.72	0.25	0.100	142.49	540	658	1.0866	0.8165
wka3	381	8.4	1196.9468	2.1	179.56	0.25	0.150	142.49	540	658	1.0714	0.8124
wka4	381	8.4	1196.9468	2.1	239.6	0.25	0.200	142.49	540	658	1.0714	0.8103
wka5	381	8.4	1196.9468	2.1	297.24	0.25	0.250	142.49	540	658	1.0760	0.8090
wkb1	381	8.4	1196.9468	4.2	59.84	0.5	0.050	142.49	540	658	1.0137	0.6556
wkb2	381	8.4	1196.9468	4.2	119.72	0.5	0.100	142.49	540	658	0.9863	0.6330
wkb3	381	8.4	1196.9468	4.2	179.56	0.5	0.150	142.49	540	658	0.9848	0.6249
wkb4	381	8.4	1196.9468	4.2	239.6	0.5	0.200	142.49	540	658	0.9909	0.6206
wkb5	381	8.4	1196.9468	4.2	297.24	0.5	0.250	142.49	540	658	0.9985	0.6181
wkc1	381	8.4	1196.9468	6.3	59.84	0.75	0.050	142.49	540	658	0.9422	0.4835
wkc2	381	8.4	1196.9468	6.3	119.72	0.75	0.100	142.49	540	658	0.8647	0.4496
wkc3	381	8.4	1196.9468	6.3	179.56	0.75	0.150	142.49	540	658	0.8100	0.4373
wkc4	381	8.4	1196.9468	6.3	239.6	0.75	0.200	142.49	540	658	0.7401	0.4309
wkc5	381	8.4	1196.9468	6.3	297.24	0.75	0.250	142.49	540	658	0.7052	0.4271
jwa1	381	8.4	152.55	1.05	19.06875	0.125	0.125	18.16	540	658	1.0152	0.9318
jwa2	381	8.4	152.55	1.05	38.1375	0.125	0.250	18.16	540	658	1.0274	0.9195
jwa3	381	8.4	152.55	1.05	76.275	0.125	0.500	18.16	540	658	1.0532	0.9116
jwa4	381	8.4	152.55	1.05	114.4125	0.125	0.750	18.16	540	658	1.0790	0.9085
jwb1	381	8.4	152.55	2.1	19.06875	0.25	0.125	18.16	540	658	1.0182	0.8637
jwb2	381	8.4	152.55	2.1	38.1375	0.25	0.250	18.16	540	658	1.0304	0.8391
jwb3	381	8.4	152.55	2.1	76.275	0.25	0.500	18.16	540	658	1.0638	0.8231
jwb4	381	8.4	152.55	2.1	114.4125	0.25	0.750	18.16	540	658	1.1125	0.8171
jwc1	381	8.4	152.55	4.2	19.06875	0.5	0.125	18.16	540	658	1.0030	0.7274
jwc2	381	8.4	152.55	4.2	38.1375	0.5	0.250	18.16	540	658	1.0015	0.6782
jwc3	381	8.4	152.55	4.2	76.275	0.5	0.500	18.16	540	658	1.0274	0.6463
jwc4	381	8.4	152.55	4.2	114.4125	0.5	0.750	18.16	540	658	1.1079	0.6342
jwd1	381	8.4	152.55	6.3	19.06875	0.75	0.125	18.16	540	658	0.9498	0.5911
jwd2	381	8.4	152.55	6.3	38.1375	0.75	0.250	18.16	540	658	0.9422	0.5173
jwd3	381	8.4	152.55	6.3	76.275	0.75	0.500	18.16	540	658	0.9802	0.4694
jwd4	381	8.4	152.55	6.3	114.4125	0.75	0.750	18.16	540	658	1.0426	0.4512
jwe1	381	8.4	152.55	7.35	19.06875	0.875	0.125	18.16	540	658	0.8997	0.5229
jwe2	381	8.4	152.55	7.35	38.1375	0.875	0.250	18.16	540	658	0.9012	0.4368
jwe3	381	8.4	152.55	7.35	76.275	0.875	0.500	18.16	540	658	0.9012	0.3810
jwe4	381	8.4	152.55	7.35	114.4125	0.875	0.750	18.16	540	658	0.9088	0.3598

Table 5.3 Summary of wide plate analyses with various crack geometries.

TEST NO	D	t	Grade	Sy	Sflow	2c	a	S failure	Mode	a c	2c pID	a c	CEGB R6 PD6493-91	Willoughby's PC Solution	CSA Z184	CSA Z184 (W O SF)
	mm	mm		MPa	MPa	mm	mm	MPa						Safety Margin		
49	762	19	448	472	541	105	3.48	566	D+BF	0.1832	0.0439	0.0663	1.074	1.090	1.252	1.198
50	762	19	448	472	541	139	3.73	595	D+BF	0.1963	0.0581	0.0537	1.140	1.167	1.359	1.275
51	762	19	448	472	541	125	5	520	D+BF	0.2632	0.0522	0.08	0.995	1.032	1.216	1.124
9	914	11.1	483	531	600	81.8	8.8	622	D	0.7928	0.0285	0.2152	1.064	1.169	1.417	1.235
11	914	11.1	483	531	600	79	9.3	627	D	0.8378	0.0275	0.2354	1.072	1.182	1.436	1.247
14	914	11.1	483	531	600	64.8	5.5	686	D	0.4955	0.0226	0.1698	1.163	1.211	1.390	1.305
15	914	11.1	483	531	600	60.3	5.5	651	D	0.4955	0.021	0.1824	1.102	1.145	1.309	1.235
18	914	11.1	483	531	600	265	3.3	569	D	0.2973	0.0923	0.0249	1.011	1.100	1.368	1.151
19	914	11.1	483	531	600	278	3.2	635	D	0.2883	0.0968	0.023	1.131	1.231	1.536	1.287
21	914	11.1	483	466	535	279	3.9	411	D	0.3514	0.0972	0.028	0.824	0.927	1.220	0.972
22	914	11.1	483	466	535	331	3.7	390	D	0.3333	0.1153	0.0224	0.792	0.903	1.223	0.939
23	914	11.1	483	466	535	75	3.5	671	D	0.3153	0.0261	0.0933	1.276	1.308	1.506	1.439
28	914	11.1	483	466	535	282	3.1	470	D	0.2793	0.0982	0.022	0.939	1.019	1.288	1.083
29	914	11.72	483	470	539	280	2.9	533	D	0.2474	0.0975	0.0207	1.055	1.125	1.395	1.202
31	914	11.72	483	470	539	116	2.2	656	D	0.1877	0.0404	0.0379	1.247	1.265	1.451	1.392
32	610	6.76	448	532	601	100	3.1	487	D	0.4586	0.0522	0.062	0.843	0.921	1.124	0.970
33	610	6.76	448	532	601	199	2.8	427	D	0.4142	0.1038	0.0281	0.769	0.906	1.248	0.917
34	610	6.76	448	532	601	51	3.1	542	D	0.4586	0.0266	0.1216	0.920	0.961	1.107	1.033
35	610	6.76	448	532	601	107	3.9	513	D	0.5769	0.0558	0.0729	0.894	1.018	1.303	1.055
46	914	11.7	483	460	530	112	2	635	D	0.1709	0.039	0.0357	1.226	1.240	1.423	1.372
47	914	11.7	483	460	530	141	3.9	629	D	0.3333	0.0491	0.0553	1.228	1.293	1.549	1.408
48	914	11.7	448	460	530	300	3.5	462	D	0.2991	0.1045	0.0233	0.937	1.034	1.341	1.095
52	711	25.4	414	470	539	127	10.9	586	D	0.4291	0.0569	0.1717	1.134	1.239	1.538	1.323
36	508	8.74	414	469	538	108	8.74	579	D	1	0.0677	0.1619	1.157	1.631	2.933	1.570
38	508	8.74	414	469	538	44.9	8.74	619	D	1	0.0281	0.3893	1.184	1.340	1.699	1.421
39	508	8.74	414	469	538	52.4	6.35	613	D	0.7265	0.0328	0.2424	1.173	1.295	1.603	1.384
40	508	8.74	414	469	538	52.4	6.76	625	D	0.7735	0.0328	0.258	1.197	1.332	1.663	1.420
41	508	8.74	414	469	538	50	5.94	637	D	0.6796	0.0313	0.2376	1.216	1.326	1.620	1.425
42	762	15.8	414	573	642	239	11.9	443	D	0.7532	0.0998	0.0996	0.759	1.109	2.189	1.018
44	762	15.8	414	573	642	119	7.9	591	D	0.5	0.0497	0.1328	0.957	1.052	1.279	1.097
45	762	15.8	414	573	642	239	7.9	526	D	0.5	0.0998	0.0661	0.888	1.094	1.581	1.080
12	914	11.1	483	531	600	63.5	6.3	755	B	0.5676	0.0221	0.1984	1.281	1.343	1.550	1.444
16	914	10.28	483	689	758	300	4.1	690	B	0.3988	0.1045	0.0273	0.985	1.151	1.529	1.138
17	914	10.28	483	689	758	300	3.6	690	B	0.3502	0.1045	0.024	0.982	1.115	1.429	1.115
26	1067	15	483	496	565	70	8	606	B	0.5333	0.0209	0.2286	1.090	1.136	1.314	1.234
37	508	8.74	414	469	538	42.6	4.76	637	B	0.5446	0.0267	0.2235	1.209	1.277	1.511	1.389
4	914	11.1	483	531	600	63.5	5.9	723	S	0.5315	0.0221	0.1858	1.226	1.281	1.473	1.379
5	914	11.1	483	531	600	69.8	5.5	723	S	0.4955	0.0243	0.1576	1.228	1.283	1.477	1.380
24	1067	15	483	496	565	14	0.9	606	S	0.06	0.0042	0.1286	1.075	1.074	1.189	1.187
25	1067	15	483	496	565	38	3	606	S	0.2	0.0113	0.1579	1.080	1.085	1.210	1.196

Table 6.1 Full pipe test results by Coote et. al. (1981).

INDEX	Yield Strength MPa	Ultimate Strength MPa	a/t	2c/piR	R/t	Geometry Correction Factor	CEGB/R6 Correction Factor	CSA Z662 Correction Factor	CSA Z662 Correction (W/O SF)
fla1	540	658	0.25	0.050	11.3	1.1717	0.9984	0.8136	0.8934
fla2	540	658	0.25	0.100	11.3	1.1717	0.9969	0.7138	0.8734
fla3	540	658	0.25	0.150	11.3	1.1672	0.9953	0.6140	0.8534
fla4	540	658	0.25	0.200	11.3	1.1550	0.9937	0.5139	0.8334
fla5	540	658	0.25	0.250	11.3	1.1505	0.9922	0.4179	0.8142
flb1	540	658	0.5	0.050	11.3	1.1550	0.9969	0.7138	0.8734
flb2	540	658	0.5	0.100	11.3	1.1064	0.9937	0.5143	0.8335
flb3	540	658	0.5	0.150	11.3	1.0653	0.9906	0.3147	0.7936
flb4	540	658	0.5	0.200	11.3	1.0319	0.9874	0.1146	0.7536
flb5	540	658	0.5	0.250	11.3	1.0091	0.9844	-0.0776	0.7151
flc1	540	658	0.75	0.050	11.3	1.0532	0.9953	0.6141	0.8535
flc2	540	658	0.75	0.100	11.3	0.9544	0.9906	0.3149	0.7936
flc3	540	658	0.75	0.150	11.3	0.8875	0.9858	0.0154	0.7337
flc4	540	658	0.75	0.200	11.3	0.8465	0.9811	-0.2848	0.6737
flc5	540	658	0.75	0.250	11.3	0.7903	0.9765	-0.5730	0.6160
fpa1	540	658	0.25	0.050	22.7	1.1064	0.9984	0.8136	0.8934
fpa2	540	658	0.25	0.100	22.7	1.1064	0.9969	0.7138	0.8734
fpa3	540	658	0.25	0.150	22.7	1.1079	0.9953	0.6140	0.8534
fpa4	540	658	0.25	0.200	22.7	1.1094	0.9937	0.5139	0.8334
fpa5	540	658	0.25	0.250	22.7	1.1079	0.9922	0.4179	0.8142
fpb1	540	658	0.5	0.050	22.7	1.1064	0.9969	0.7138	0.8734
fpb2	540	658	0.5	0.100	22.7	1.0578	0.9937	0.5143	0.8335
fpb3	540	658	0.5	0.150	22.7	1.0274	0.9906	0.3147	0.7936
fpb4	540	658	0.5	0.200	22.7	0.9970	0.9874	0.1146	0.7536
fpb5	540	658	0.5	0.250	22.7	0.9620	0.9844	-0.0776	0.7151
fpc1	540	658	0.75	0.050	22.7	1.0380	0.9953	0.6141	0.8535
fpc2	540	658	0.75	0.100	22.7	0.9757	0.9906	0.3149	0.7936
fpc3	540	658	0.75	0.150	22.7	0.8055	0.9858	0.0154	0.7337
fpc4	540	658	0.75	0.200	22.7	0.7295	0.9811	-0.2848	0.6737
fpc5	540	658	0.75	0.250	22.7	0.6581	0.9765	-0.5730	0.6160
fma1	540	658	0.25	0.050	45.4	0.9650	0.9984	0.8136	0.8934
fma2	540	658	0.25	0.100	45.4	0.9650	0.9969	0.7138	0.8734
fma3	540	658	0.25	0.150	45.4	0.9650	0.9953	0.6140	0.8534
fma4	540	658	0.25	0.200	45.4	0.9650	0.9937	0.5139	0.8334
fma5	540	658	0.25	0.250	45.4	0.9650	0.9922	0.4179	0.8142
fmb1	540	658	0.5	0.050	45.4	0.9650	0.9969	0.7138	0.8734
fmb2	540	658	0.5	0.100	45.4	0.9650	0.9937	0.5143	0.8335
fmb3	540	658	0.5	0.150	45.4	0.9650	0.9906	0.3147	0.7936
fmb4	540	658	0.5	0.200	45.4	0.9650	0.9874	0.1146	0.7536
fmb5	540	658	0.5	0.250	45.4	0.9149	0.9844	-0.0776	0.7151
fmc1	540	658	0.75	0.050	45.4	0.9650	0.9953	0.6141	0.8535
fmc2	540	658	0.75	0.100	45.4	0.8845	0.9906	0.3149	0.7936
fmc3	540	658	0.75	0.150	45.4	0.7143	0.9858	0.0154	0.7337
fmc4	540	658	0.75	0.200	45.4	0.6307	0.9811	-0.2848	0.6737
fmc5	540	658	0.75	0.250	45.4	0.5578	0.9765	-0.5730	0.6160
fka1	540	658	0.25	0.050	90.7	0.8389	0.9992	0.8634	0.9033
fka2	540	658	0.25	0.100	90.7	0.8374	0.9984	0.8136	0.8934
fka3	540	658	0.25	0.150	90.7	0.8359	0.9977	0.7637	0.8834
fka4	540	658	0.25	0.200	90.7	0.8328	0.9969	0.7136	0.8734
fka5	540	658	0.25	0.250	90.7	0.8313	0.9961	0.6656	0.8638
fkb1	540	658	0.5	0.050	90.7	0.8328	0.9984	0.8136	0.8934
fkb2	540	658	0.5	0.100	90.7	0.8328	0.9969	0.7138	0.8734
fkb3	540	658	0.5	0.150	90.7	0.8313	0.9953	0.6140	0.8534
fkb4	540	658	0.5	0.200	90.7	0.8298	0.9937	0.5139	0.8334
fkb5	540	658	0.5	0.250	90.7	0.8267	0.9922	0.4179	0.8142
fkc1	540	658	0.75	0.050	90.7	0.8298	0.9977	0.7637	0.8834
fkc2	540	658	0.75	0.100	90.7	0.8283	0.9953	0.6141	0.8535
fkc3	540	658	0.75	0.150	90.7	0.8267	0.9929	0.4644	0.8235
fkc4	540	658	0.75	0.200	90.7	0.8237	0.9906	0.3143	0.7935
fkc5	540	658	0.75	0.250	90.7	0.8222	0.9883	0.1701	0.7647

Table 6.2 Finite element analysis results for various crack geometries.

Figures

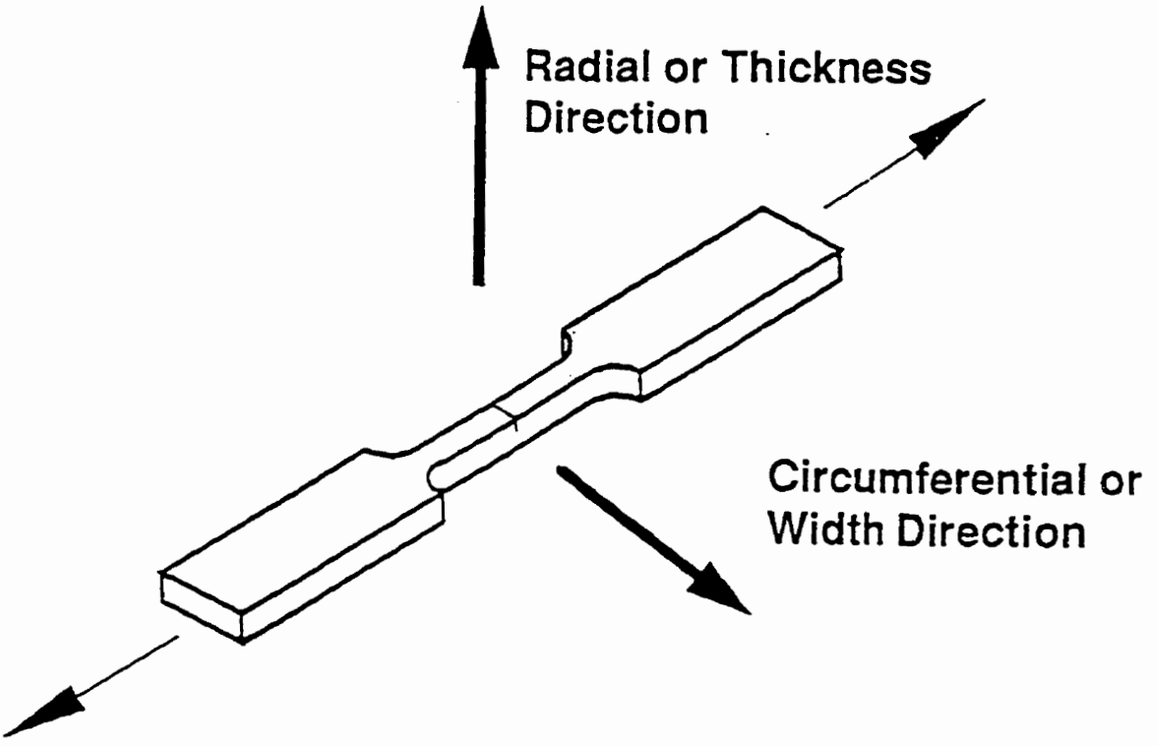

Figure 1.1 Pipeline Fracture Specimen.

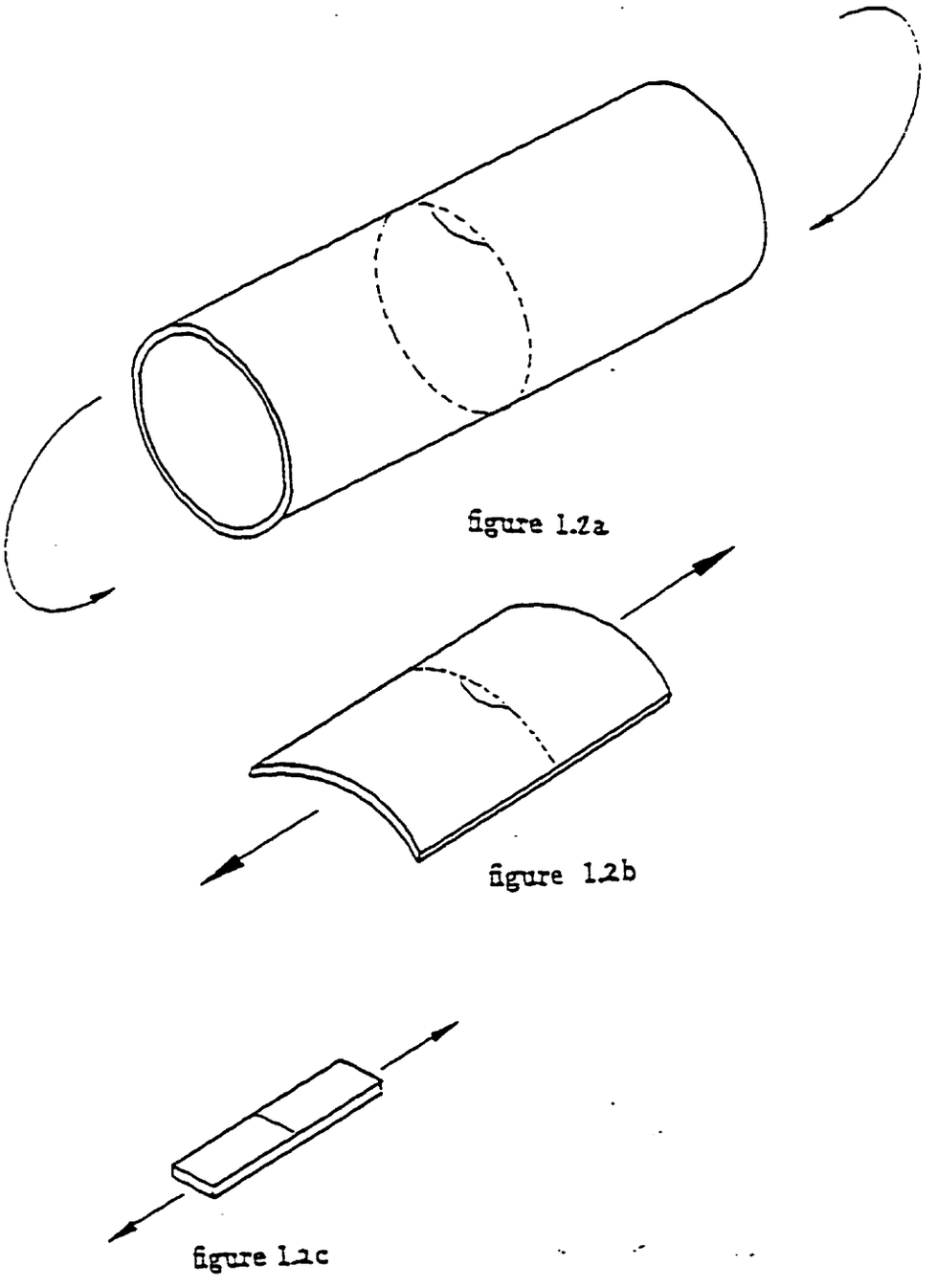

Figure 1.2 Specimen and model configurations.

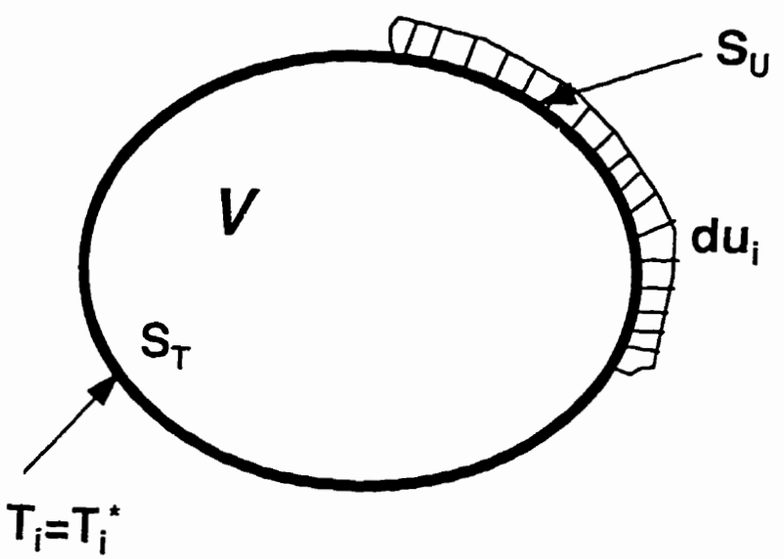

Figure 2.1 A schematic explanation of the virtual work principle.

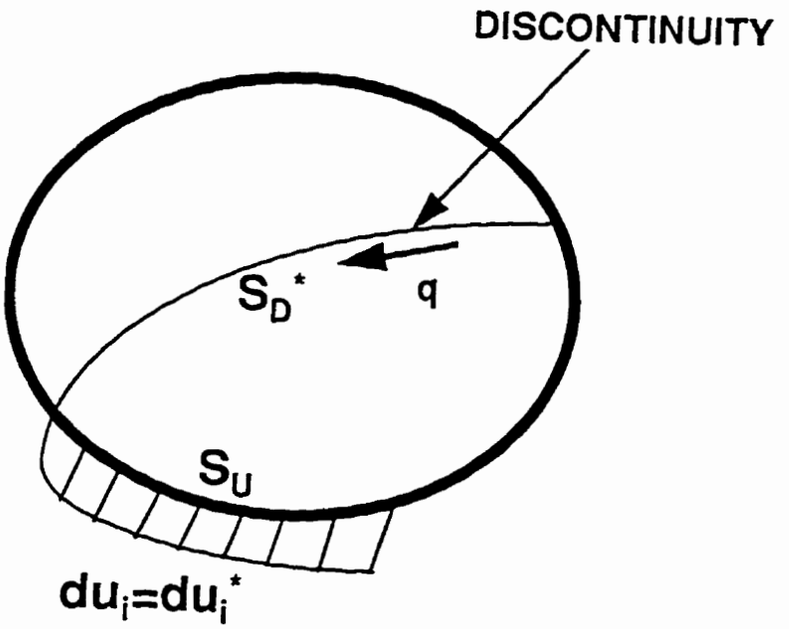

Figure 2.2 The kinematically admissible displacement increment field.

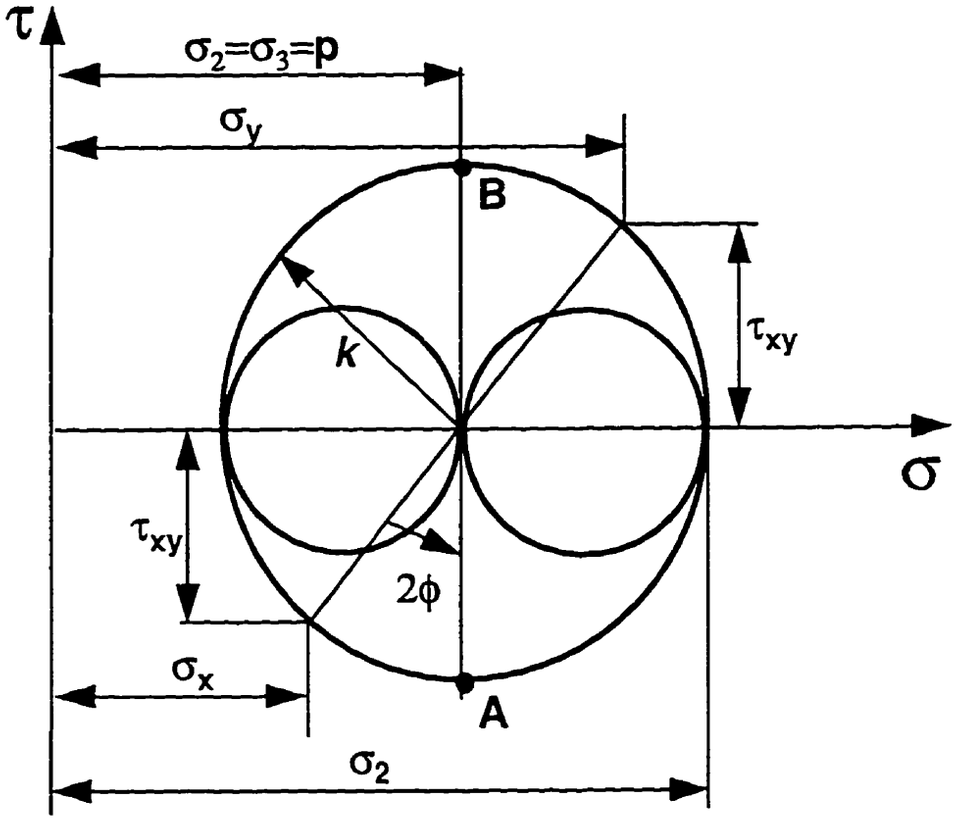

Figure 2.3 The Mohr circle diagram representing the state of stress.

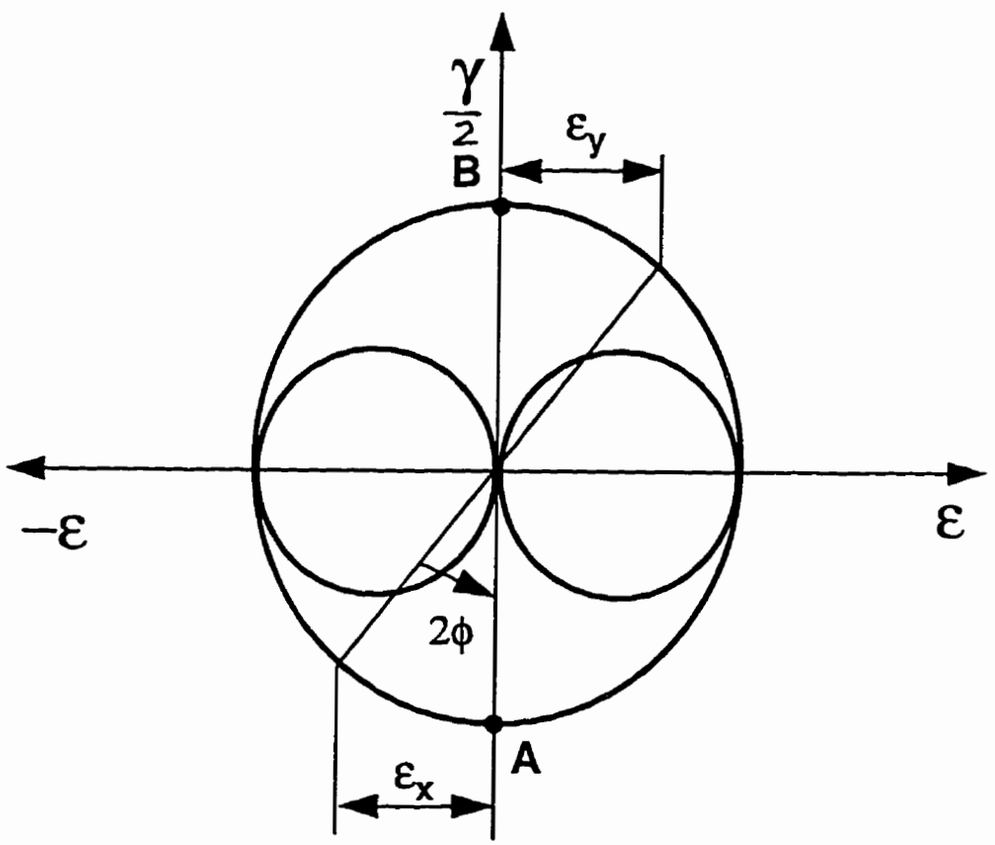

Figure 2.4 The Mohr circle diagram representing the state of strain-rates.

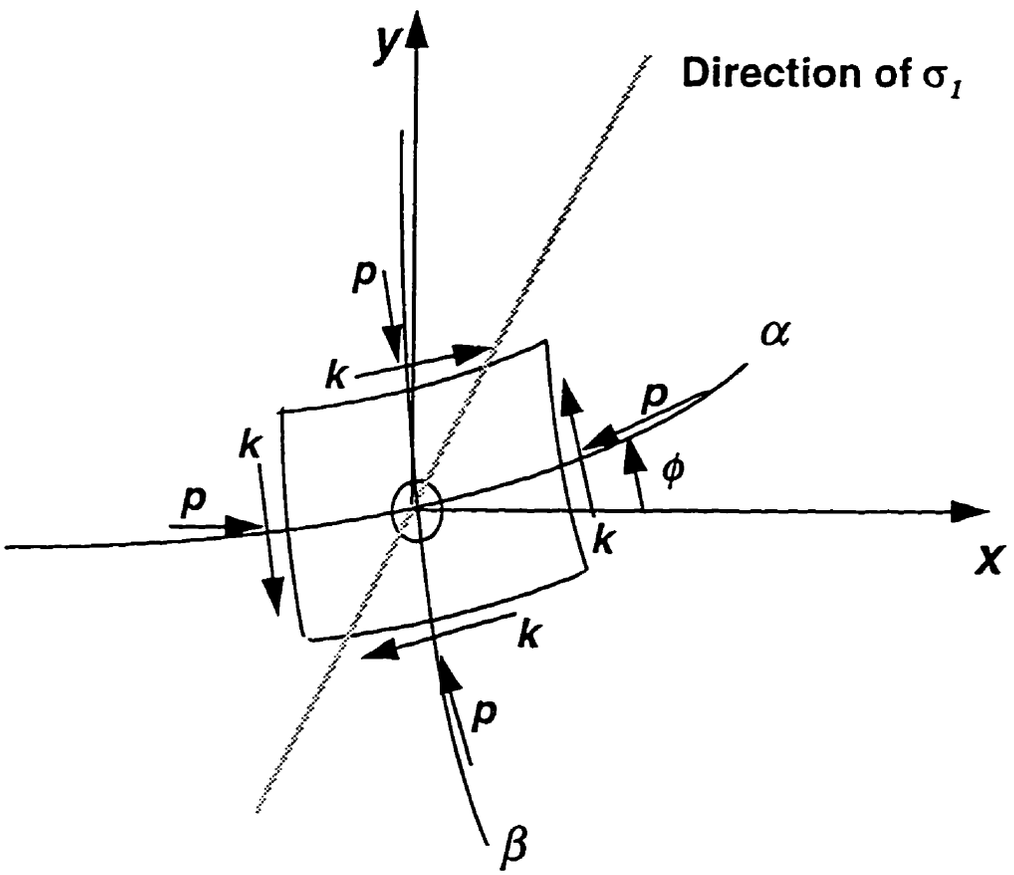

Figure 2.5 A schematic illustration of slip lines.

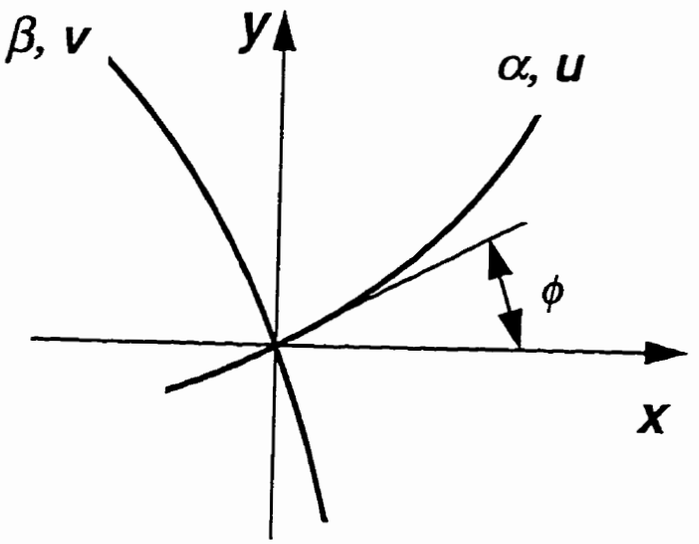

Figure 2.6 The maximum shear velocity lines and the velocity slip-lines.

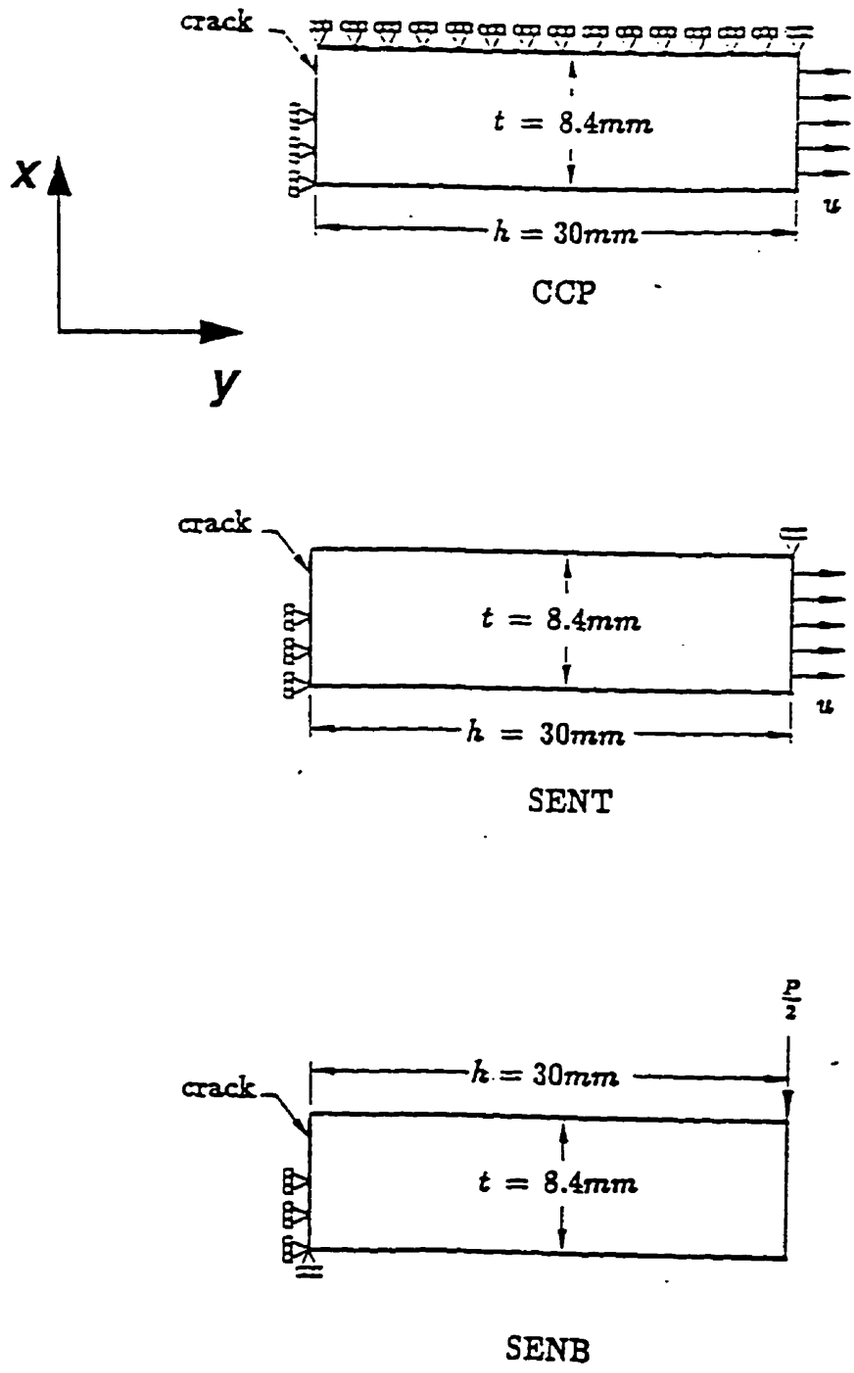

Figure 2.7 Schematic illustration of test specimens.

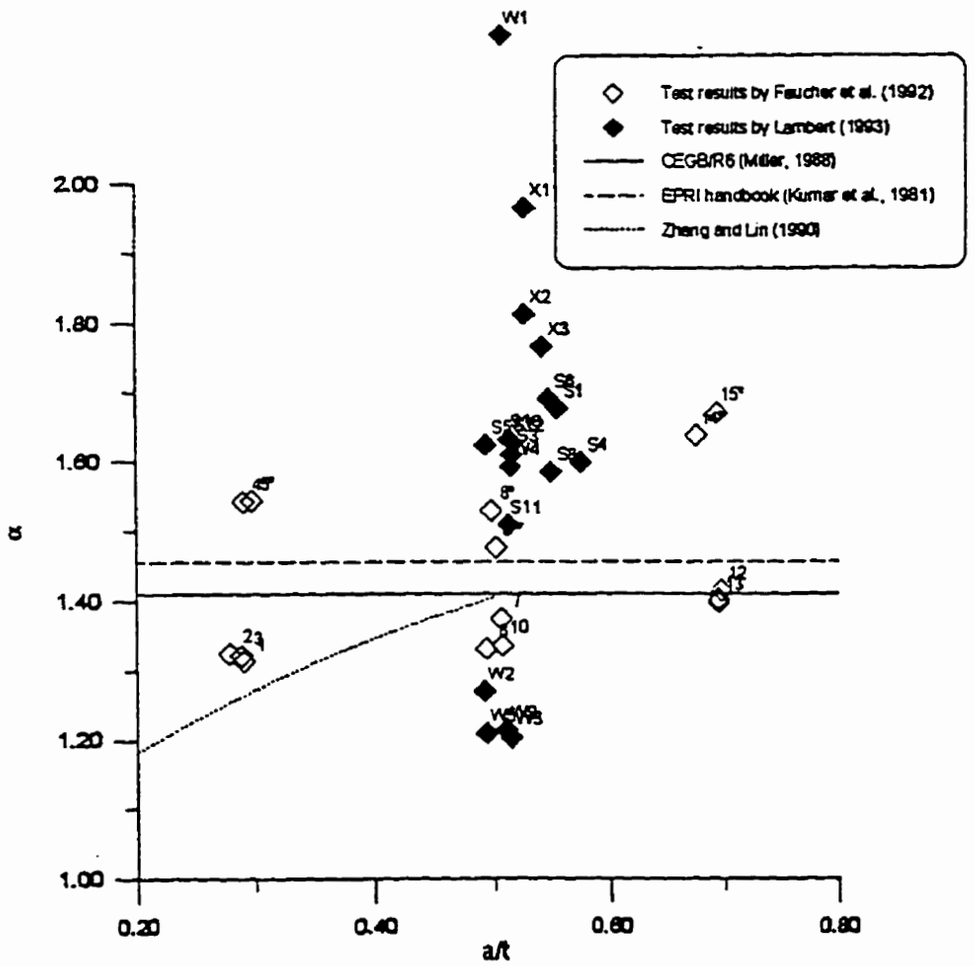

Figure 2.8 SENB specimen test results by Faucher et al. (1992) and Lambert (1993).

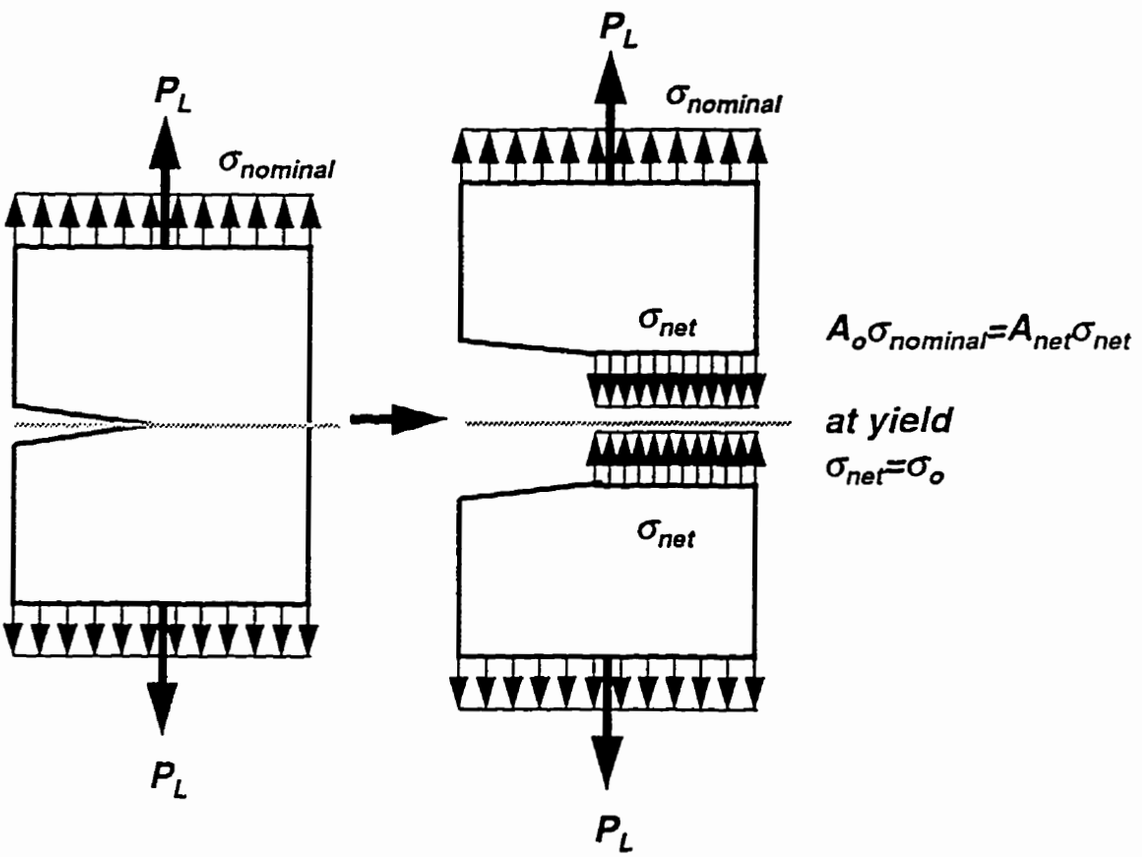

Figure 2.9 A schematic illustration of the lower-bound solution of an SENT specimen.

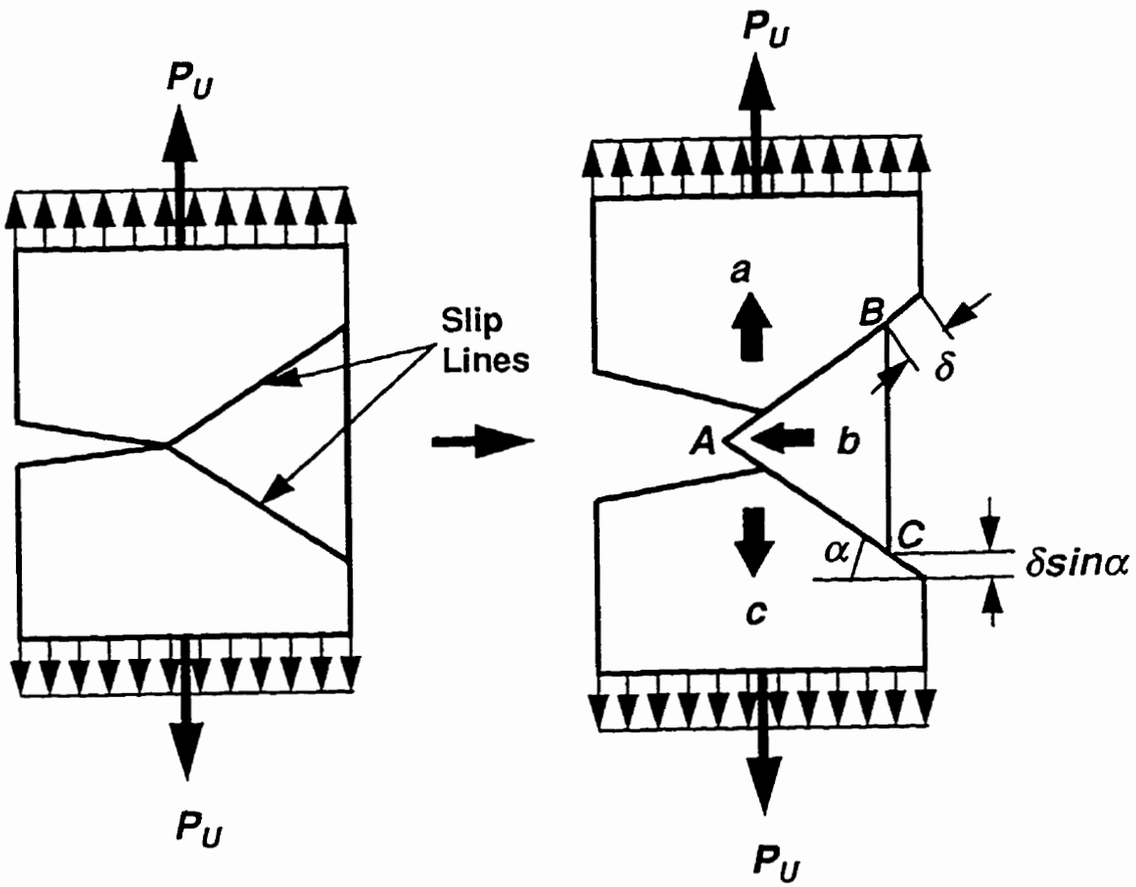

Figure 2.10 A schematic illustration of the upper-bound solution of an SENT specimen.

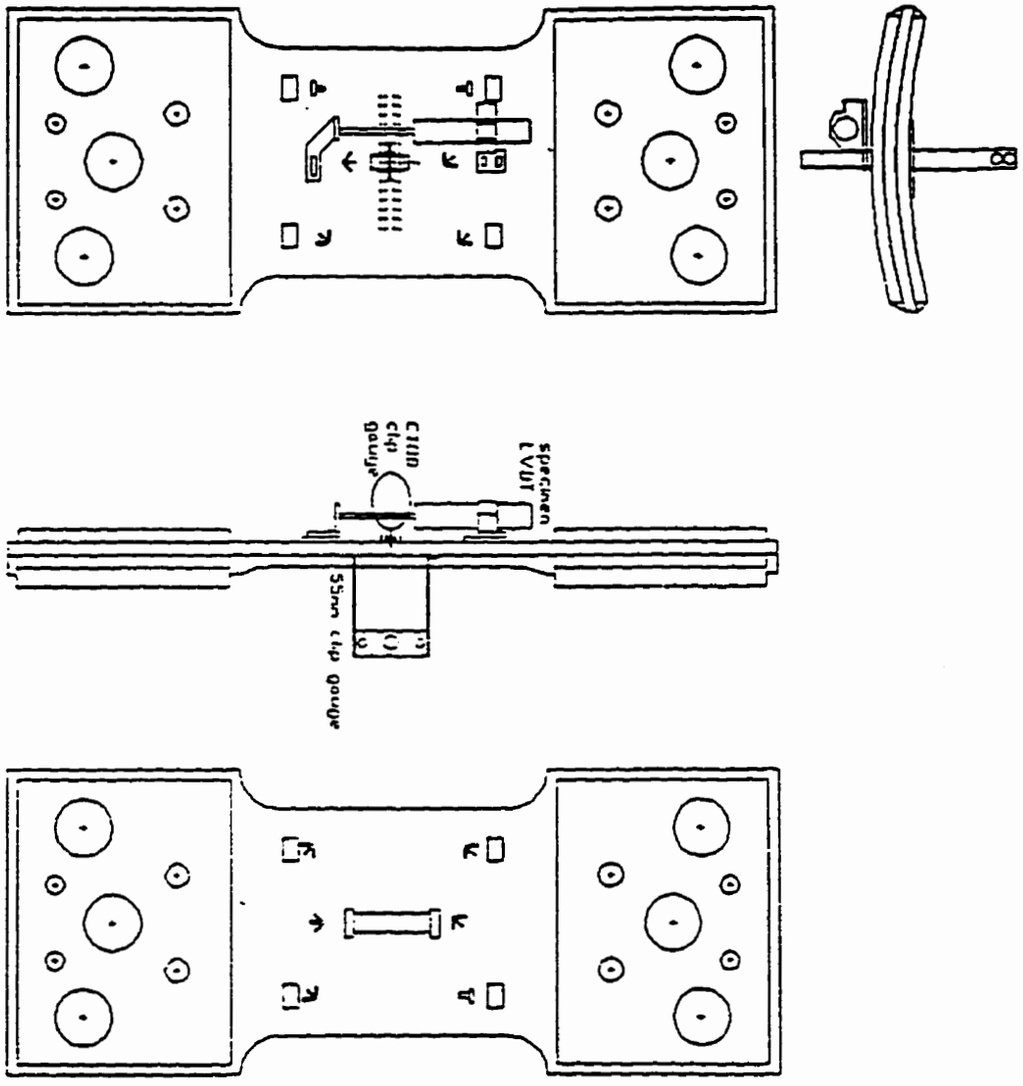

Figure 2.11 Wide plate test specimen configuration (Lescek, 1991).

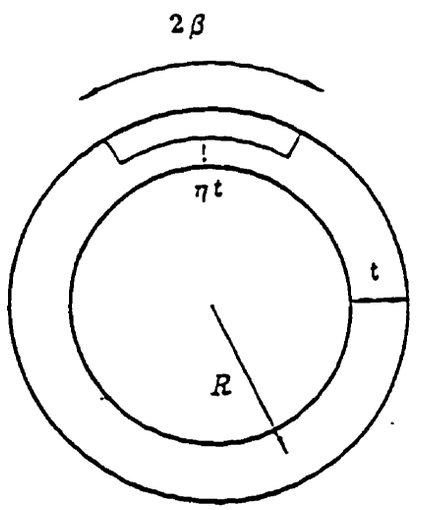

Figure 2.12 Geometry for pipeline surface defect limit load solutions (Miller, 1988).

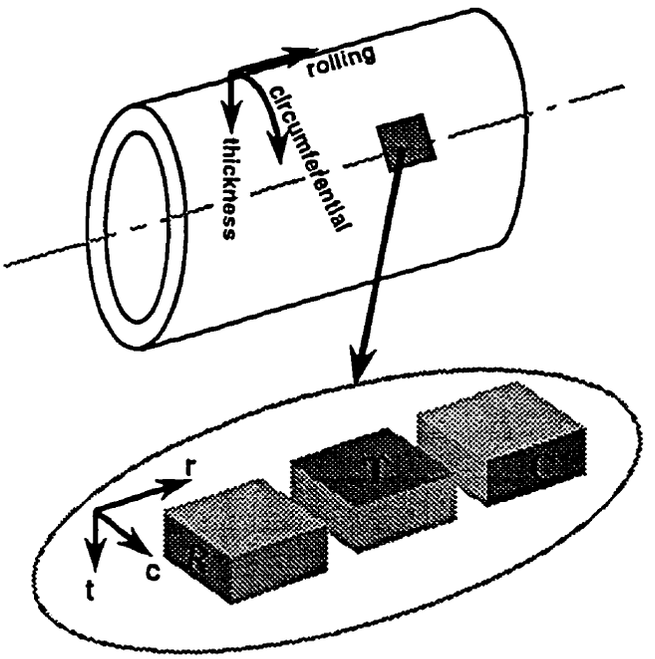

Figure 3.1 Samples used for microscopic observation.

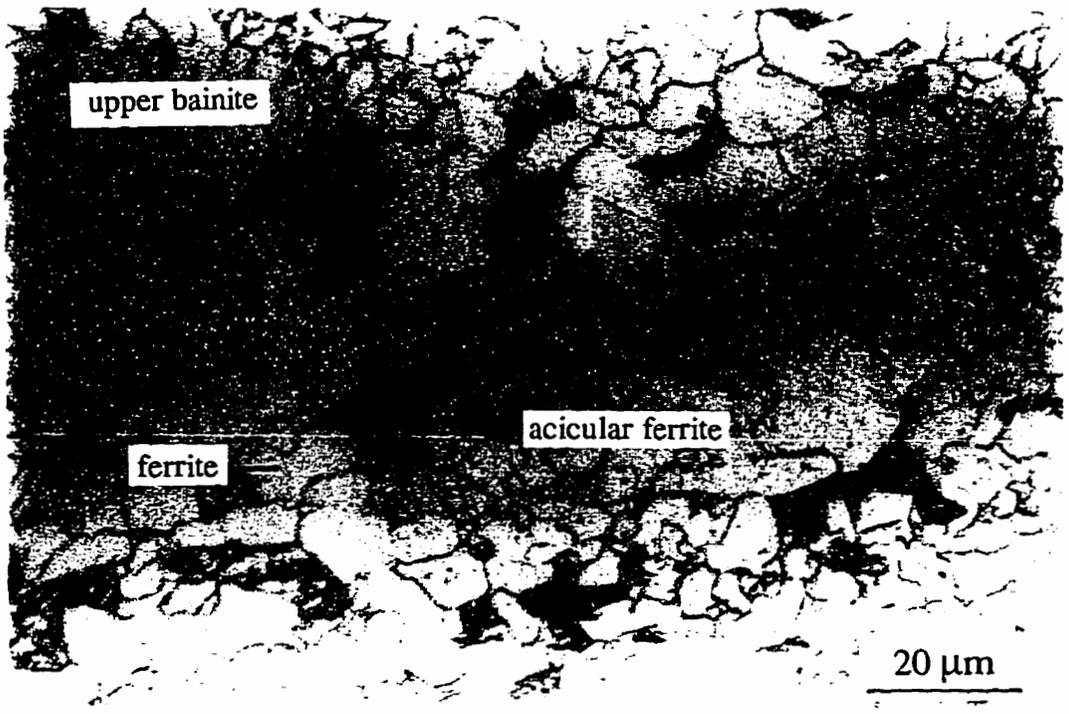

Figure 3.2 Microstructure of Grade 483 pipeline steel.

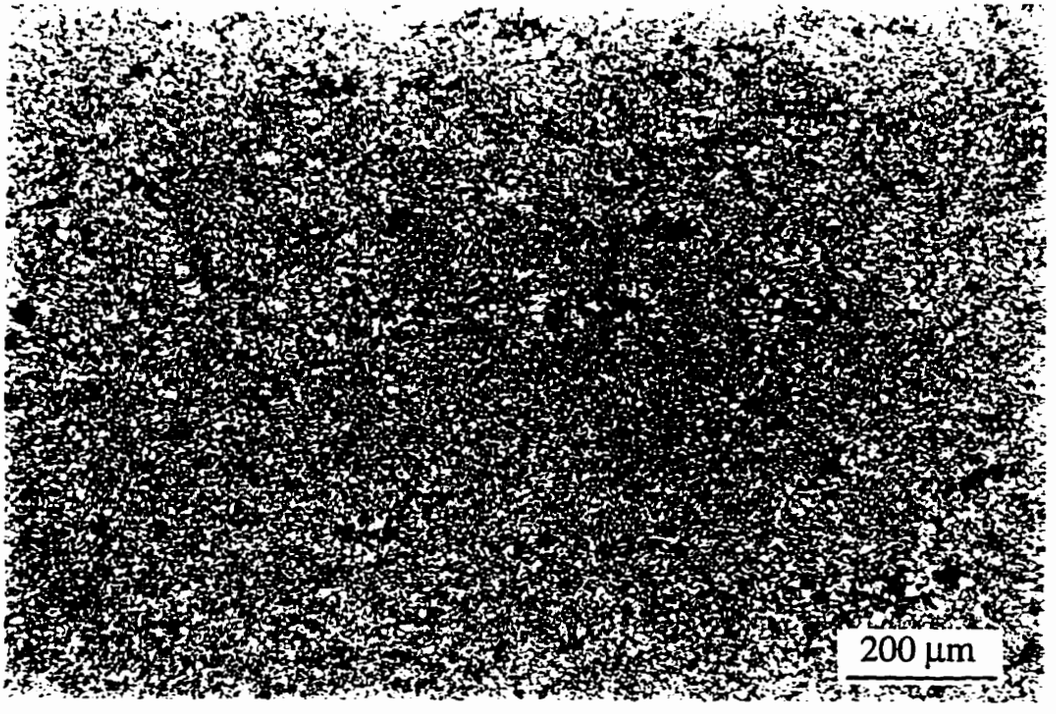

Figure 3.3 Microstructure of Grade 483 steel observed from T plane (8.4mm thickness pipe).

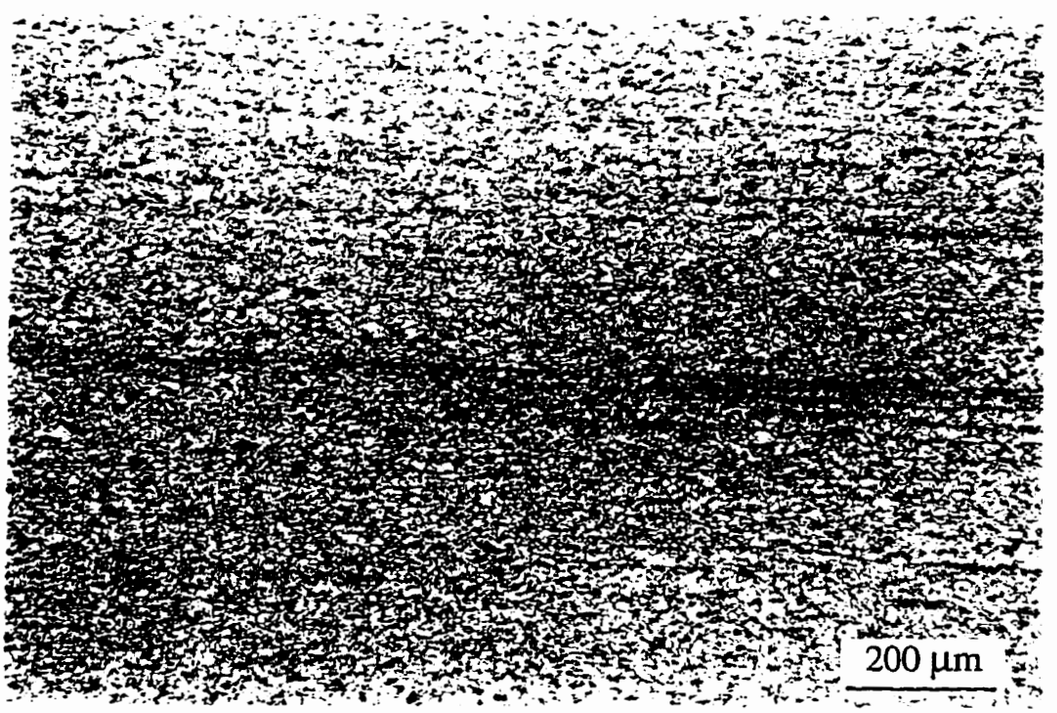

Figure 3.4 Microstructure of Grade 483 steel observed from C plane (8.4mm thickness pipe).

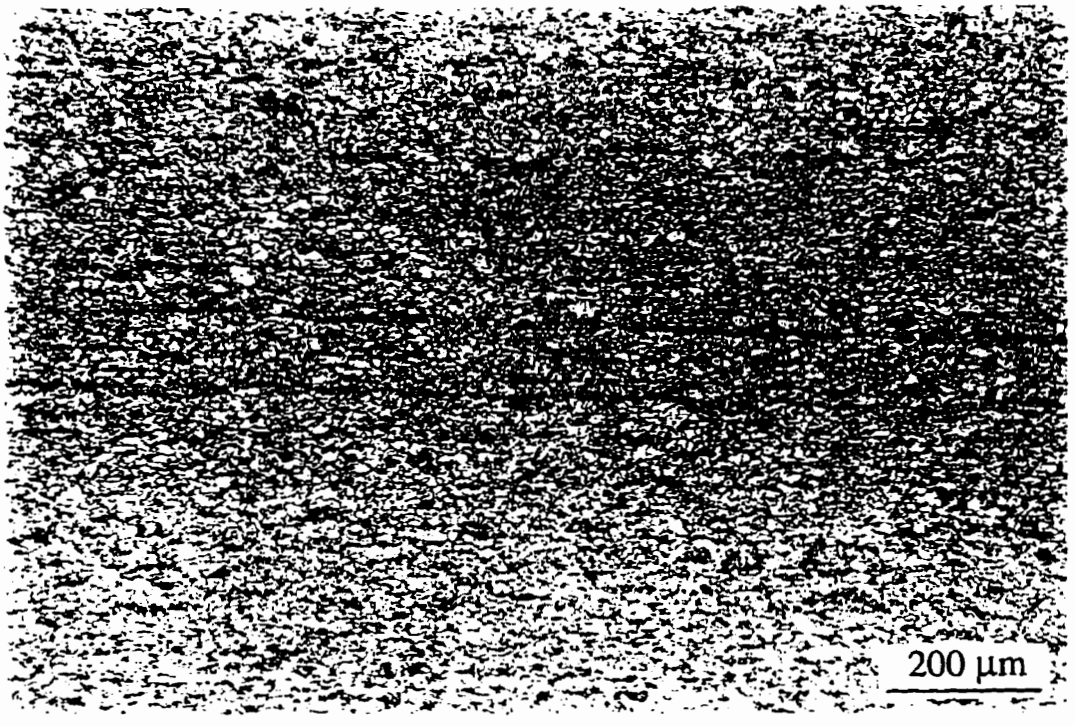

Figure 3.5 Microstructure of Grade 483 steel observed from **R** plane (8.4mm thickness pipe).

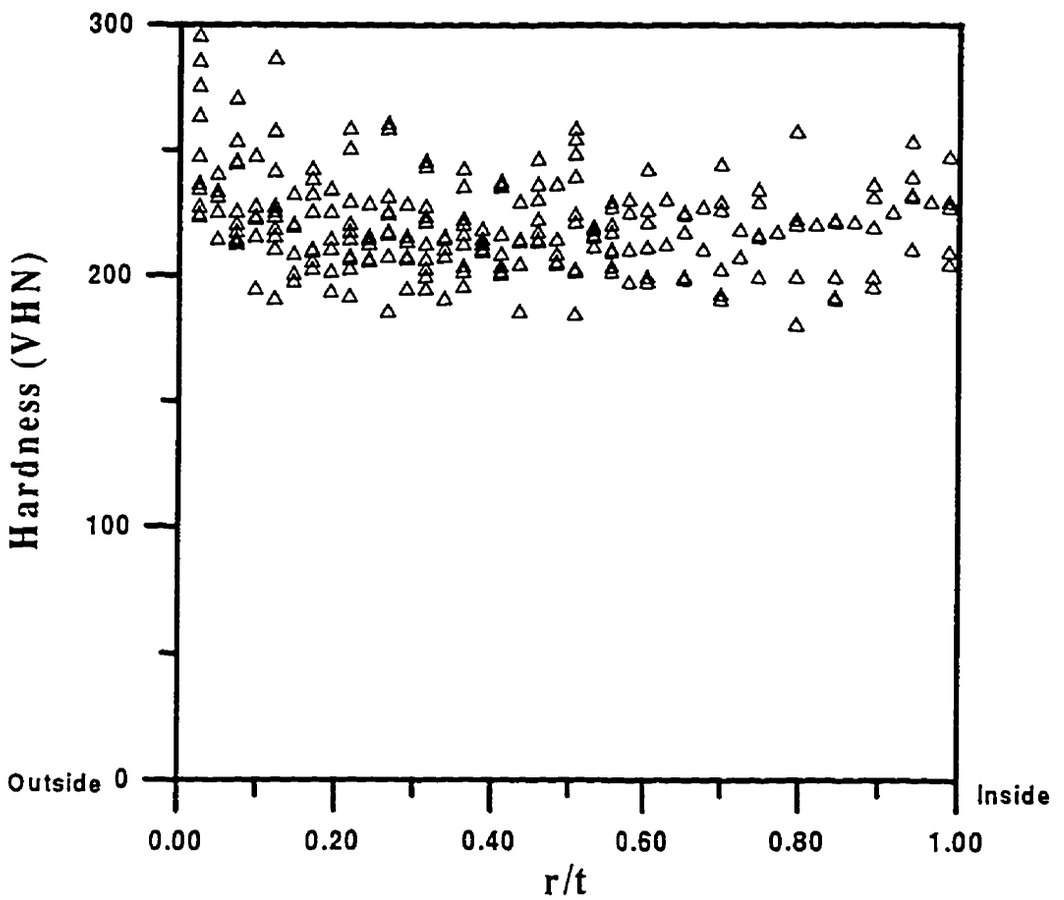

Figure 3.6 Vickers hardness numbers for 8.4 mm specimen.

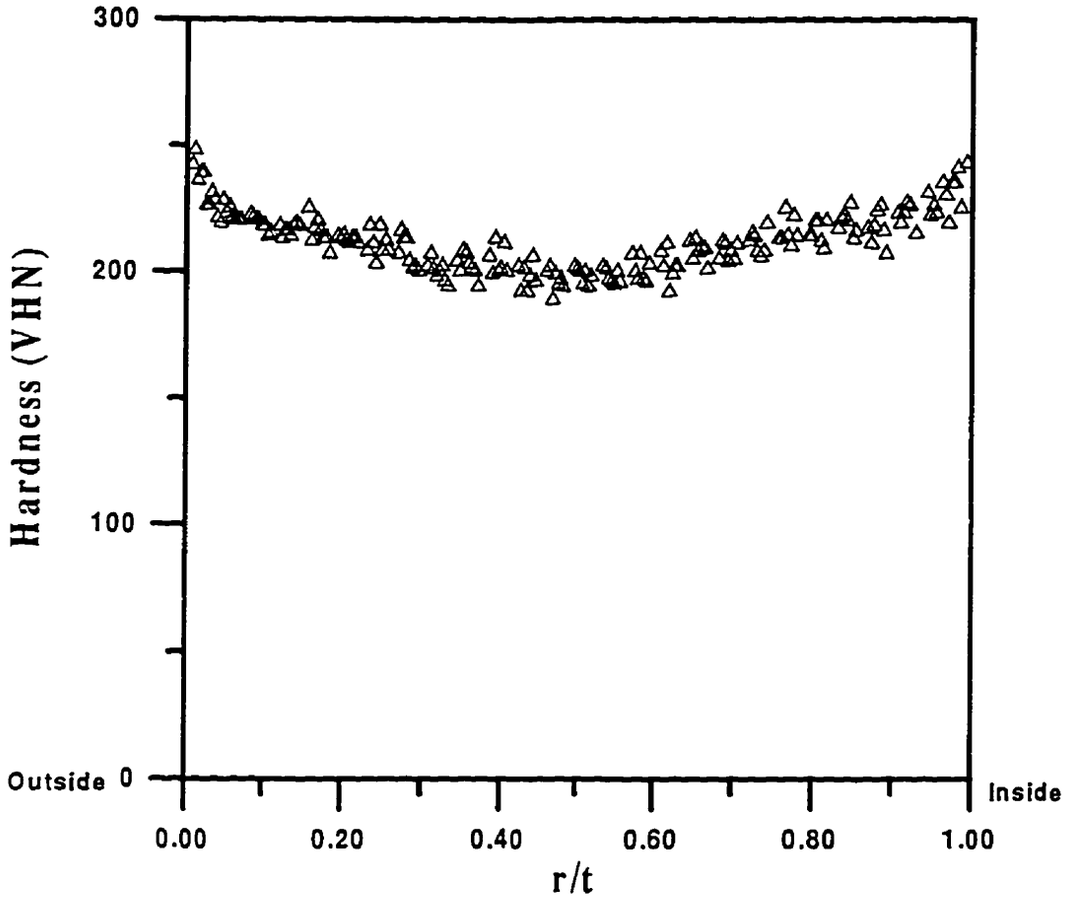

Figure 3.7 Vickers hardness numbers for 13.4 mm specimen.

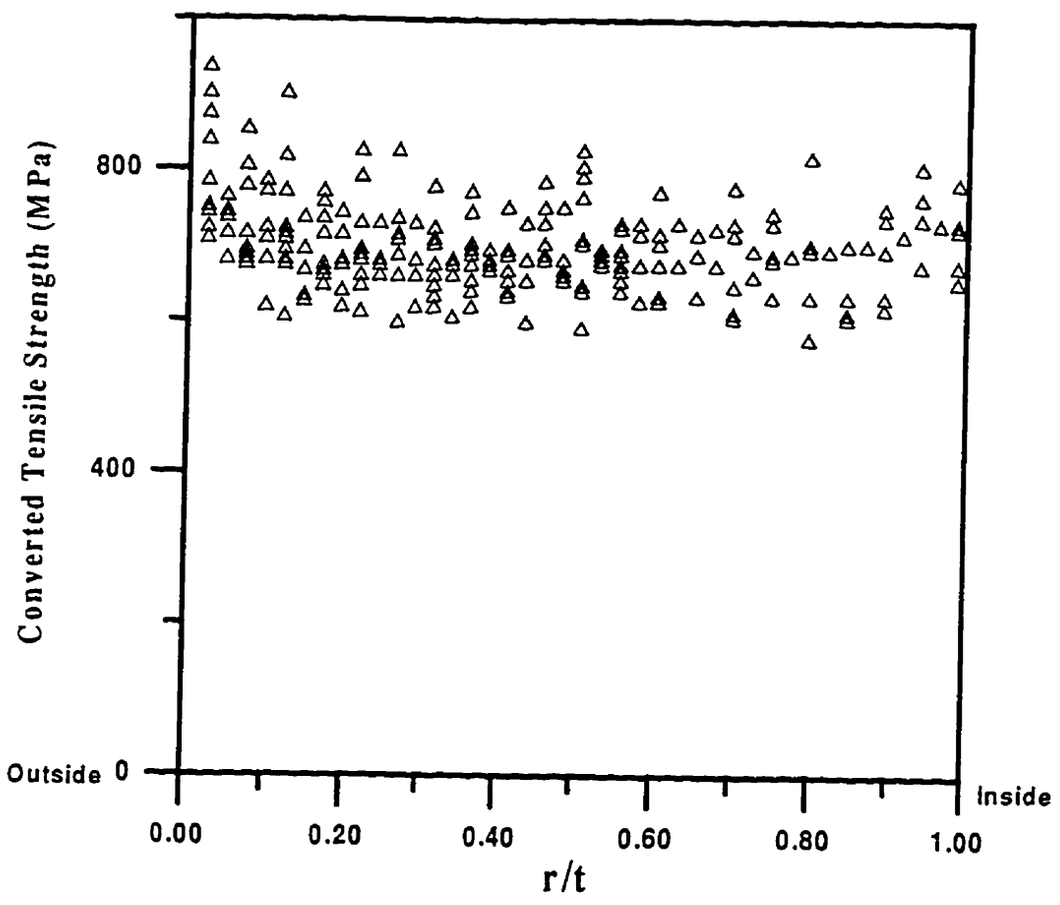

Figure 3.8 Converted tensile strength for 8.4 mm specimen.

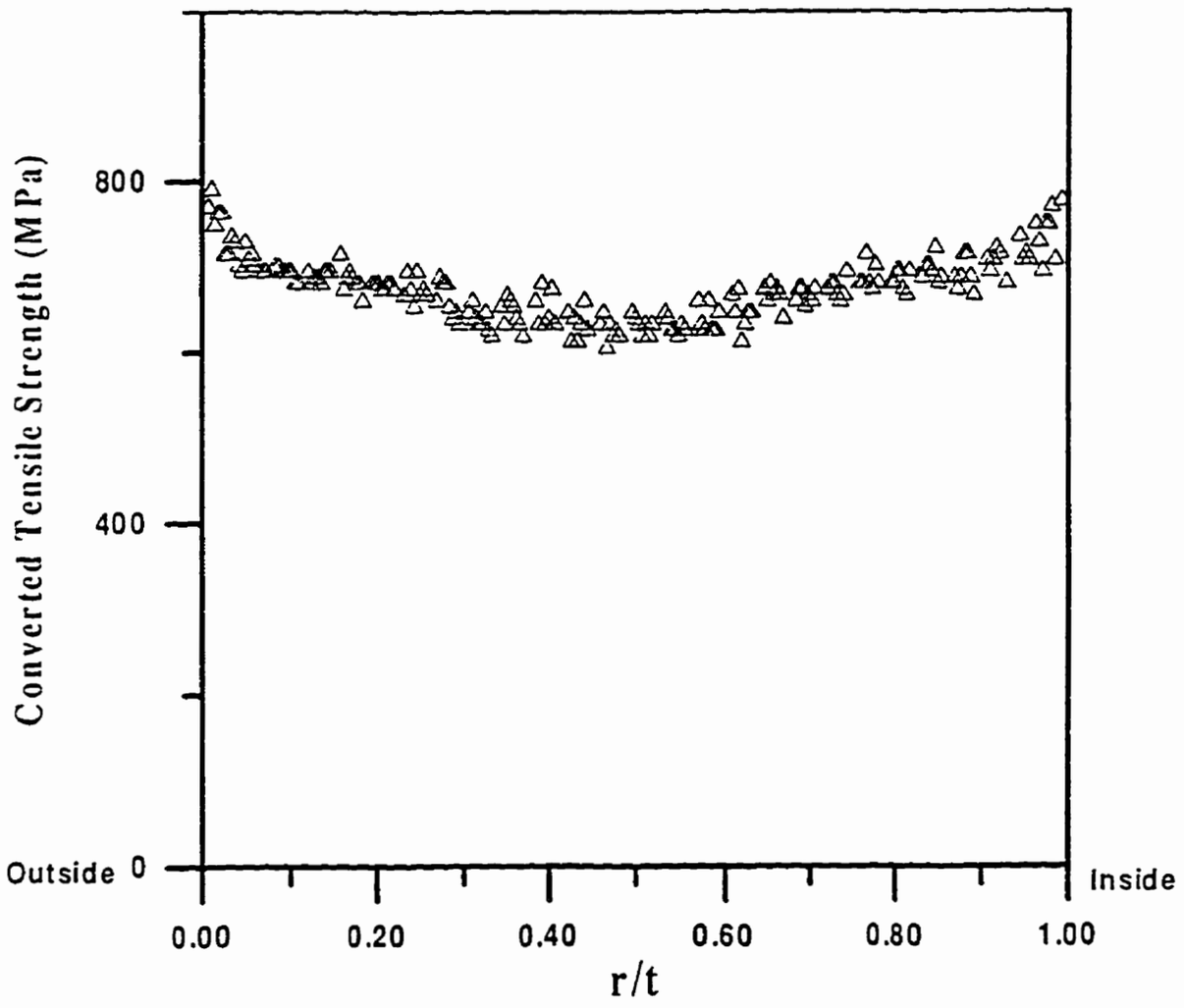

Figure 3.9 Converted tensile strength for 13.4 mm specimen.

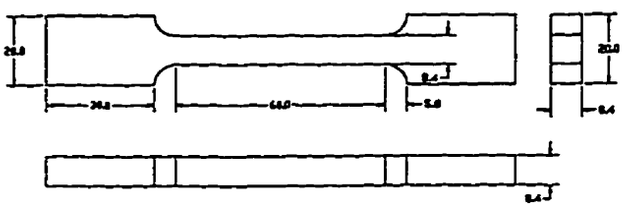

(a) 8.4x8.4mm square bar tensile specimen

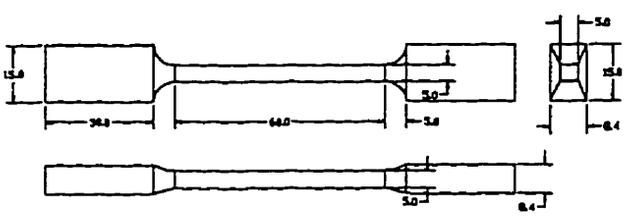

(b) 8x8 square bar tensile specimen

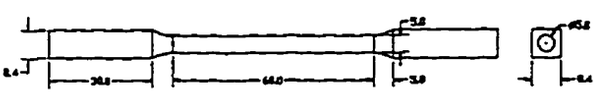

(c) D5mm circular bar tensile specimen

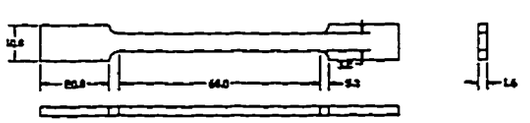

(d) 3.2x1.6mm rectangular bar tensile specimen
from inner and outer surfaces (8.4mm)

Figure 3.10 Dimension of tensile test specimens for 8.4 mm thickness pipe.

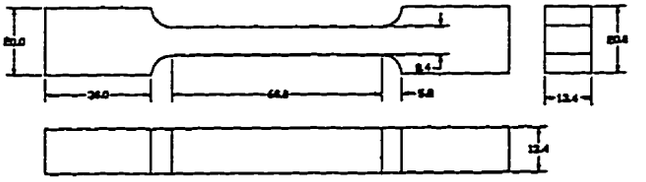

(a) 13.4x8.4mm rectangular bar tensile specimen

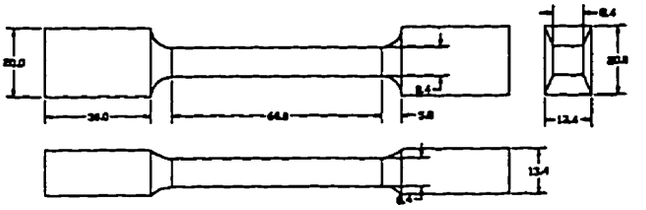

(b) 8x8mm square bar tensile specimen

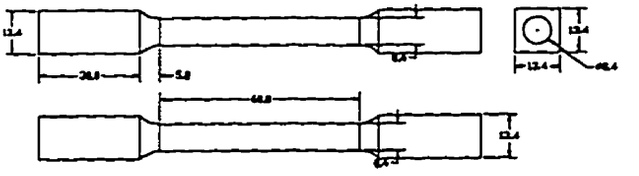

(c) D8mm circular bar tensile specimen

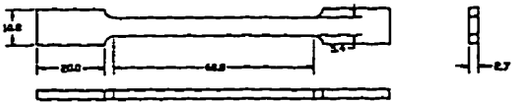

(d) 5.4x2.7mm square bar tensile specimen
from inner and outer surfaces (13.4mm material)

Figure 3.11 Dimension of tensile test specimens for 13.4 mm thickness pipe.

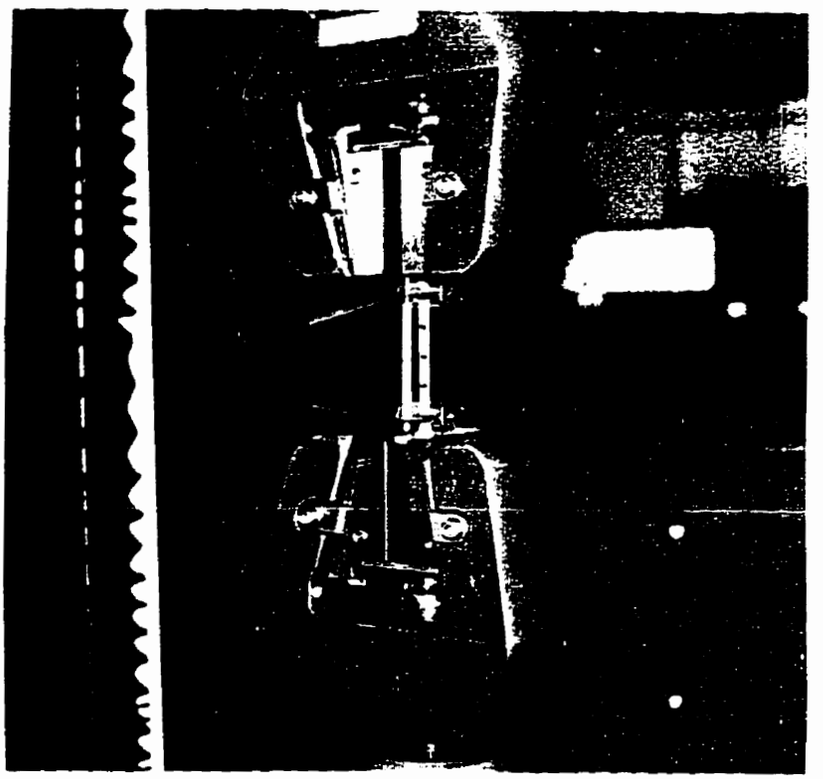

Figure 3.12 Tensile test equipment.

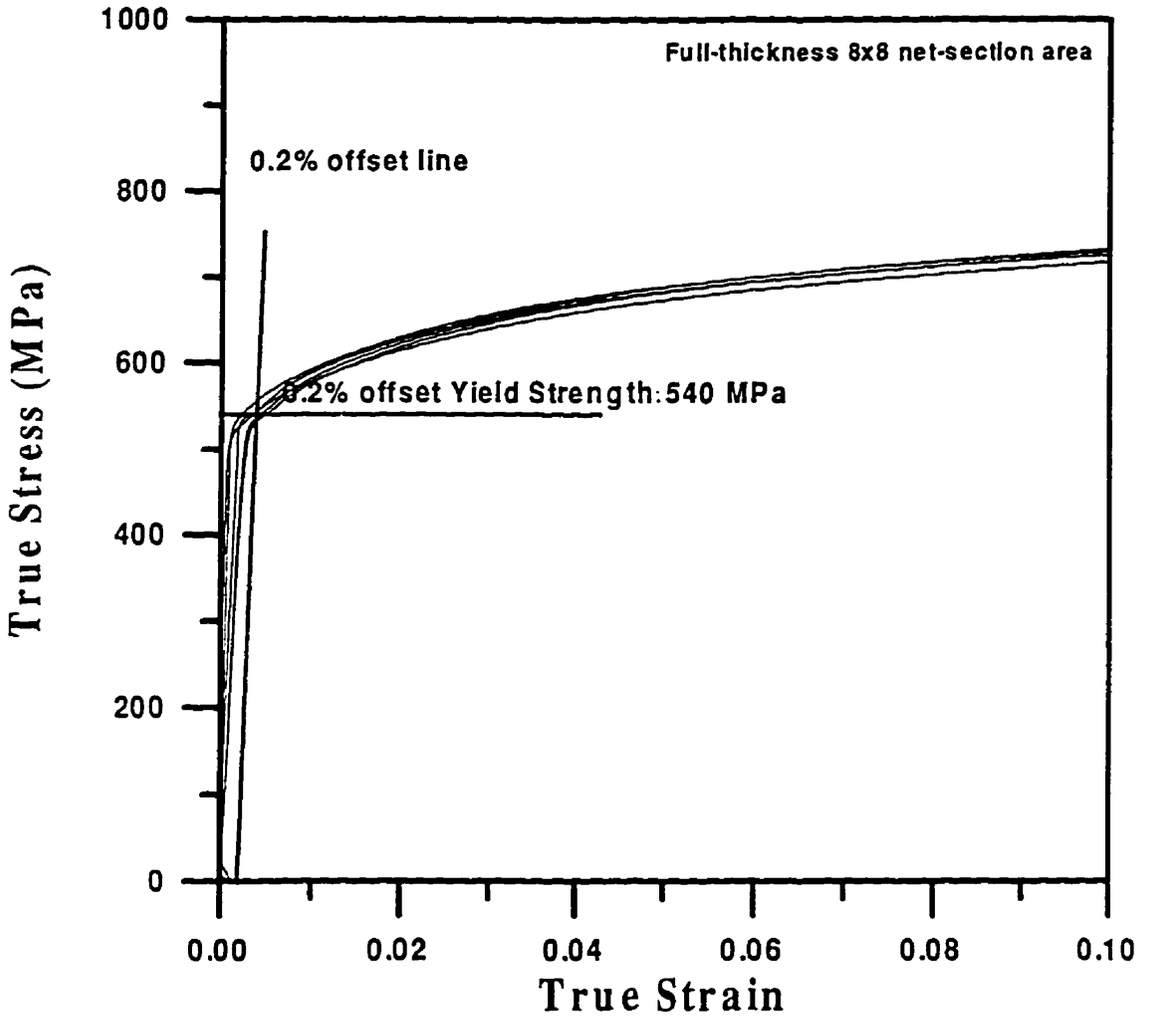

Figure 3.13 Stress-strain curves obtained from full-thickness (8x8 mm^2 net-section area) test specimens (8.4mm thickness pipe).

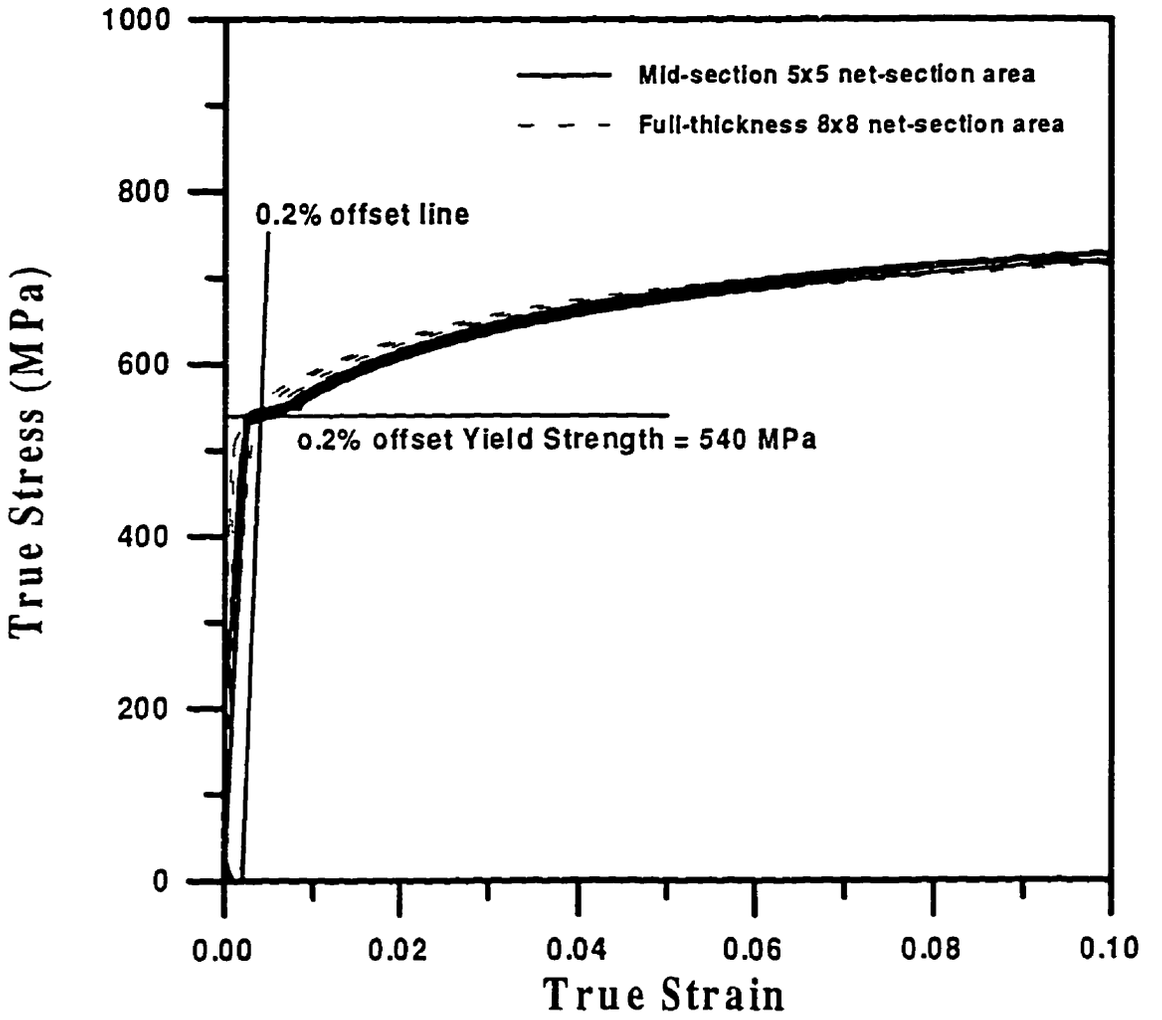

Figure 3.14 Stress-strain curves resulting from 5x5 tensile test specimens (8.4mm thickness pipe).

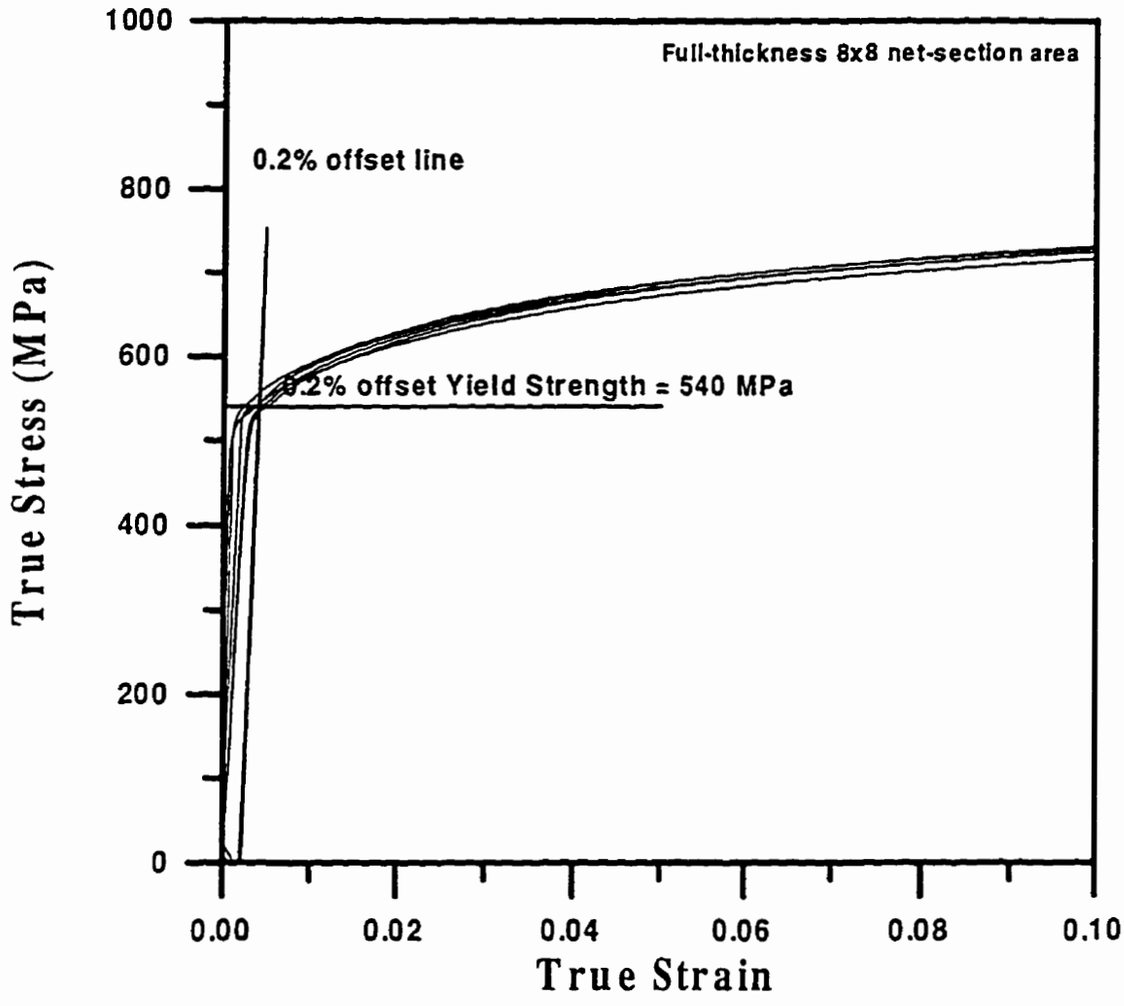

Figure 3.15 Stress-strain curves resulting from circular (D=5mm) bar tensile test specimens (8.4mm thickness pipe).

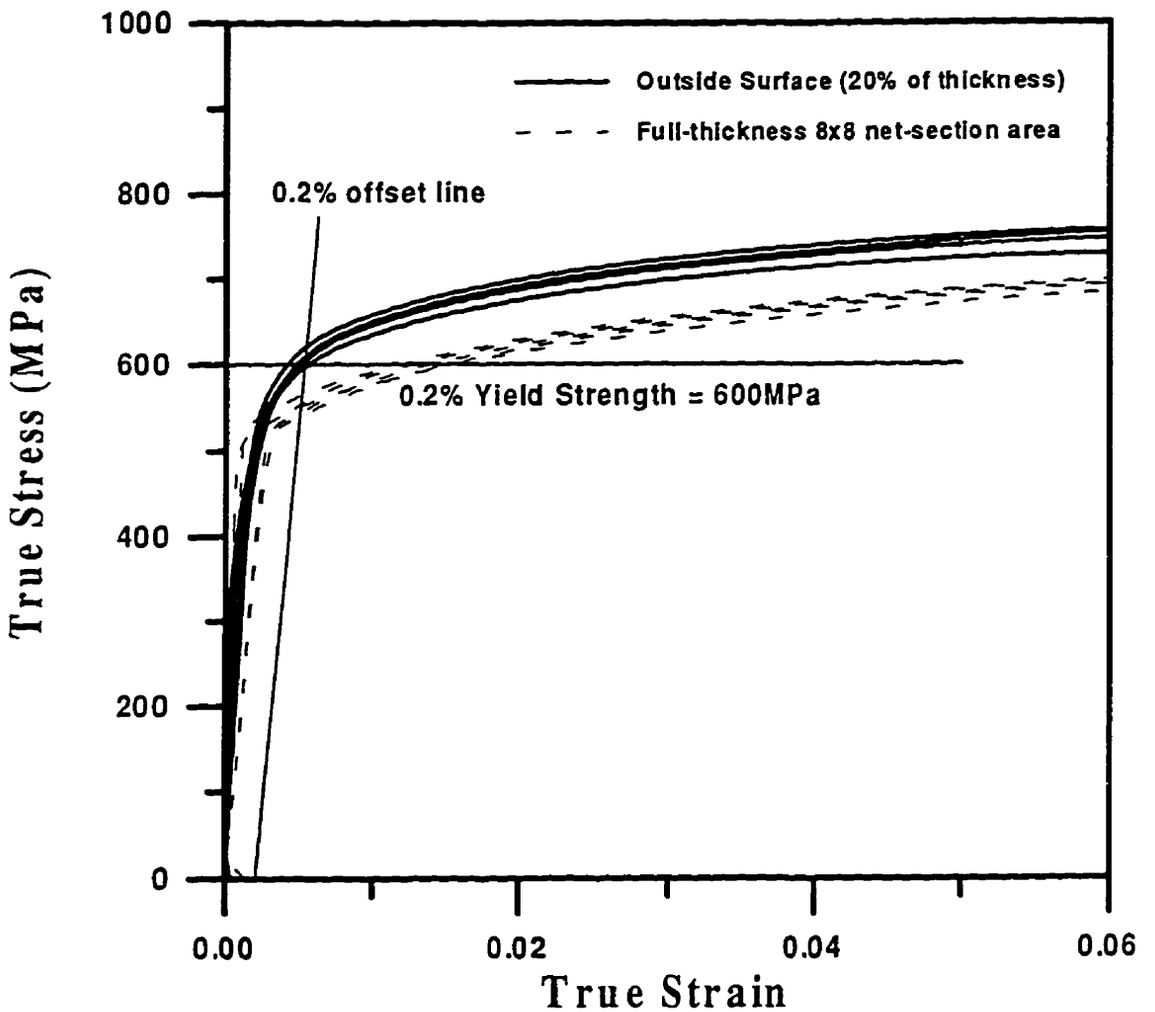

Figure 3.16 Stress-strain curves resulting from outside surface strip test specimens (20% of thickness – 8.4mm thickness pipe).

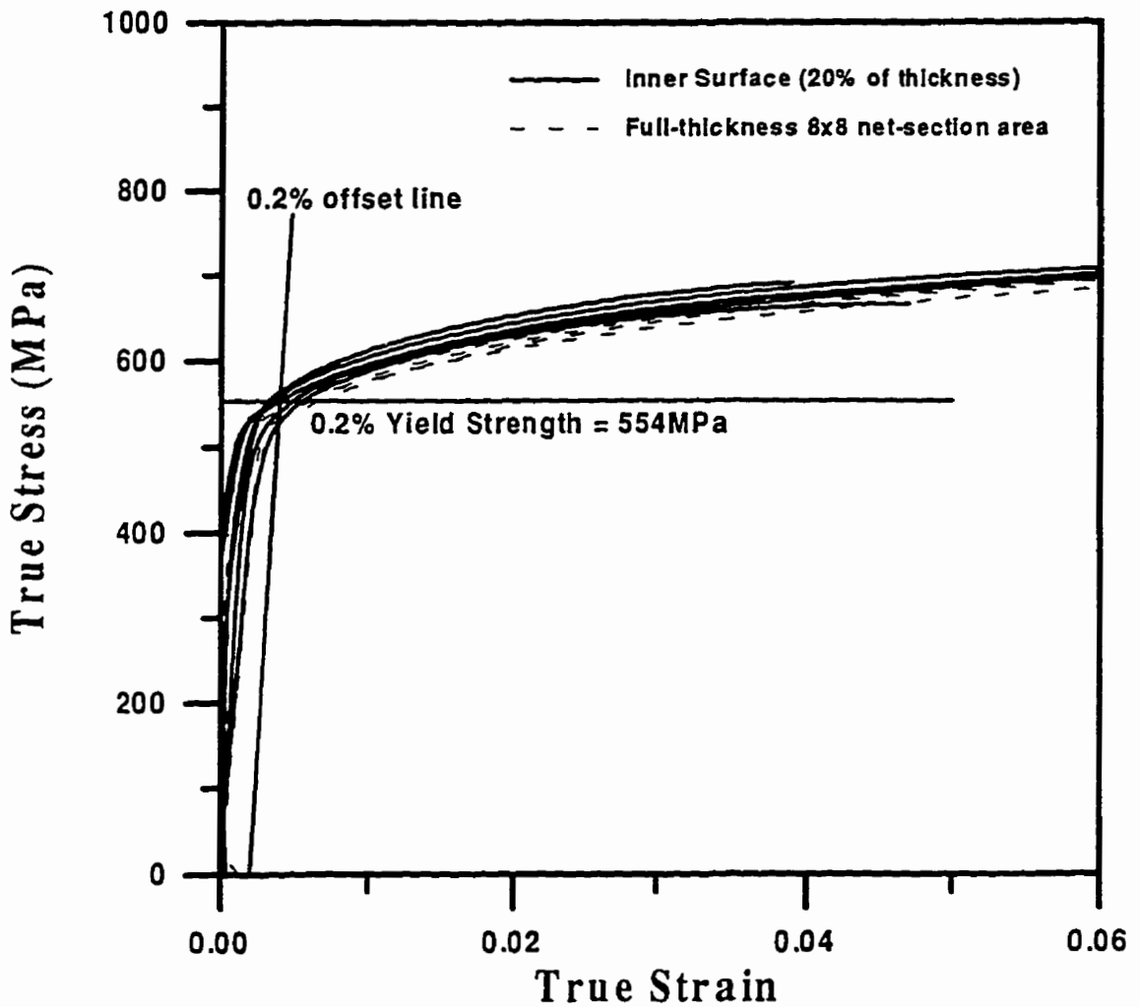

Figure 3.17 Stress-strain curves resulting from inside surface strip test specimens (20% of thickness – 8.4mm thickness pipe).

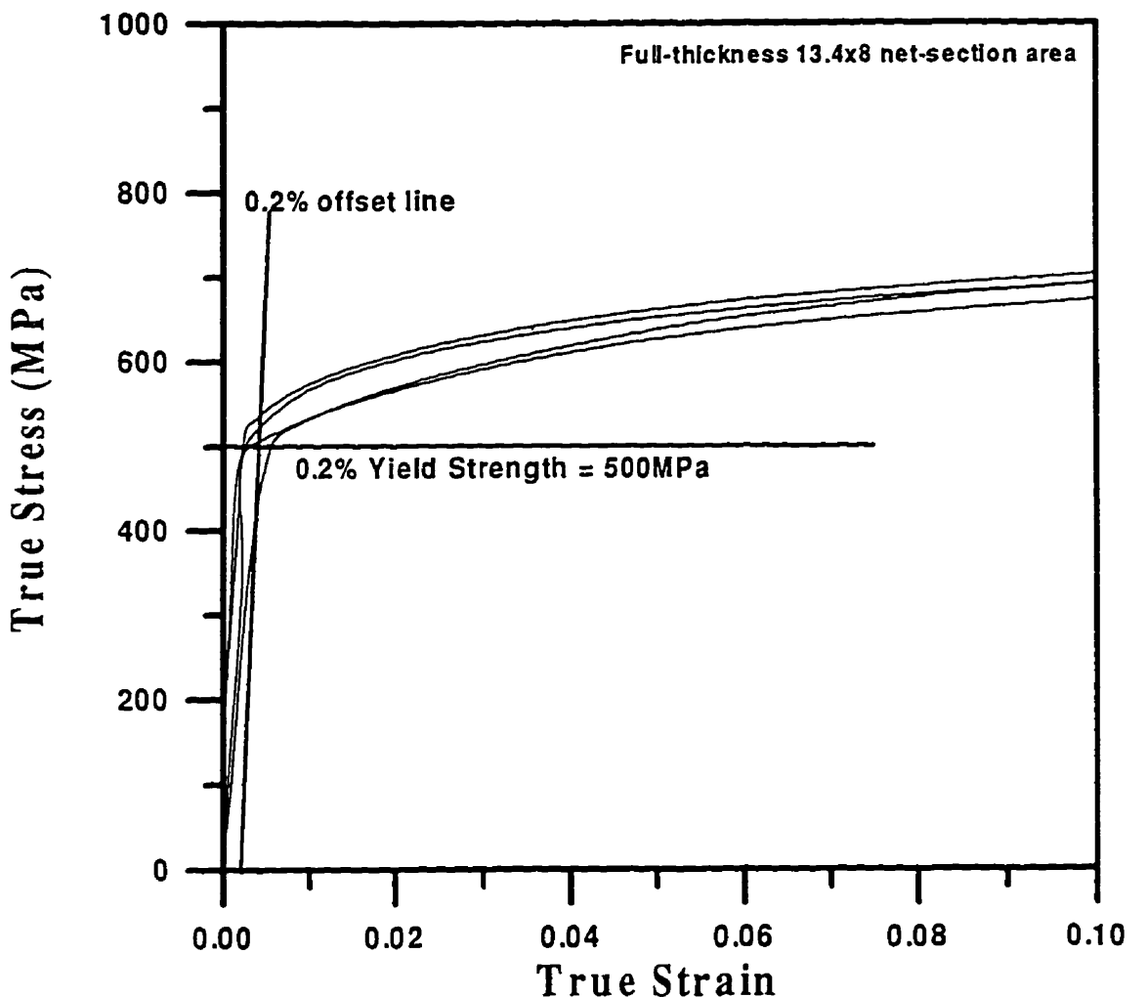

Figure 3.18 Stress-strain curves obtained from full-thickness (13.4 x 8 mm^2 net-section area) test specimens (13.4 mm thickness pipe).

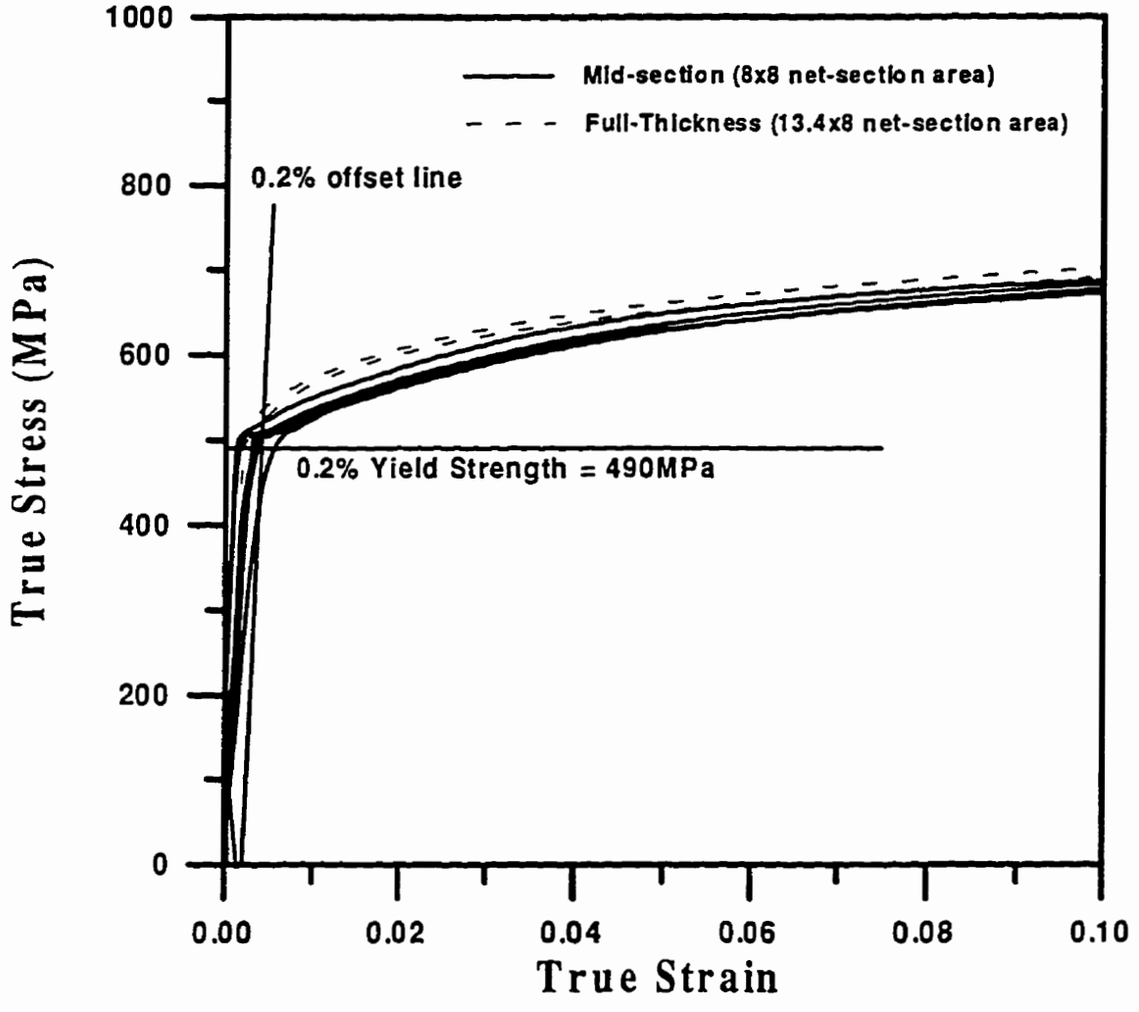

Figure 3.19 Stress-strain curves resulting from 8x8 tensile test specimens (13.4mm thickness pipe).

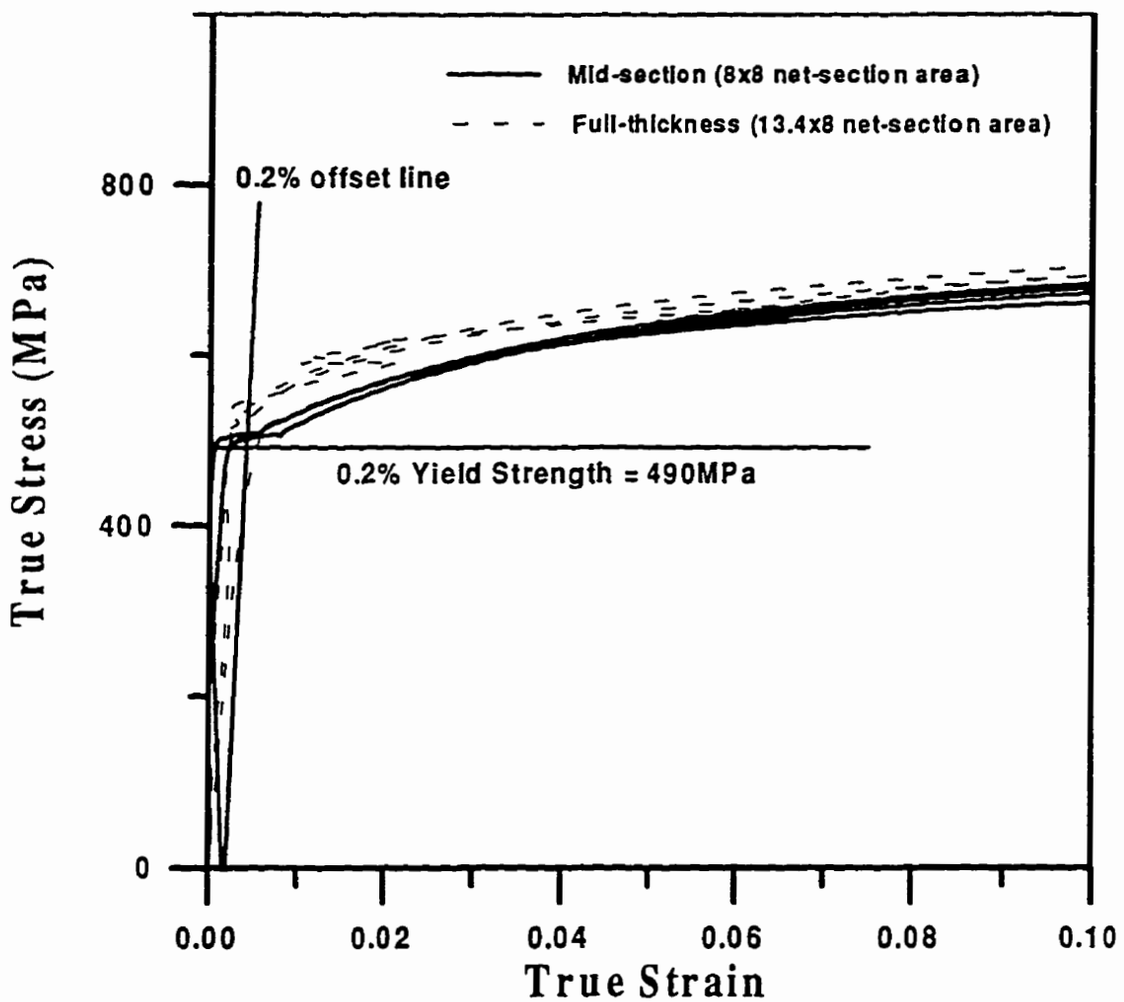

Figure 3.20 Stress-strain curves resulting from circular (D=8mm) bar tensile test specimens (13.4mm thickness pipe).

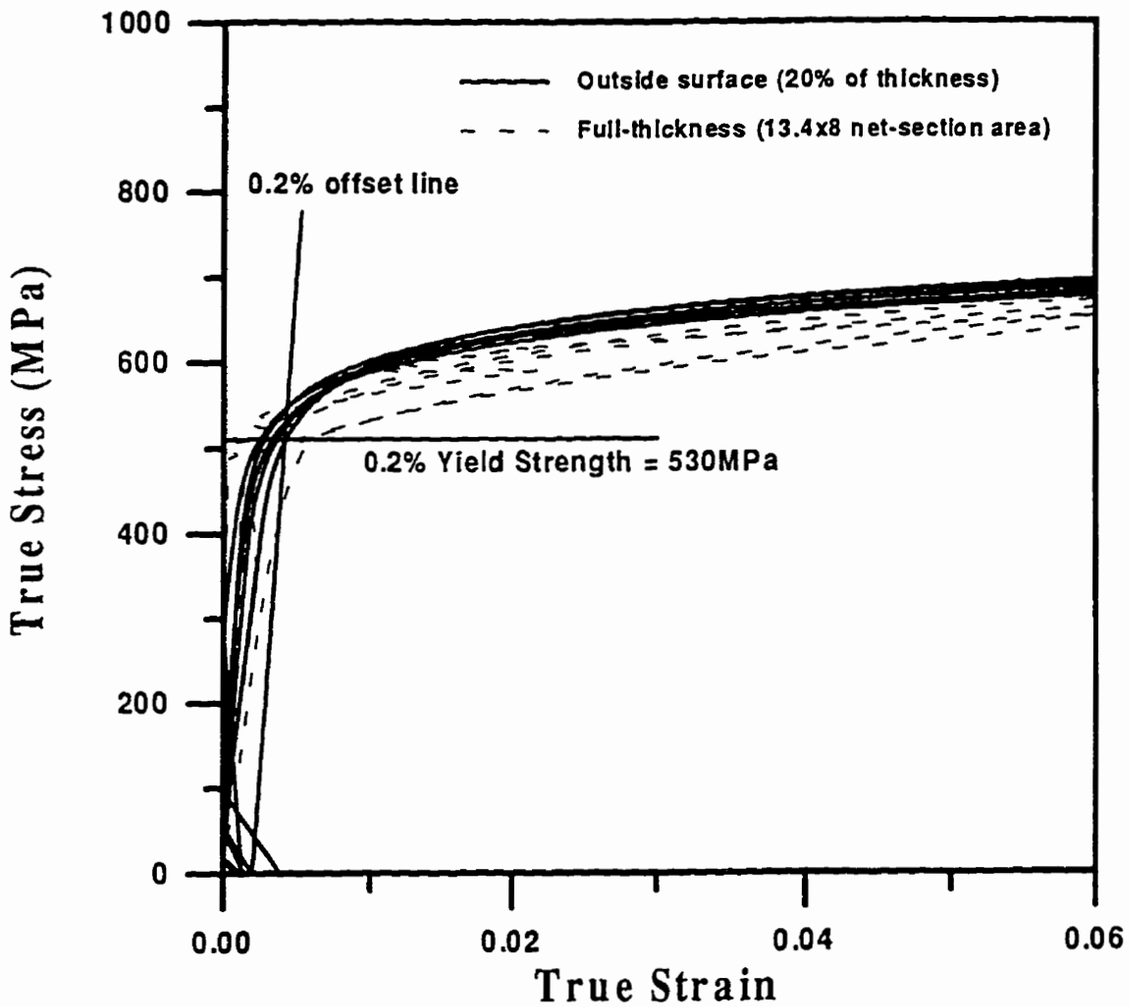

Figure 3.21 Stress-strain curves resulting from outside surface strip test specimens (20% of thickness – 13.4mm thickness pipe).

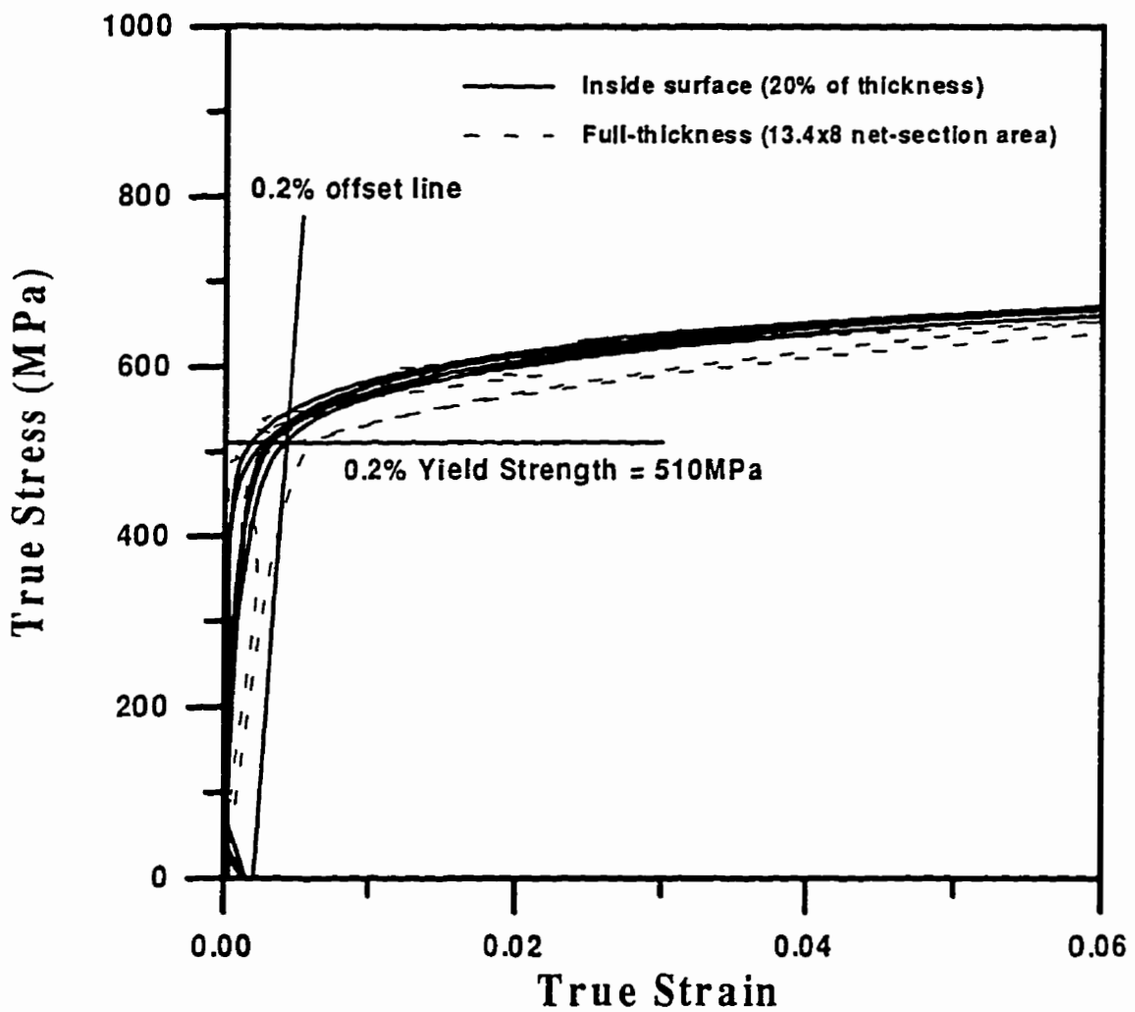

Figure 3.22 Stress-strain curves resulting from inside surface strip test specimens (20% of thickness – 13.4mm thickness pipe).

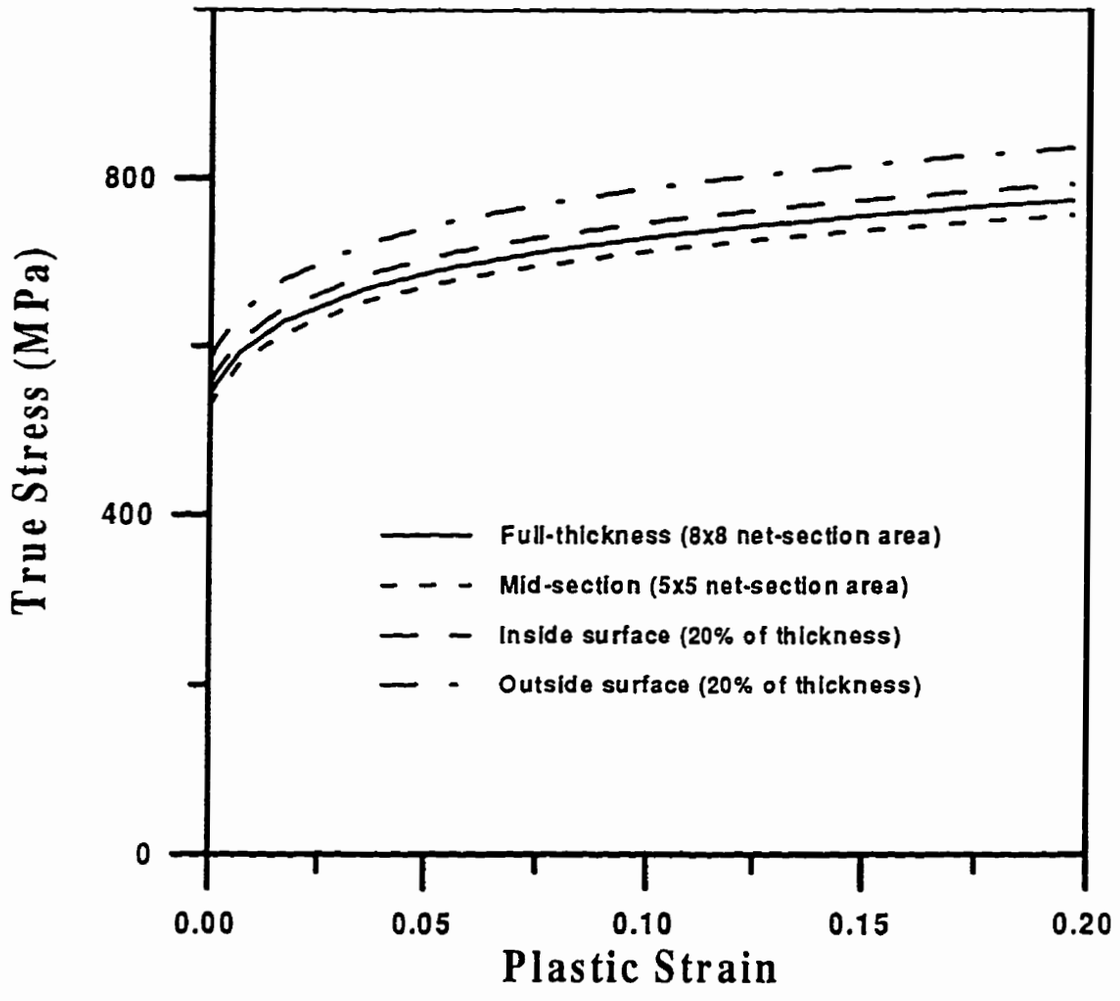

Figure 3.23 Summary of stress-strain curves resulting from the tensile test (8.4 mm thickness pipe).

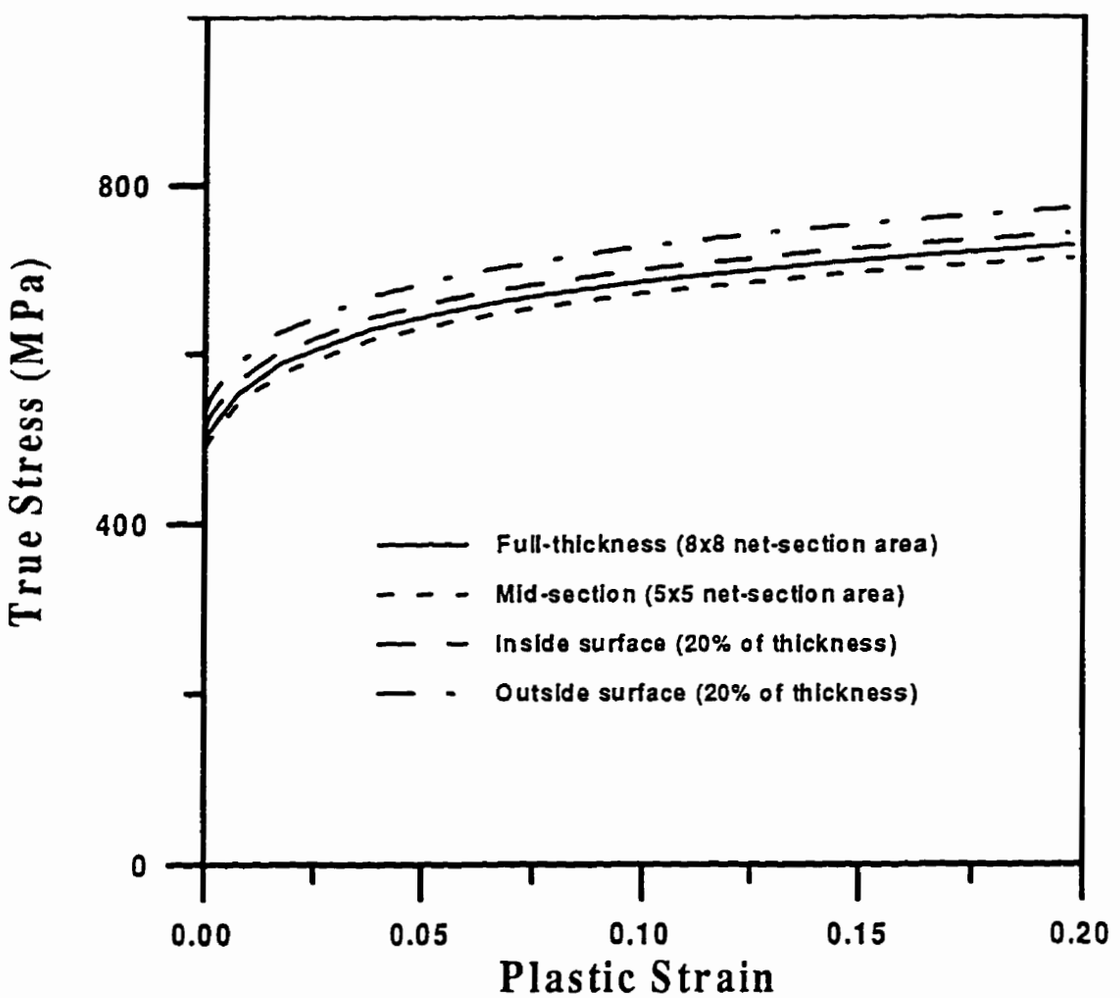

Figure 3.24 Summary of stress-strain curves resulting from the tensile test (13.4 mm thickness pipe).

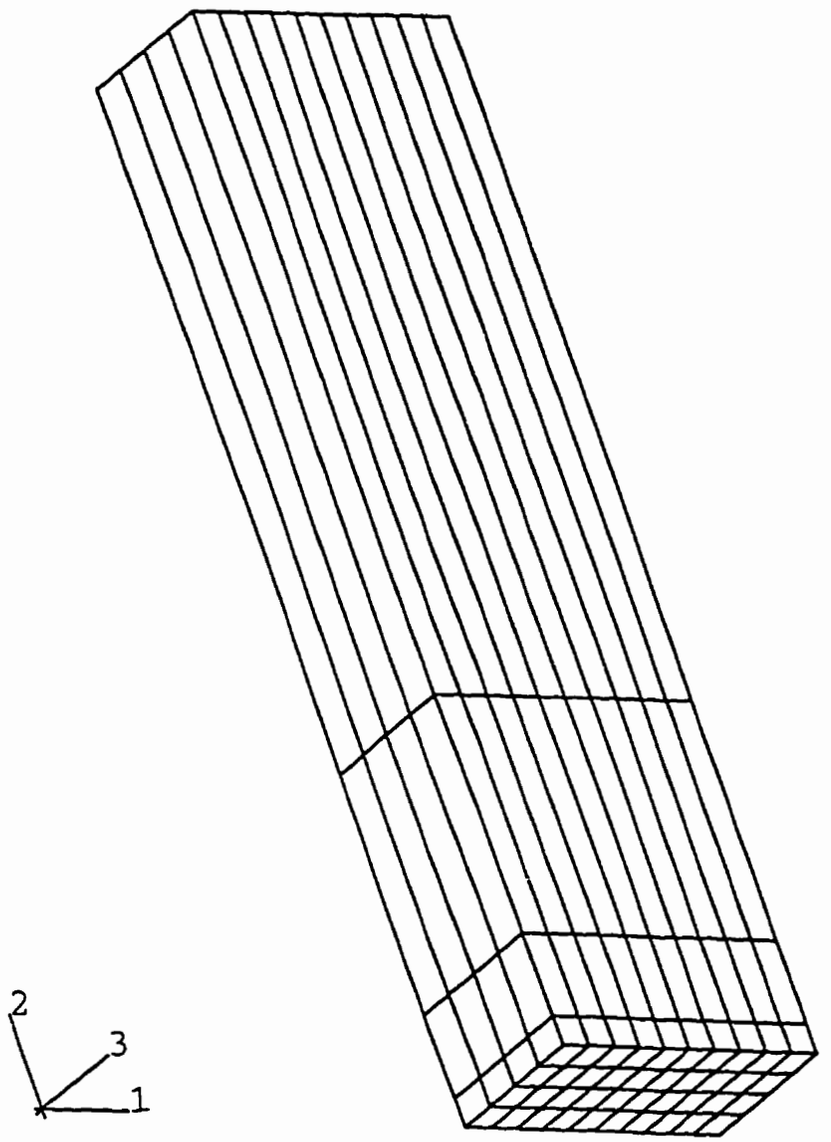

Figure 3.25 The finite element model for a tensile specimen designed with 3D brick elements.

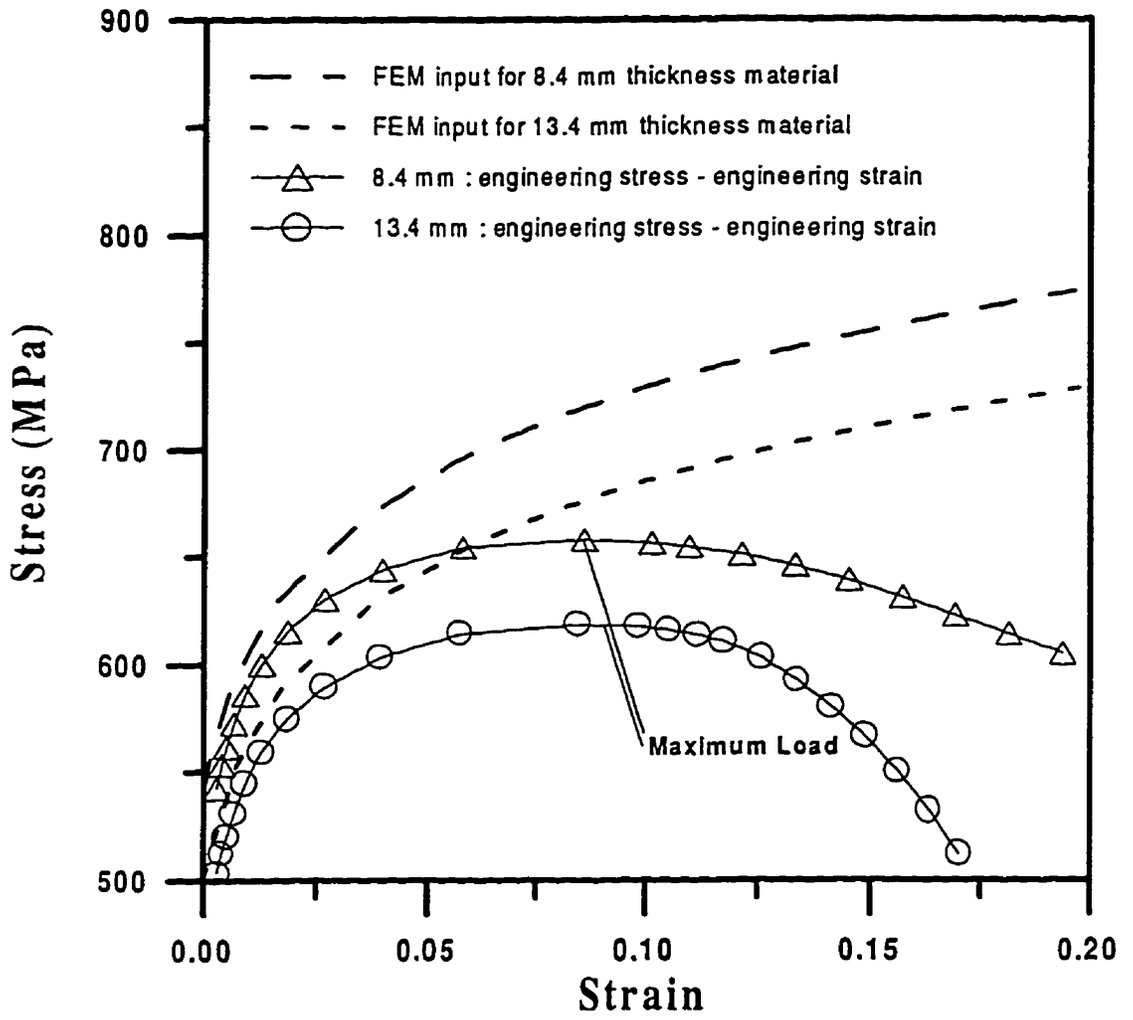

Figure 3.26 Point of instability results from the FEM analyses.

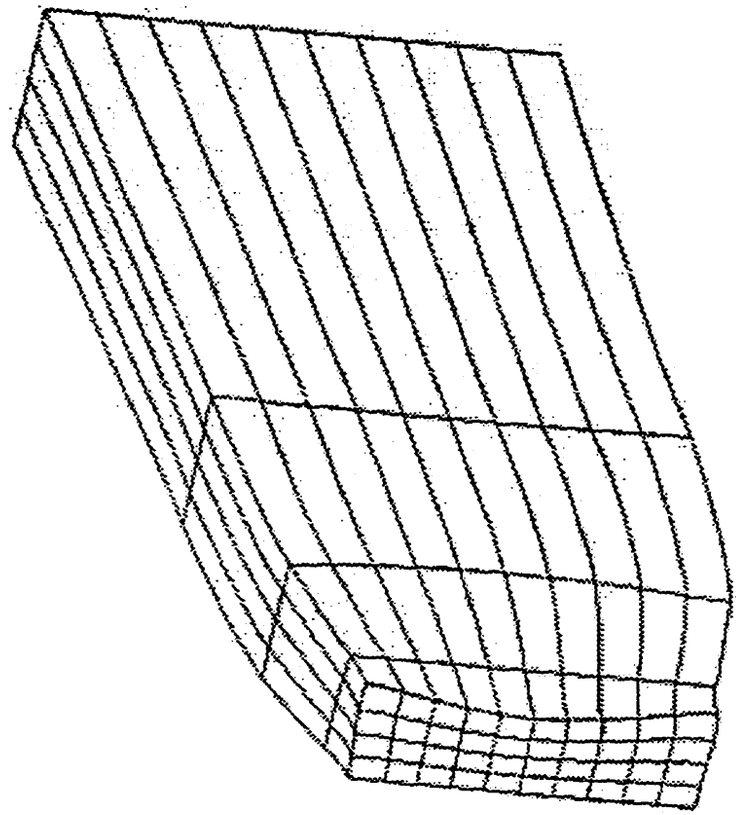

Figure 3.27 The deformed FEM mesh simulating necking.

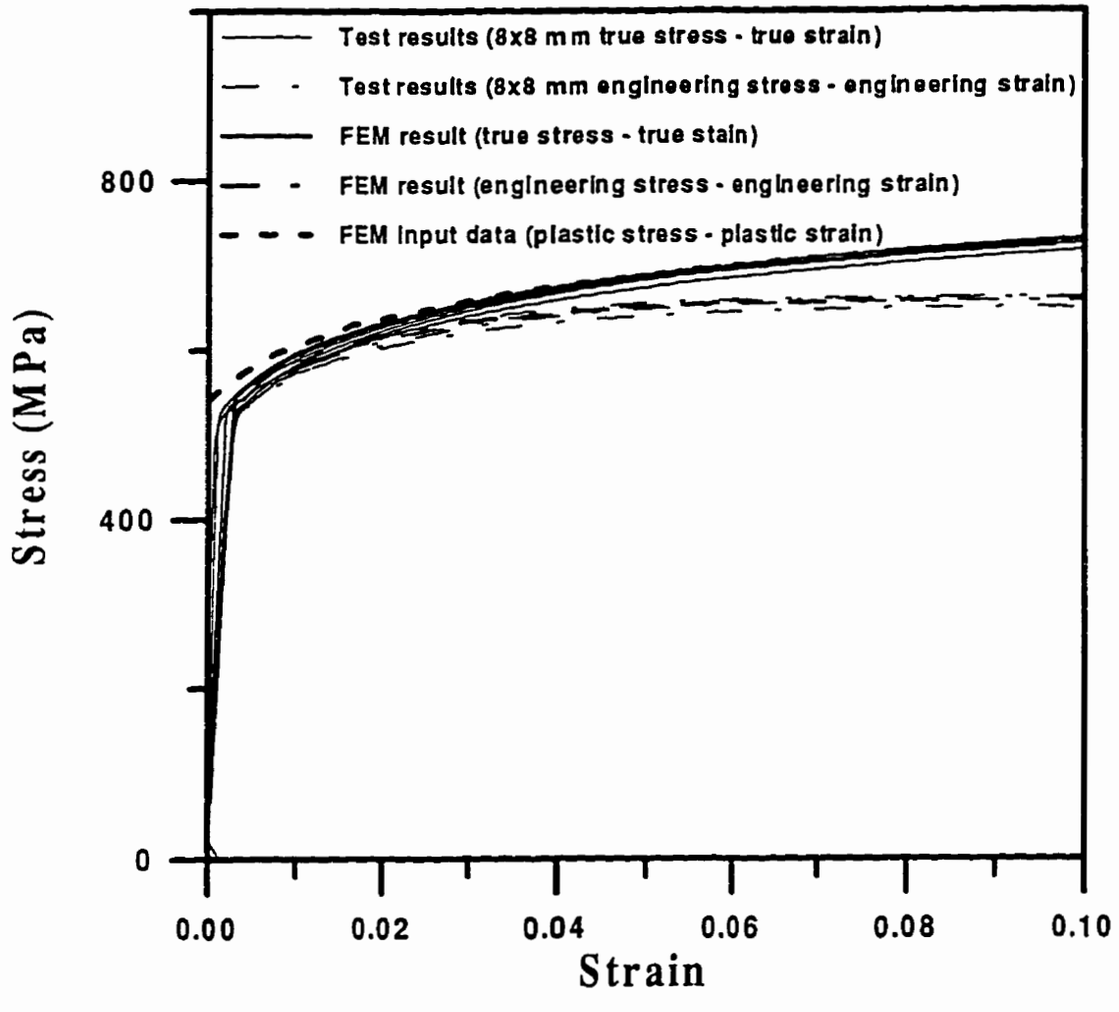

Figure 3.28 Large displacement analysis results for an 8.4 mm thickness specimen.

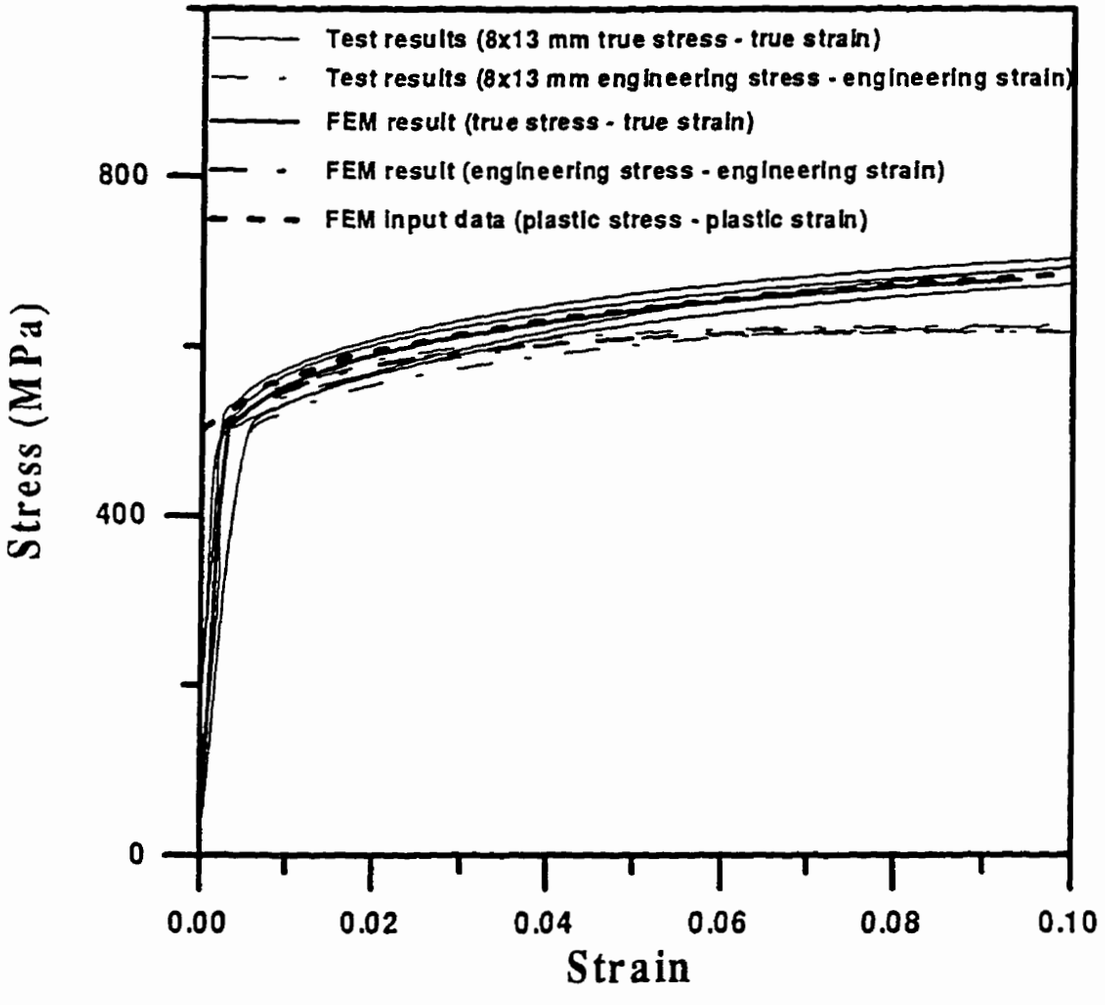

Figure 3.29 Large displacement analysis results for a 13.4 mm thickness specimen.

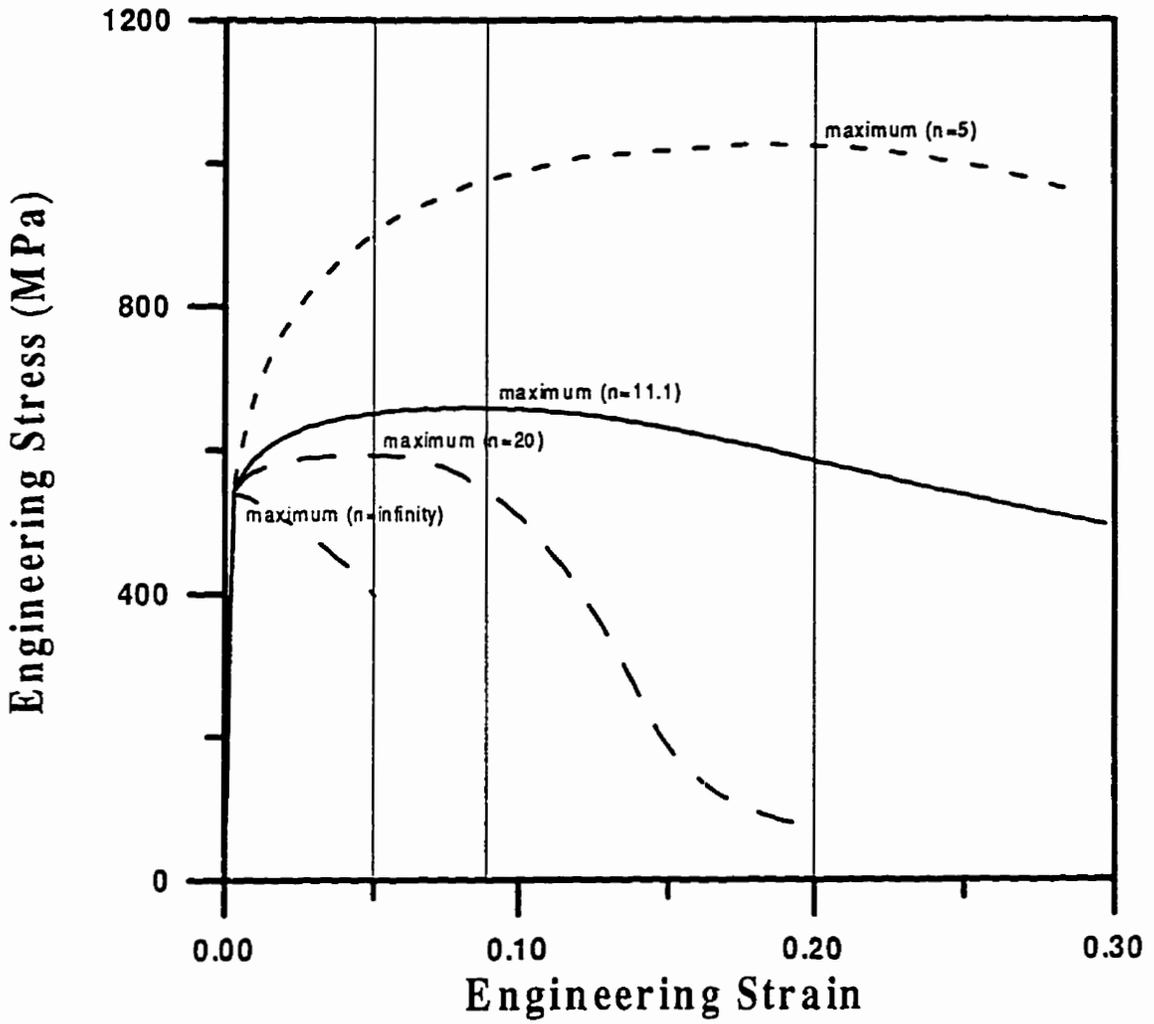

Figure 3.30 Engineering stress – strain curves for various hardening numbers.

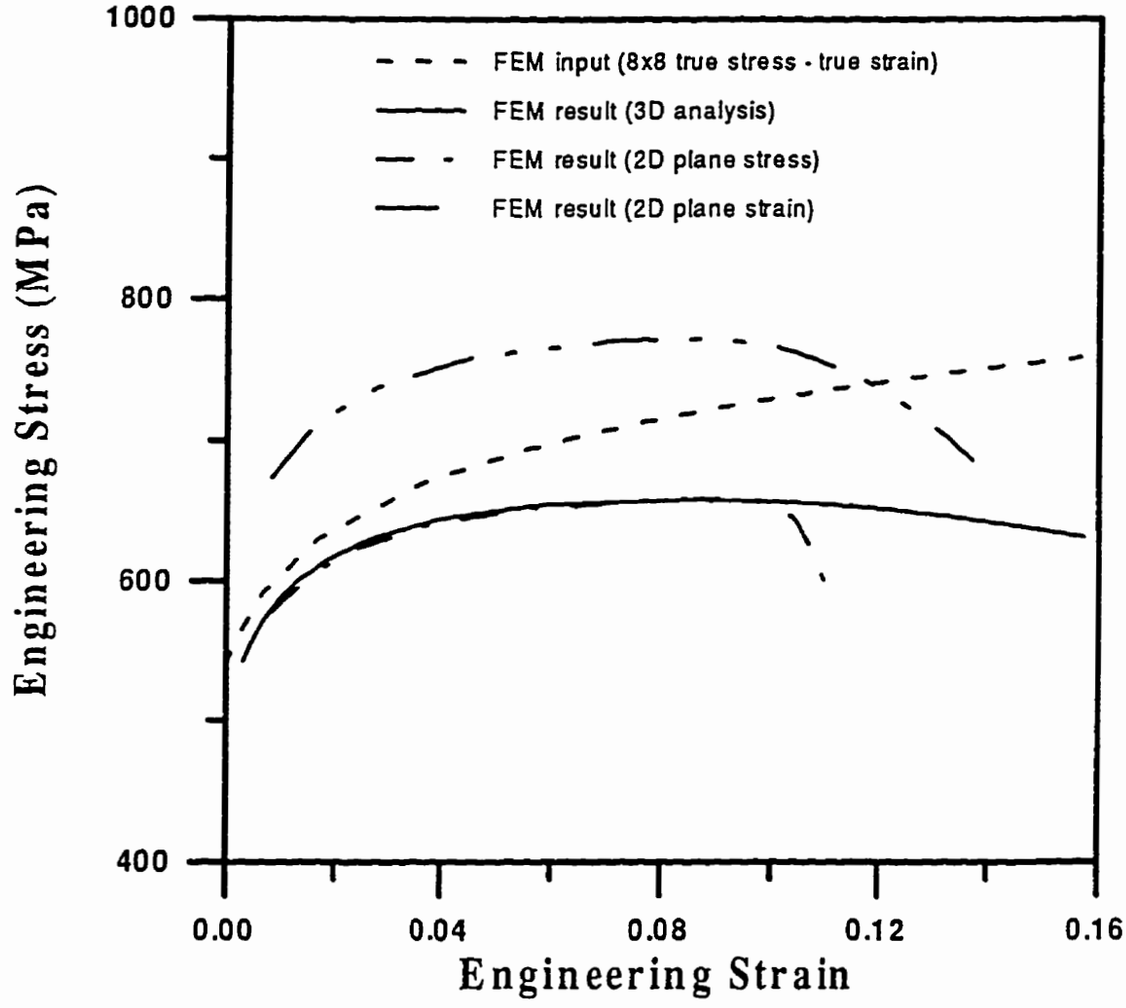

Figure 3.31 True stress – true strain curves resulting from both the plane strain and plane stress tensile bar analyses (8.4 mm thickness material).

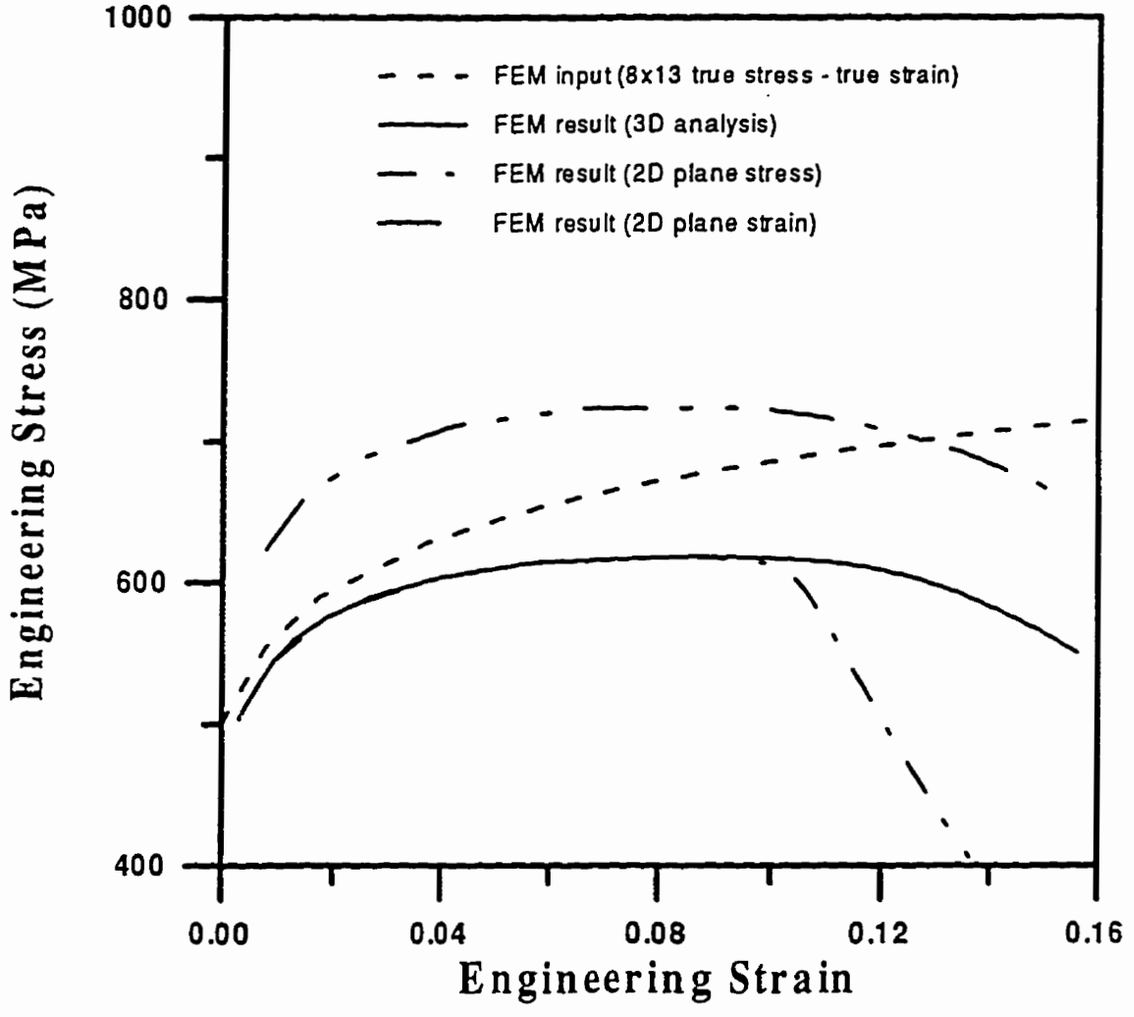

Figure 3.32 True stress – true strain curves resulting from both the plane strain and plane stress tensile bar analyses (13.4 mm thickness material).

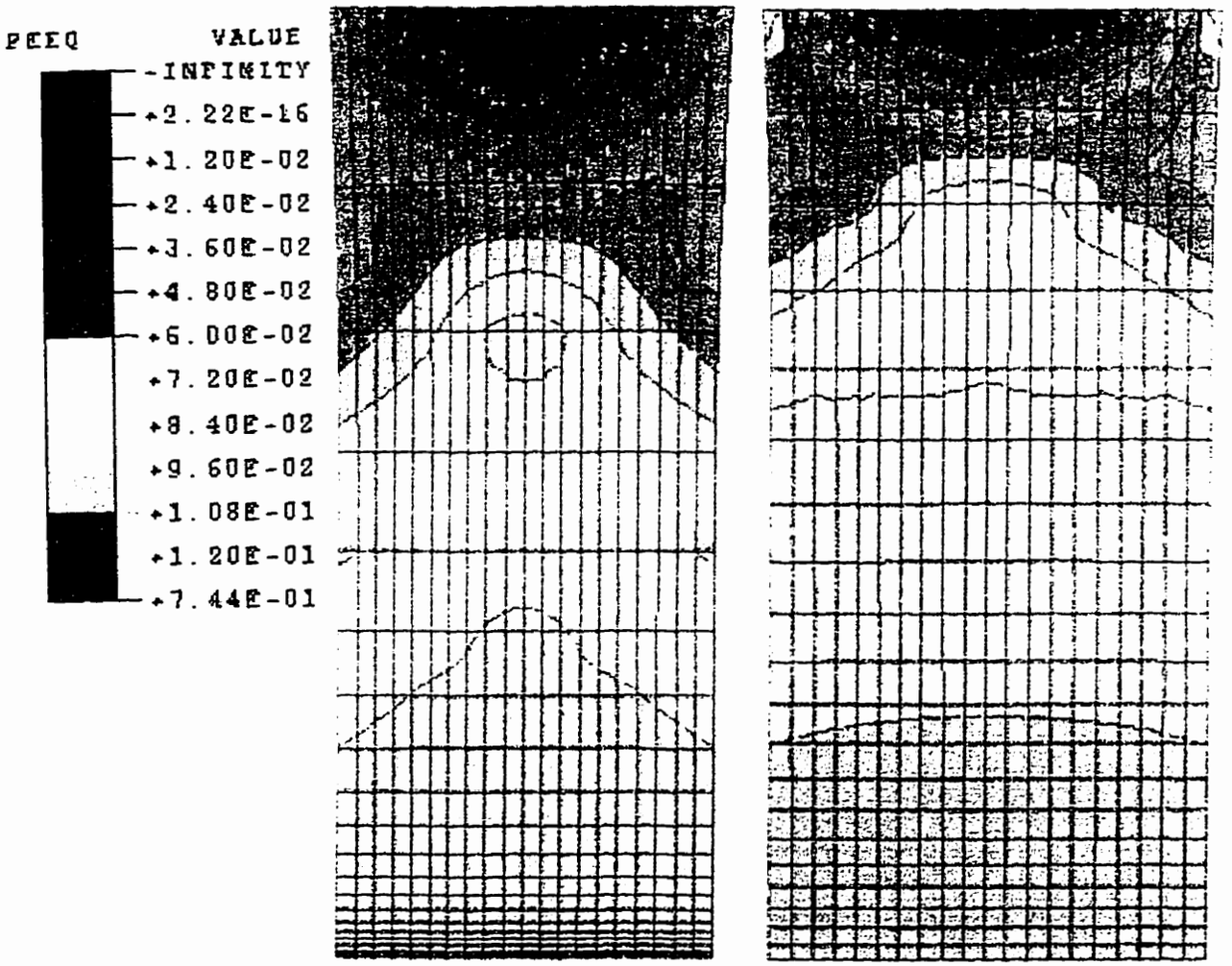

(a) plane strain (b) plane stress

Figure 3.33 The equivalent plastic strain contours at the maximum stress.

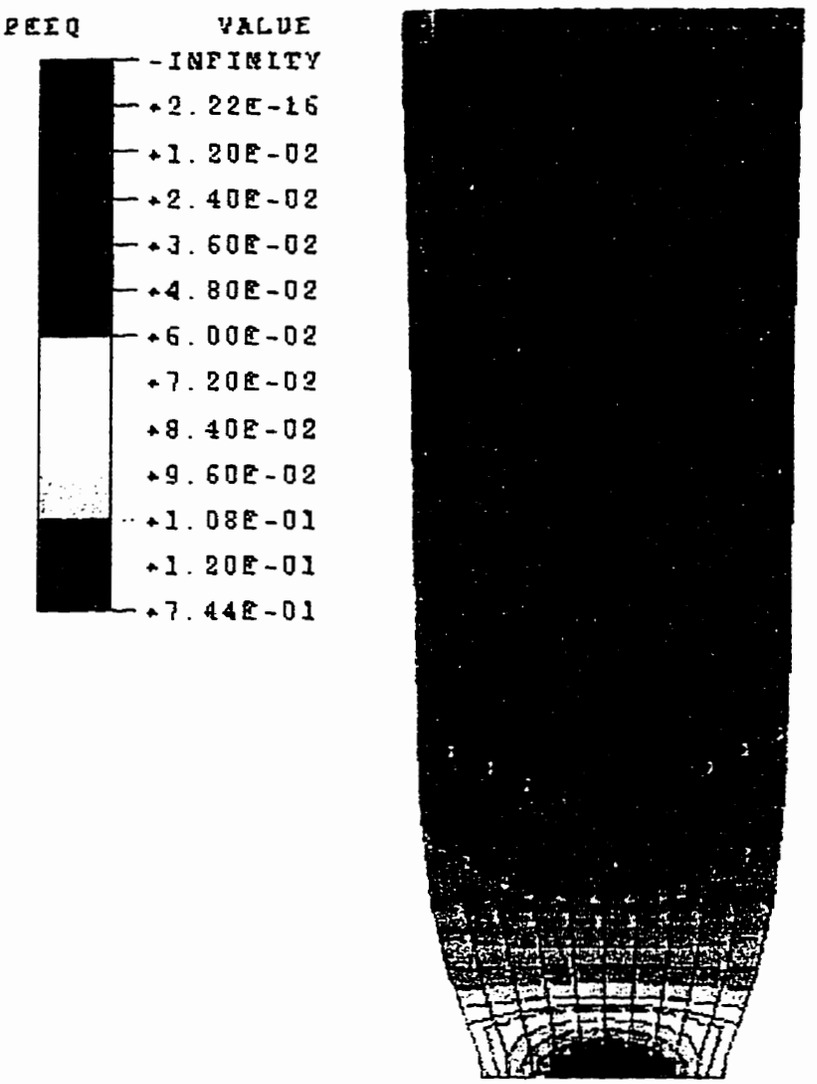

Figure 3.34 The equivalent plastic strain contours for a tensile test specimen after the point of instability.

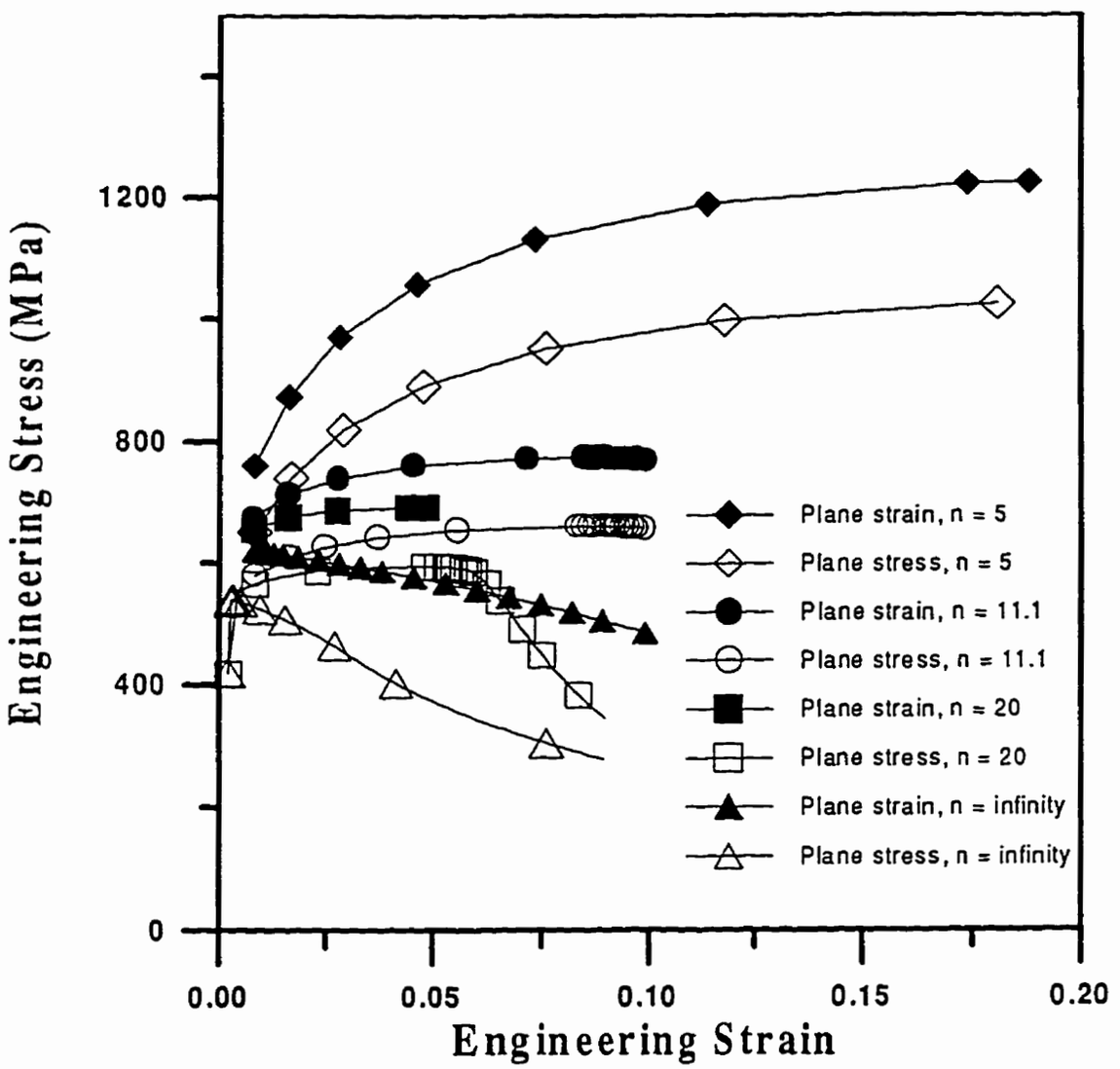

Figure 3.35 Plane stress versus plane strain analyses for various hardening materials.

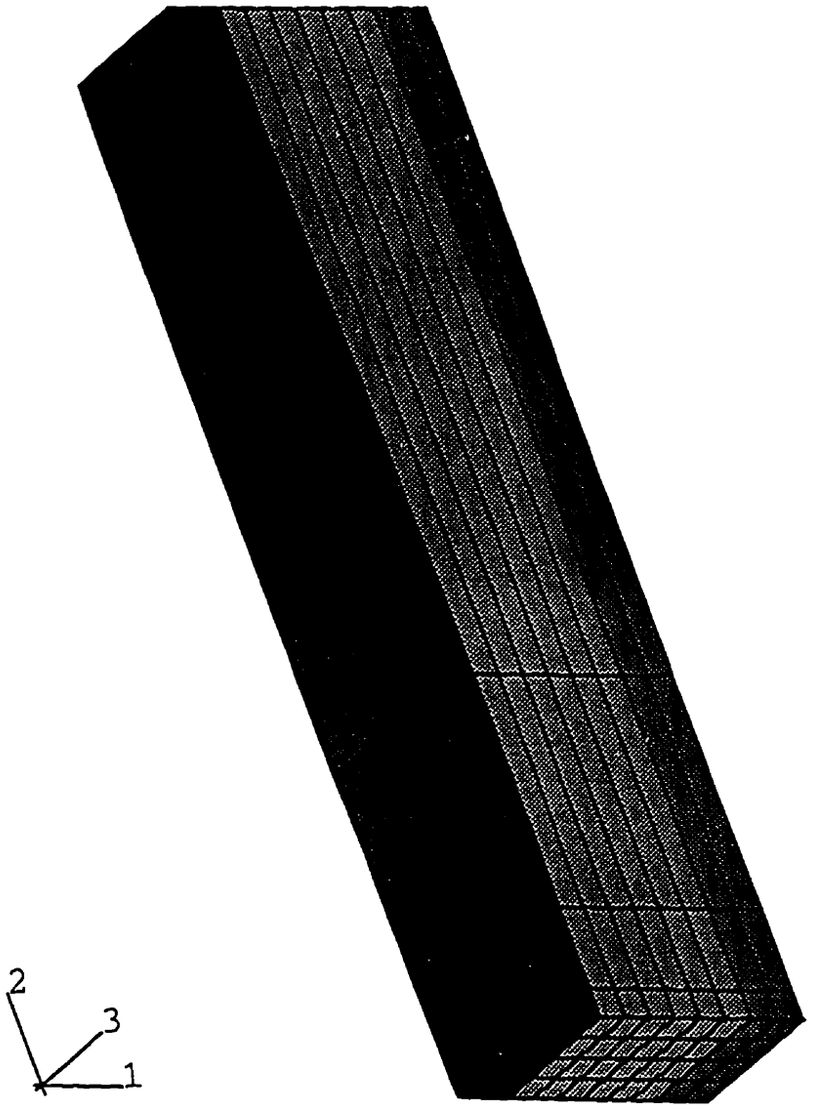

Figure 3.36 The mesh design for a tensile bar having different material properties in the thickness direction.

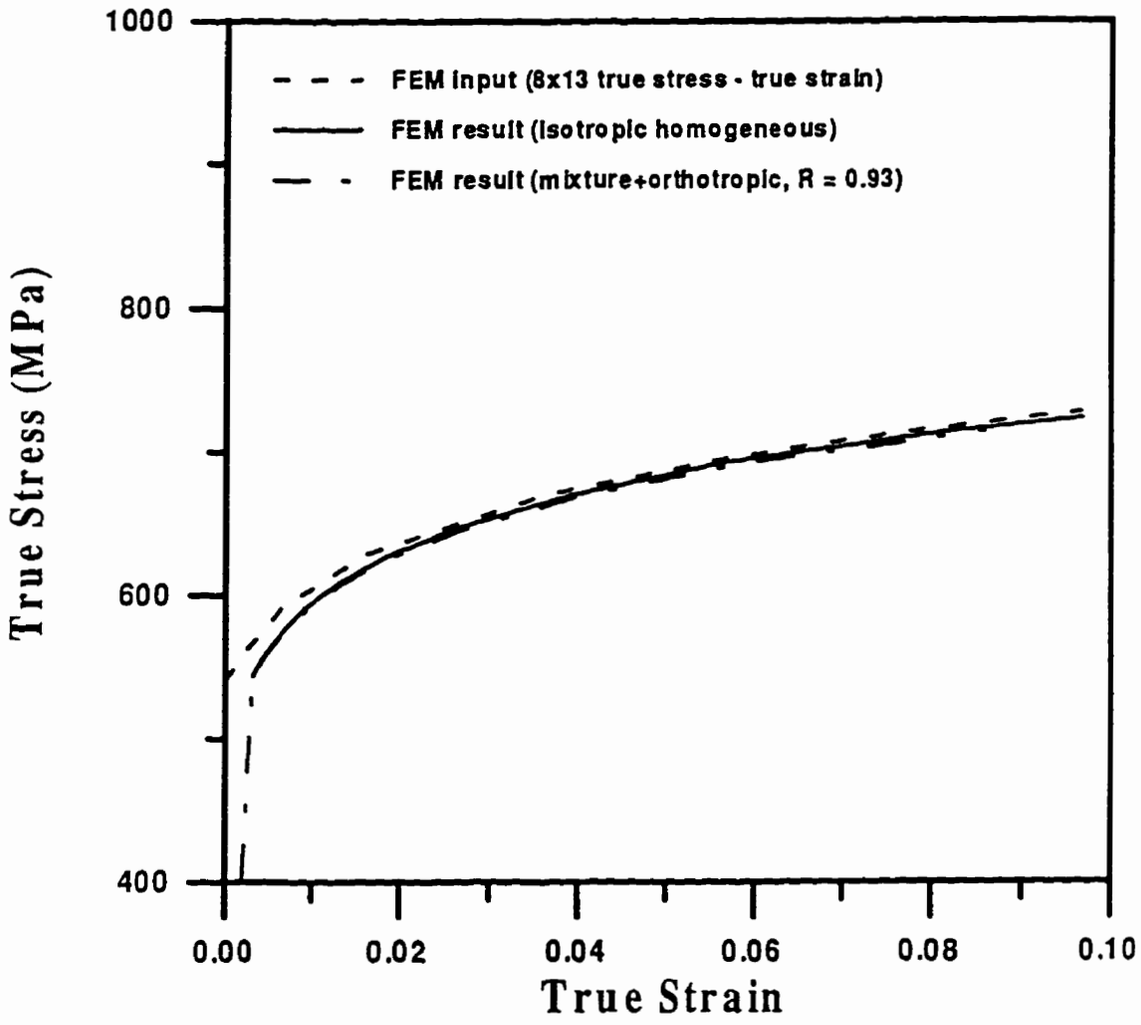

Figure 3.37 True stress – true strain curves resulting from the microstructure based finite element analysis for 8.4 mm thickness specimen.

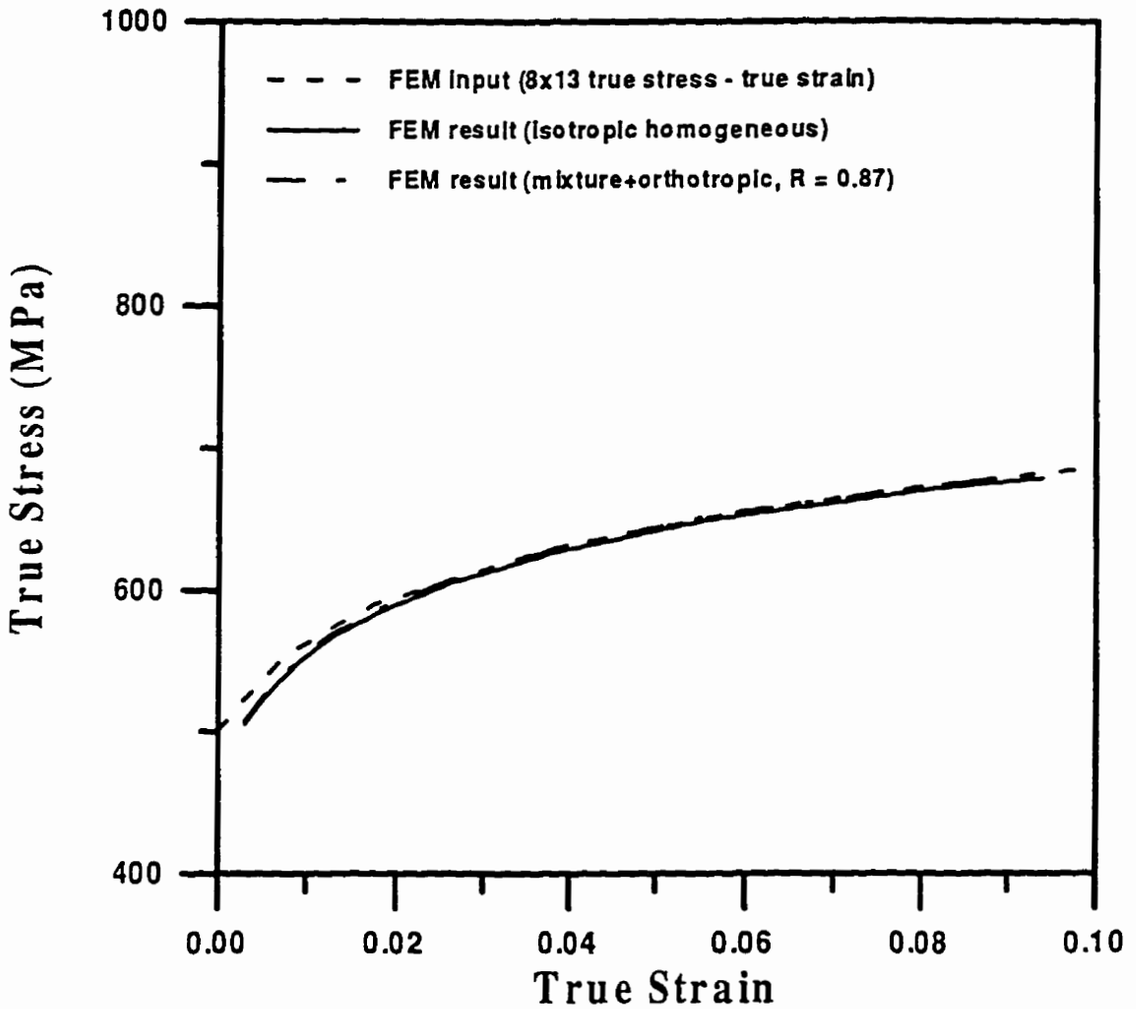

Figure 3.38 True stress – true strain curves resulting from the microstructure based finite element analysis for 13.4 mm thickness specimen.

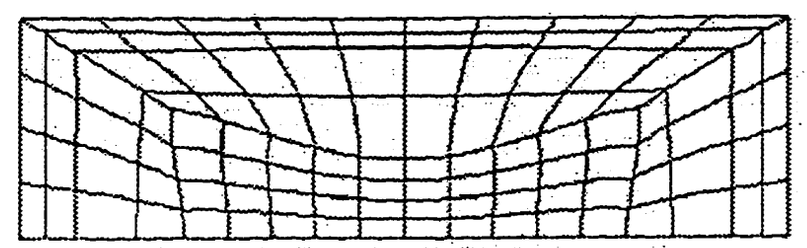

(a) isotropic homogeneous

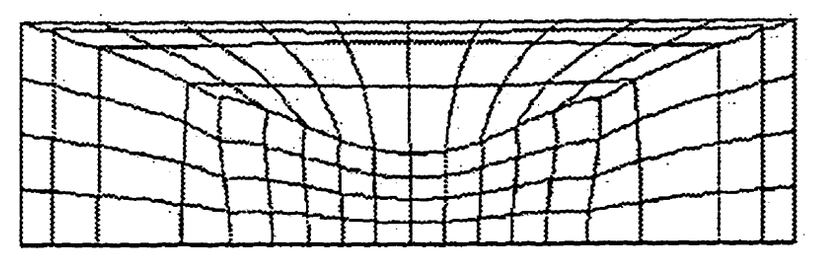

(b) microstructure based

Figure 3.39 The deformed net-section area after necking for the microstructure based finite element analysis and the isotropic homogeneous finite element analysis.

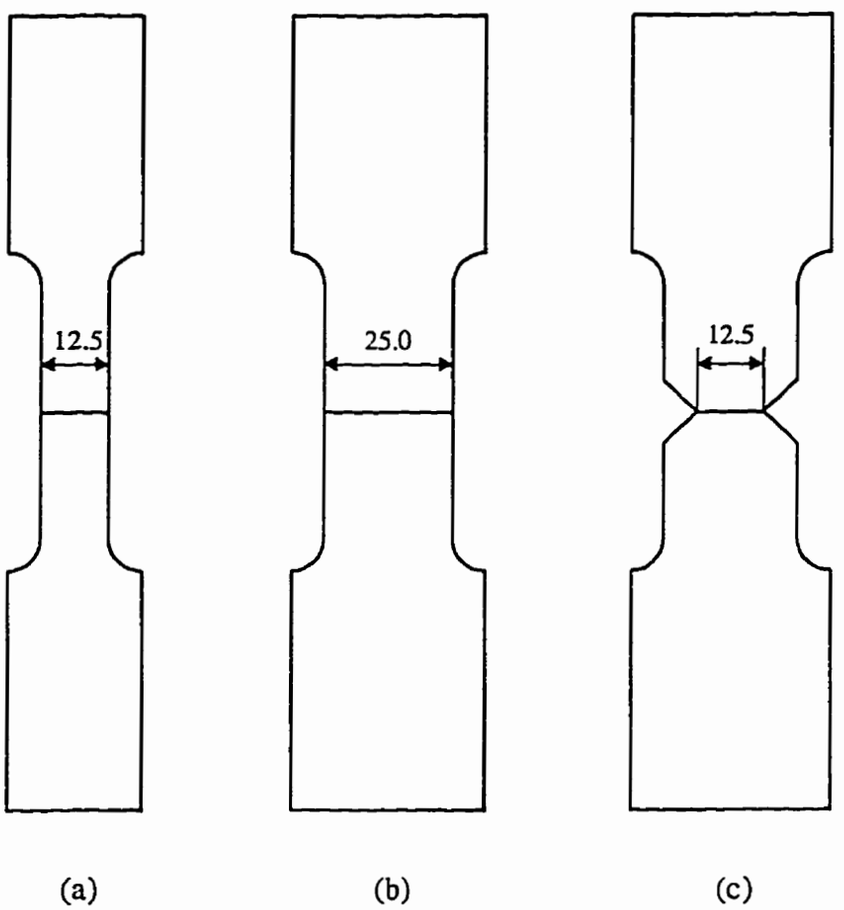

Figure 4.1 SENT specimen configurations.

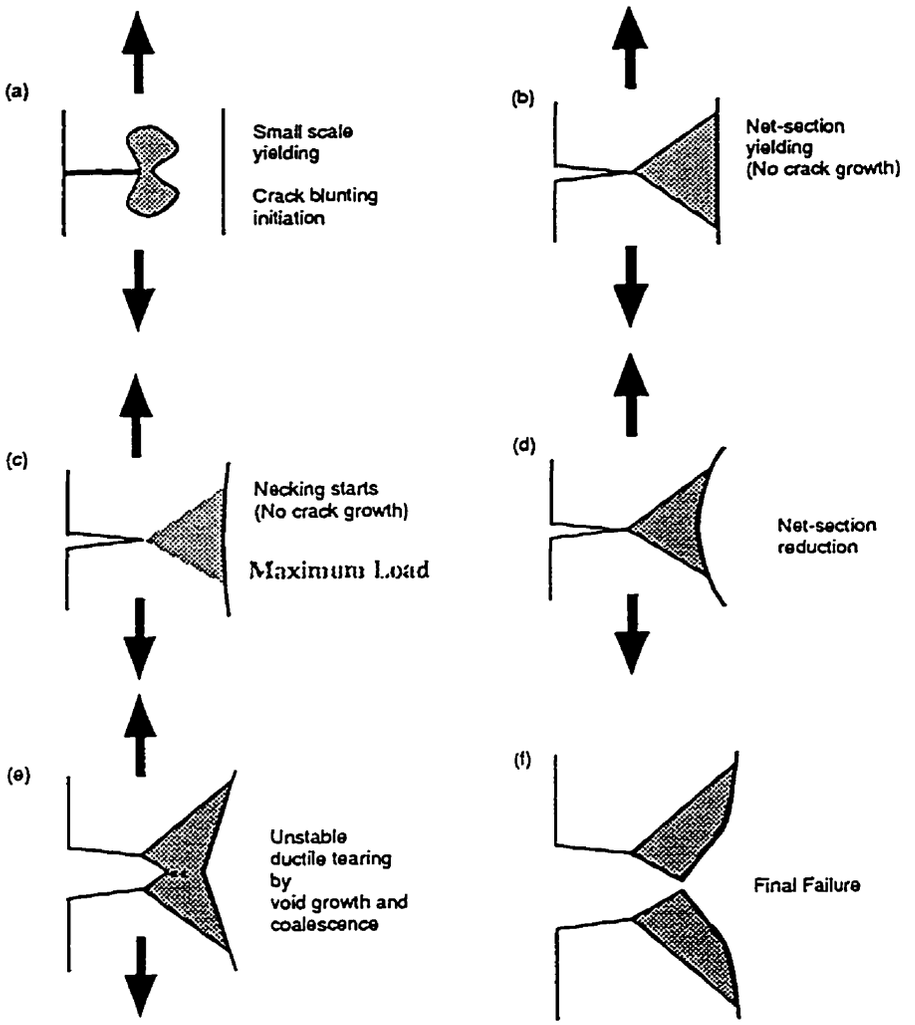

Figure 4.2 Failure mechanism of an SENT specimen.

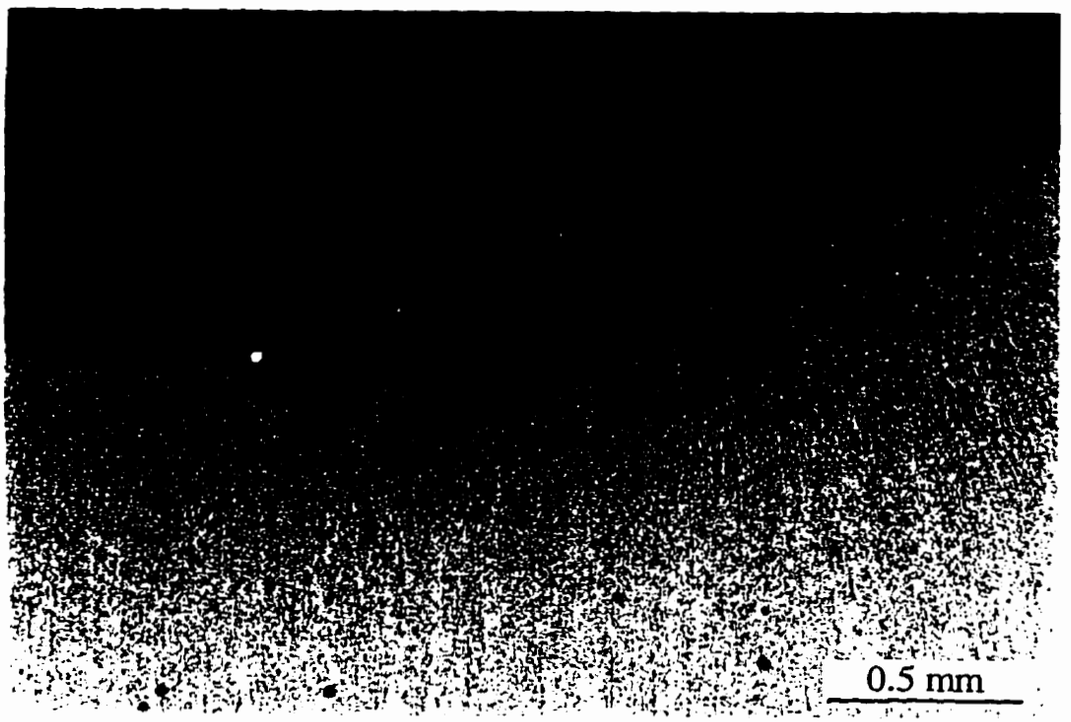

Figure 4.3 Deformation in the ligament after failure for $a/t = 0.25$ (J10)

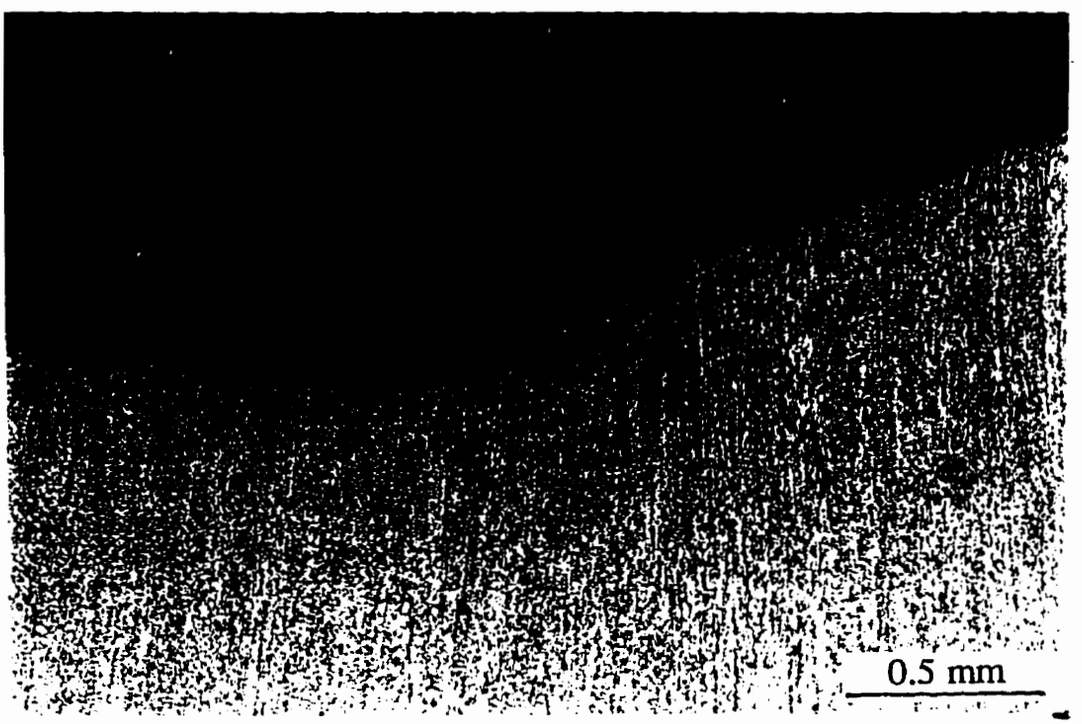

Figure 4.4 Deformation in the ligament after failure for $a/t = 0.25$ (J10)

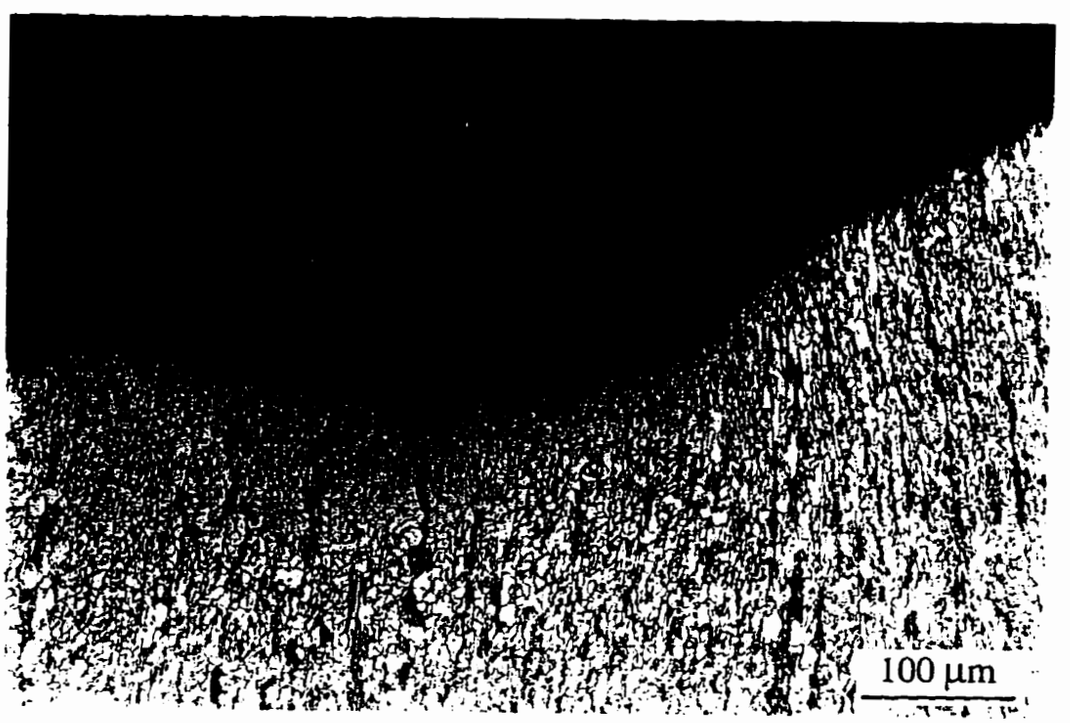

Figure 4.5 Deformed microstructure near the crack-tip.

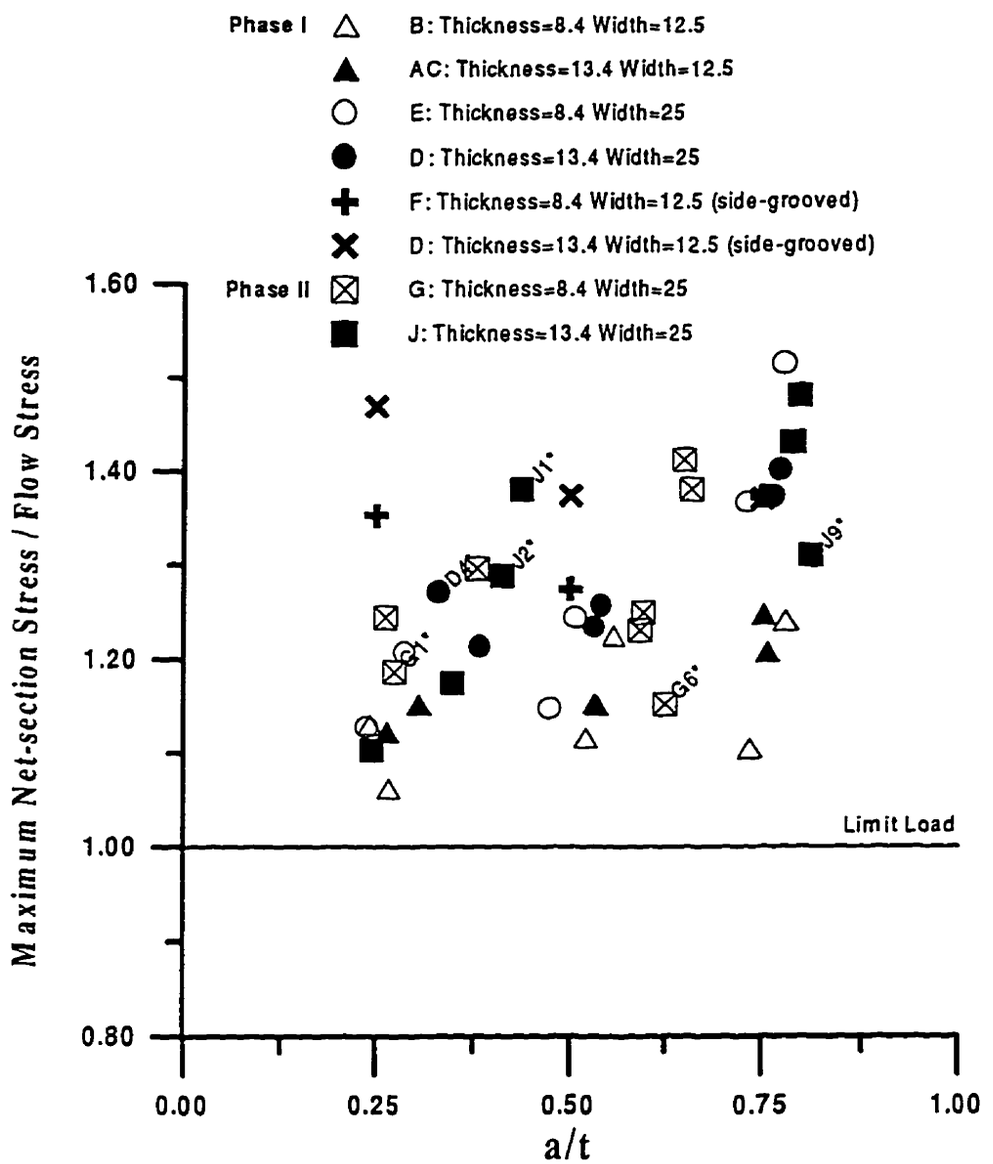

Figure 4.6 Test results analyzed with the conventional limit load analysis.

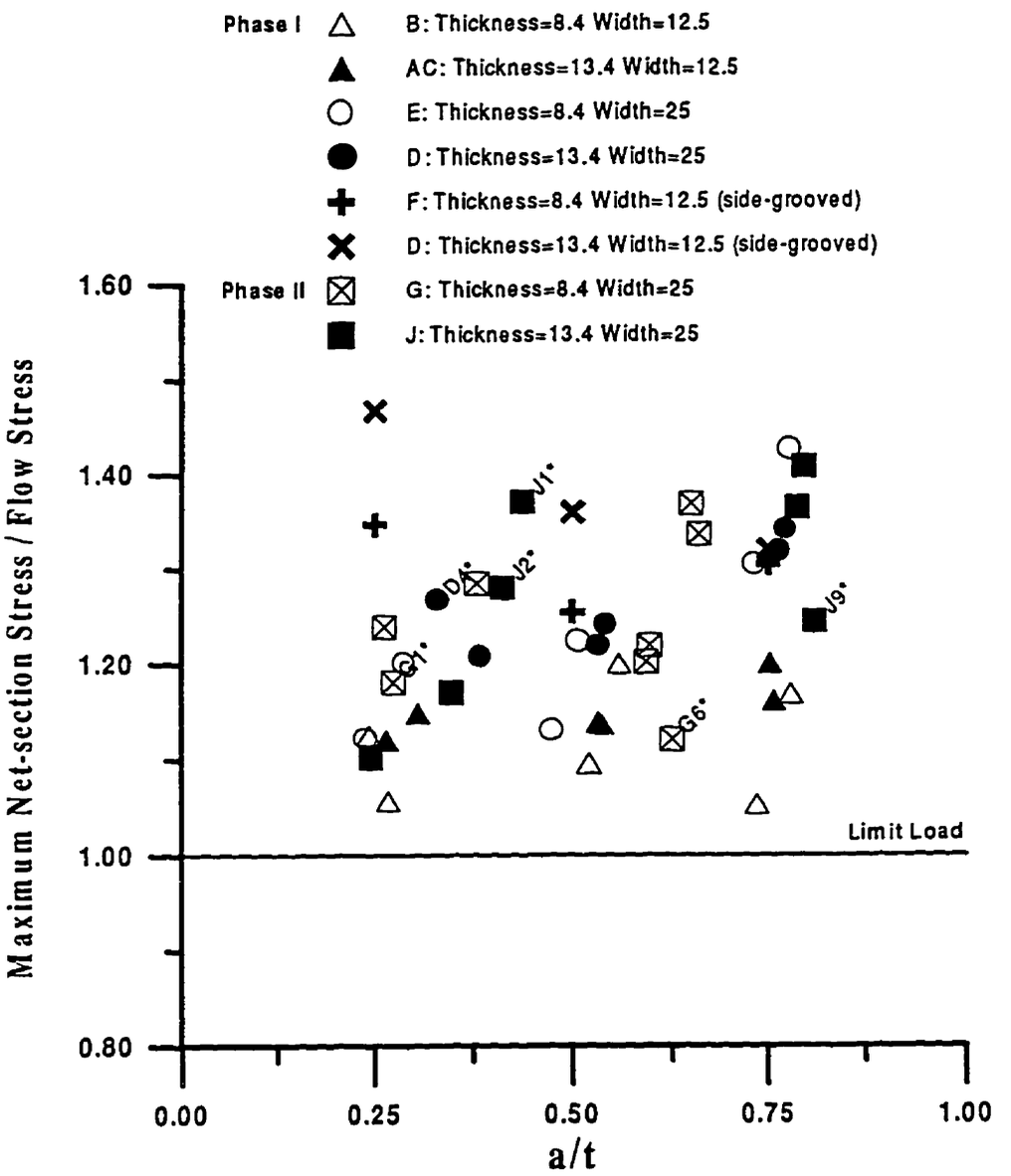

Figure 4.7 Plastic collapse analyses based on microstructure.

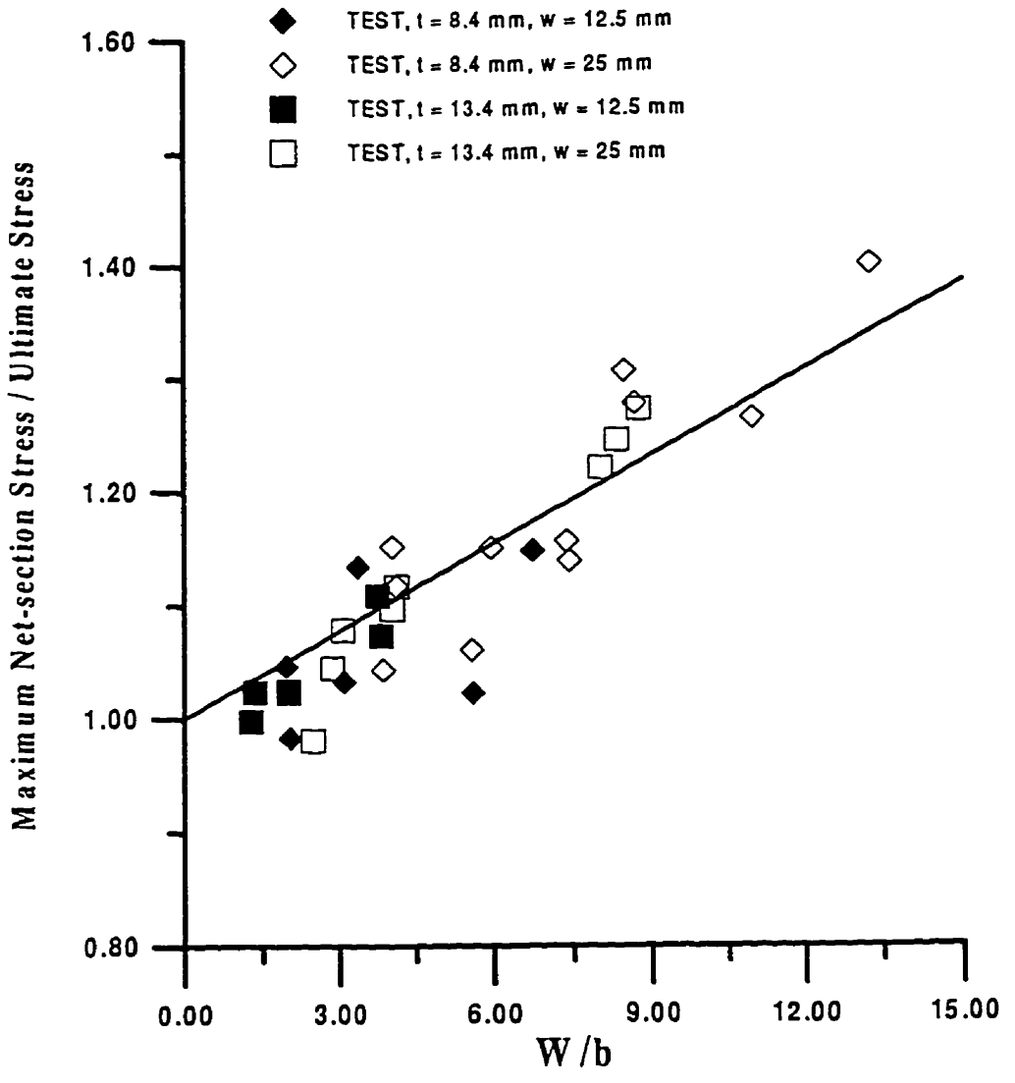

Figure 4.8 SENT test results versus *W/b*.

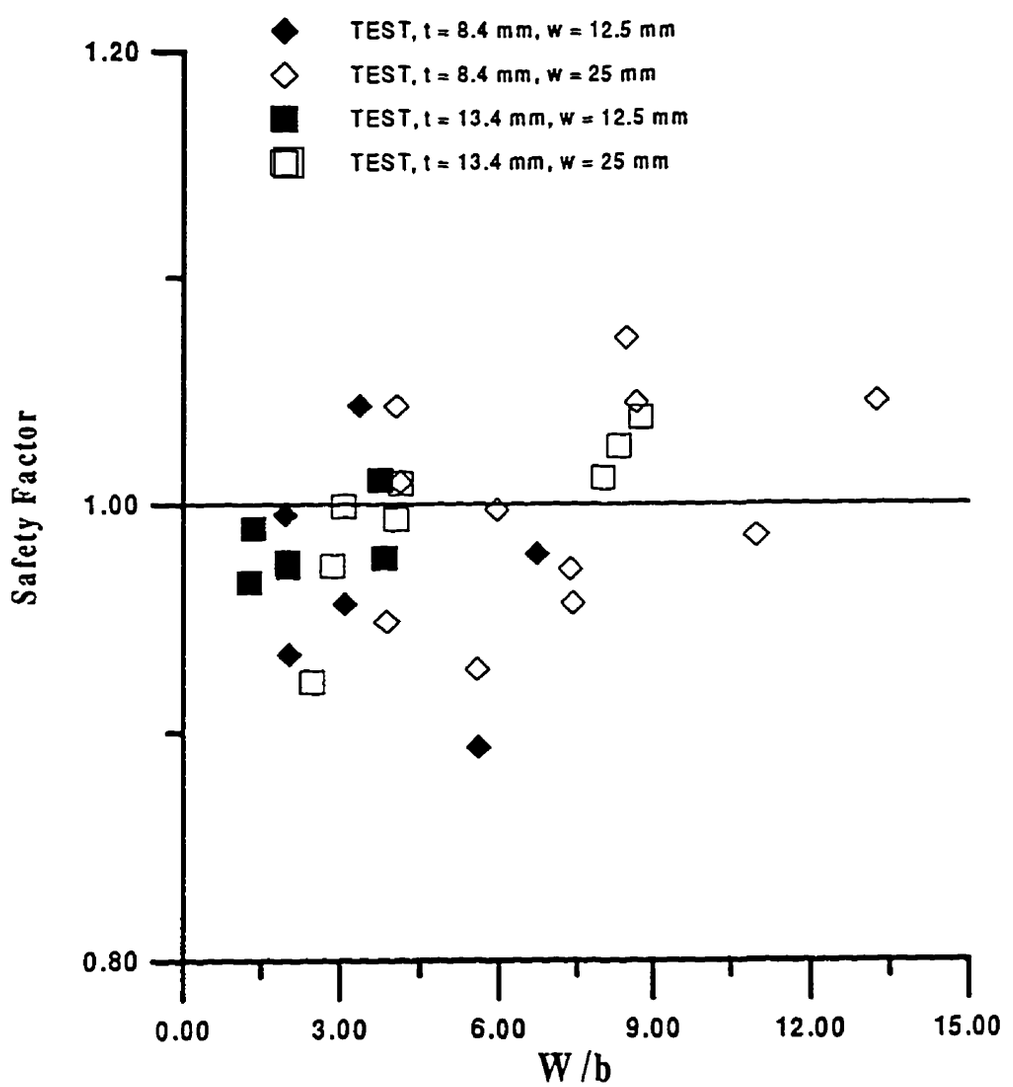

Figure 4.9 An empirical plastic collapse solution for SENT specimens.

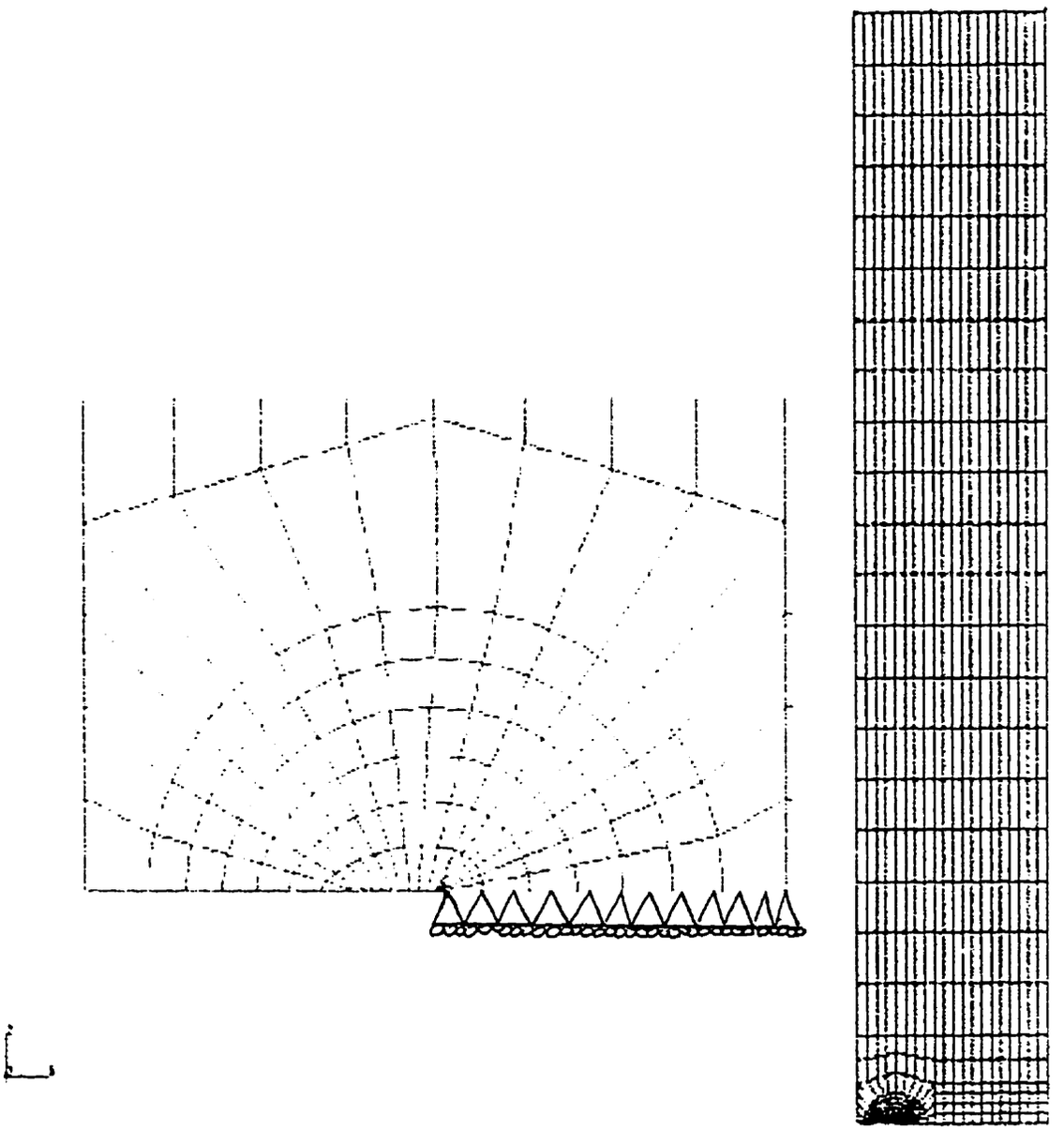

Figure 4.10 The finite element mesh for an SENT specimen ($a/t = 0.25$).

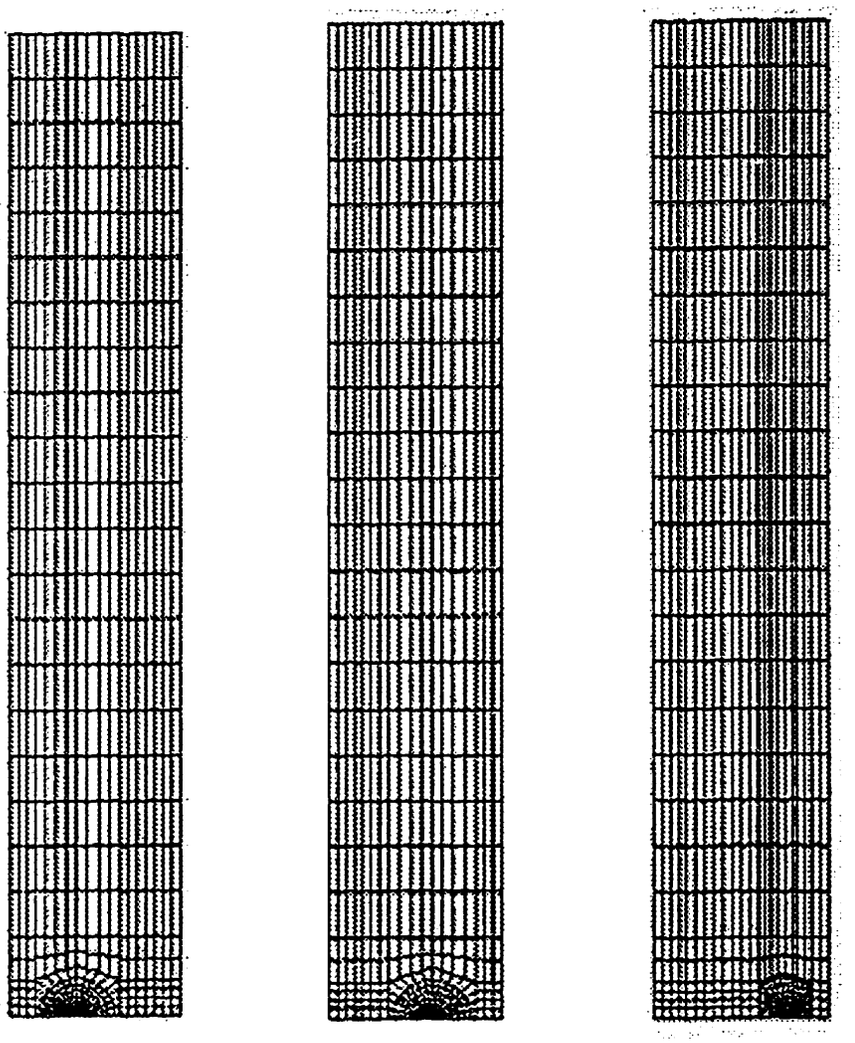

Figure 4.11 Finite element meshes for SENT specimens.

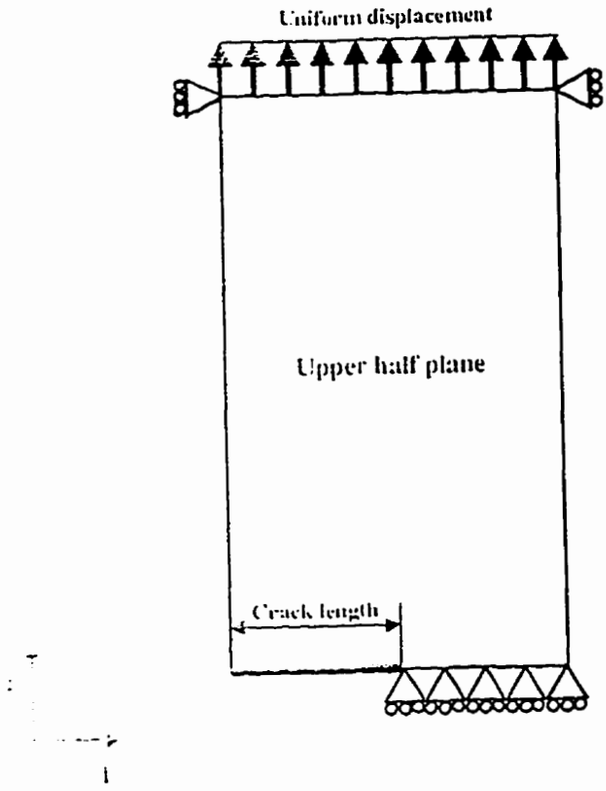

Figure 4.12 The schematic illustration of boundary condition for the SENT analysis.

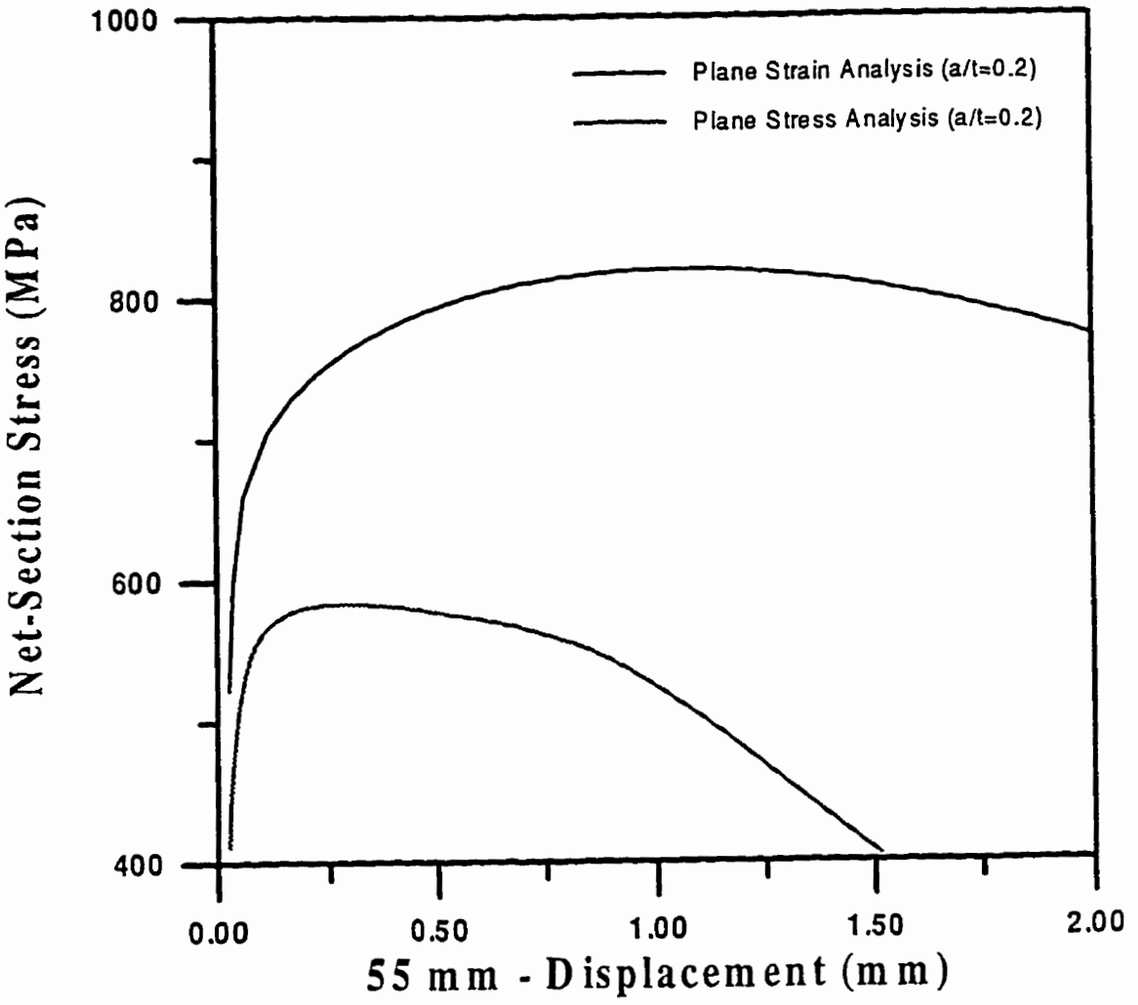

Figure 4.13 The plane stress analysis versus the plane strain analysis for a/t = 0.2 (8.4 mm thickness specimen).

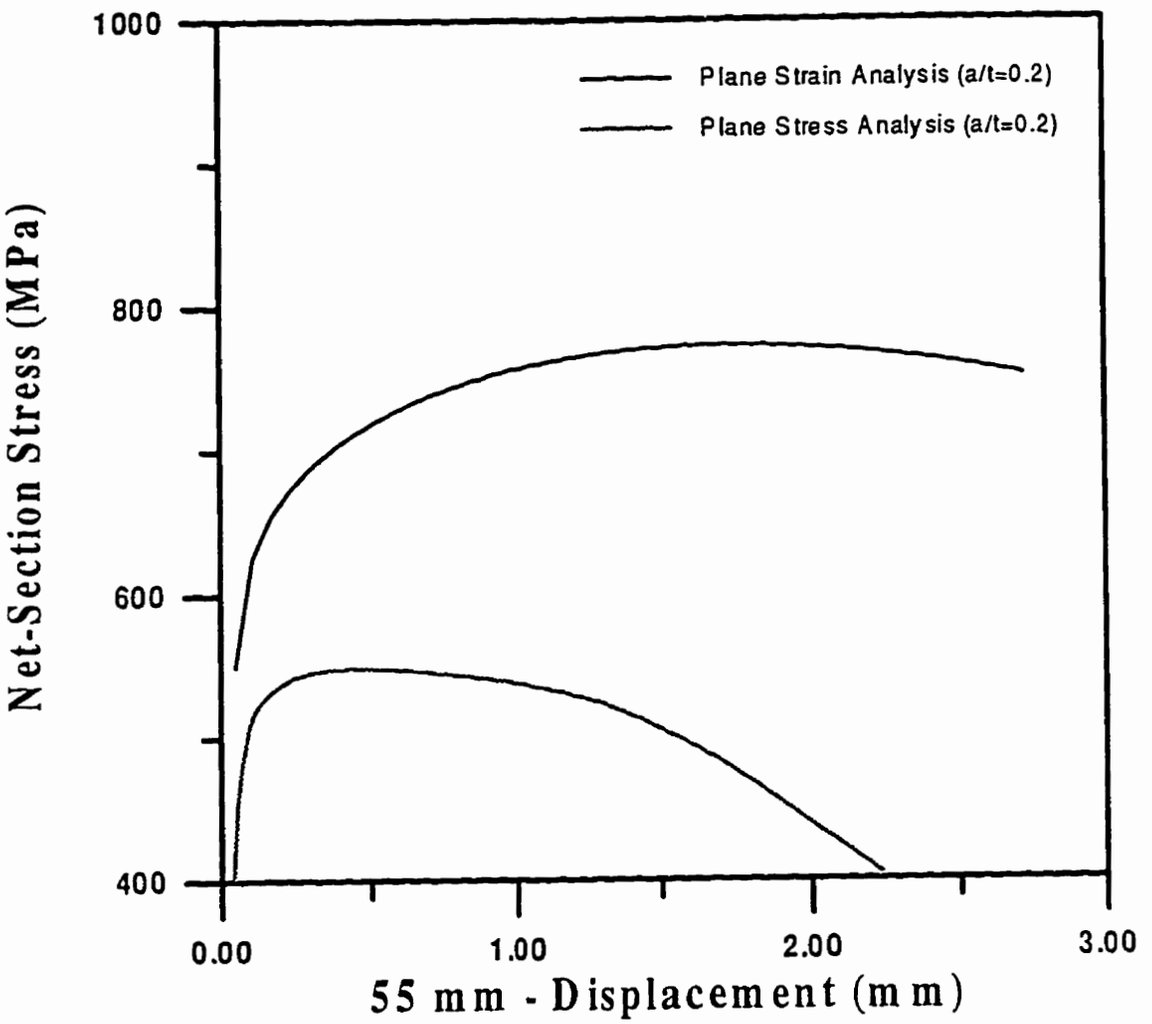

Figure 4.14 The plane stress analysis versus the plane strain analysis for a/t = 0.2 (13.4 mm thickness specimen).

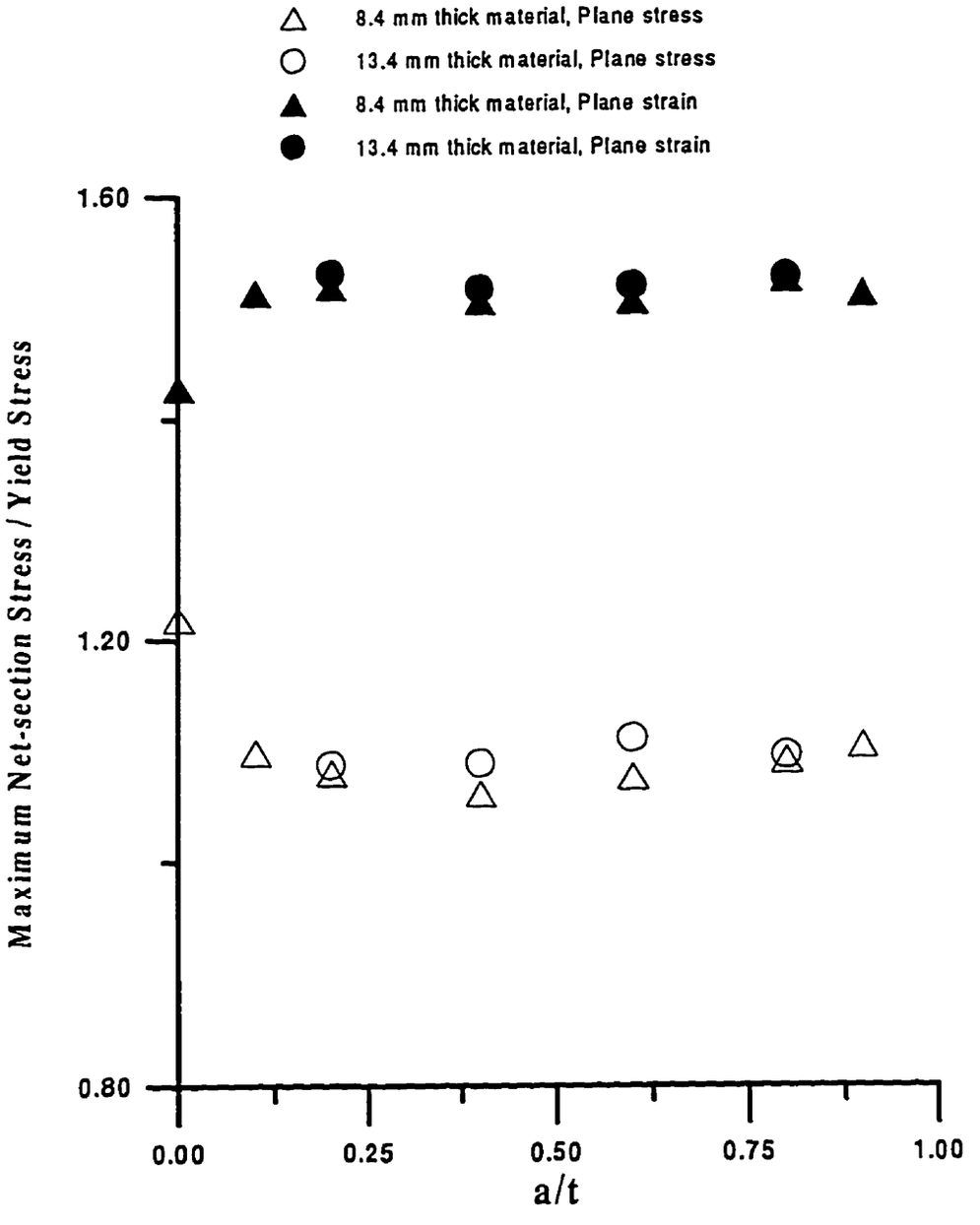

Figure 4.15 Maximum net-section stresses resulting from plane strain and plane stress analyses.

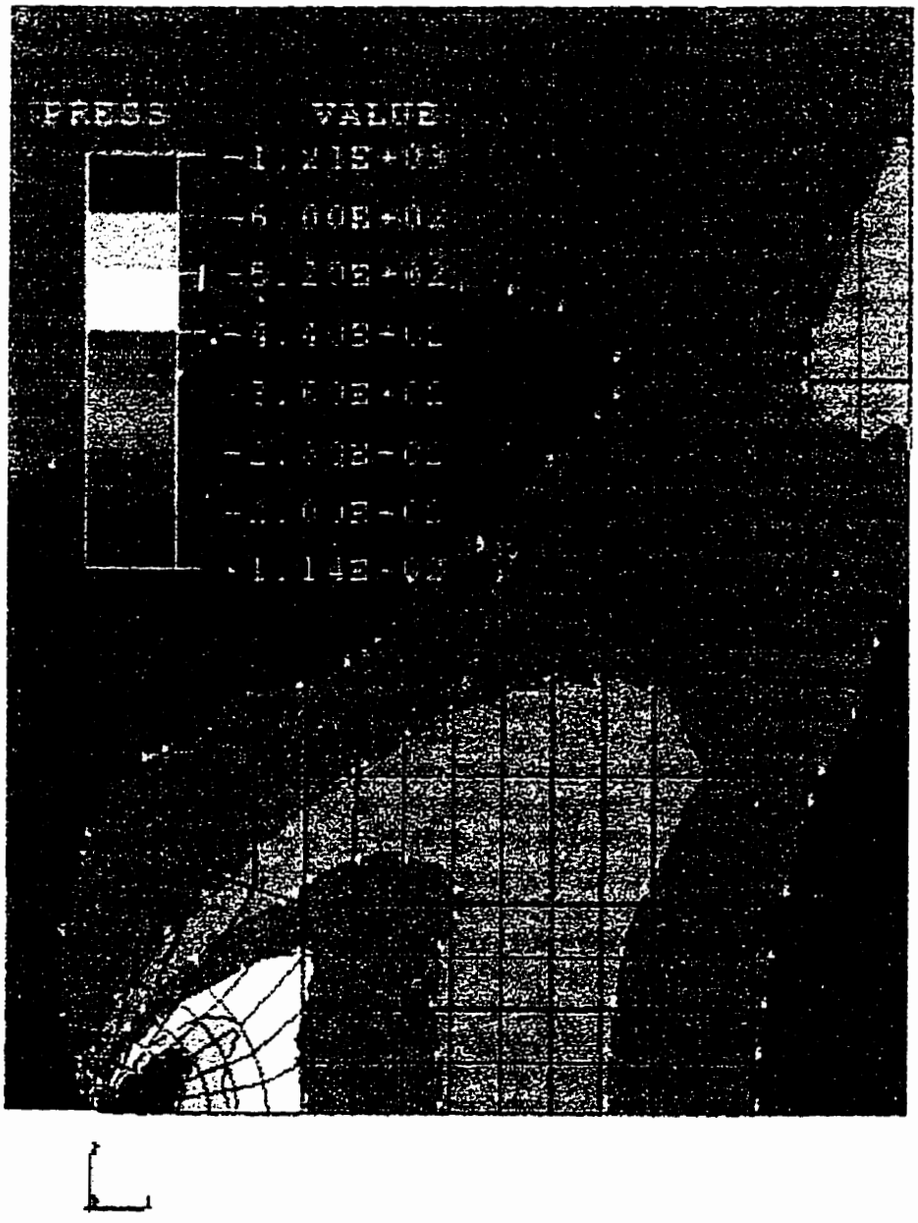

Figure 4.16 Contour plot of hydrostatic stress for net-section stress = 400 MPa, a/t = 0.2 (low level plasticity).

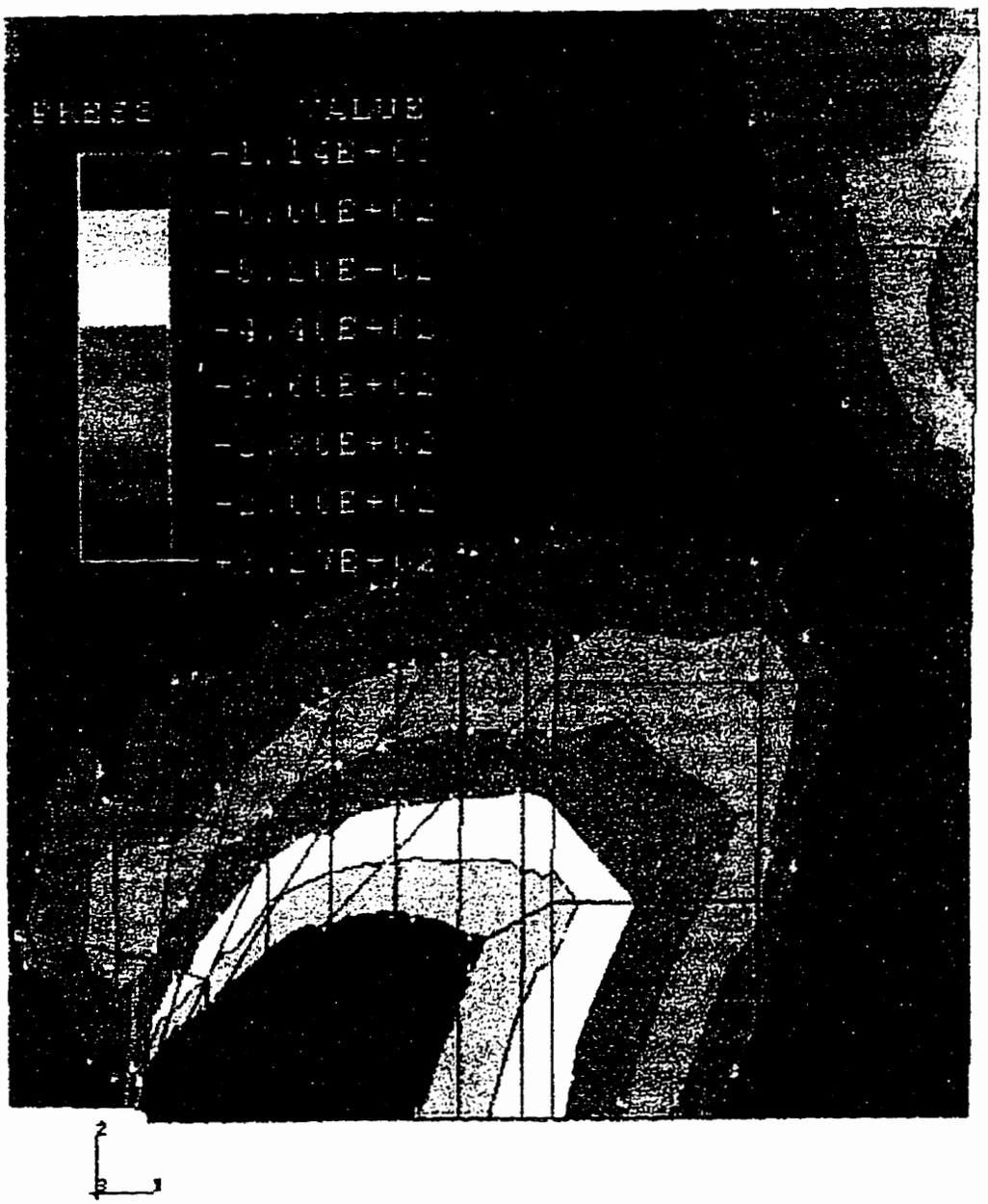

Figure 4.17 Contour plot of hydrostatic stress for net-section stress = 400 MPa, a/t = 0.8 (low level plasticity).

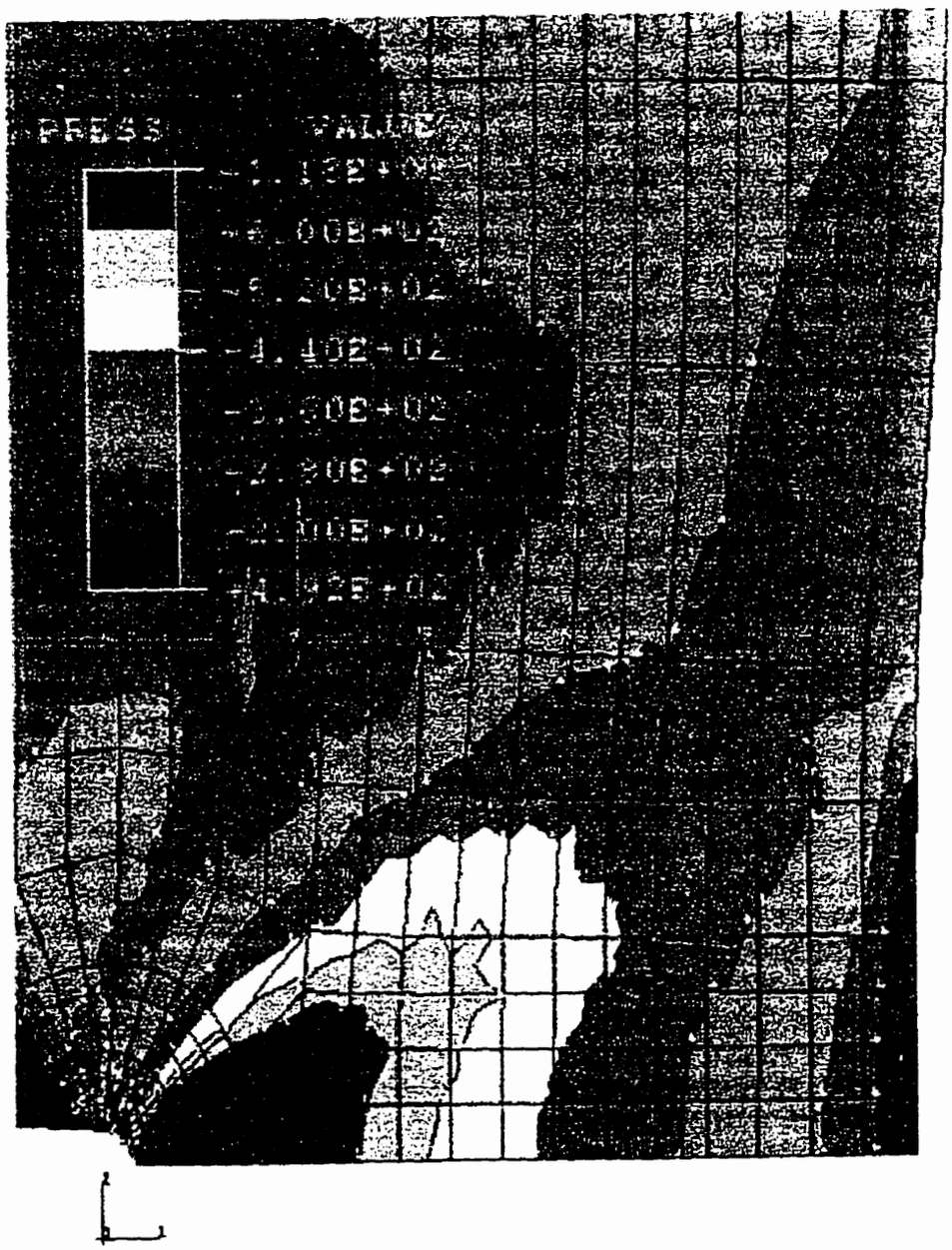

Figure 4.18 Contour plot of hydrostatic stress for net-section stress = 620 MPa, a/t = 0.2 (high level plasticity).

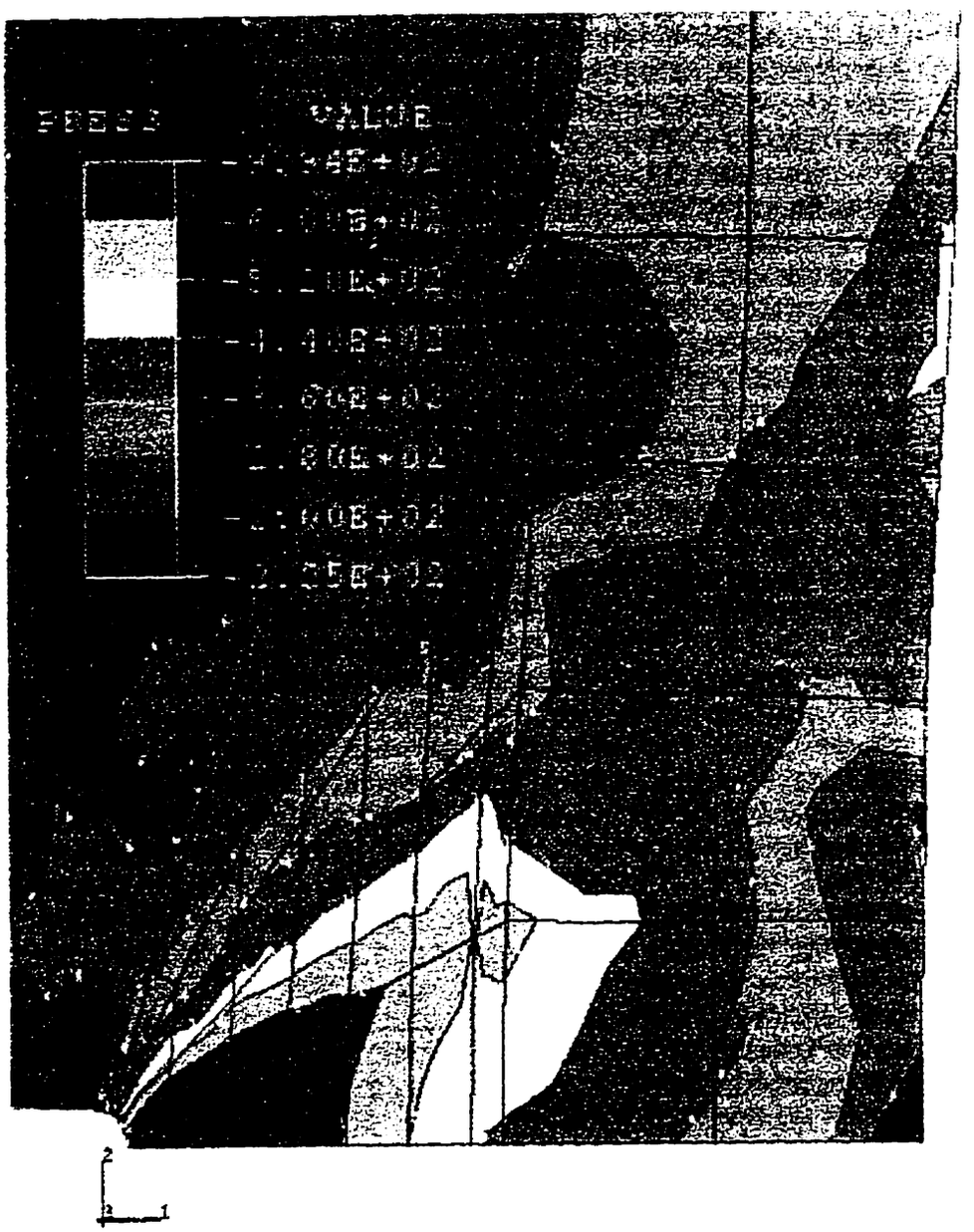

Figure 4.19 The contour plot of hydrostatic stress for net-section stress = 620 MPa, a/t = 0.8 (high level plasticity).

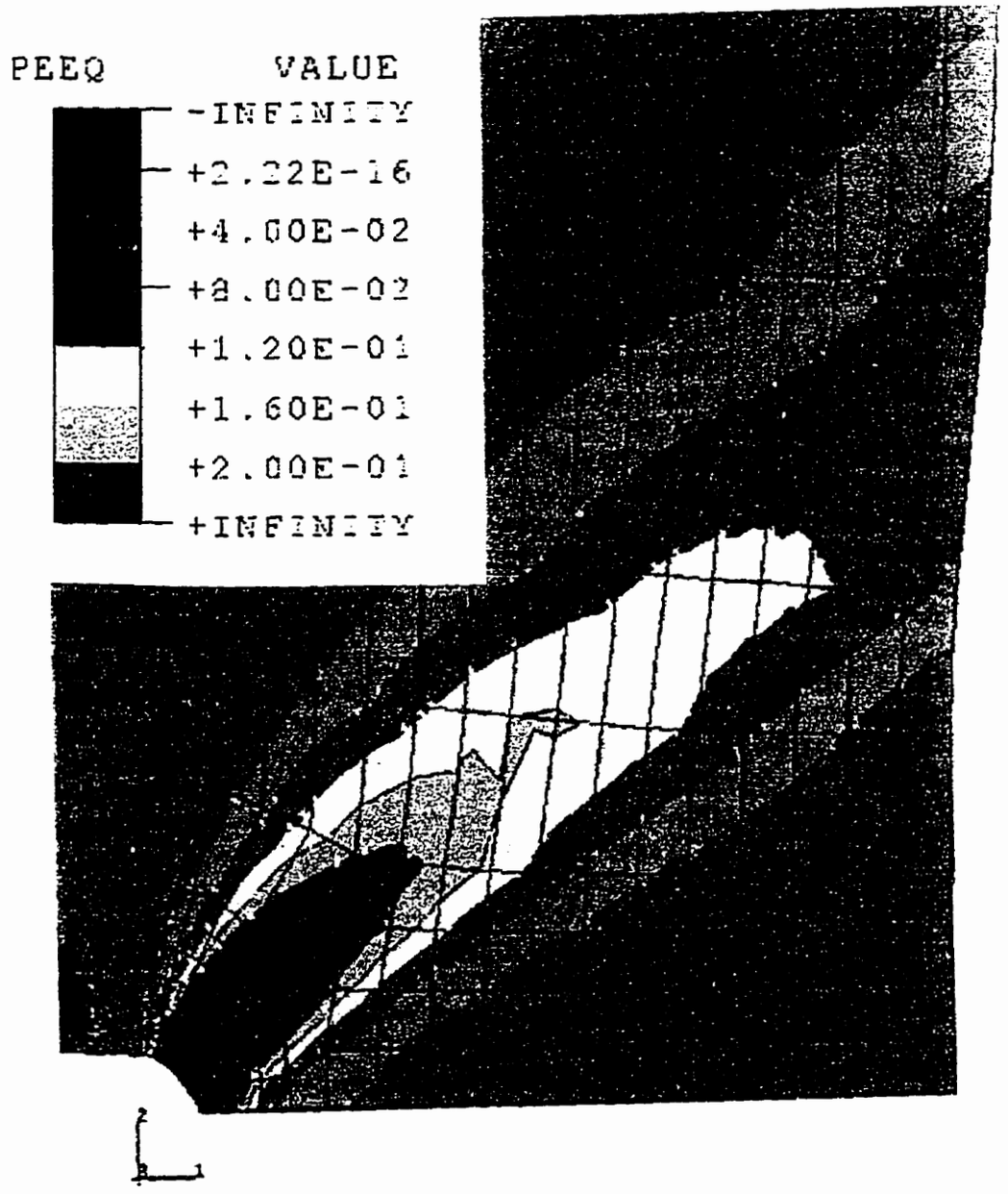

Figure 4.20 Contour plot of equivalent plastic strain at the maximum net-section stress (780 MPa) for $a/t = 0.2$.

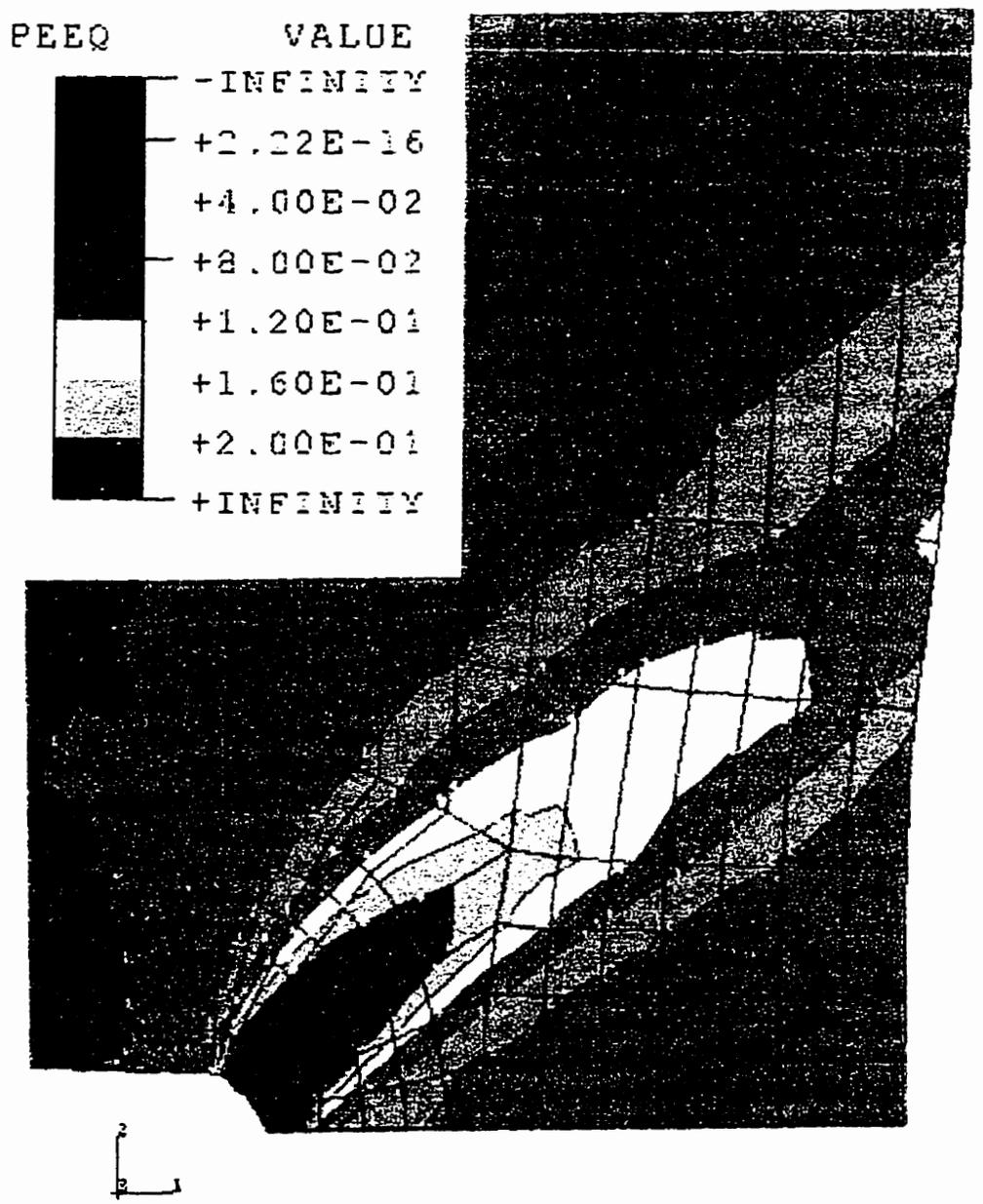

Figure 4.21 Contour plot of equivalent plastic strain at the maximum net-section stress (780 MPa) for $a/t = 0.4$.

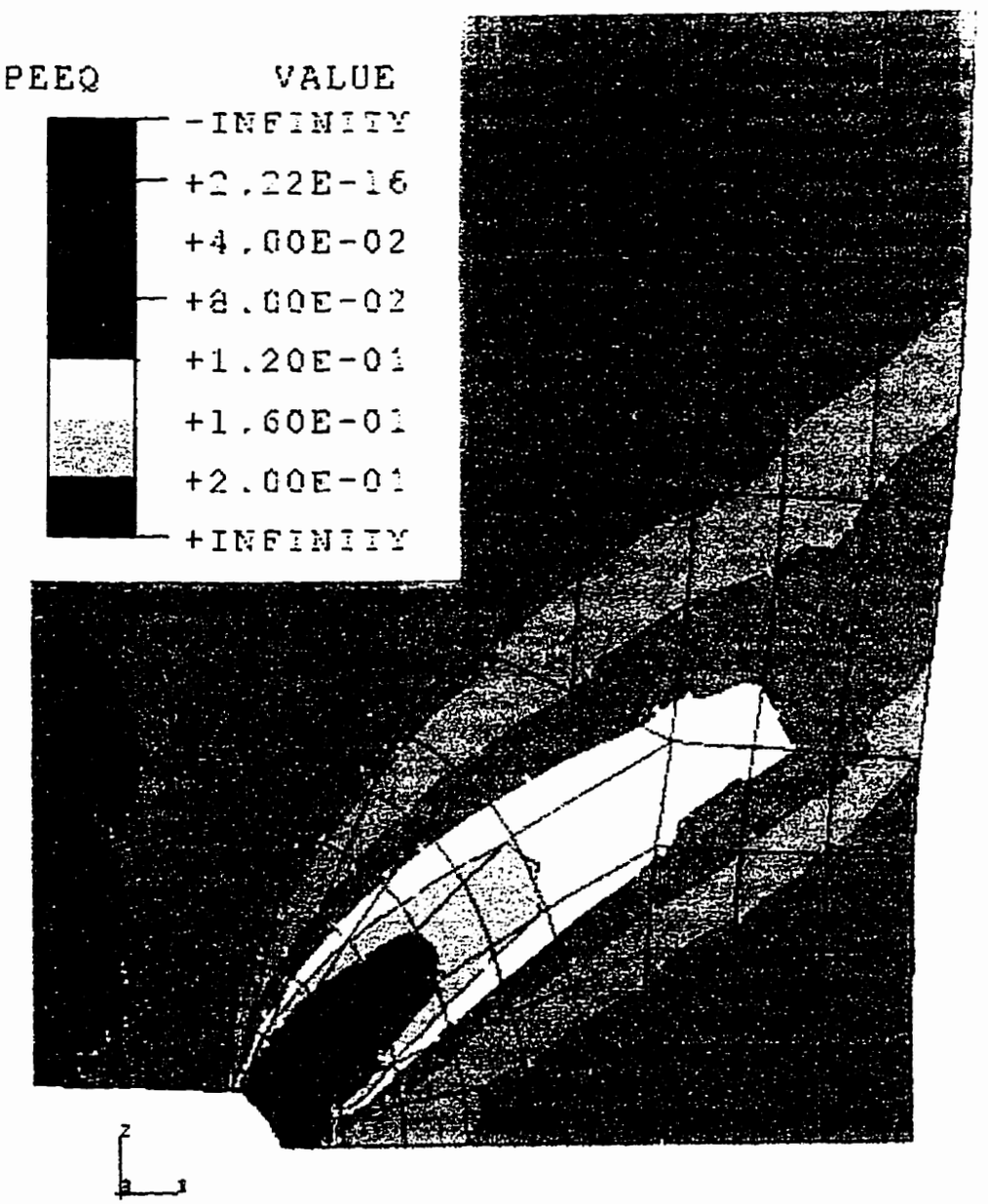

Figure 4.22 Contour plot of equivalent plastic strain at the maximum net-section stress (780 MPa) for $a/t = 0.6$.

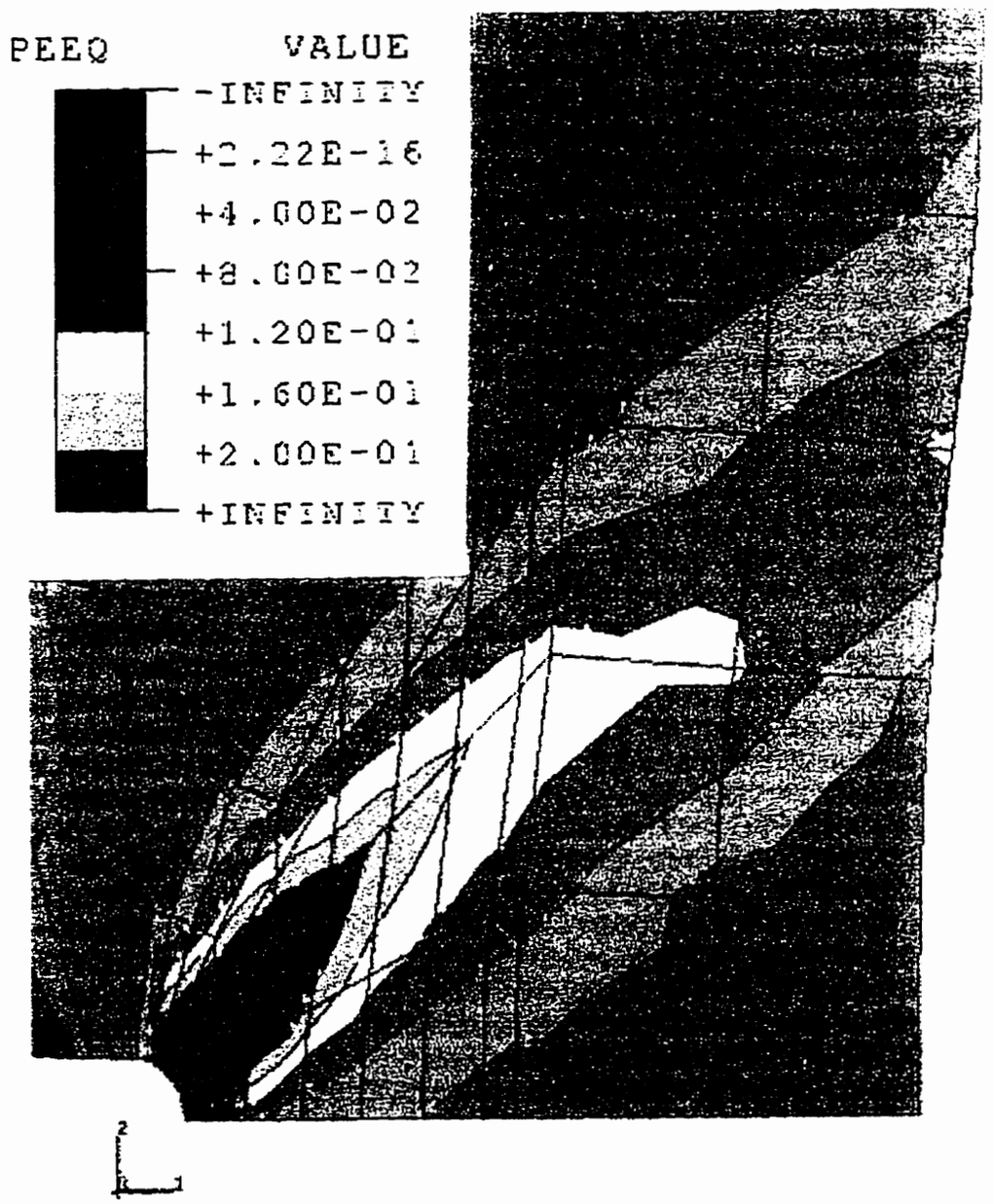

Figure 4.23 Contour plot of equivalent plastic strain at the maximum net-section stress (780 MPa) for $a/t = 0.8$.

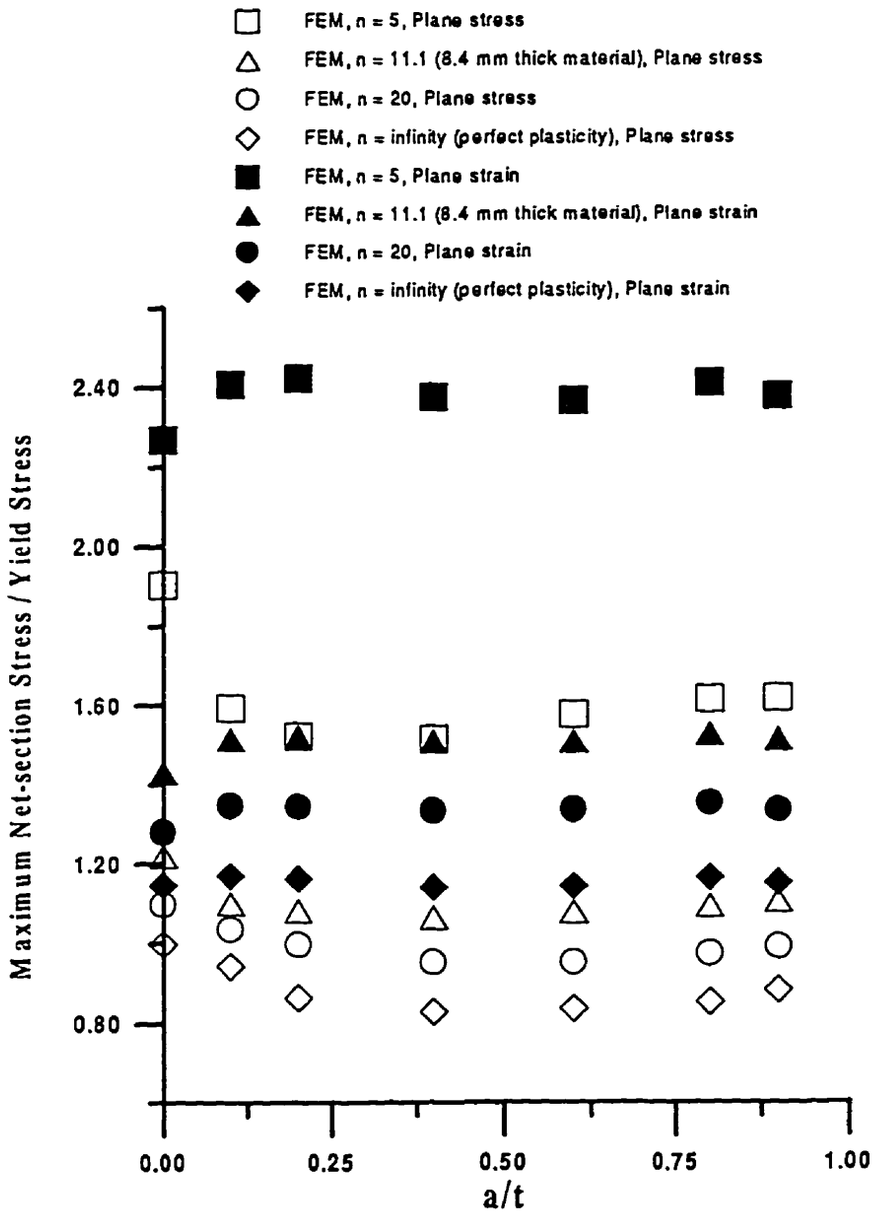

Figure 4.24 Plane strain versus plane stress analyses for various n values.

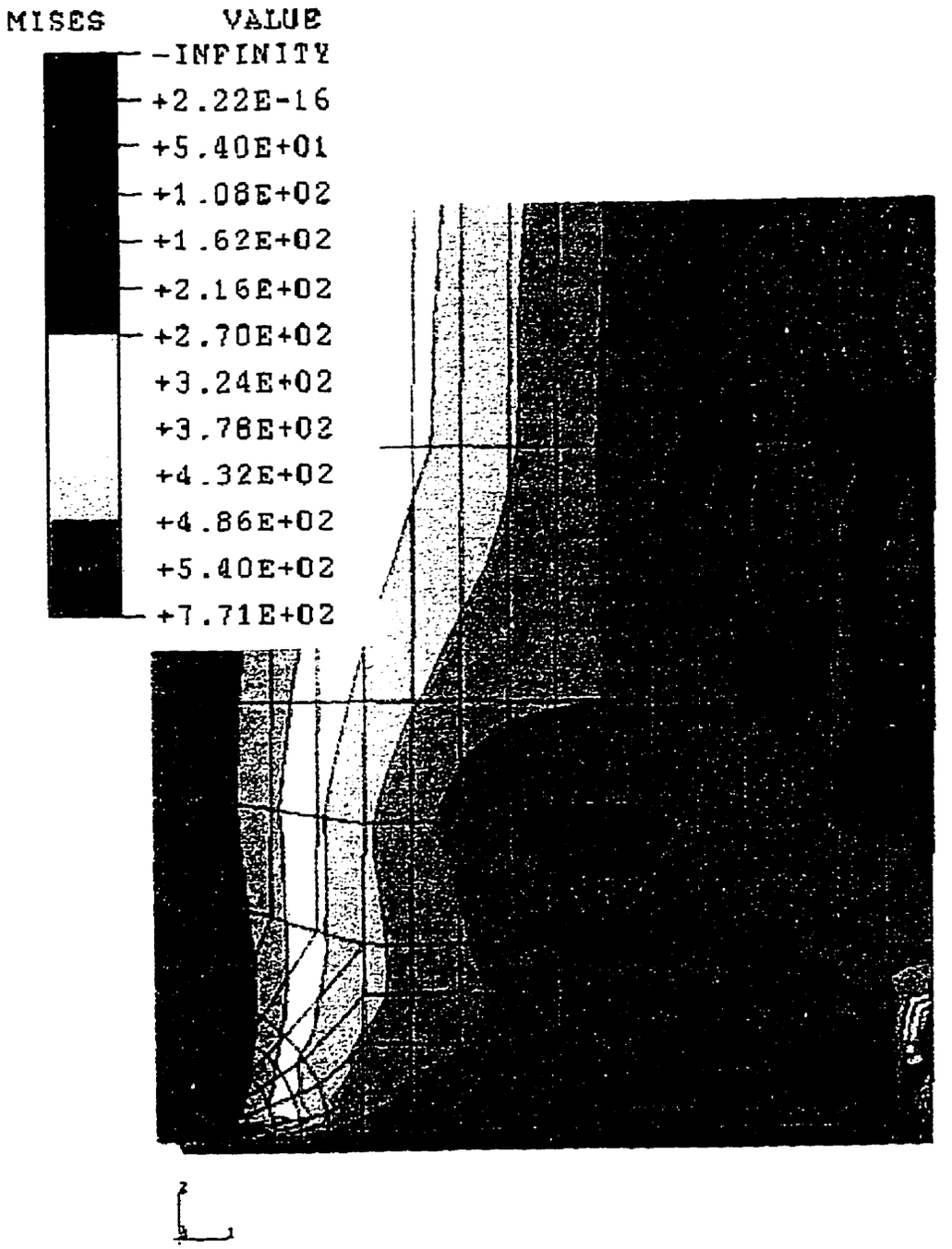

Figure 4.25 Contour plot of Mises stress for perfectly plastic material (plane stress).

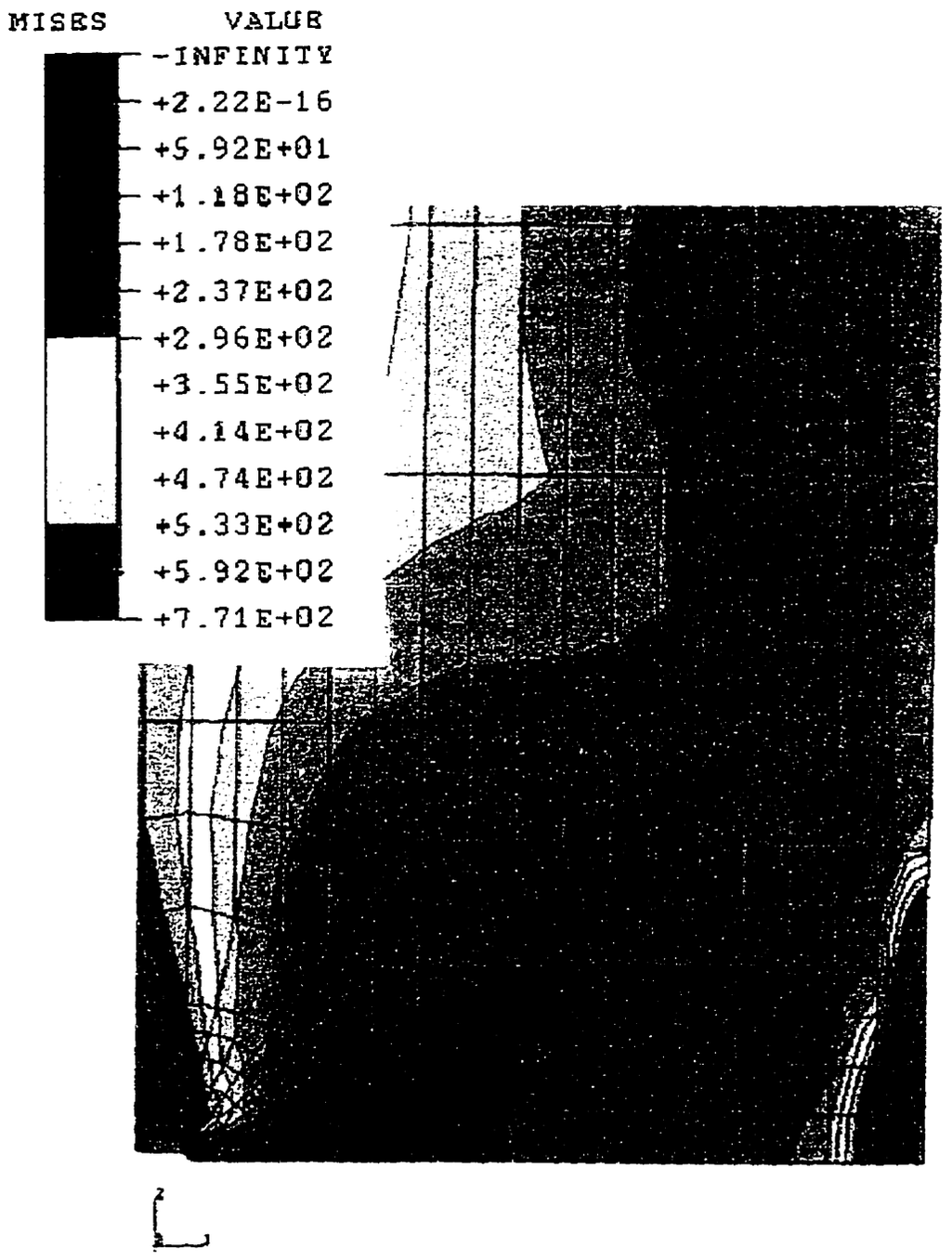

Figure 4.26 Contour plot of Mises stress for $n = 20$ material (plane stress).

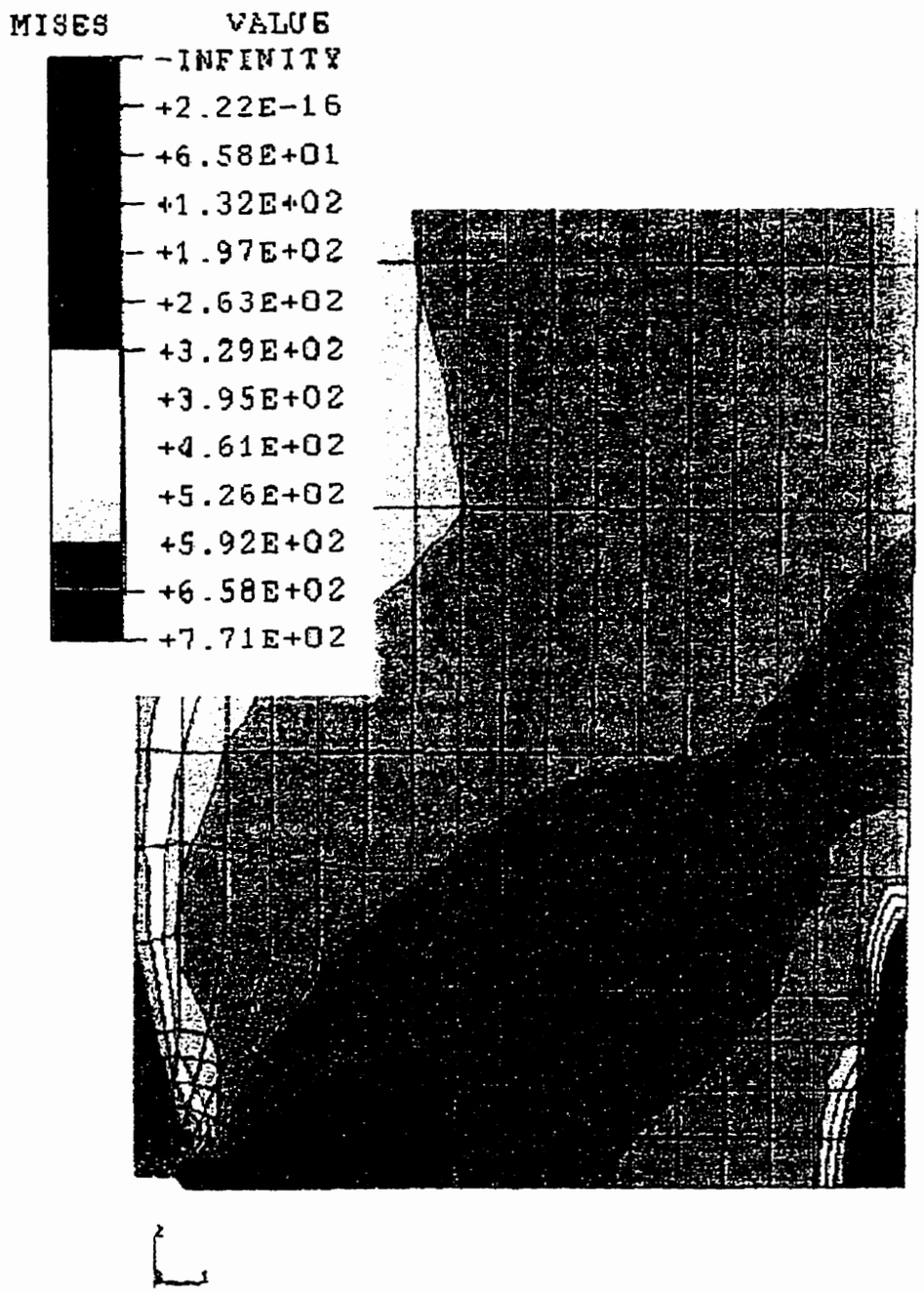

Figure 4.27 Contour plot of Mises stress for $n = 10$ material (plane stress).

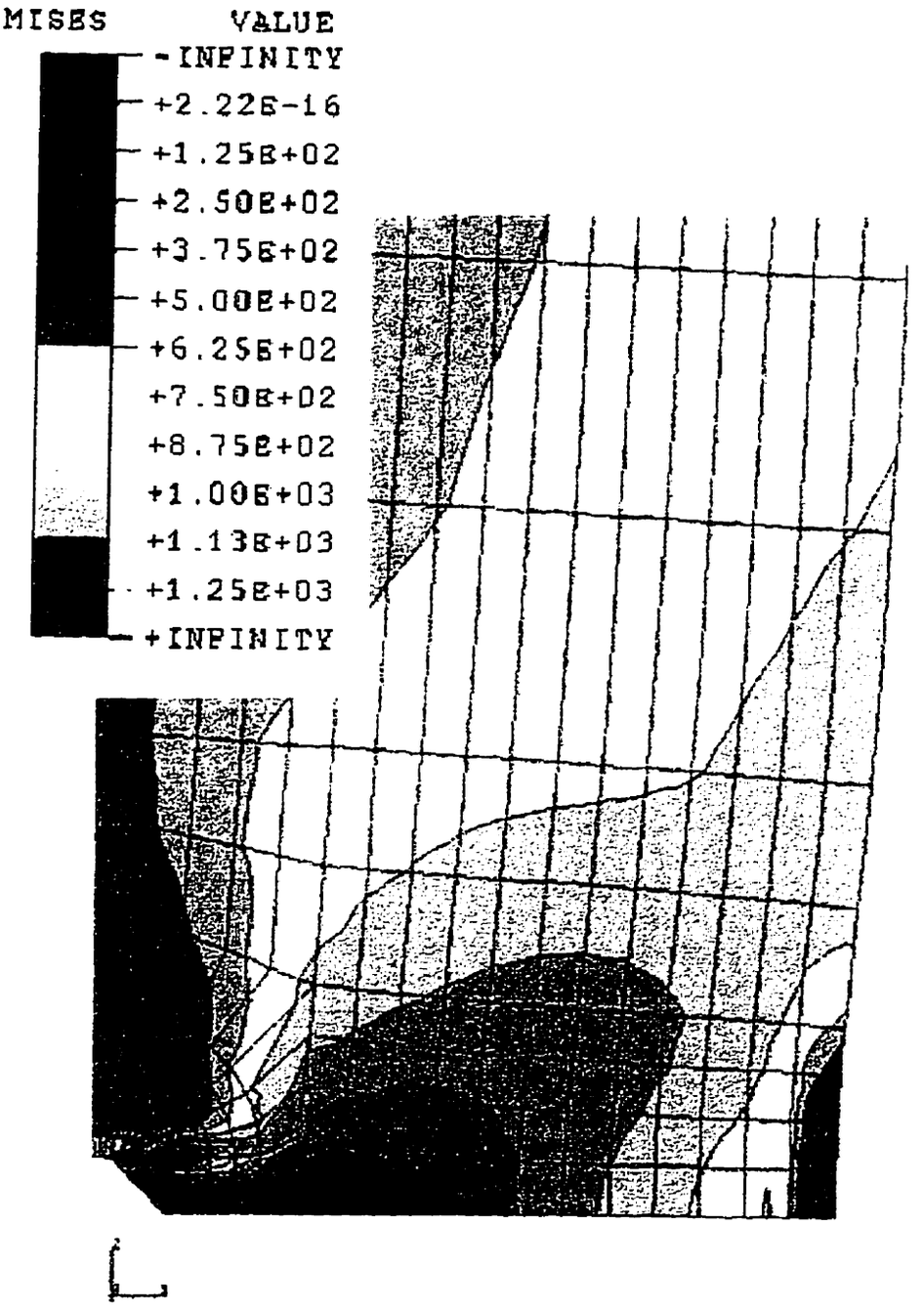

Figure 4.28 Contour plot of Mises stress for $n = 5$ material (plane stress).

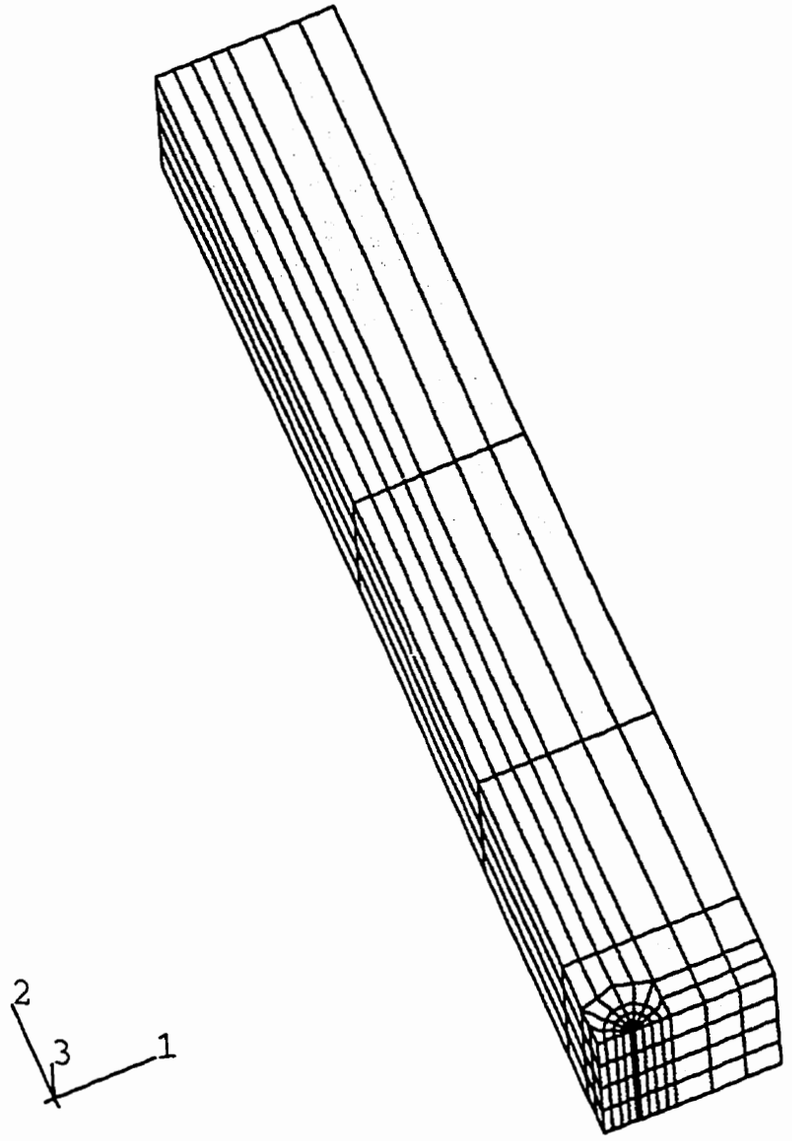

Figure 4.29 Three-dimensional finite element mesh used for SENT analysis (a/t = 0.2, 8.4 mm thickness specimen).

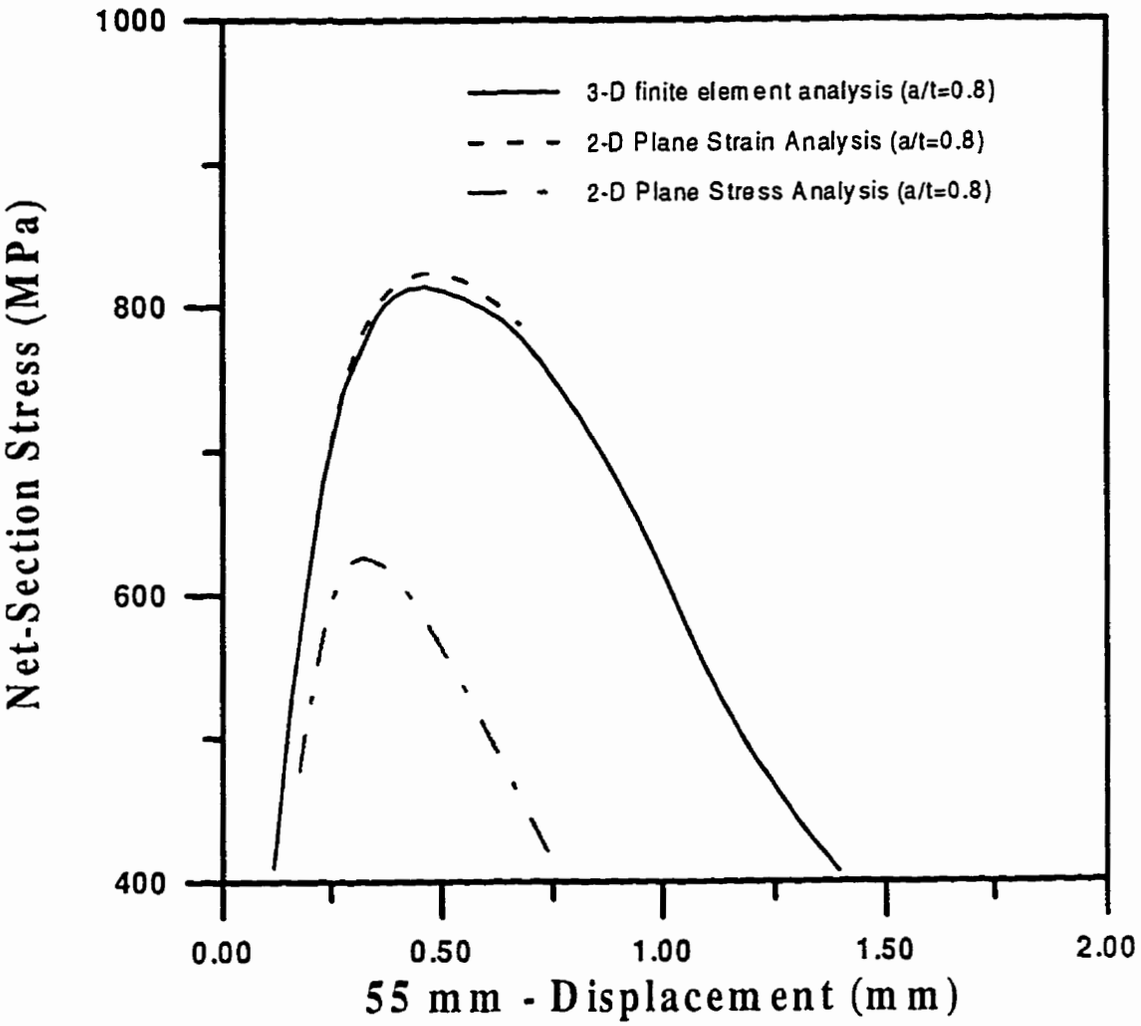

Figure 4.30 Net-section stress versus the 55 displacement resulting from 3-D finite element analysis (a/t = 0.8, 8.4 mm thickness specimen).

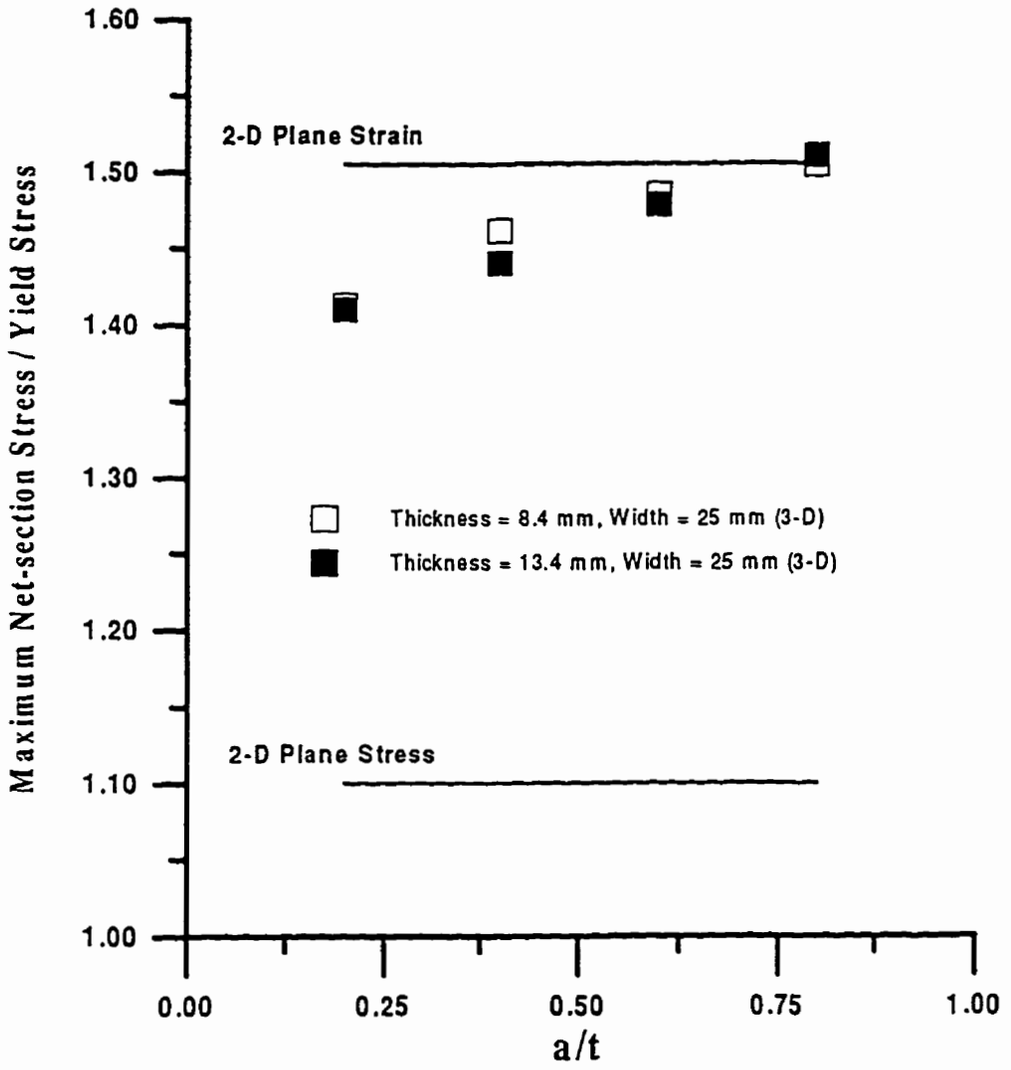

Figure 4.31. Three dimensional finite element analysis results for X70 steel.

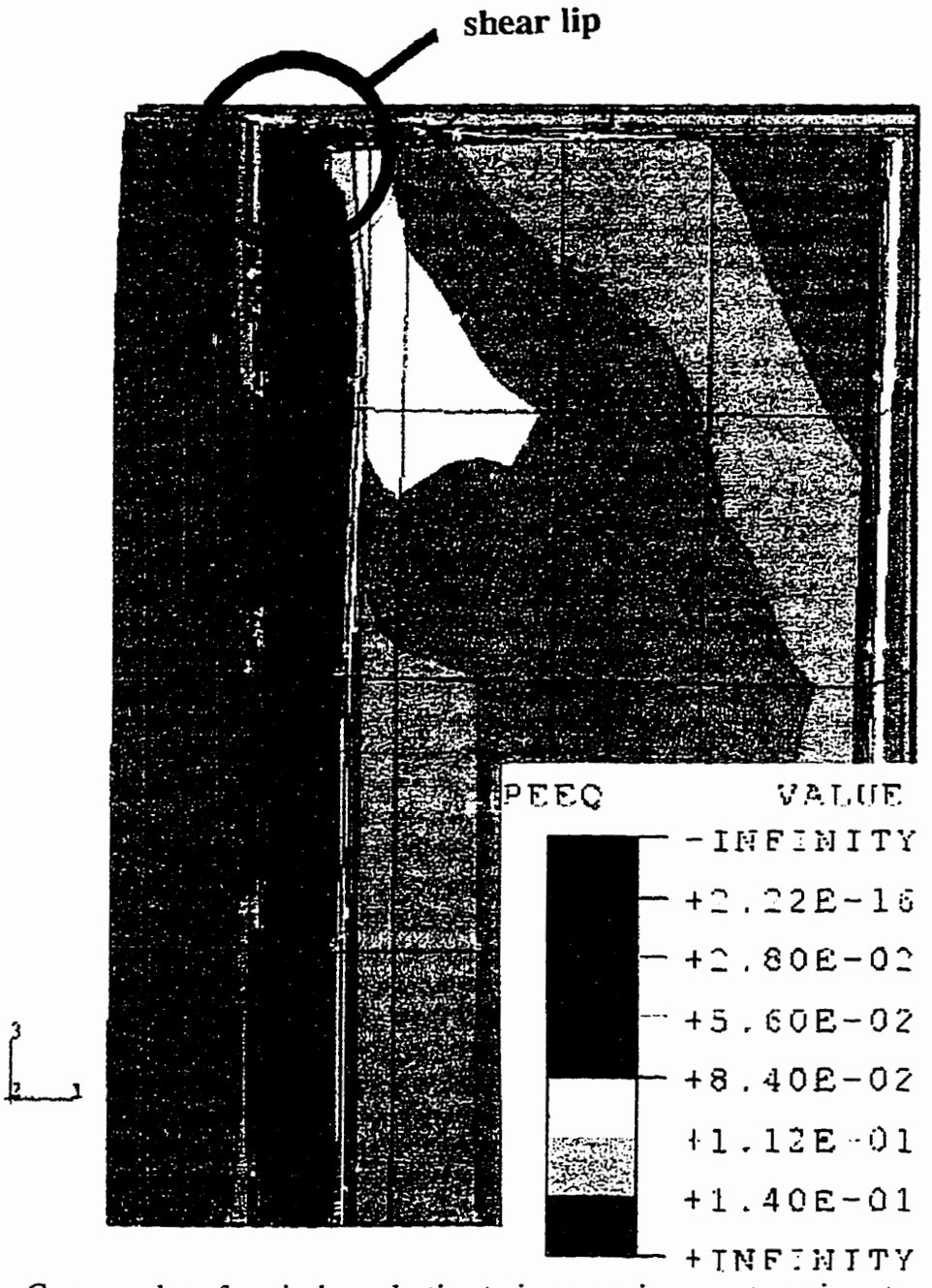

Figure 4.32 Contour plot of equivalent plastic strain at maximum net-section stress for a/t = 0.2 (thickness = 8.4 mm, width = 25 mm).

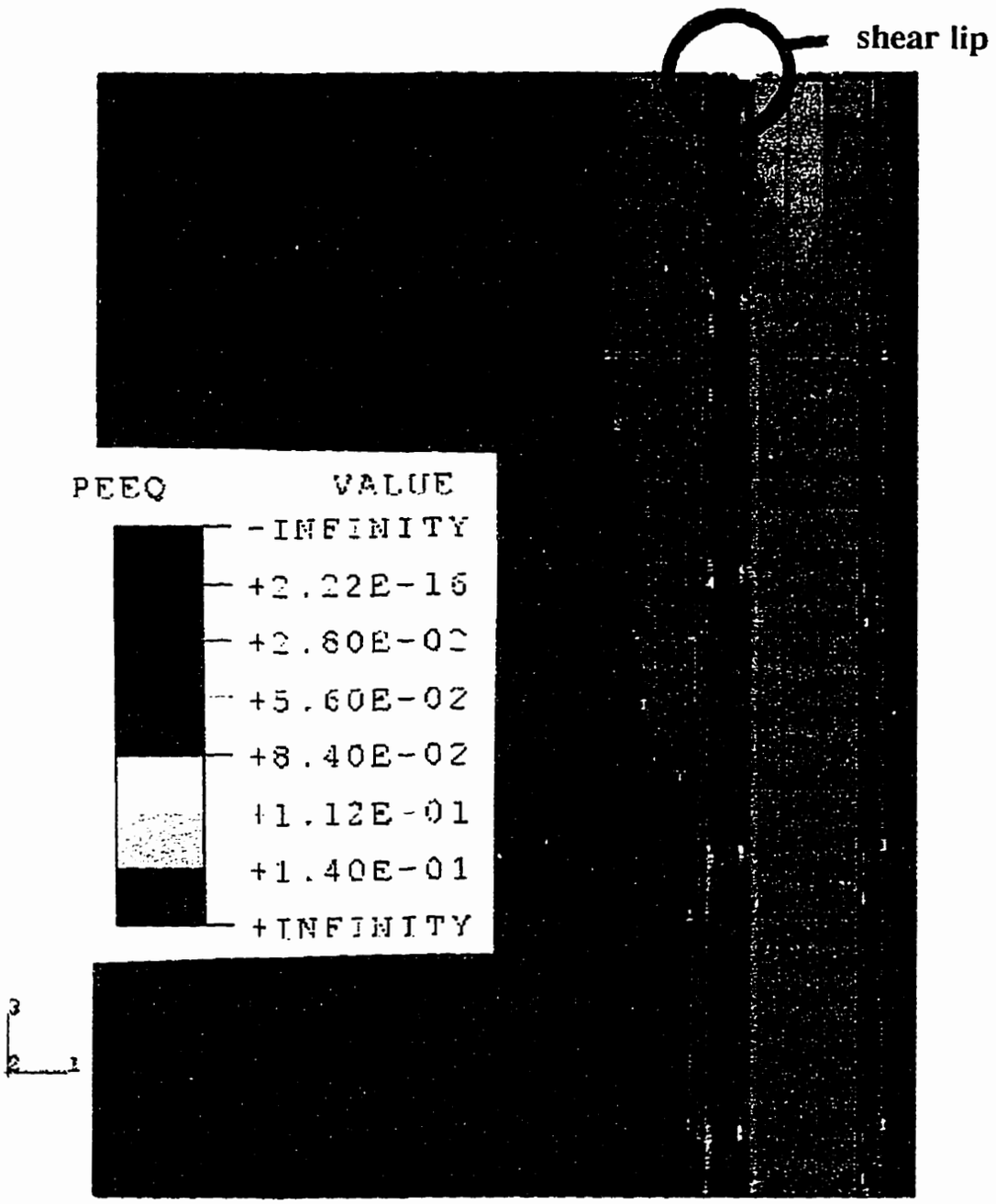

Figure 4.33 Contour plot of equivalent plastic strain at maximum net-section stress for a/t = 0.8 (thickness = 8.4 mm, width = 25 mm).

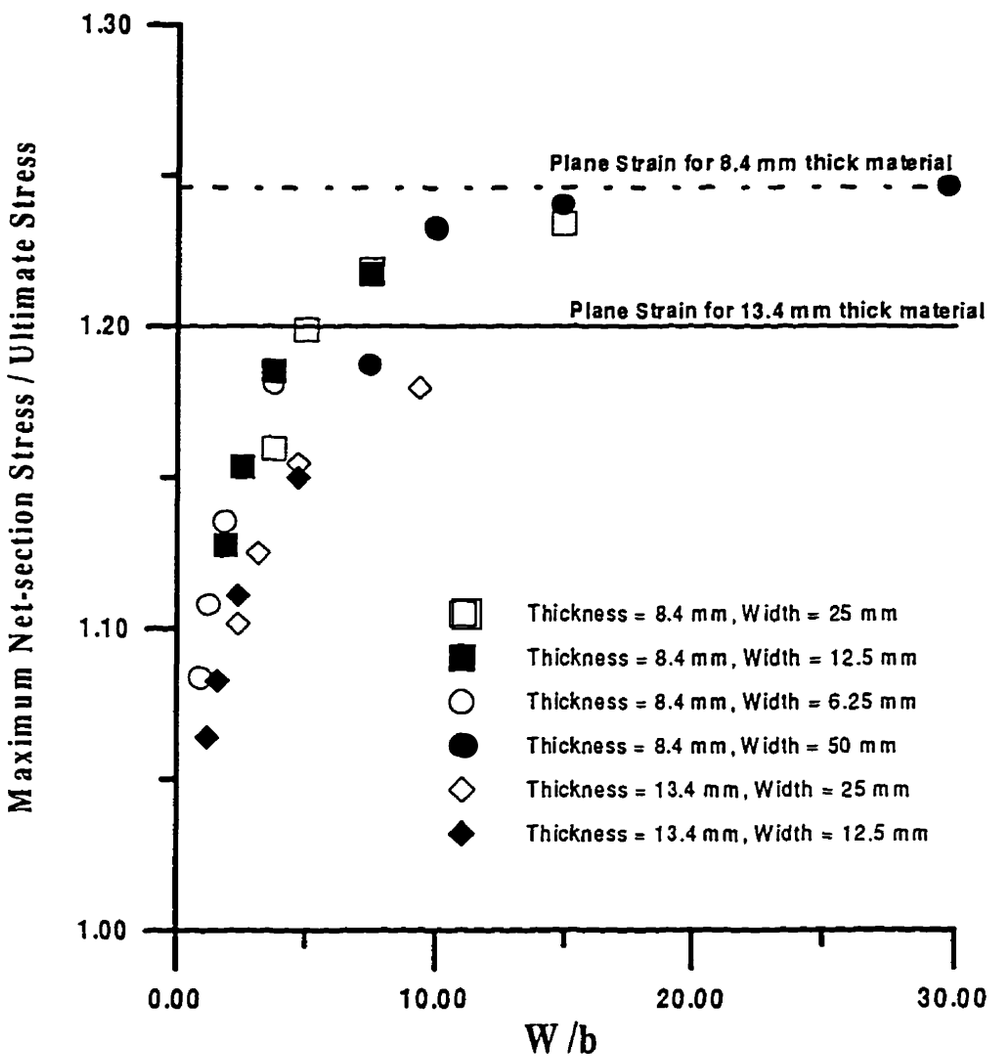

Figure 4.34 Three-dimensional finite element analyses for various widths.

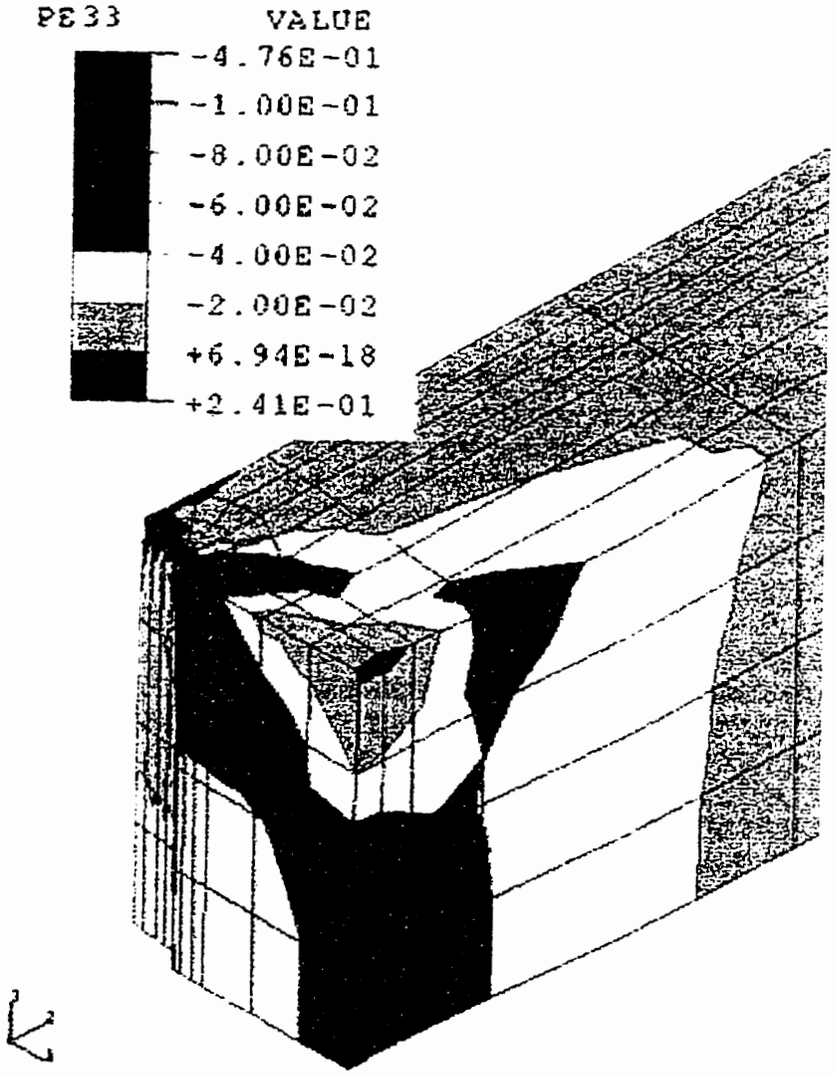

Figure 4.35 Contour plot of plastic strain in the width direction, $a/t = 0.2$.

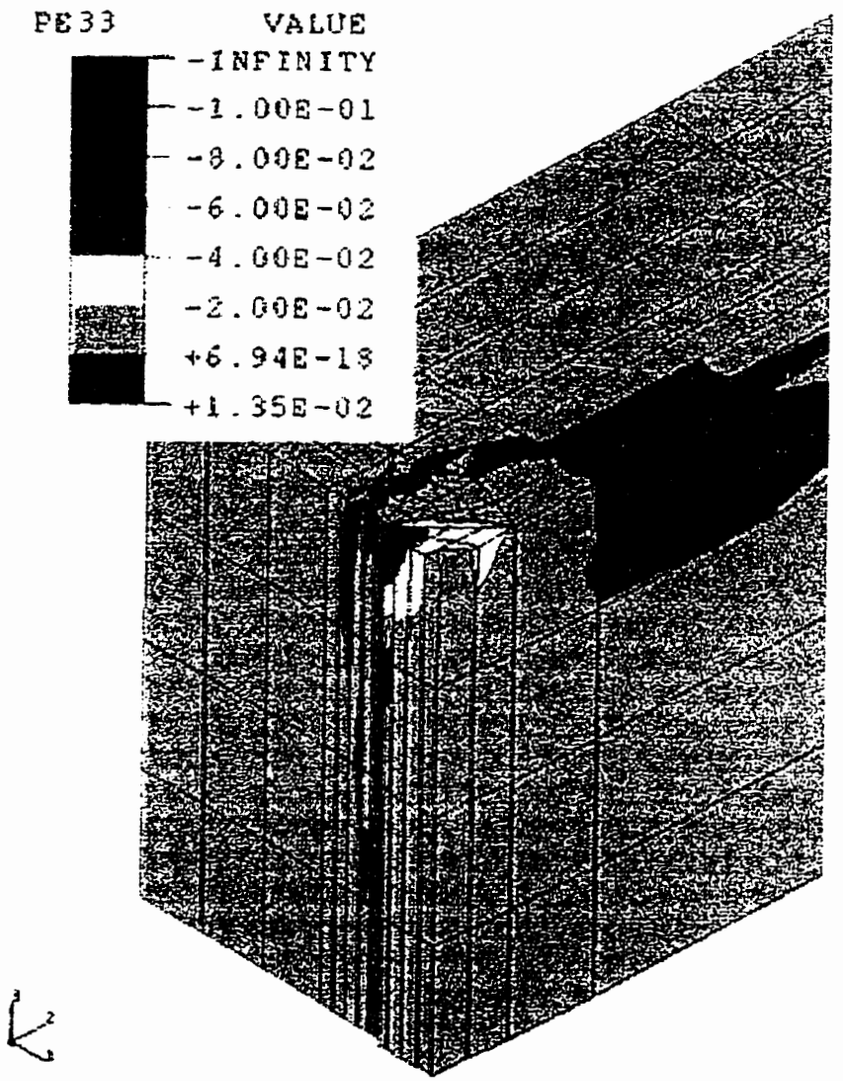

Figure 4.36 Contour plot of plastic strain in the width direction, $a/t = 0.8$.

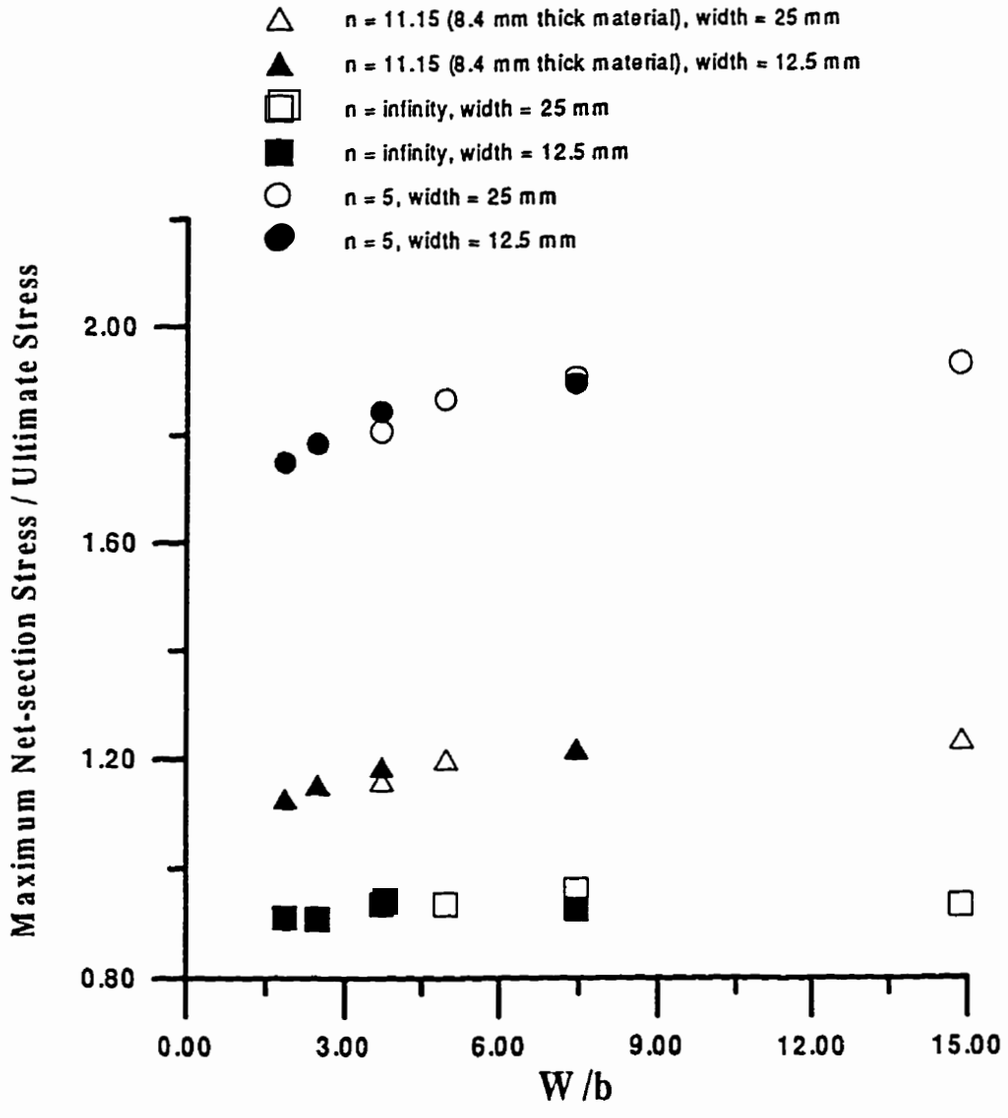

Figure 4.37 Three-dimensional finite element analyses for different hardening materials.

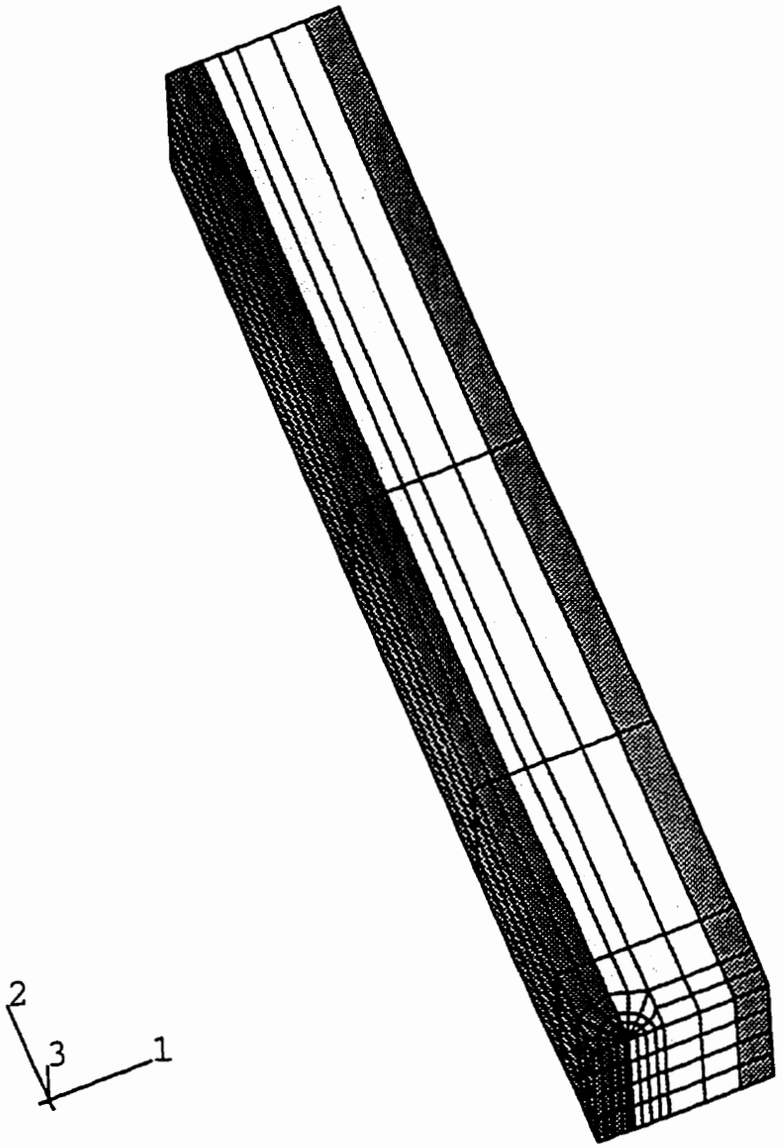

Figure 4.38 Three-dimensional finite element mesh used for microstructure based SENT analysis (a/t = 0.2, 8.4 mm thickness specimen).

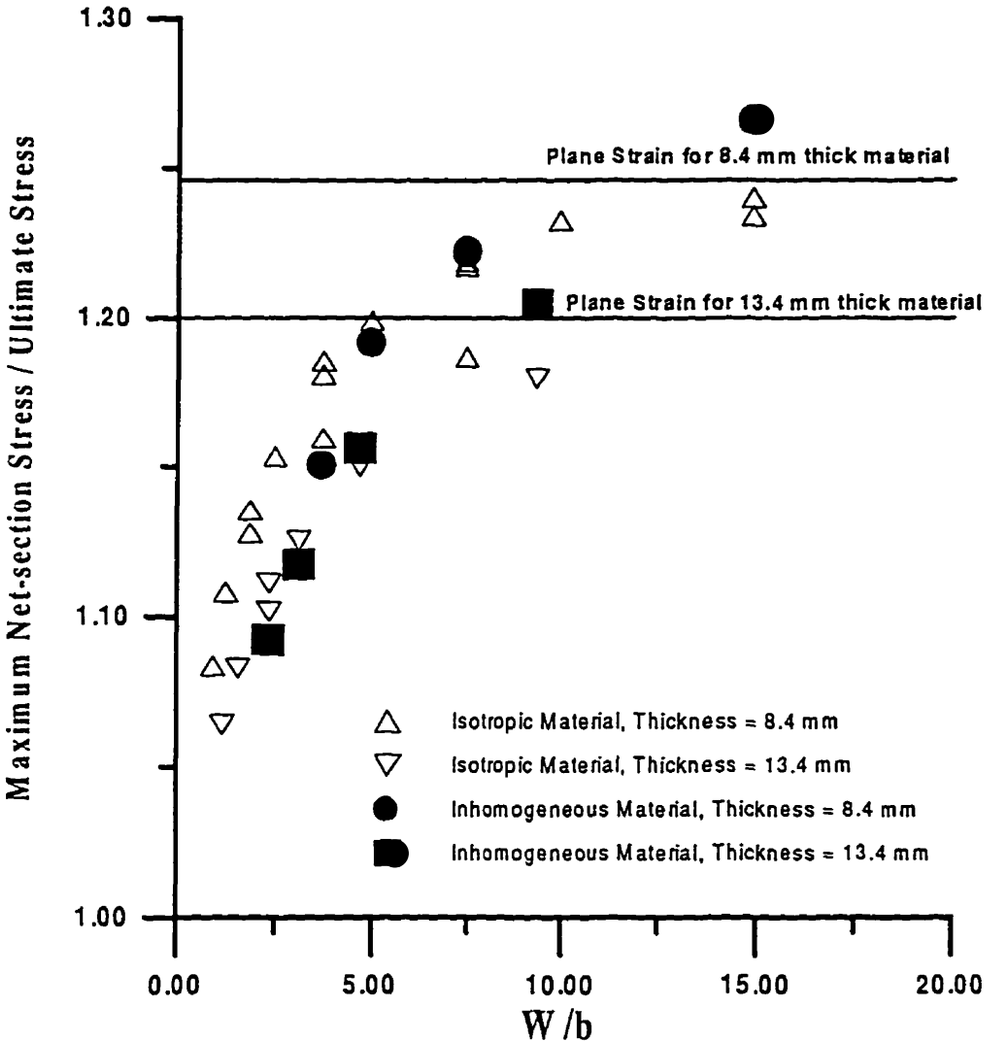

Figure 4.39 Finite element analyses with different material strength in the thickness direction.

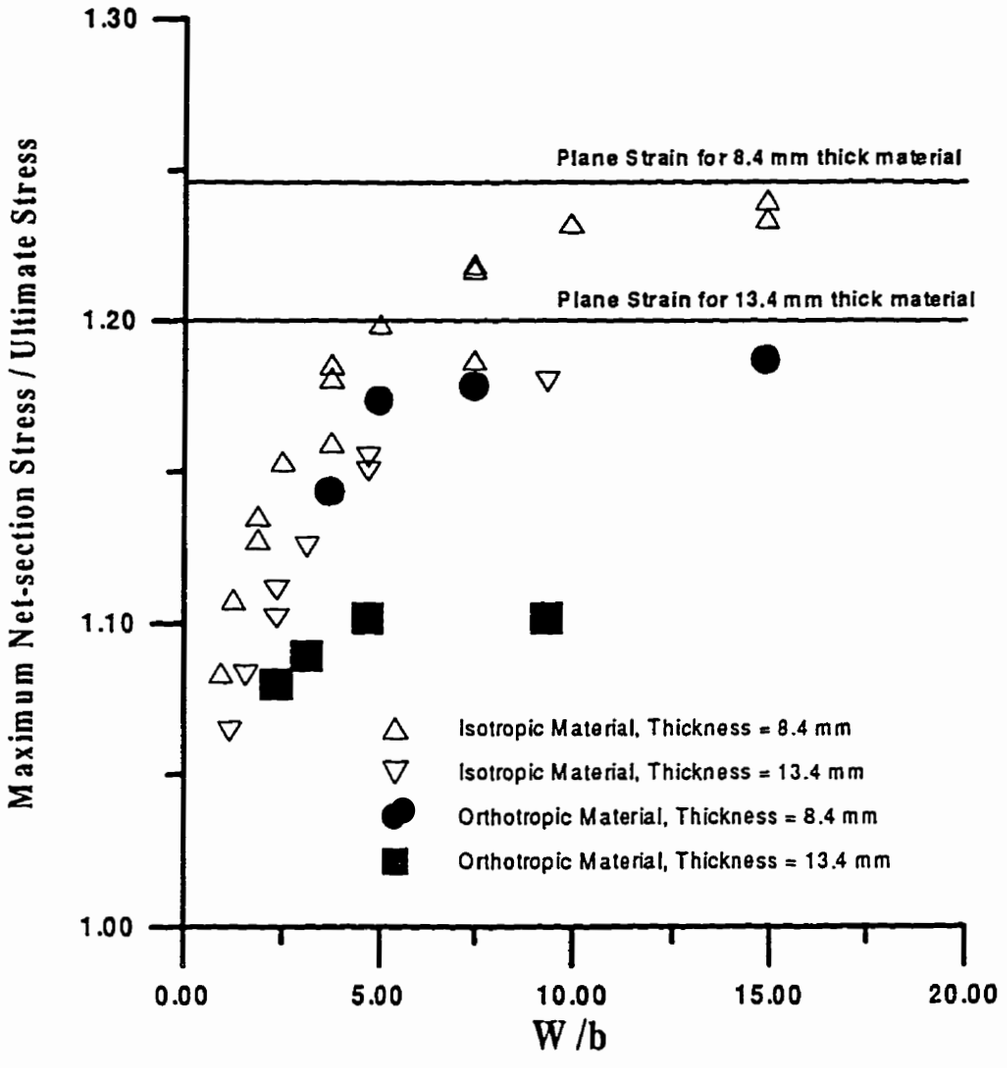

Figure 4.40 Finite element analyses with orthotropic characteristics.

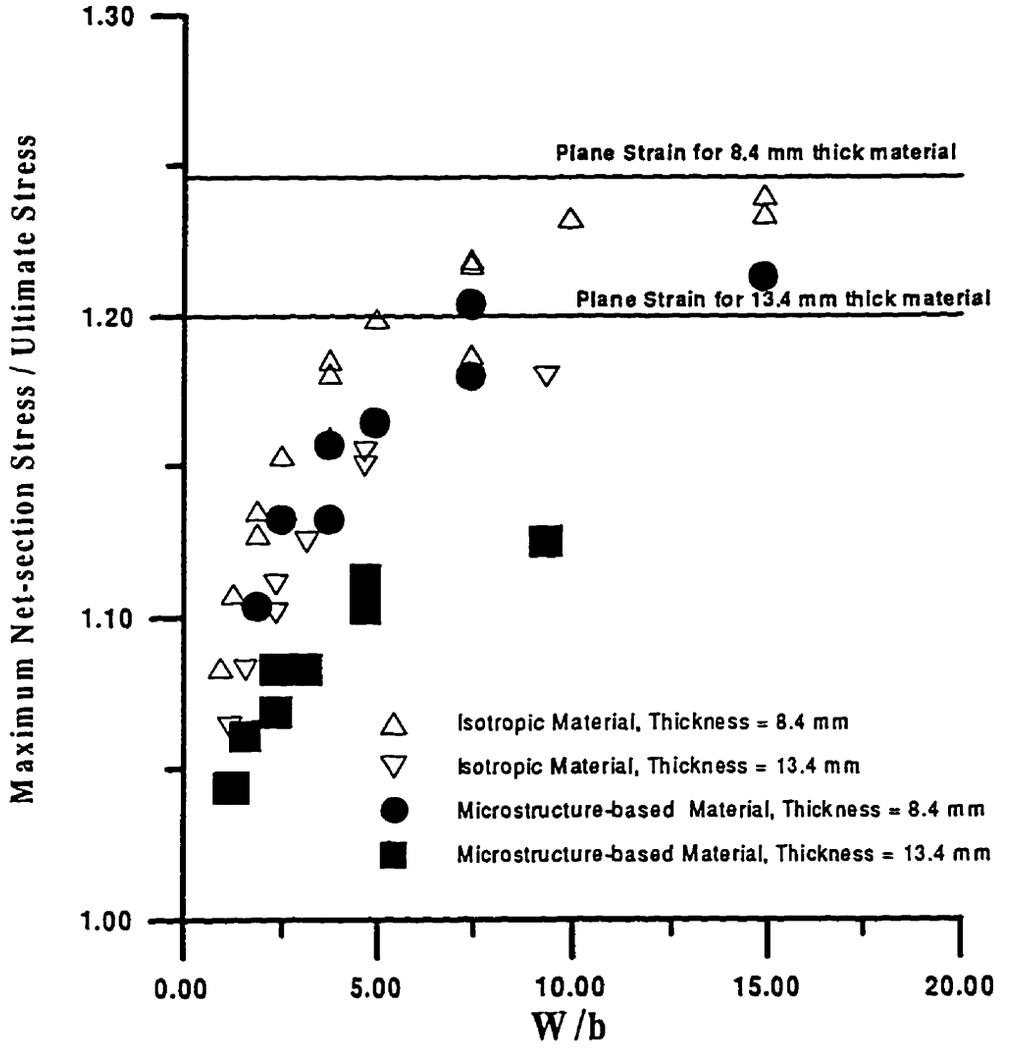

Figure 4.41 Finite element analyses based on microstructural characteristics.

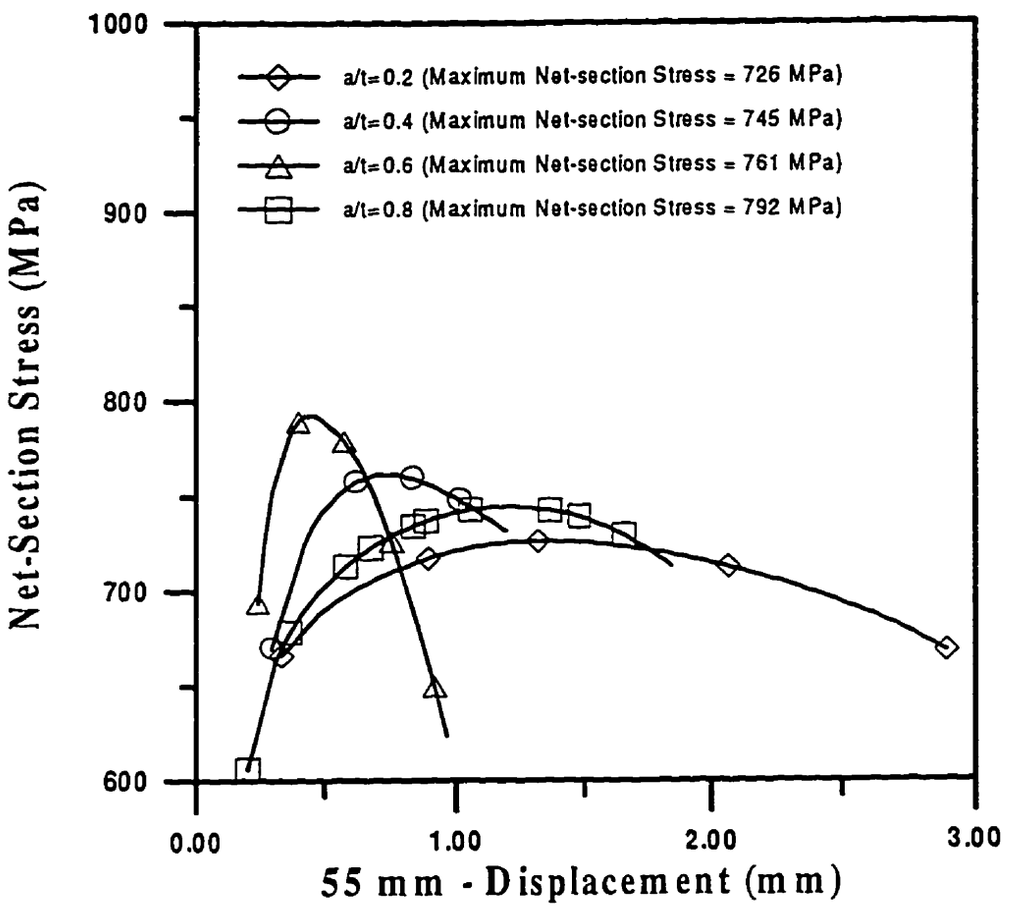

Figure 4.42 3-D microstructure based finite element analysis results for various crack geometries (8.4 mm thickness specimens).

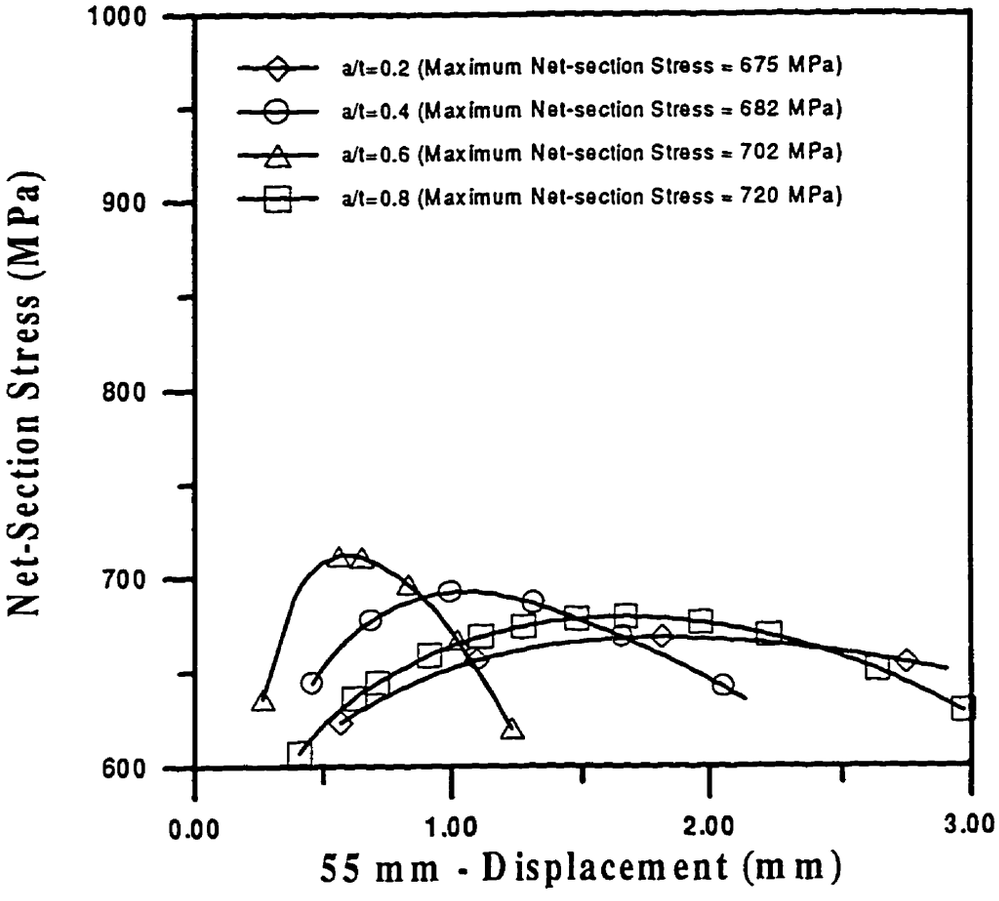

Figure 4.43 3-D microstructure based finite element analysis results for various crack geometries (13.4 mm thickness specimens).

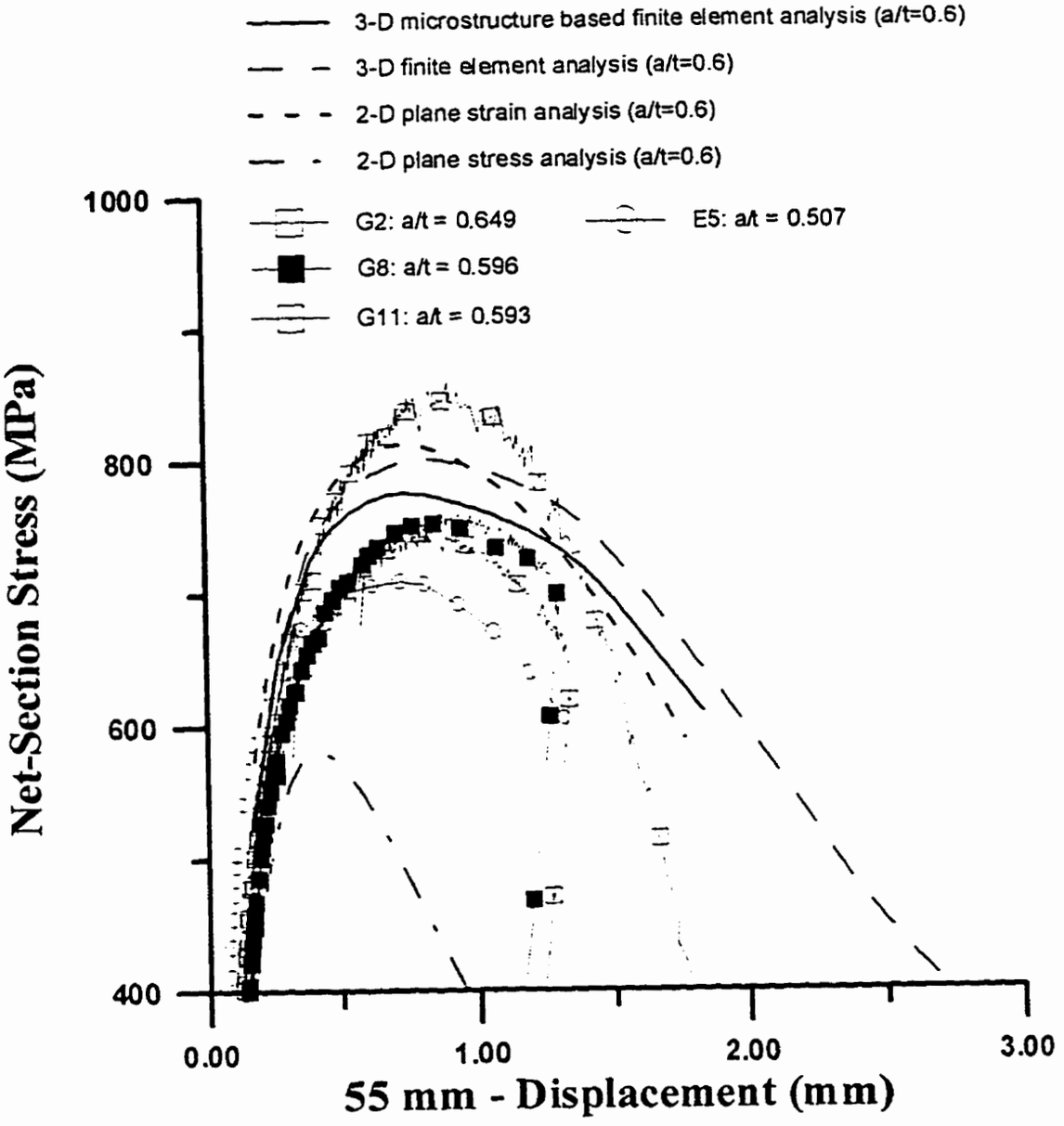

Figure 4.44 Comparison to test results for $a/t = 0.6$ (8.4 mm thickness specimen).

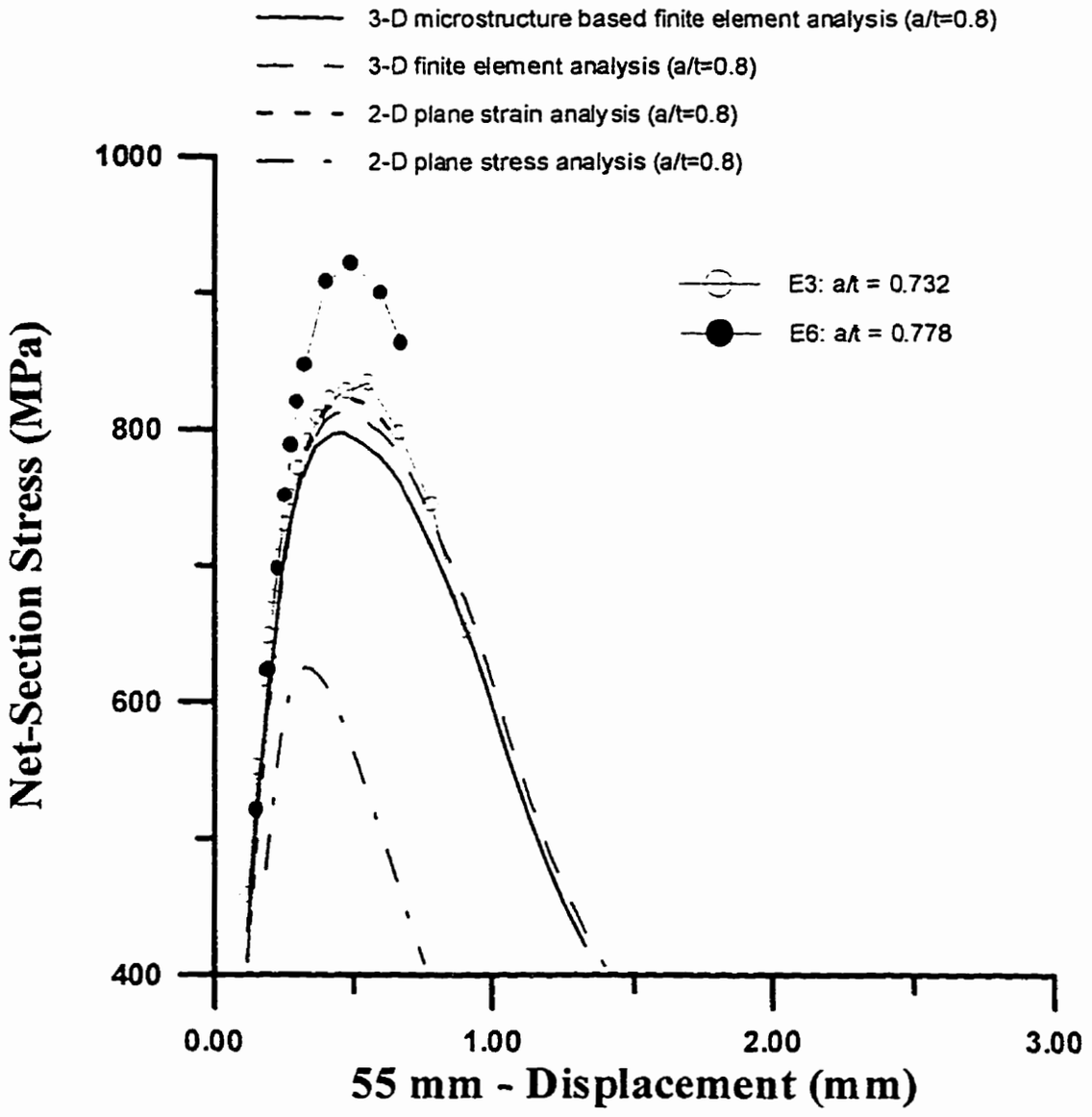

Figure 4.45 Comparison to test results for $a/t = 0.8$ (8.4 mm thickness specimen).

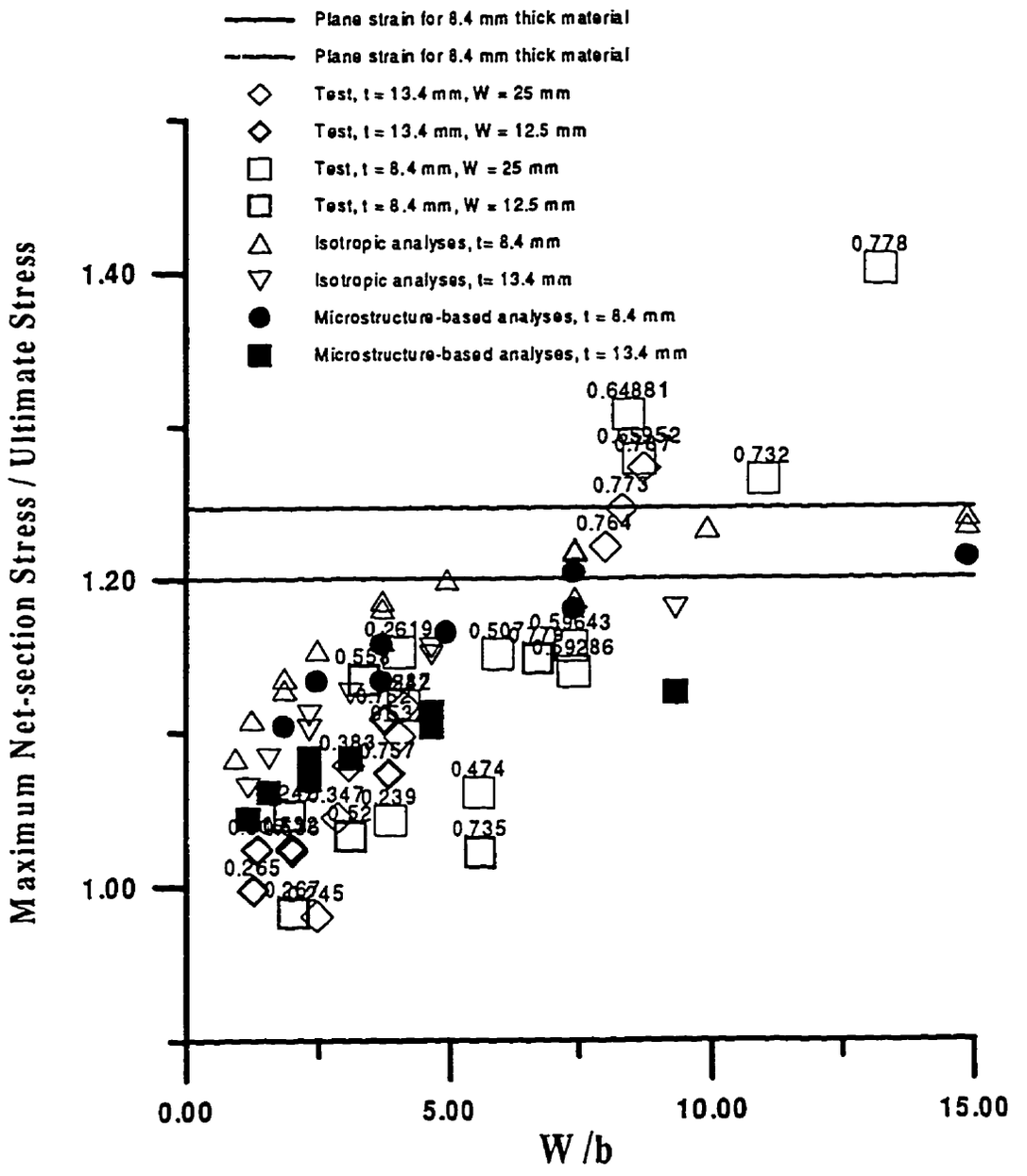

Figure 4.46 Summary of 3-D finite element analyses.

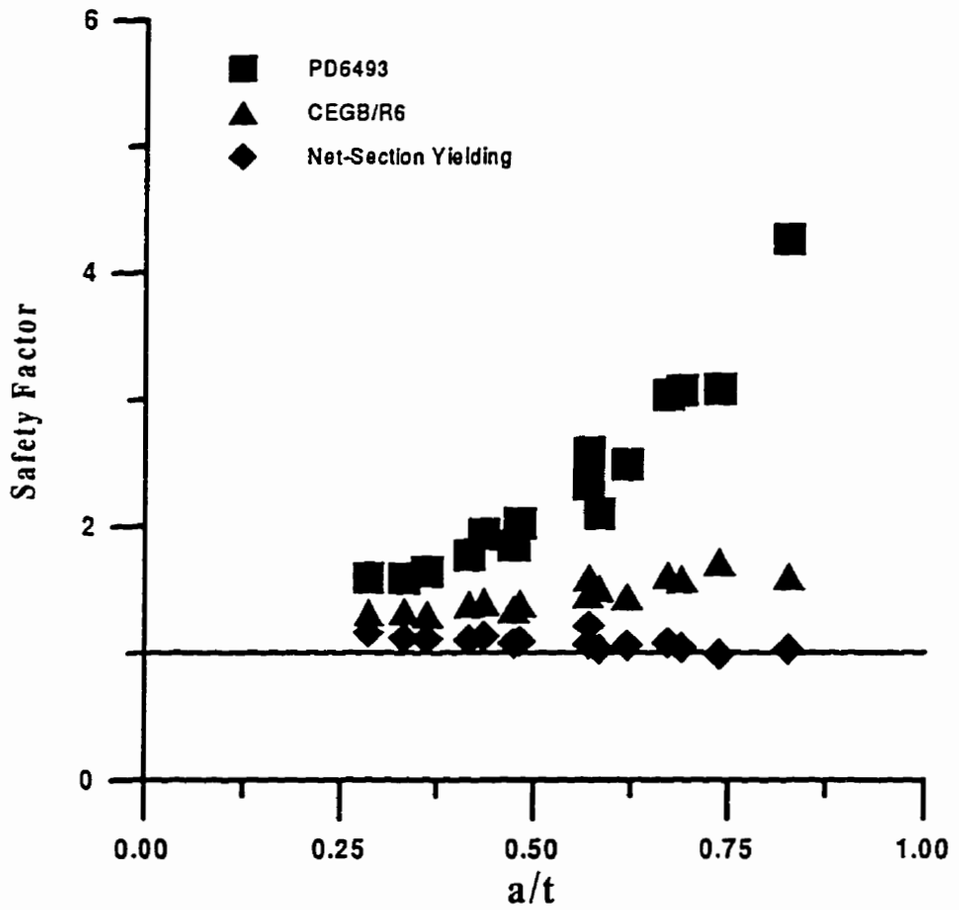

Figure 5.1 Plastic collapse solutions versus *a/t* for wide plates.

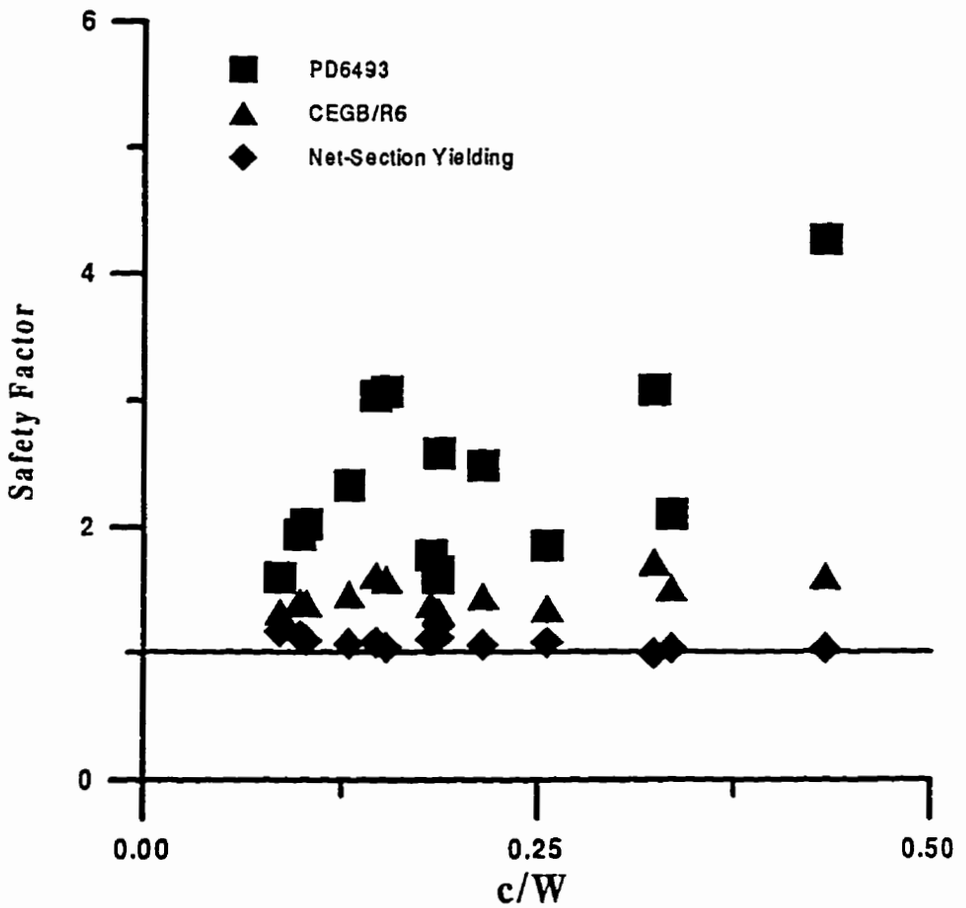

Figure 5.2 Plastic collapse solutions versus *c/W* for wide plates.

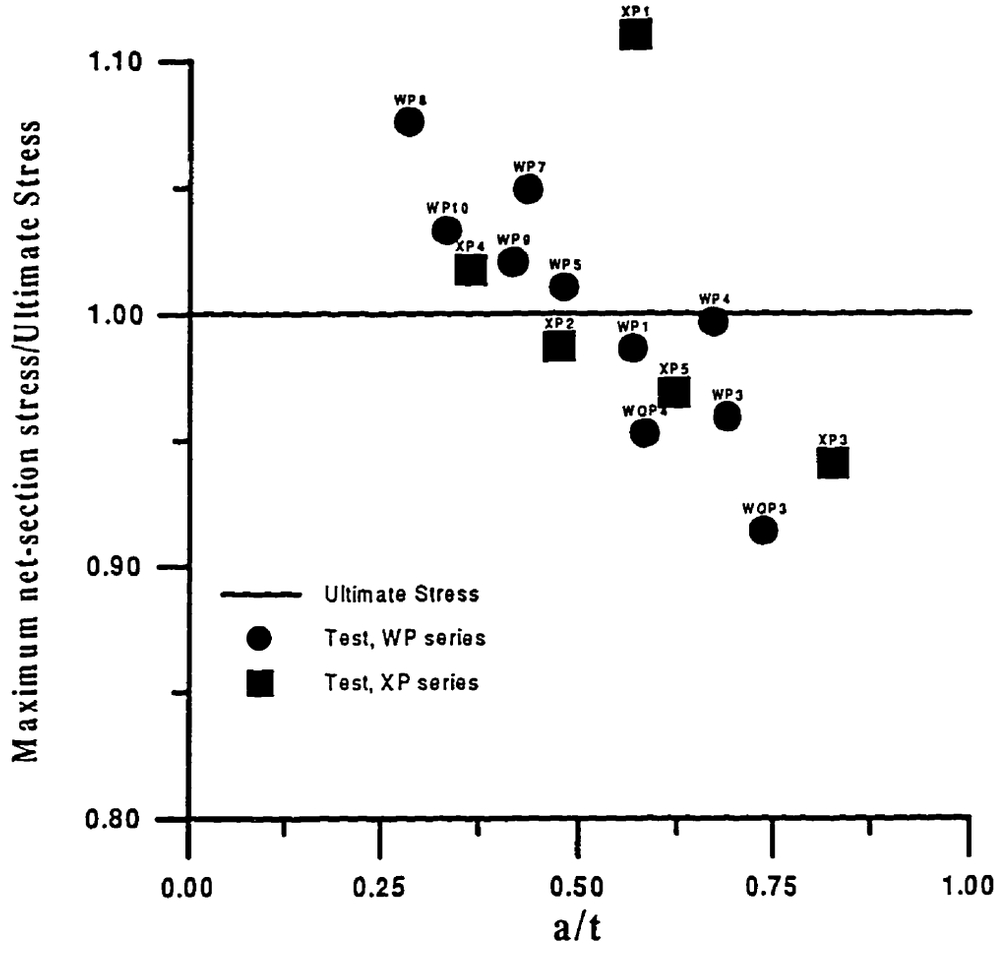

Figure 5.3 Maximum net-section stress versus *a/t*.

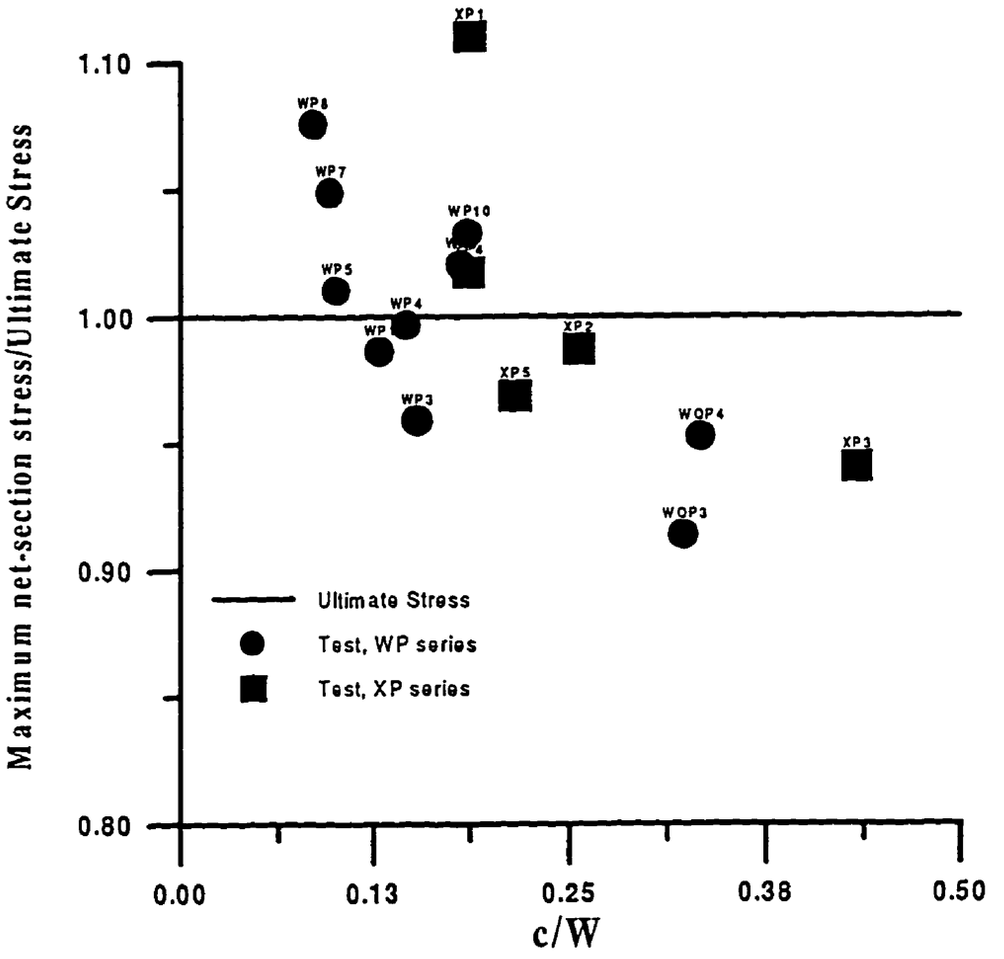

Figure 5.4 Maximum net-section stress versus *c/W*.

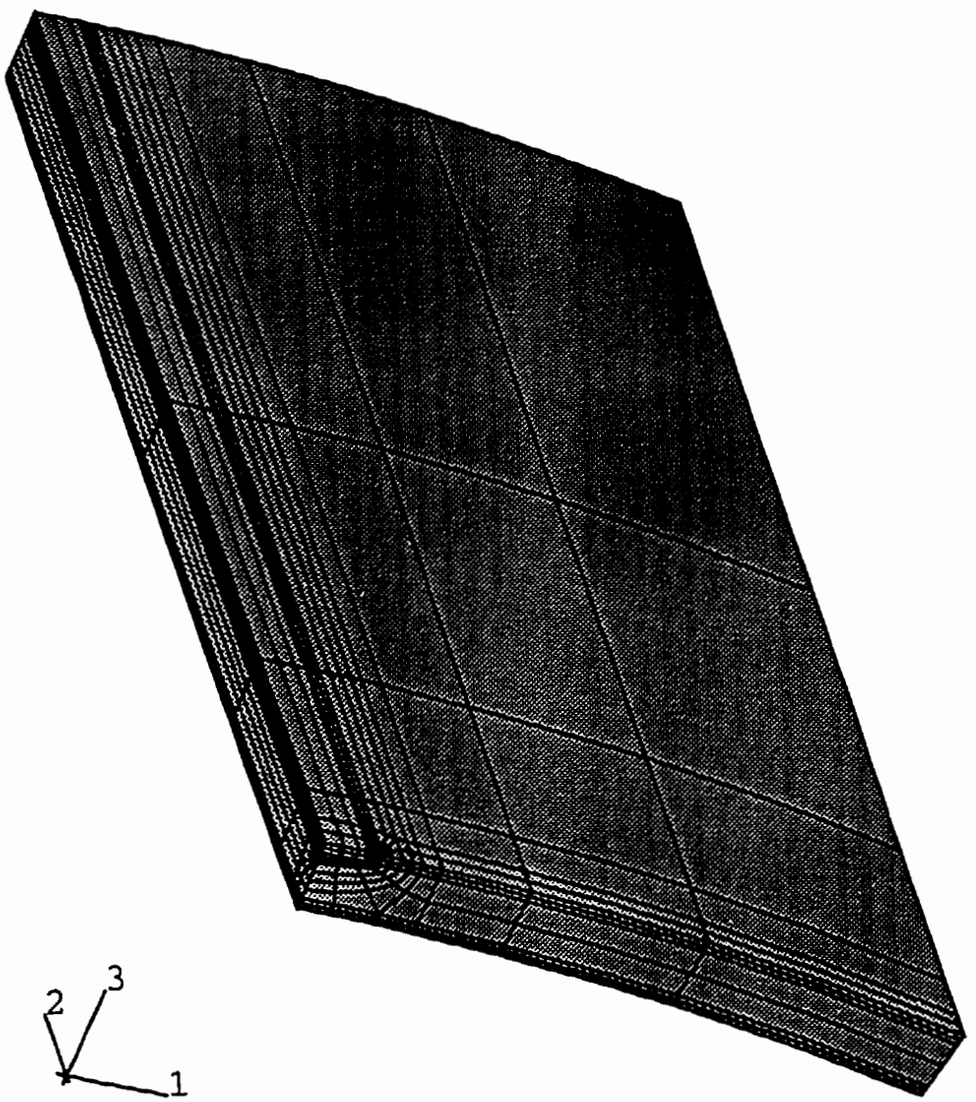

Figure 5.5 FEM mesh for a wide plate specimen (WP7).

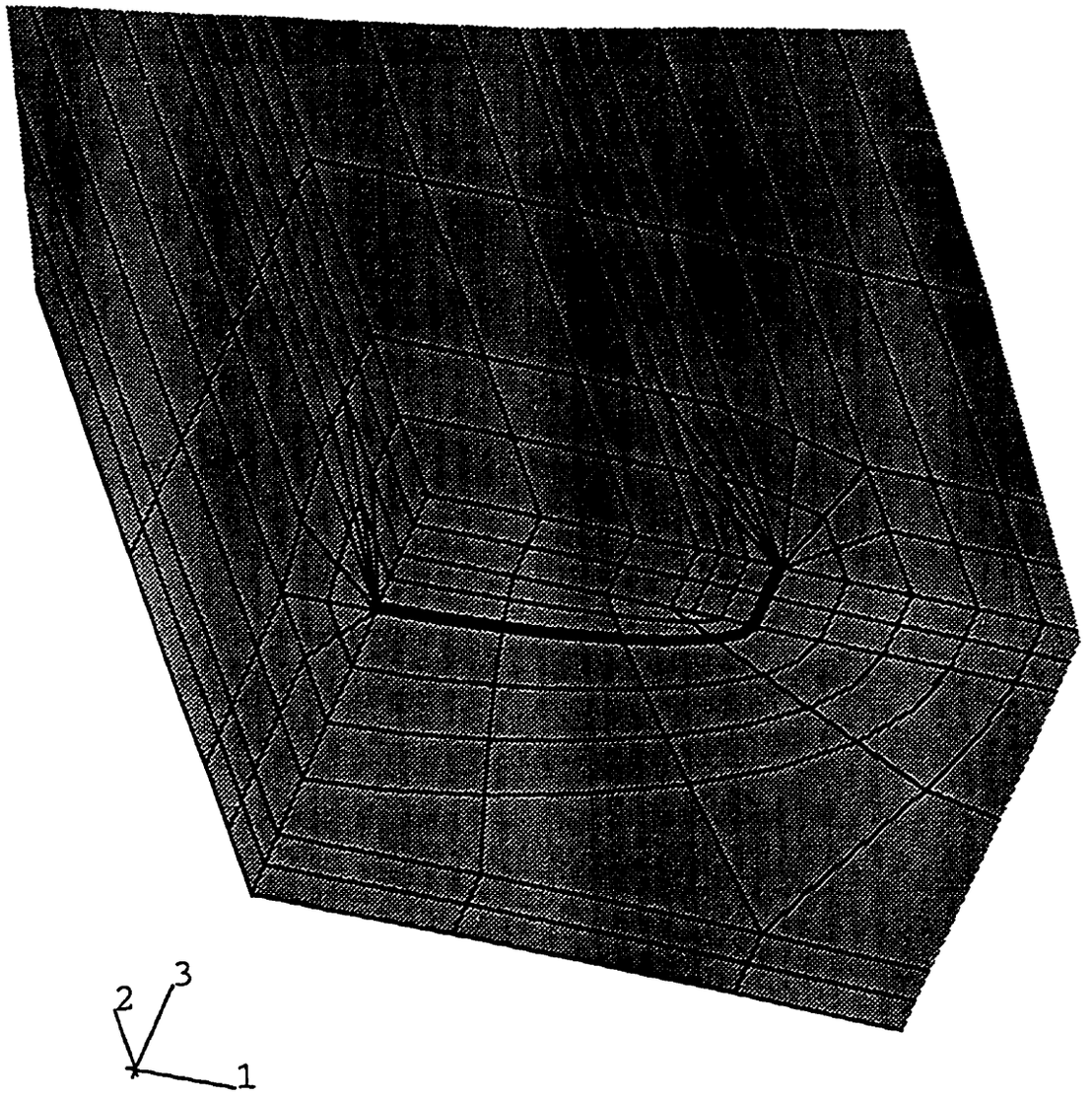

Figure 5.6 Enlarged crack-tip area (WP7).

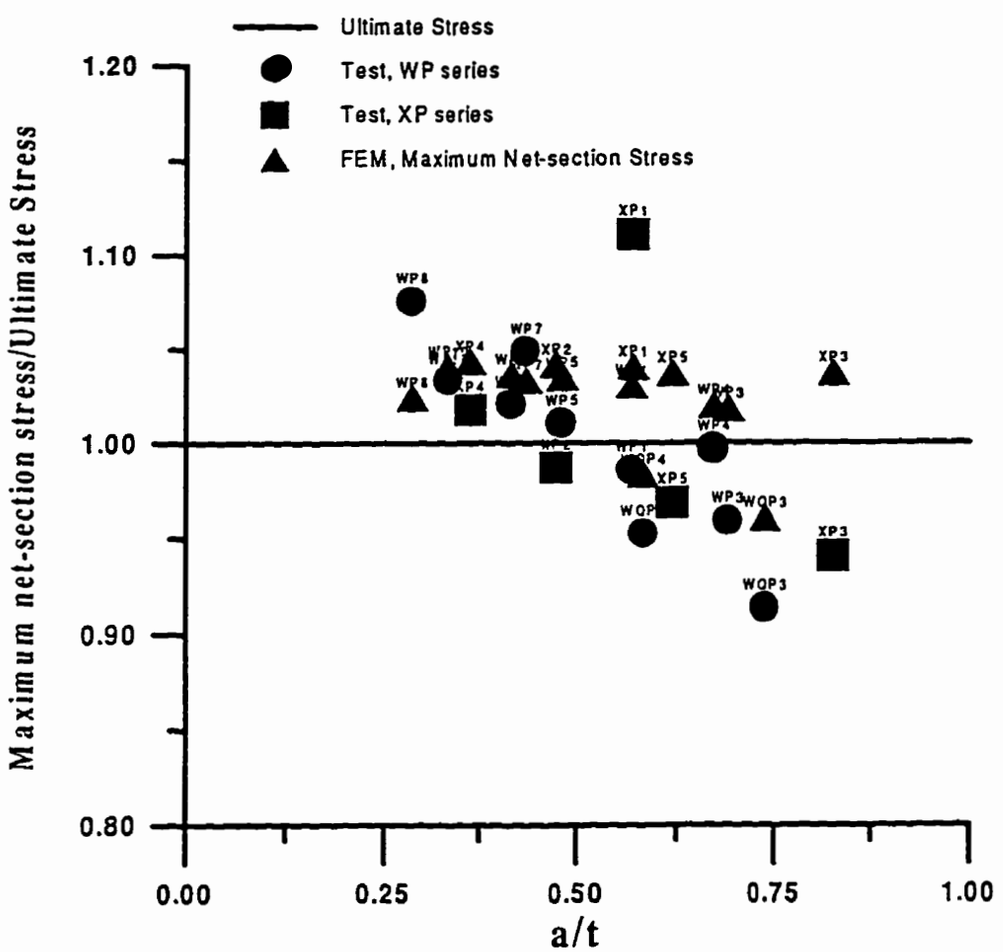

Figure 5.7 The resulting maximum net-section stresses from finite element analyses versus *a/t*.

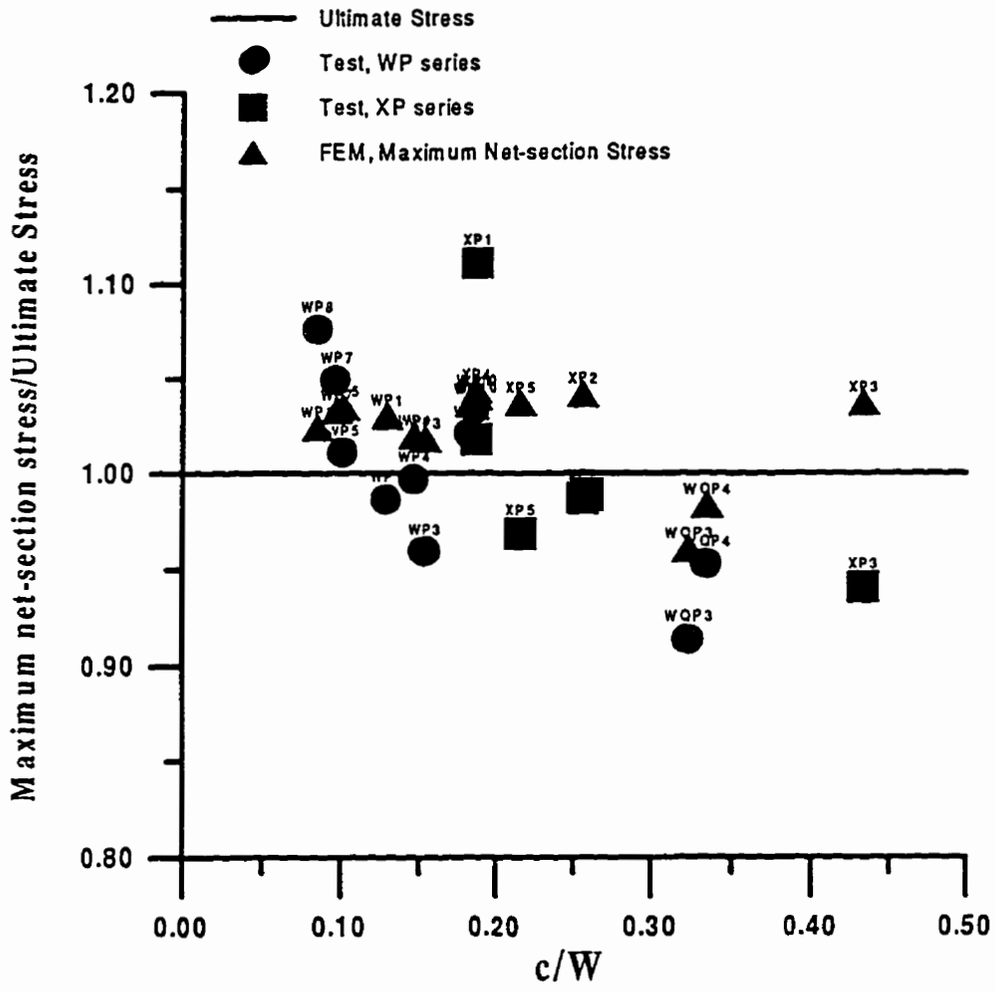

Figure 5.8 The resulting maximum net-section stresses from finite element analyses versus *c/W*.

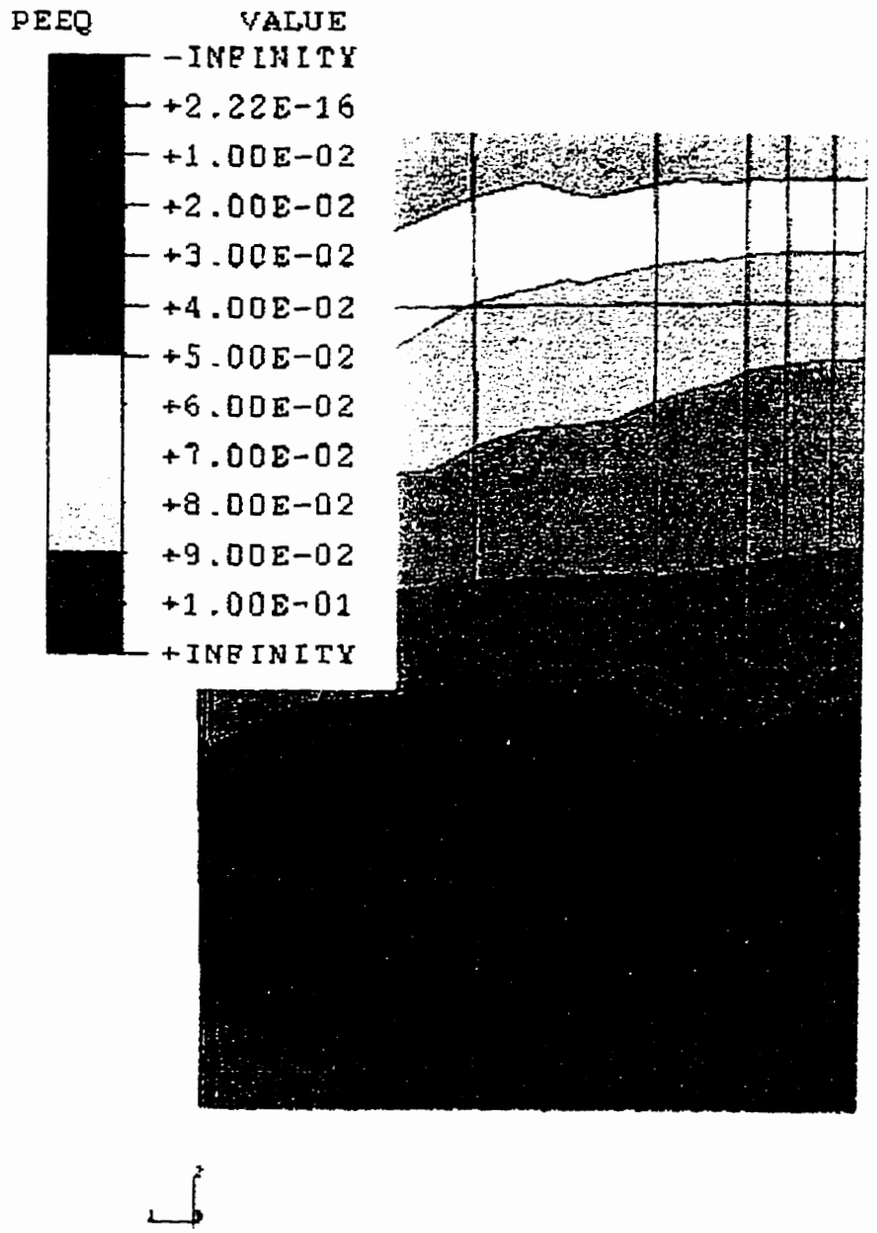

Figure 5.9 Contour plot of equivalent plastic strain at the maximum net-section stress (WP8).

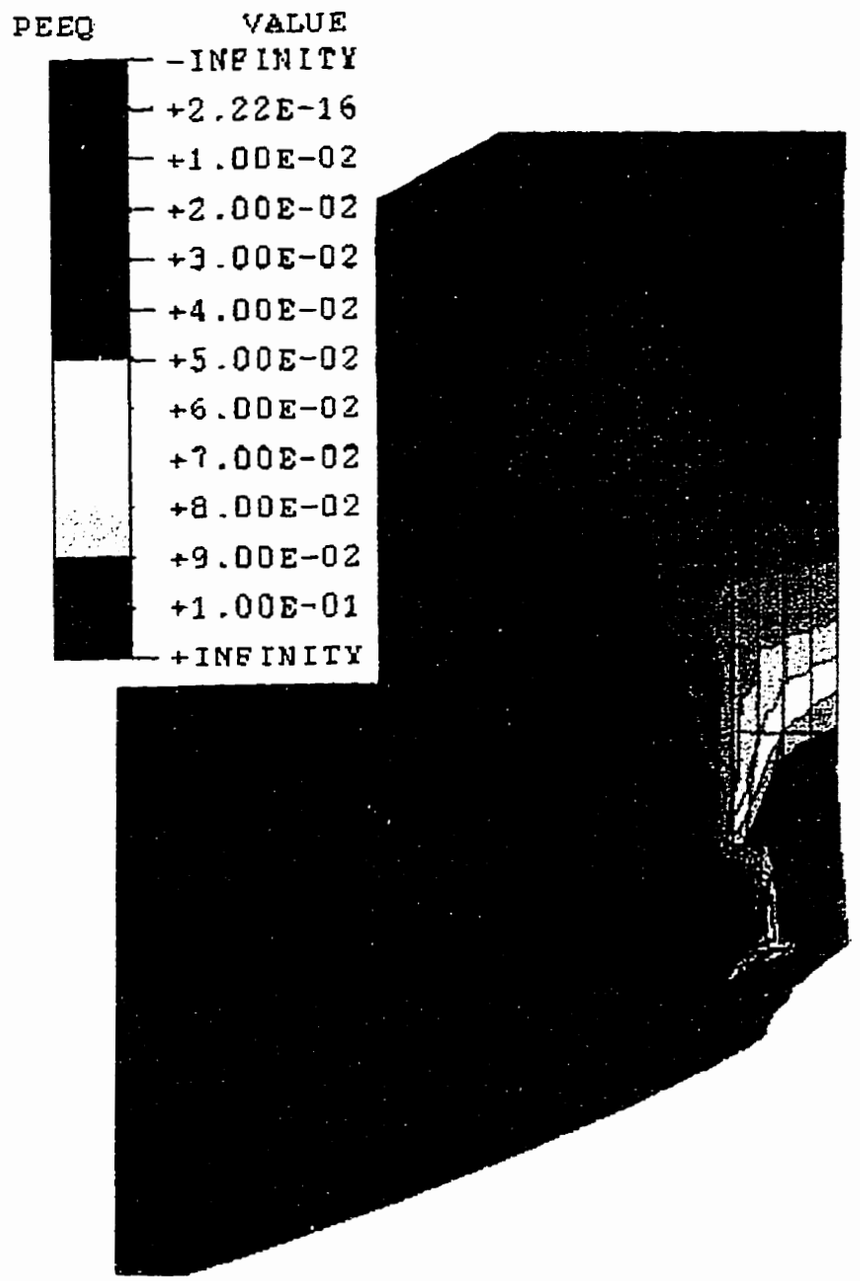

Figure 5.10 Contour plot of equivalent plastic strain at the maximum net-section stress (WP8).

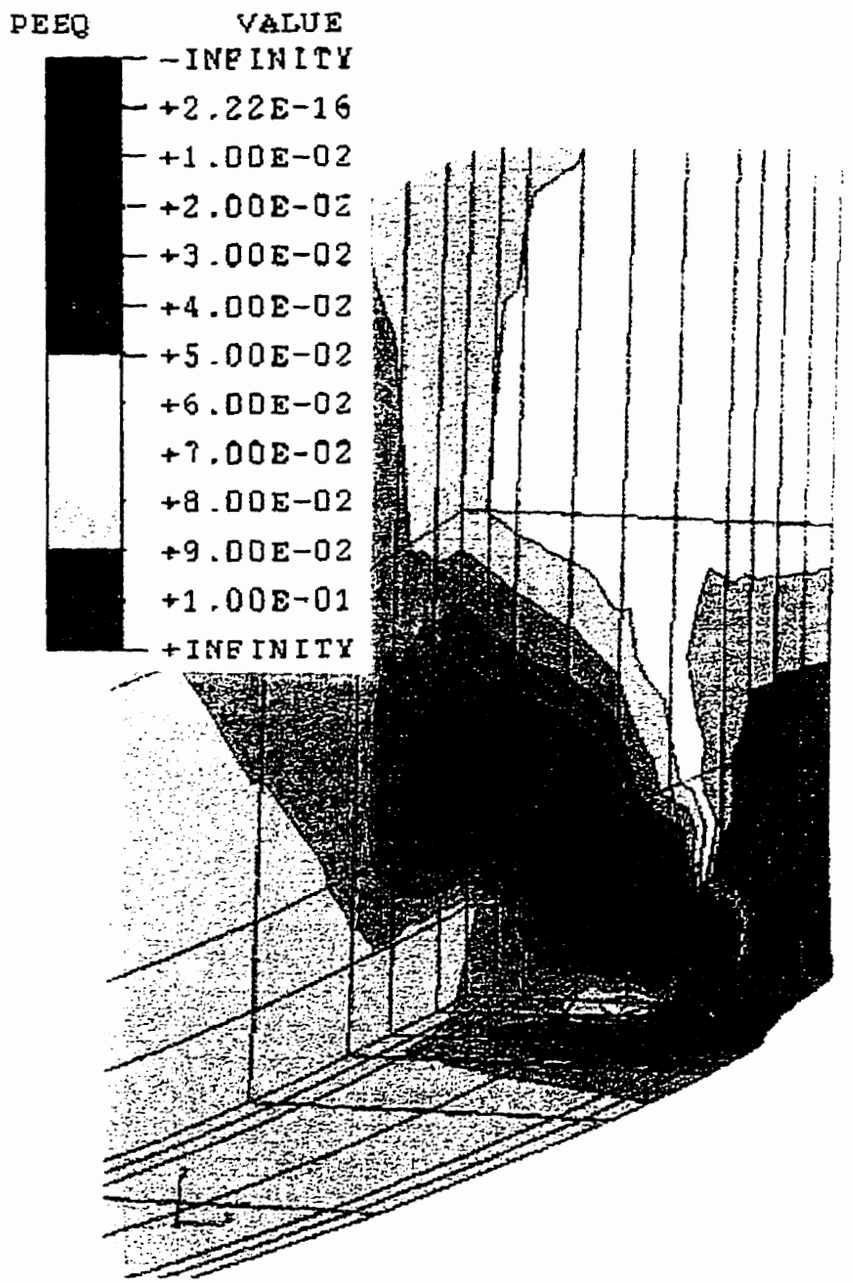

Figure 5.11 Contour plot of equivalent plastic strain at the ligament necking (WP8).

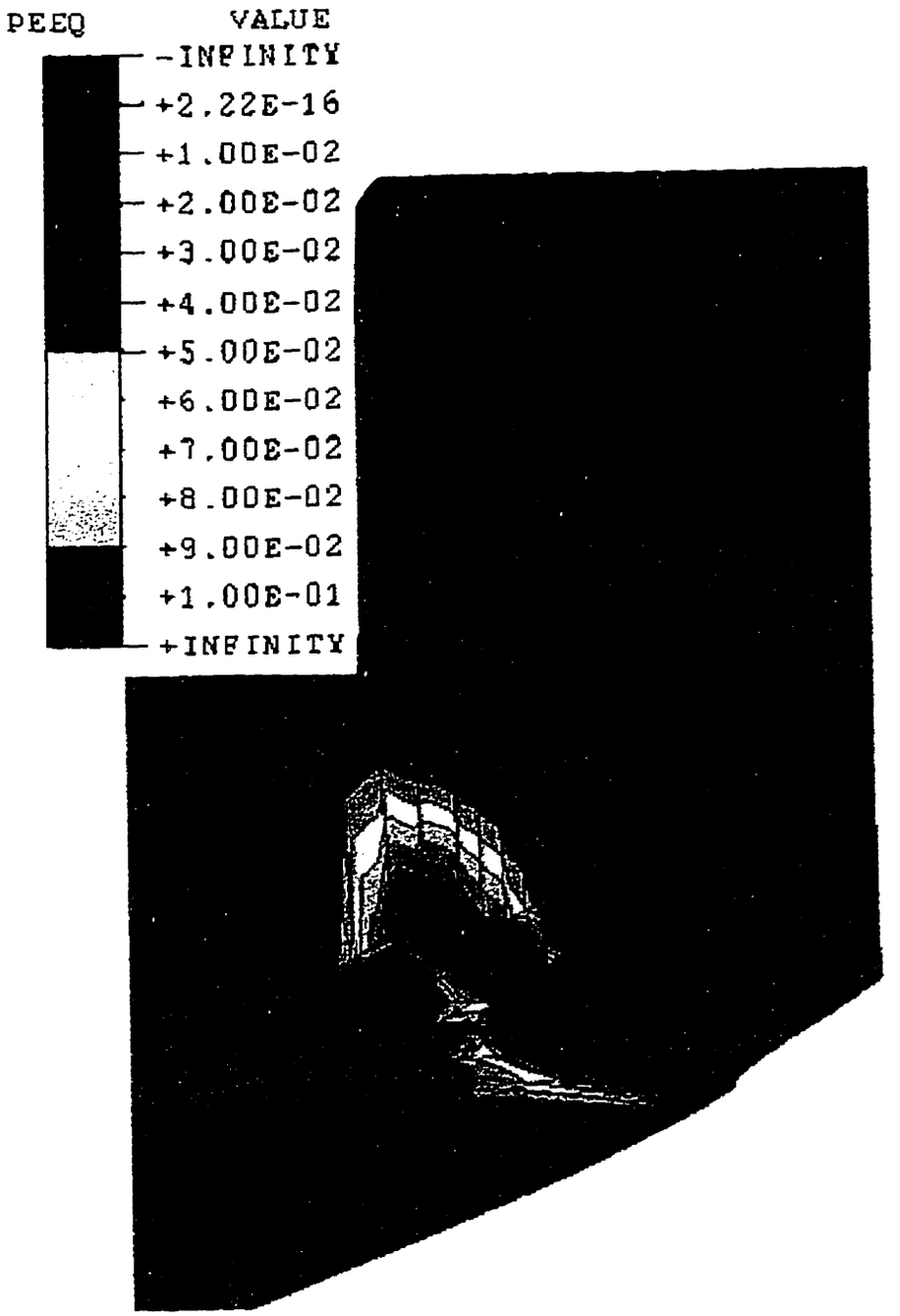

Figure 5.12 Contour plot of equivalent plastic strain at the ligament necking (WP4).

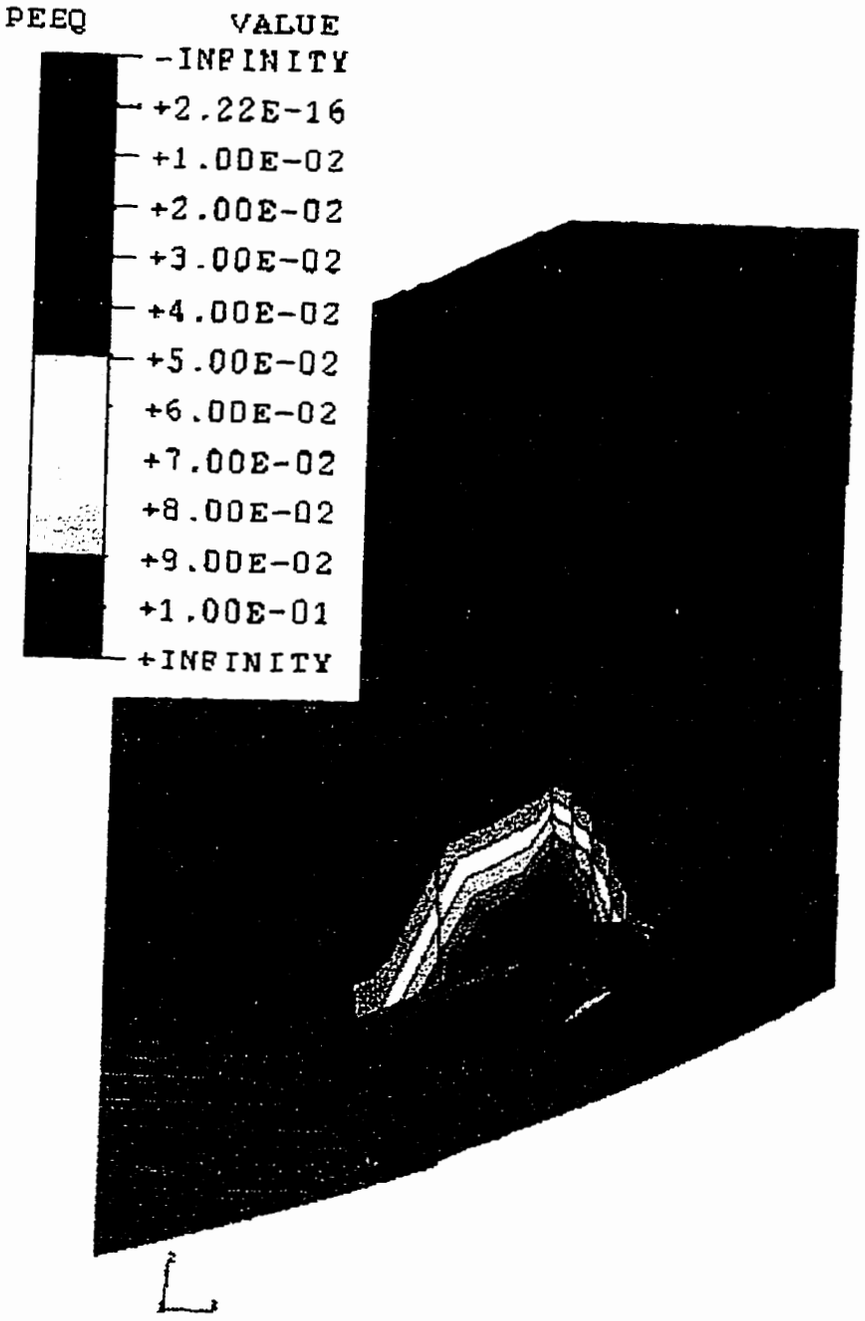

Figure 5.13 Contour plot of equivalent plastic strain at the ligament necking (WPQ4).

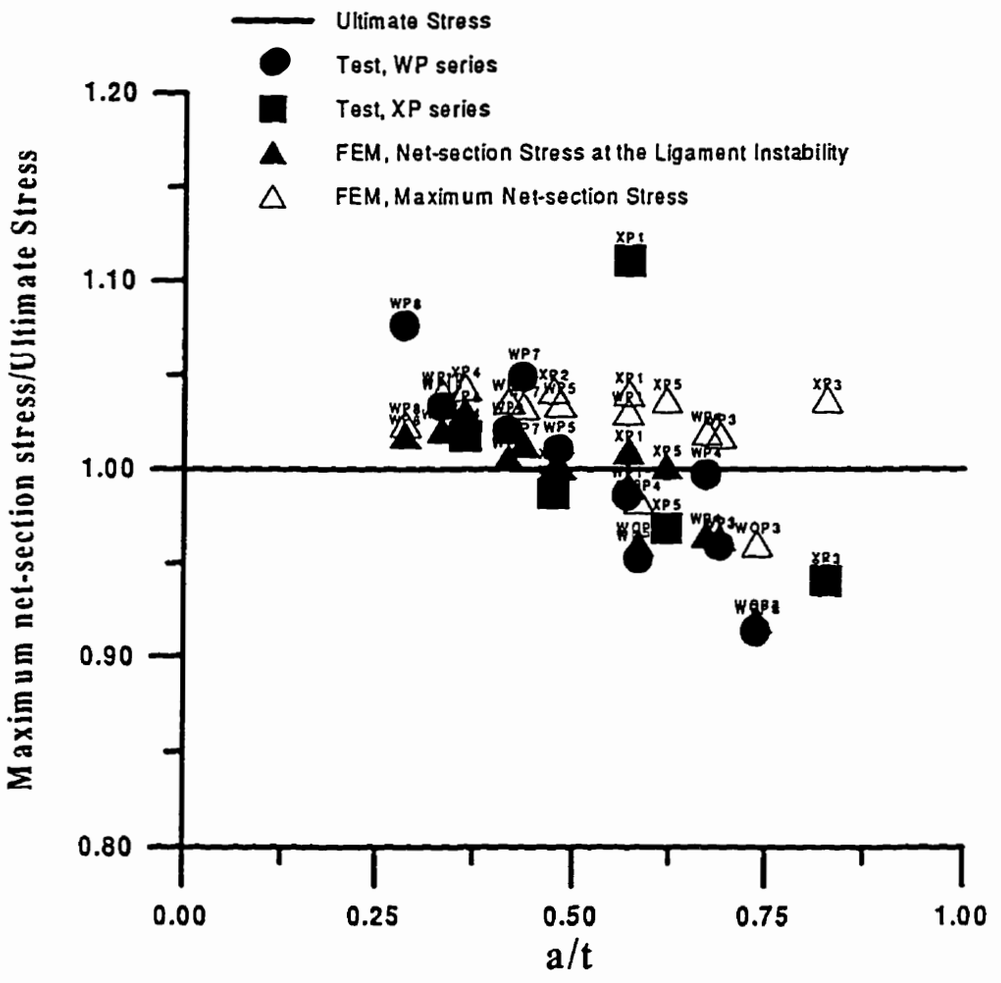

Figure 5.14 Ligament necking stresses versus *a/t*.

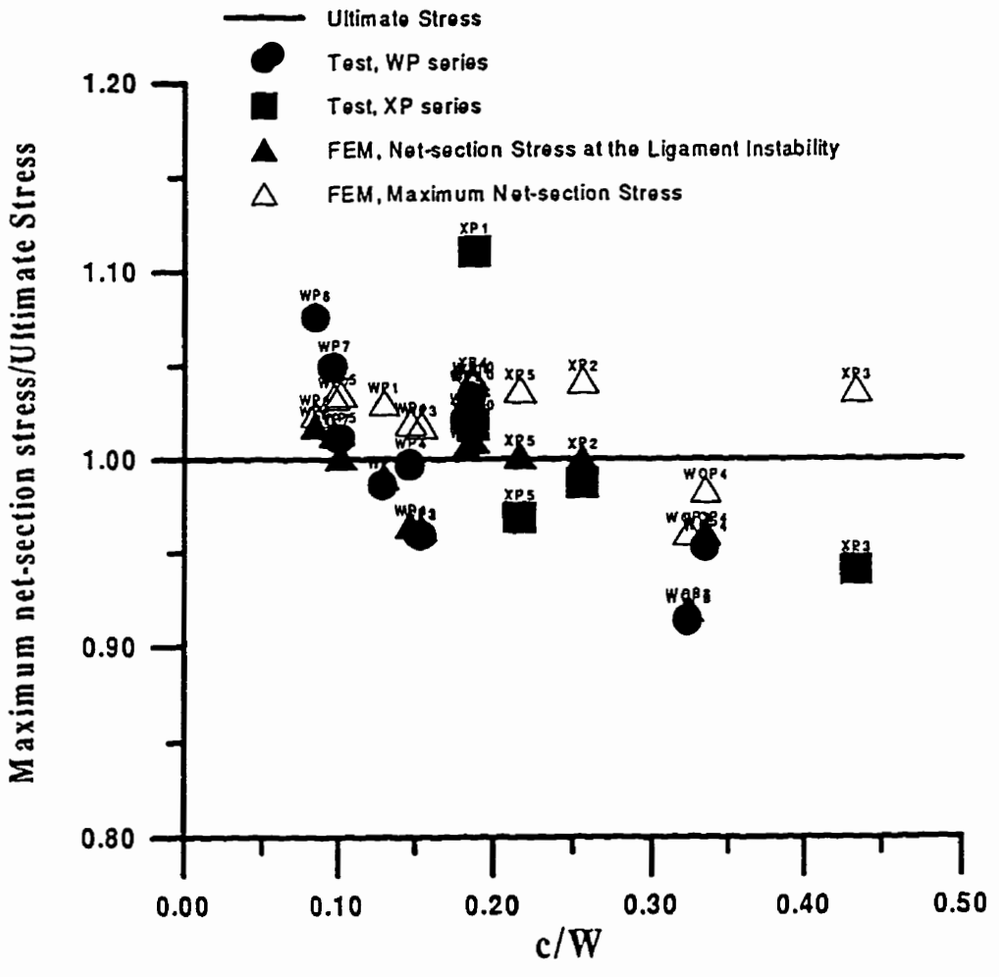

Figure 5.15 Ligament necking stresses versus *c/W*.

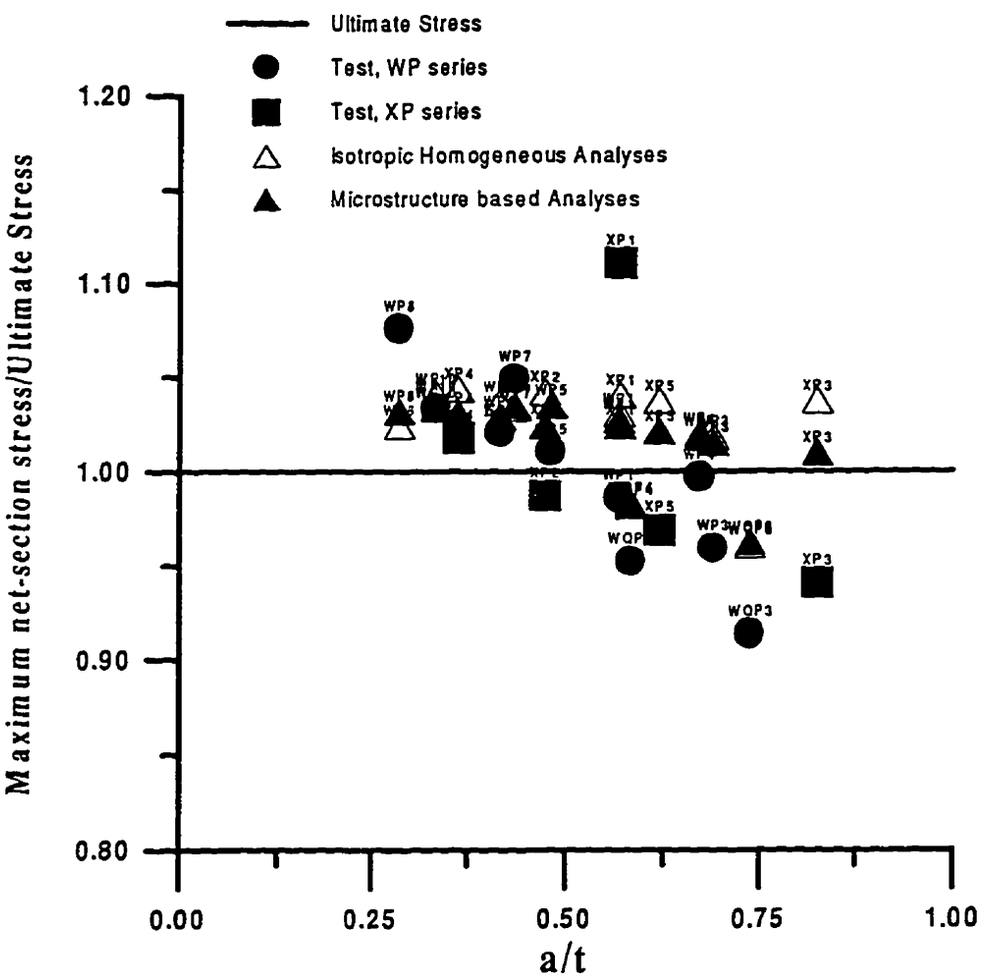

Figure 5.16 Maximum net-section stresses from microstructural based analyses versus *a/t*.

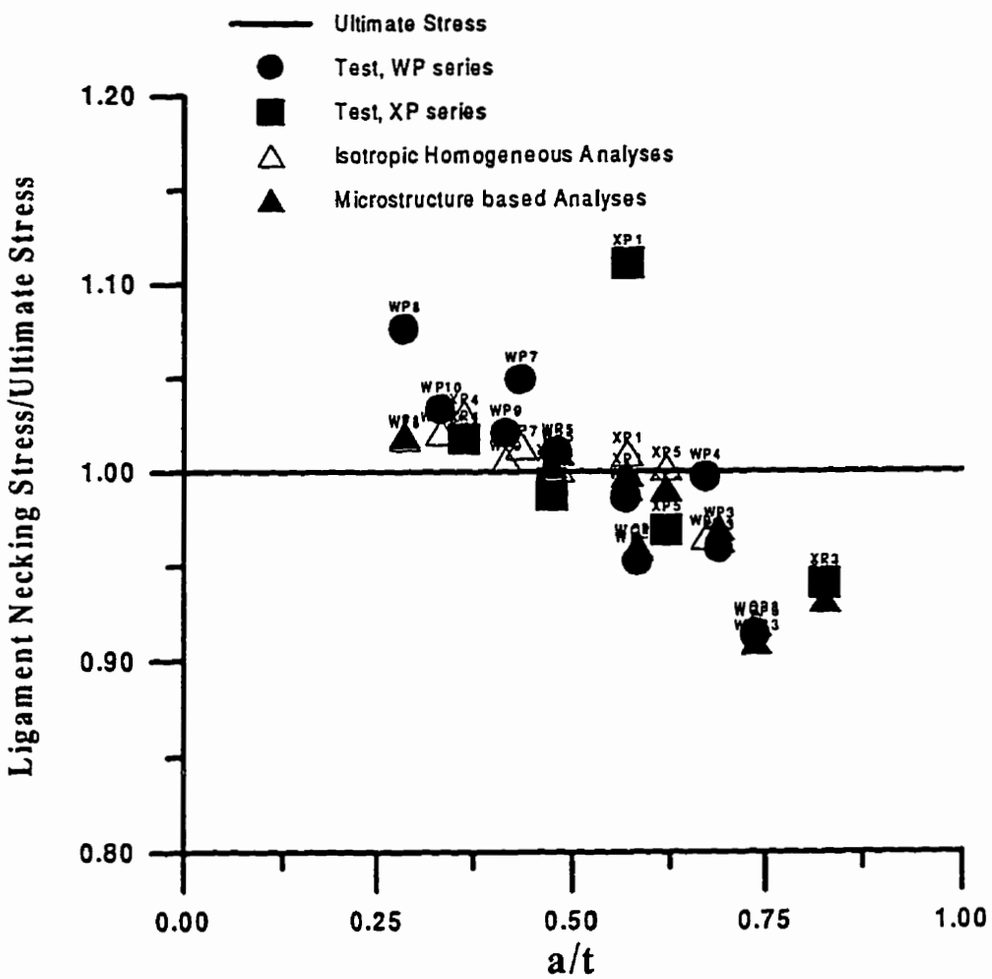

Figure 5.17 Ligament necking stresses from microstructural based analyses versus *a/t*.

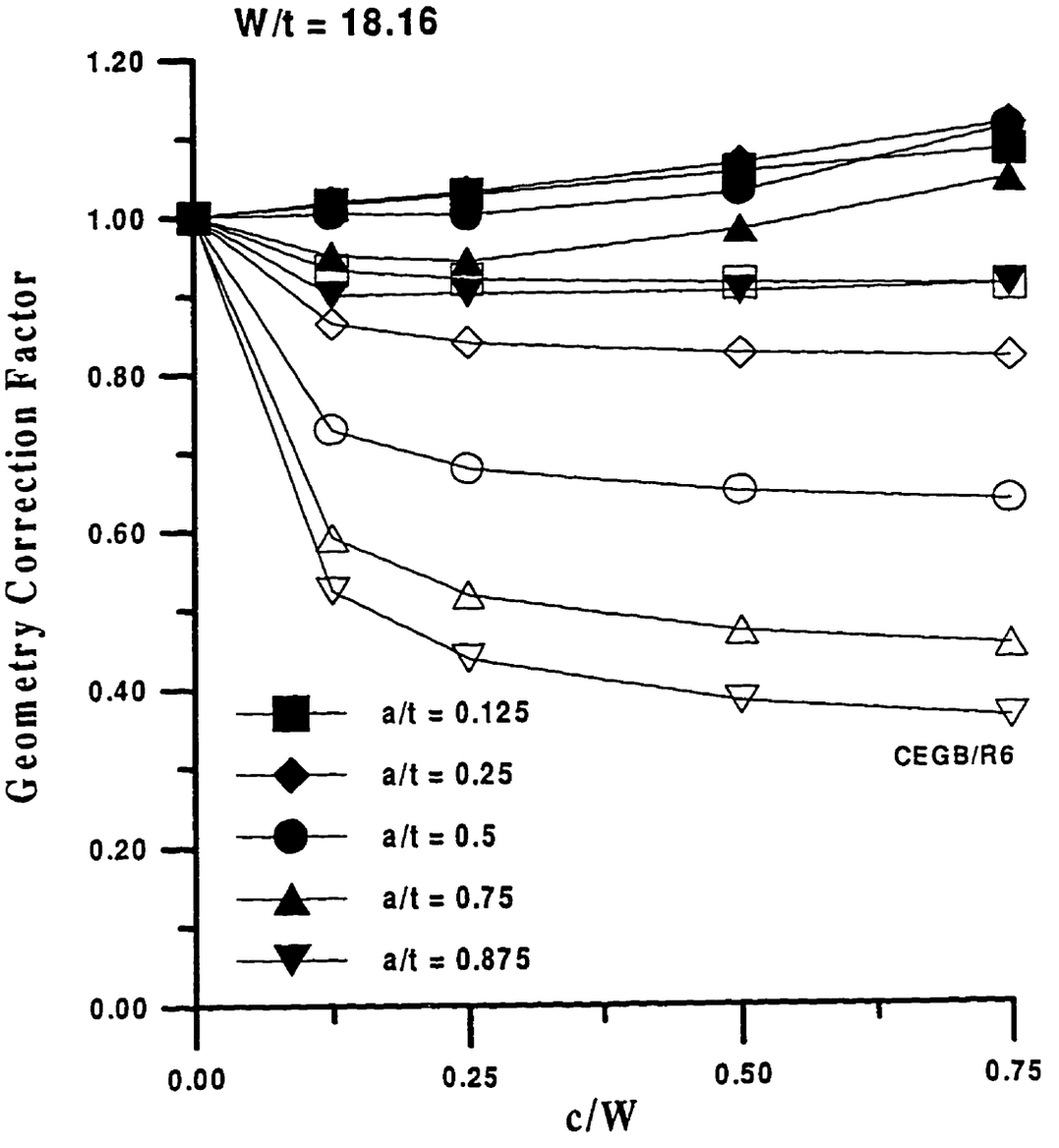

Figure 5.18 Geometry correction factors for $W/t = 18.16$.

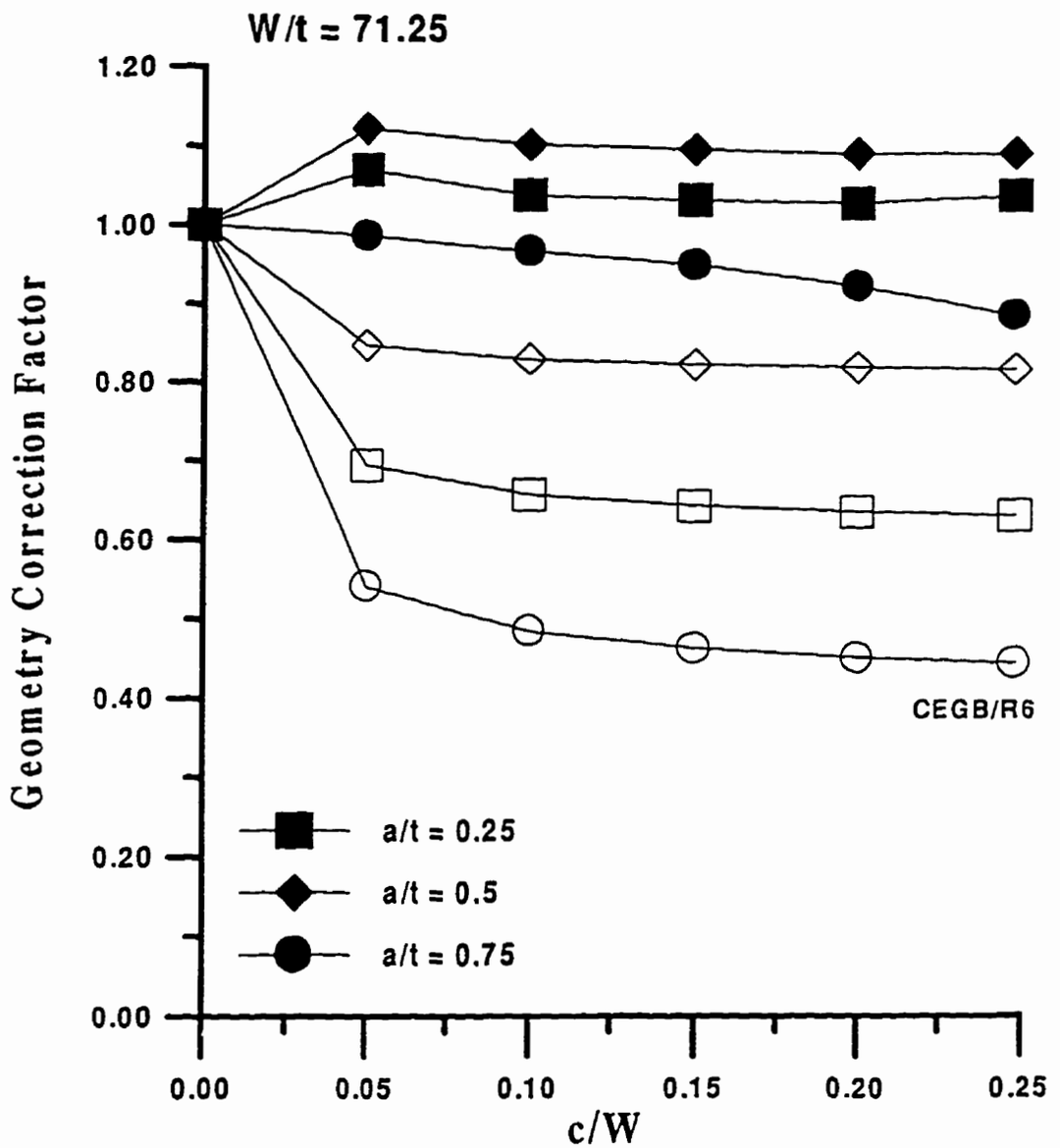

Figure 5.19 Geometry correction factors for $W/t = 71.25$.

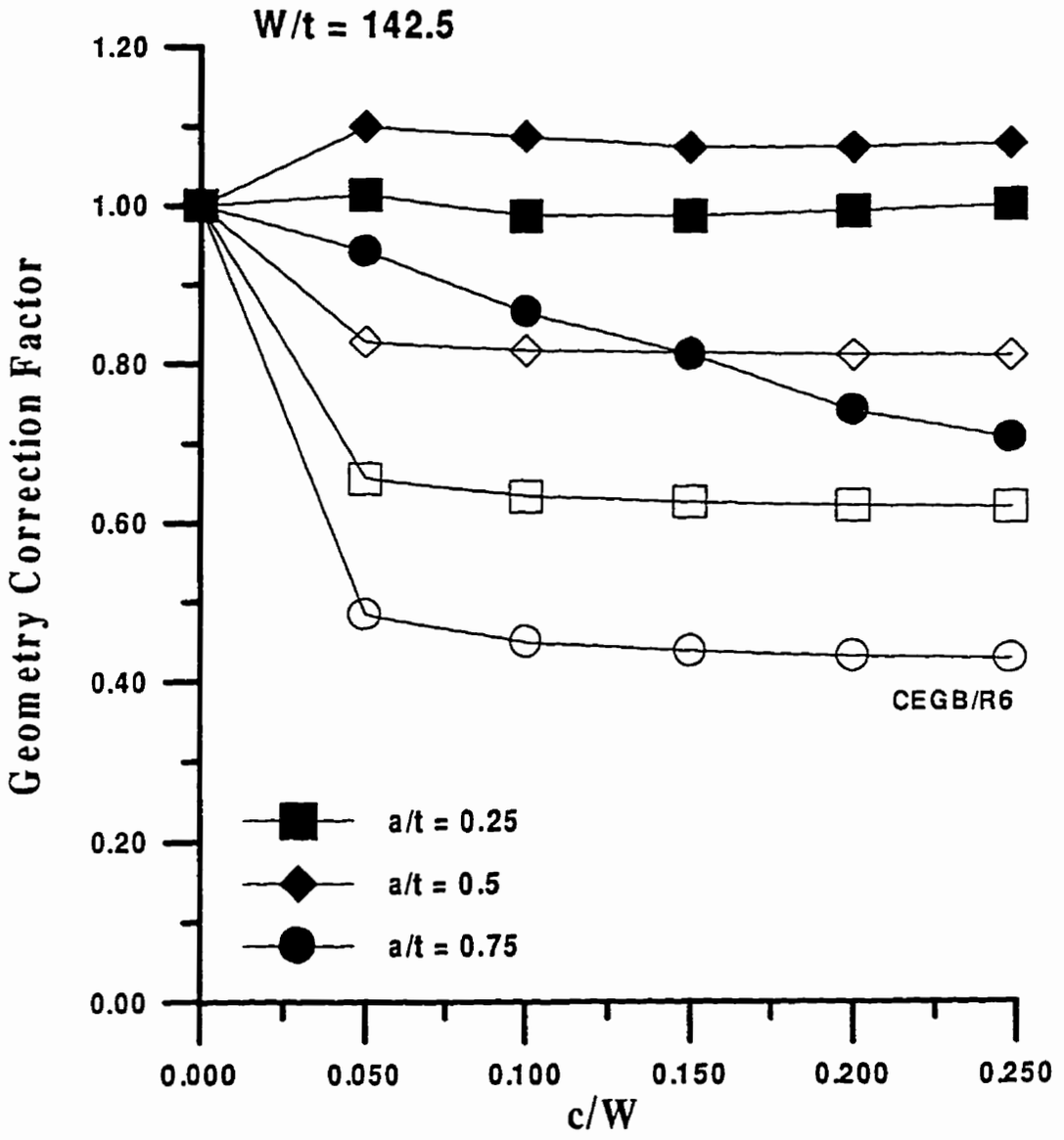

Figure 5.20 The geometry correction factors for $W/t = 142.5$.

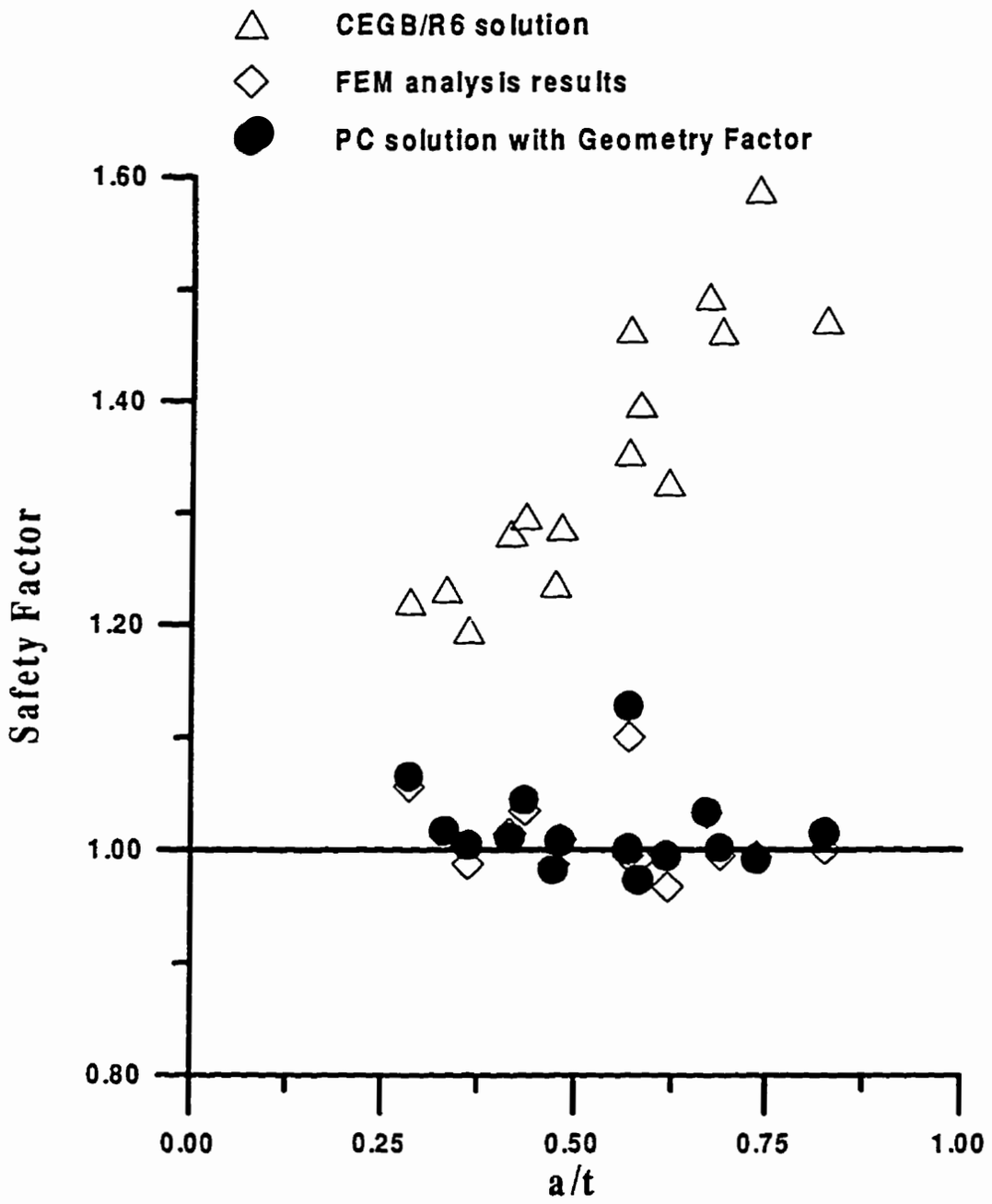

Figure 5.21 Safety factors obtained from the present plastic collapse solution.

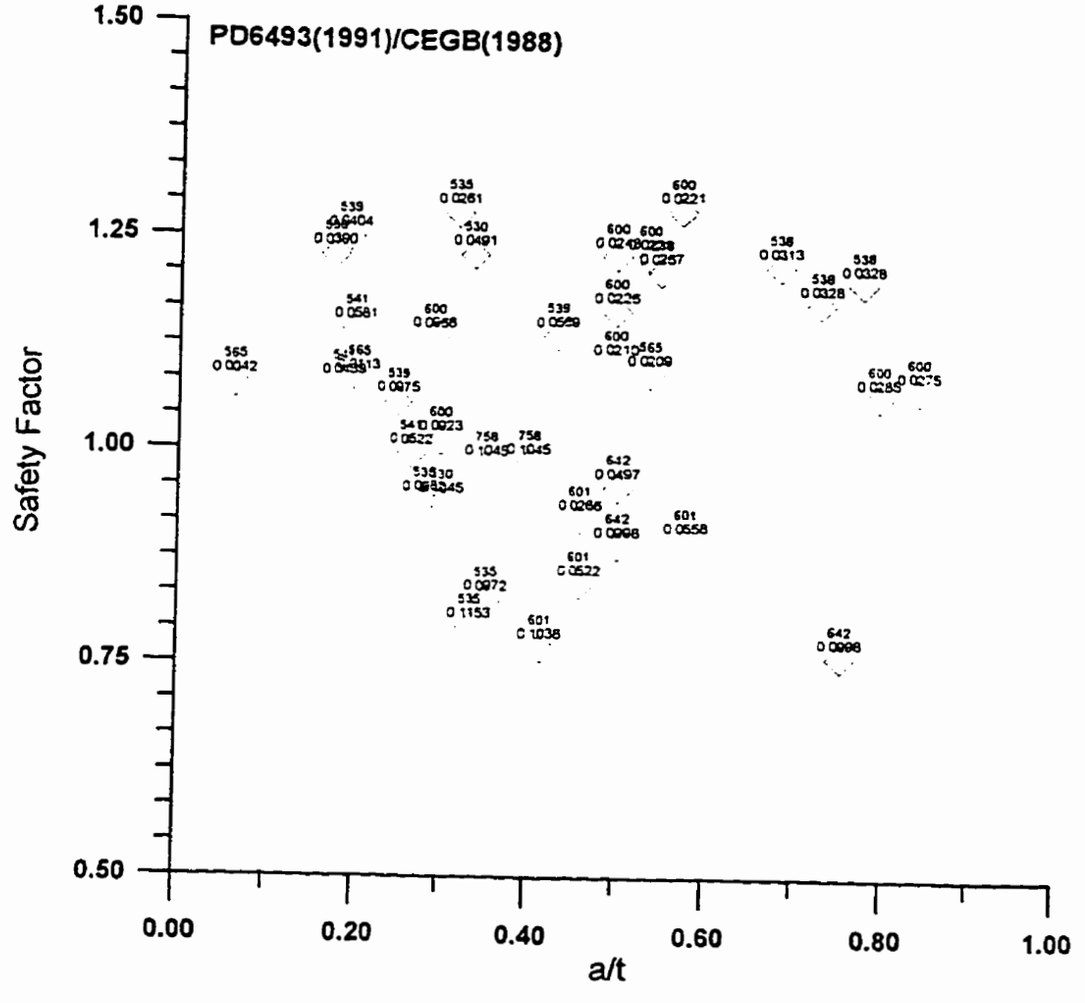

Figure 6.1 Net-section collapse solutions (PD6493:1991, CEGB/R6) versus *a/t*.

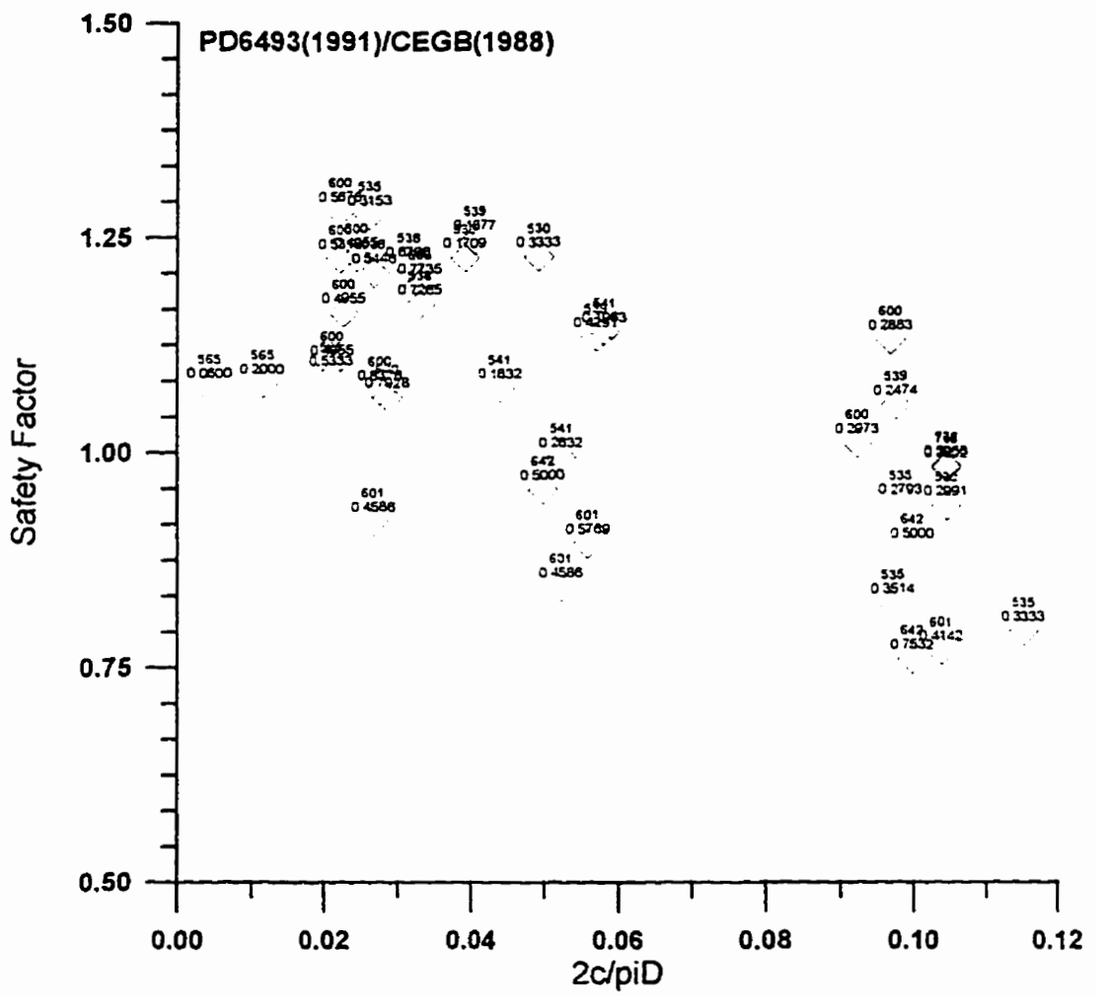

Figure 6.2 Net-section collapse solutions (PD6493:1991, CEGB/R6) versus $2c/\pi D$.

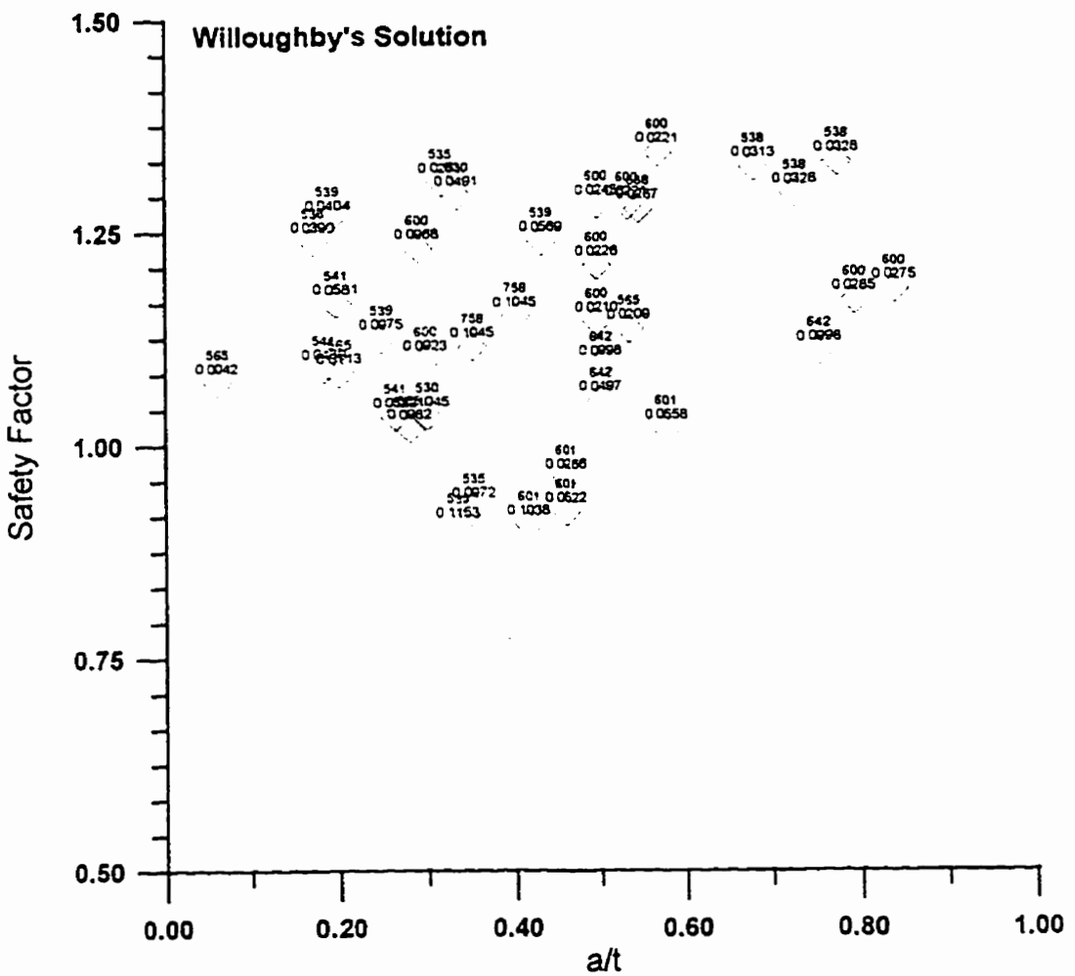

Figure 6.3 Willoughby's plastic collapse solutions versus *a/t*.

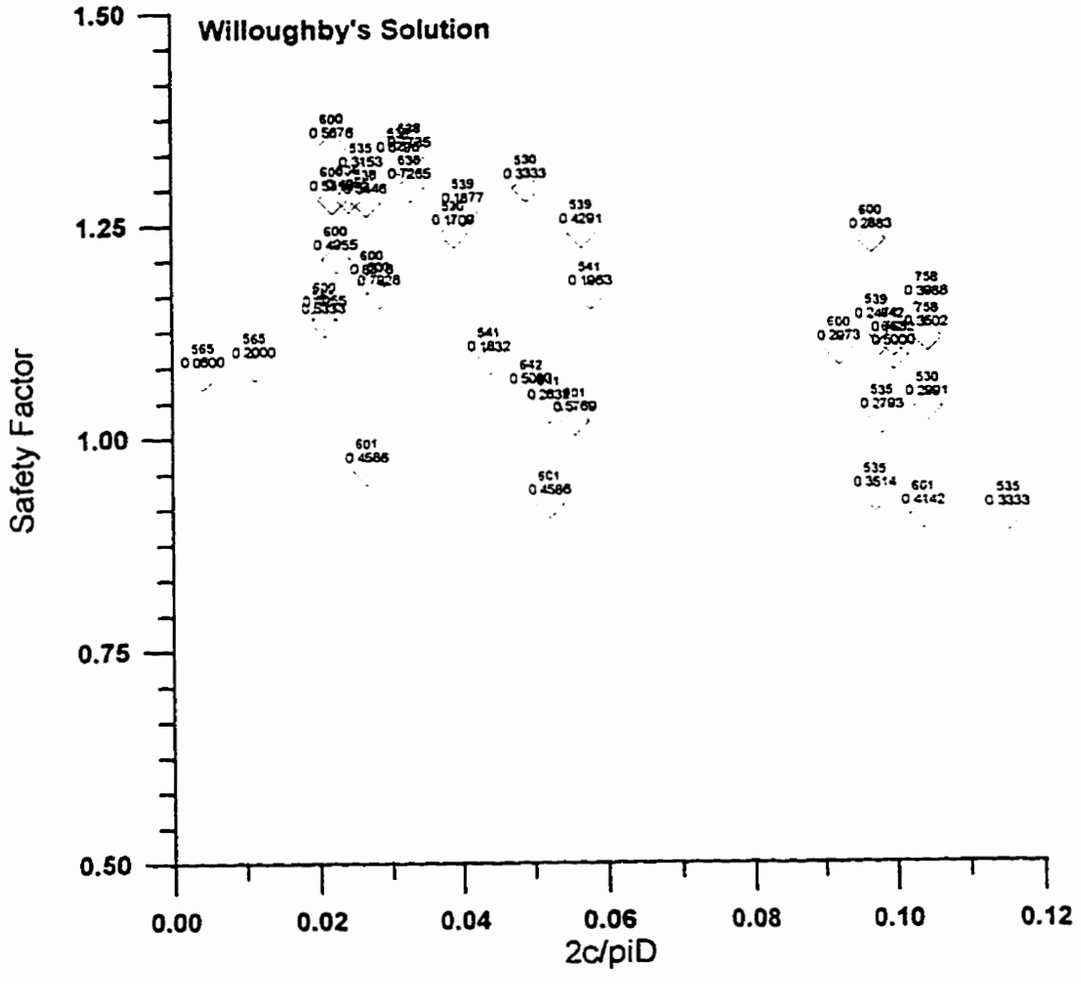

Figure 6.4 Willoughby's plastic collapse solutions versus $2c/\pi D$.

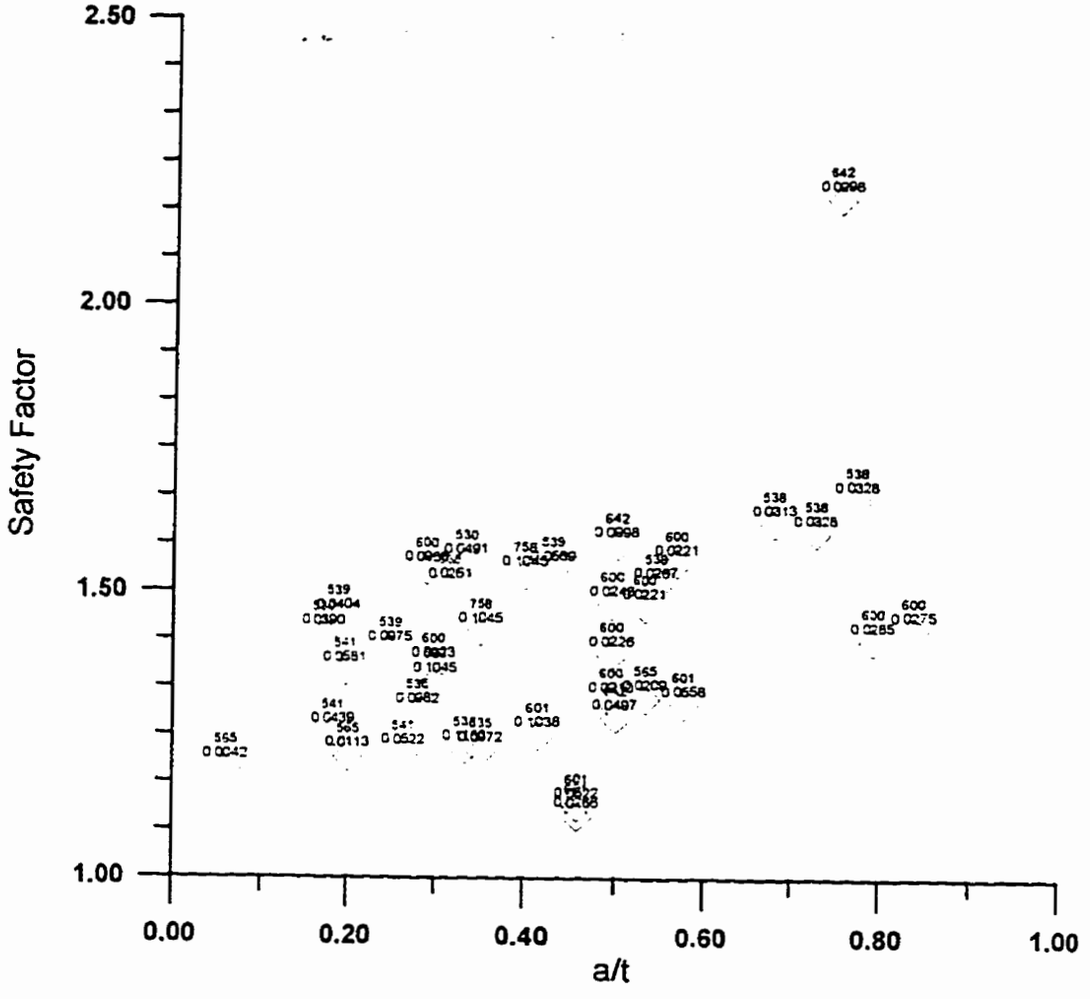

Figure 6.5 CSA Z662 plastic collapse solutions (with safety factors) versus *a/t*.

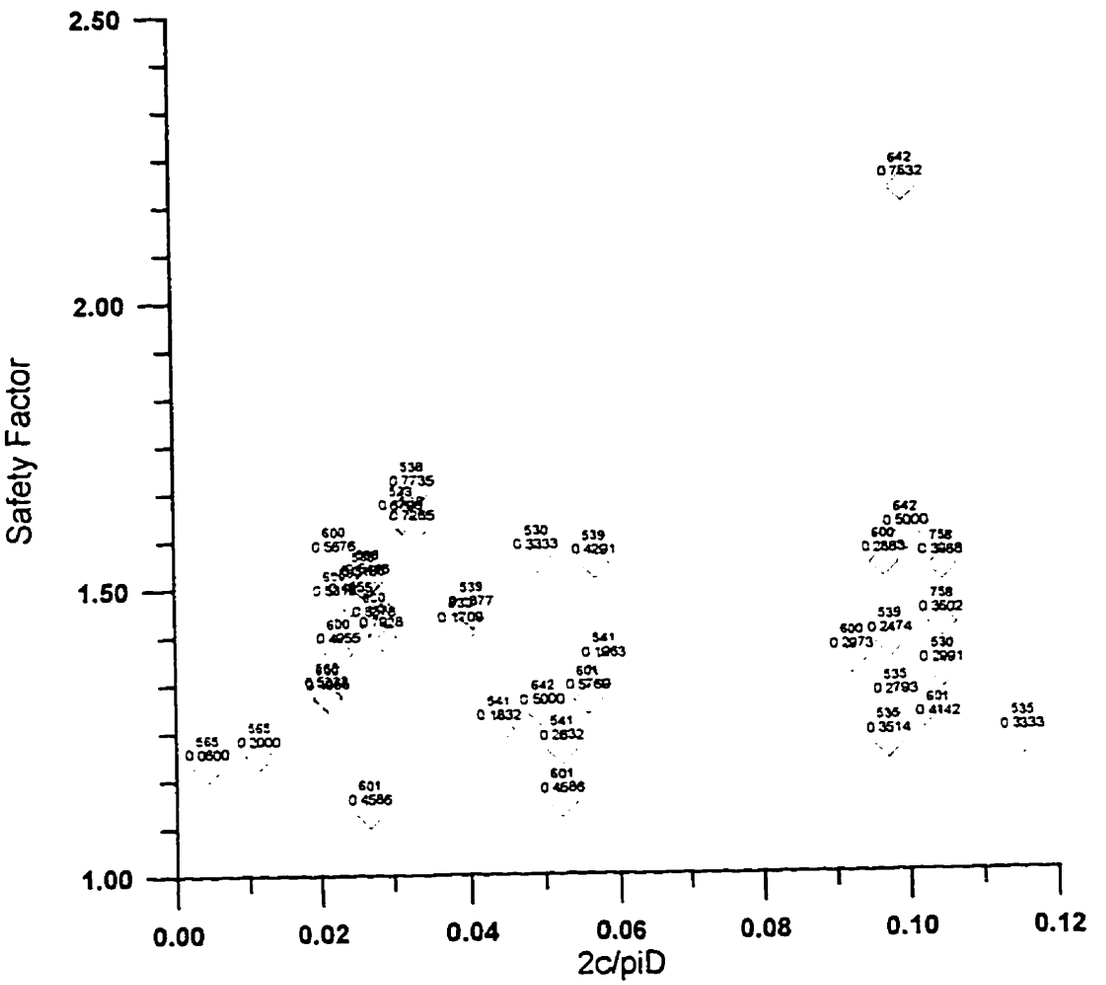

Figure 6.6 CSA Z662 plastic collapse solutions (with safety factors) versus $2c/\pi D$.

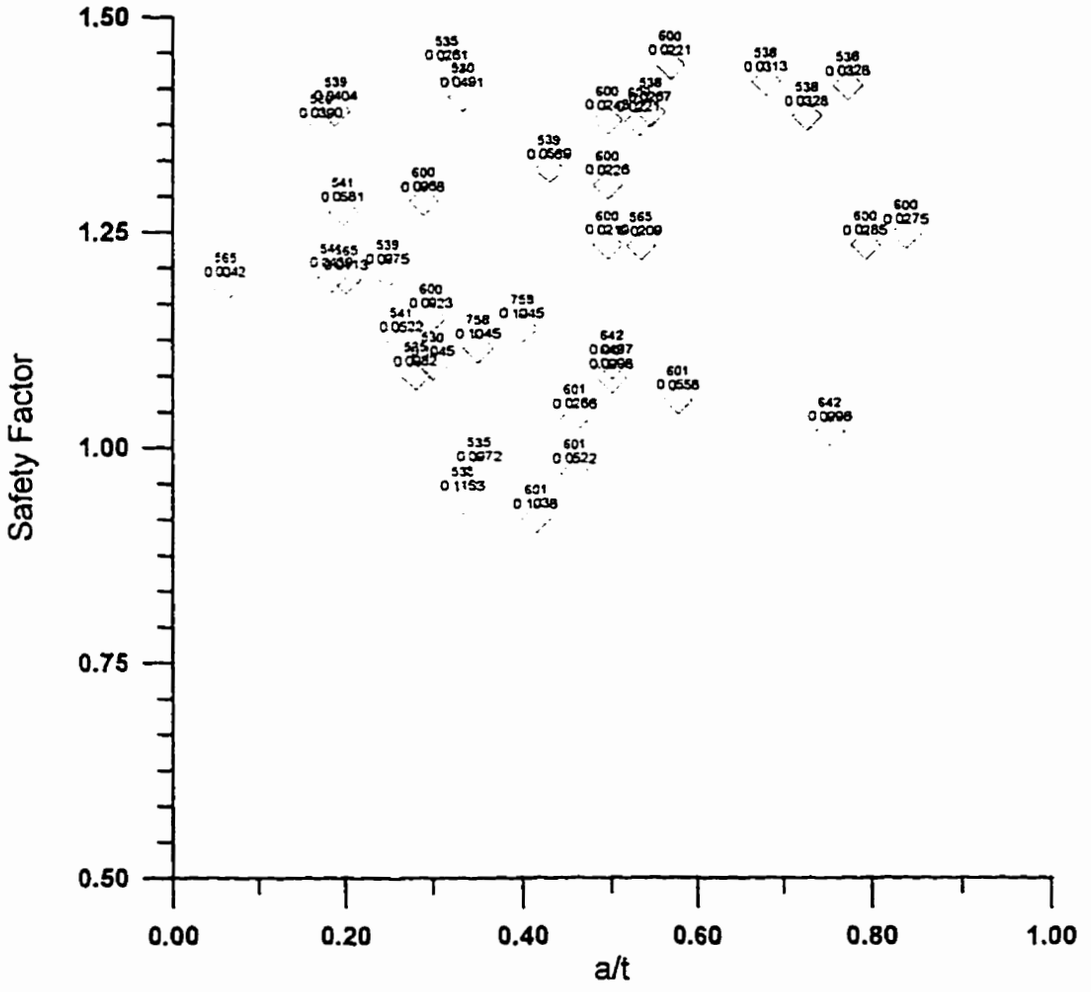

Figure 6.7 CSA Z662 plastic collapse solutions (without safety factors) versus *a/t*.

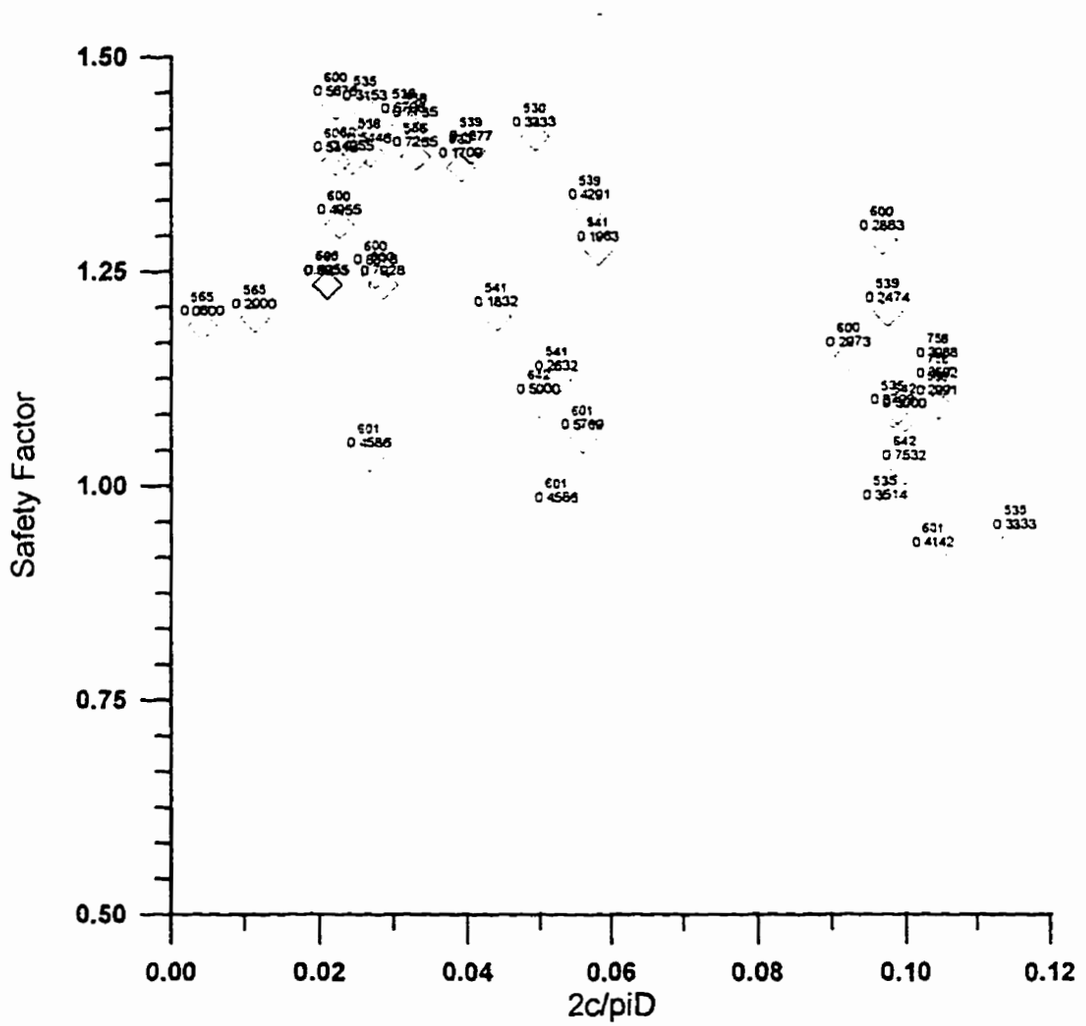

Figure 6.8 CSA Z662 plastic collapse solutions (without safety factors) versus $2c/\pi D$.

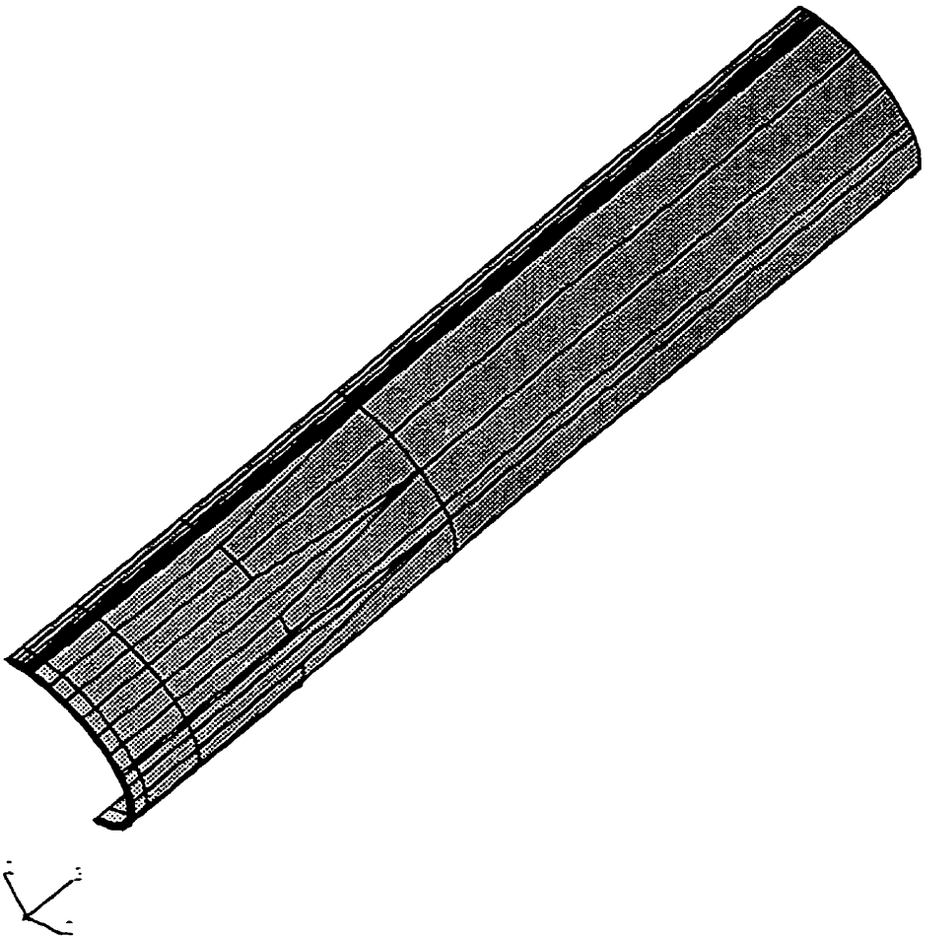

Figure 6.9 A finite element mesh for a full pipe.

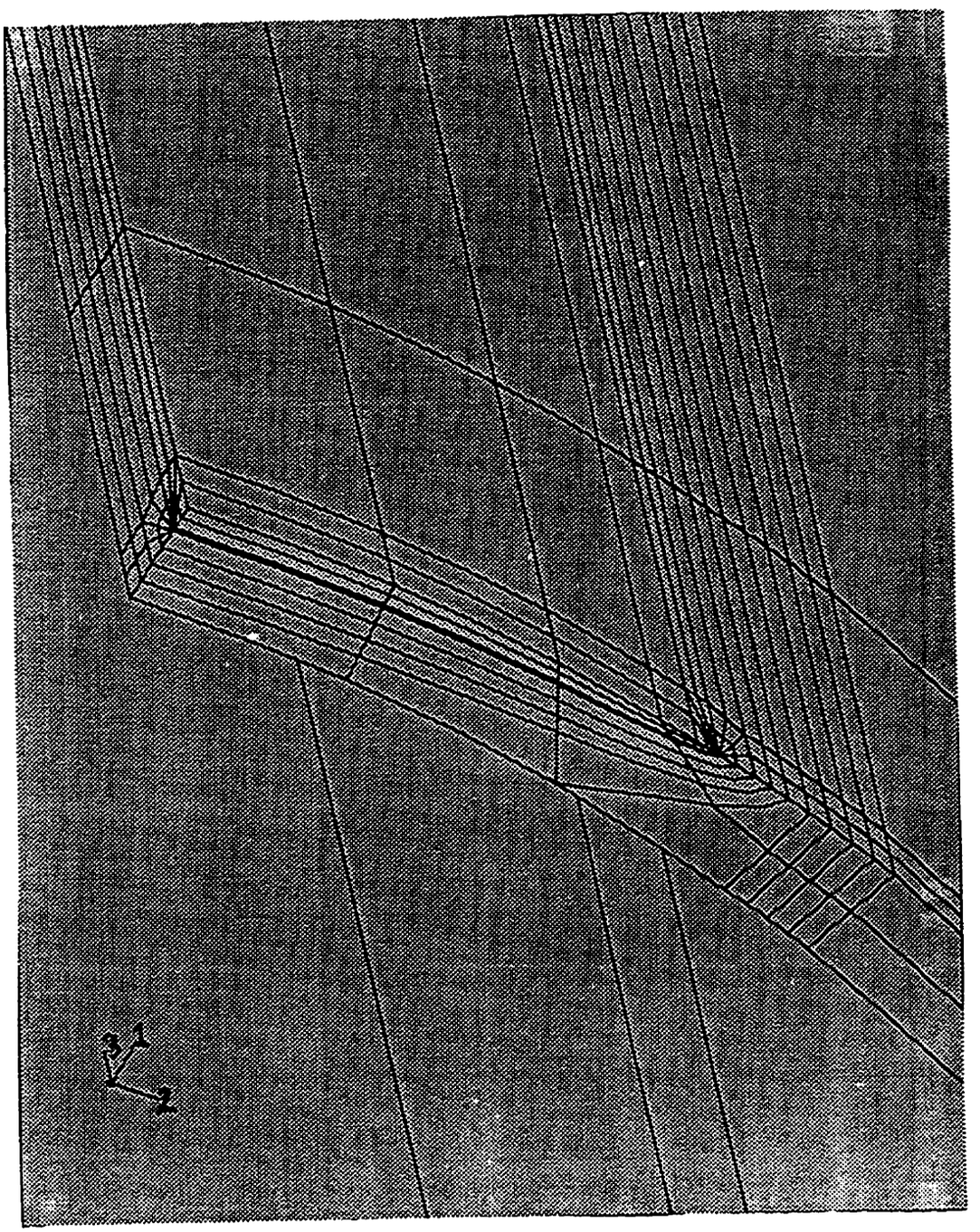

Figure 6.10 Enlarged crack-tip area.

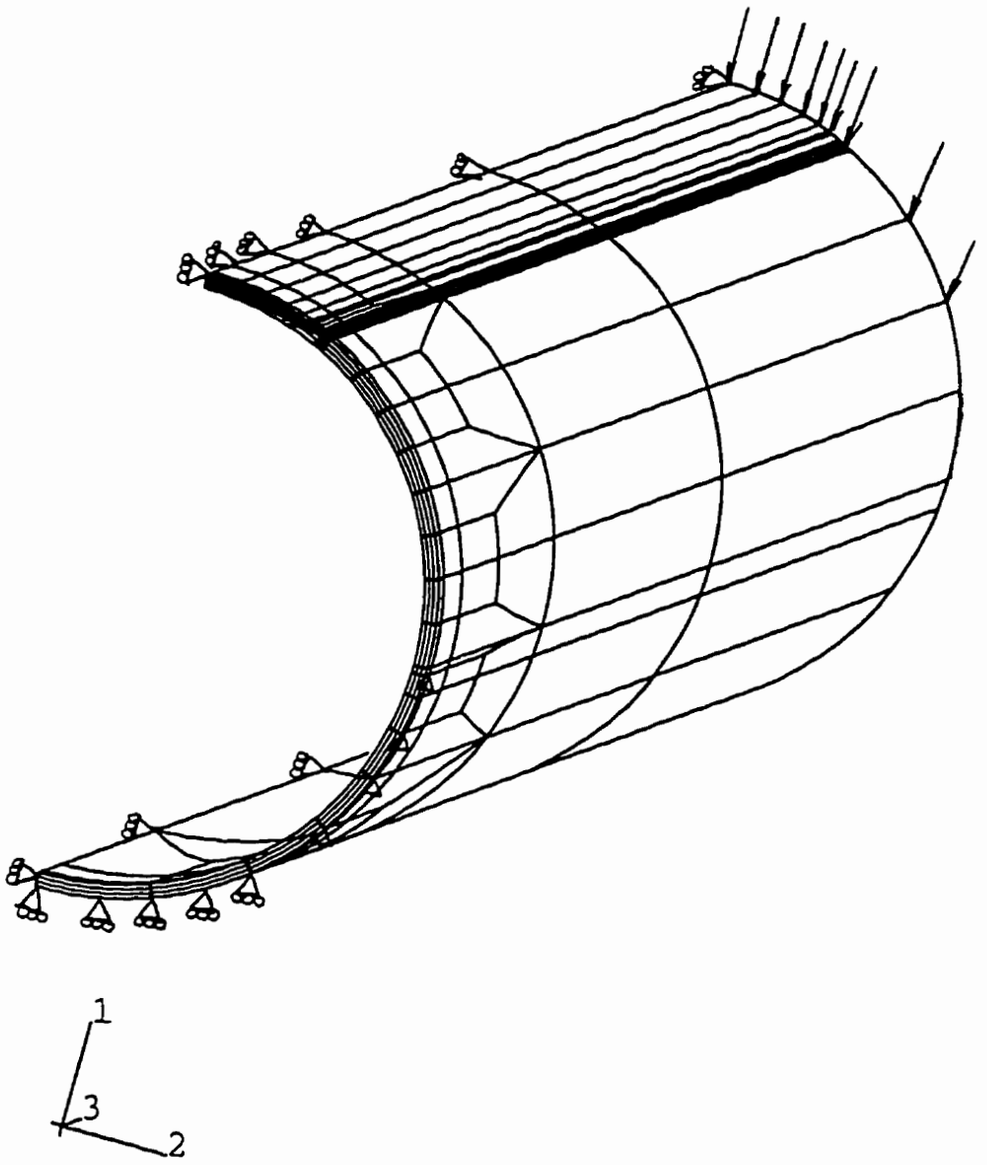

Figure 6.11 Boundary conditions for a full pipe subject to remote bending.

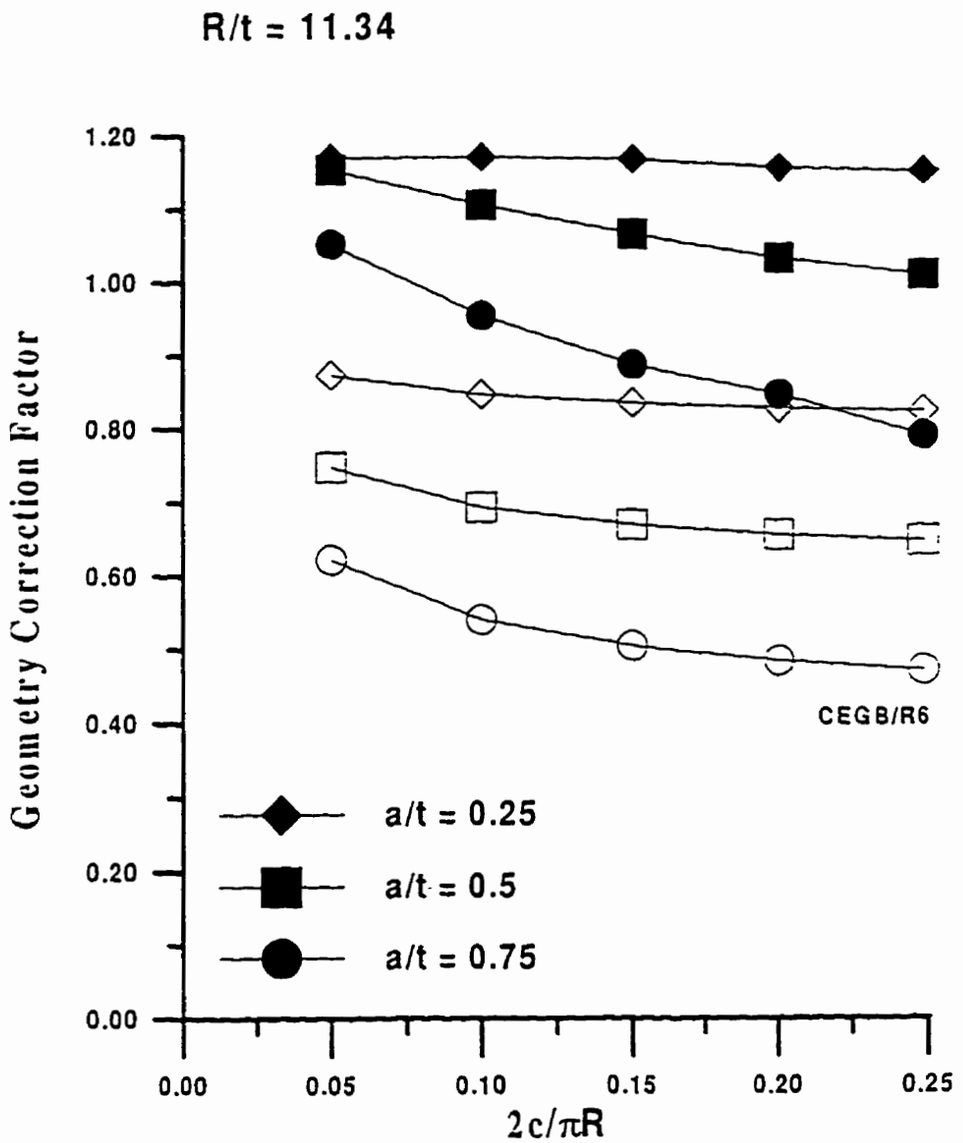

Figure 6.12 The geometry correction factors for R/t = 11.34.

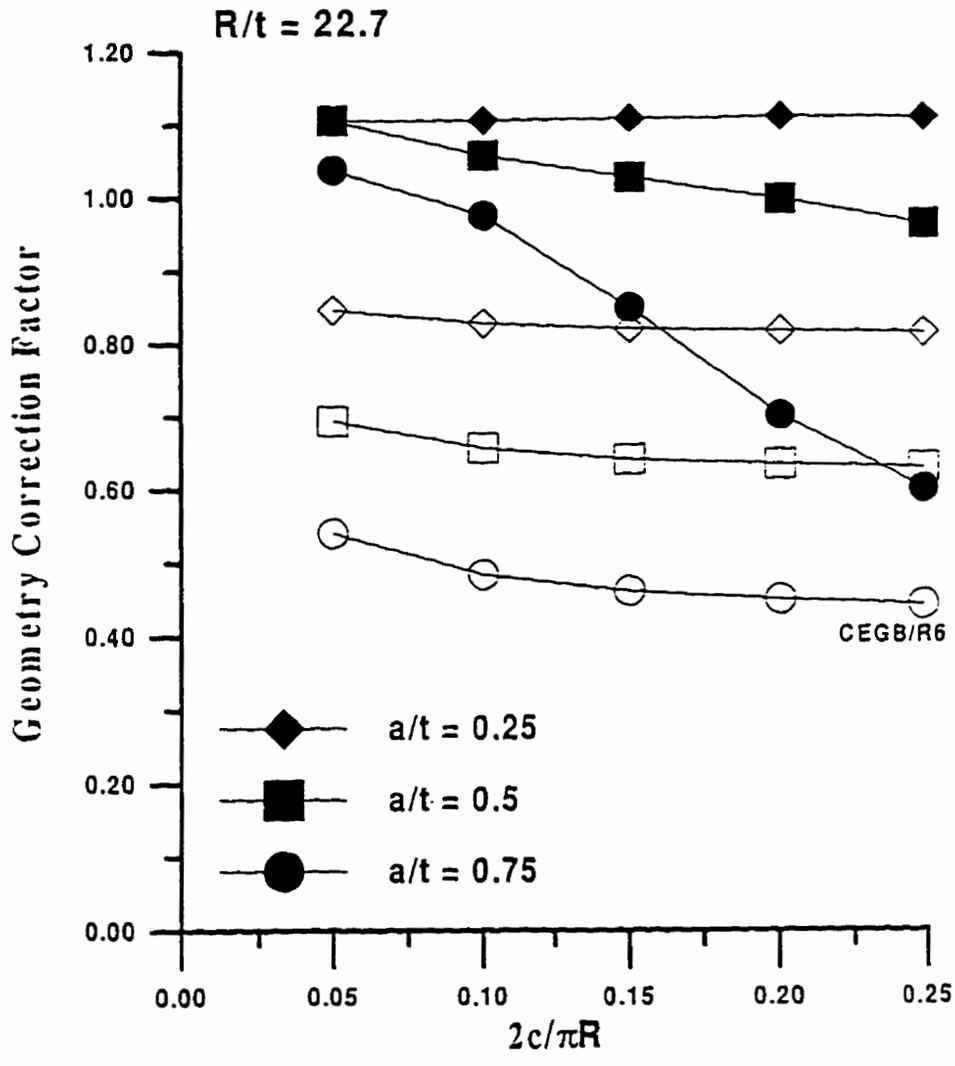

Figure 6.13 The geometry correction factors for R/t = 22.7.

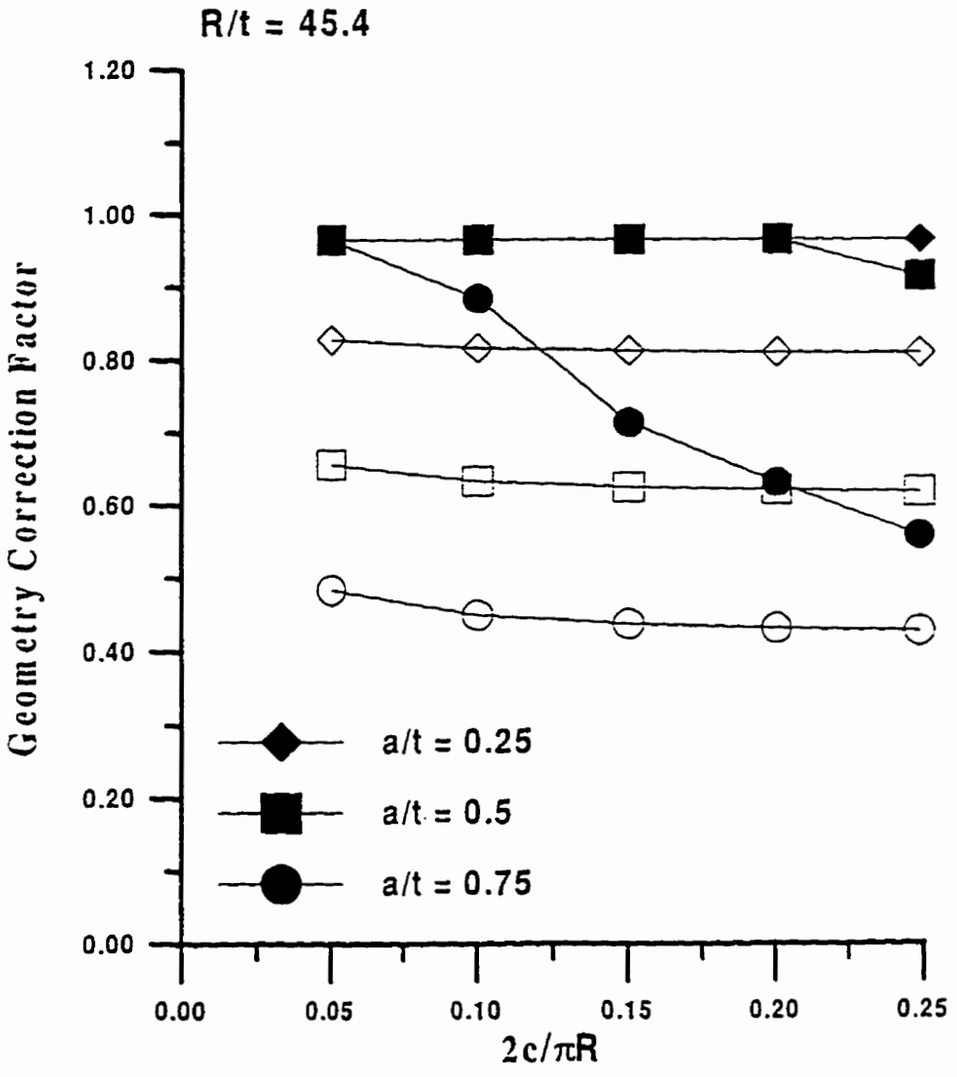

Figure 6.14 The geometry correction factors for R/t = 45.4.

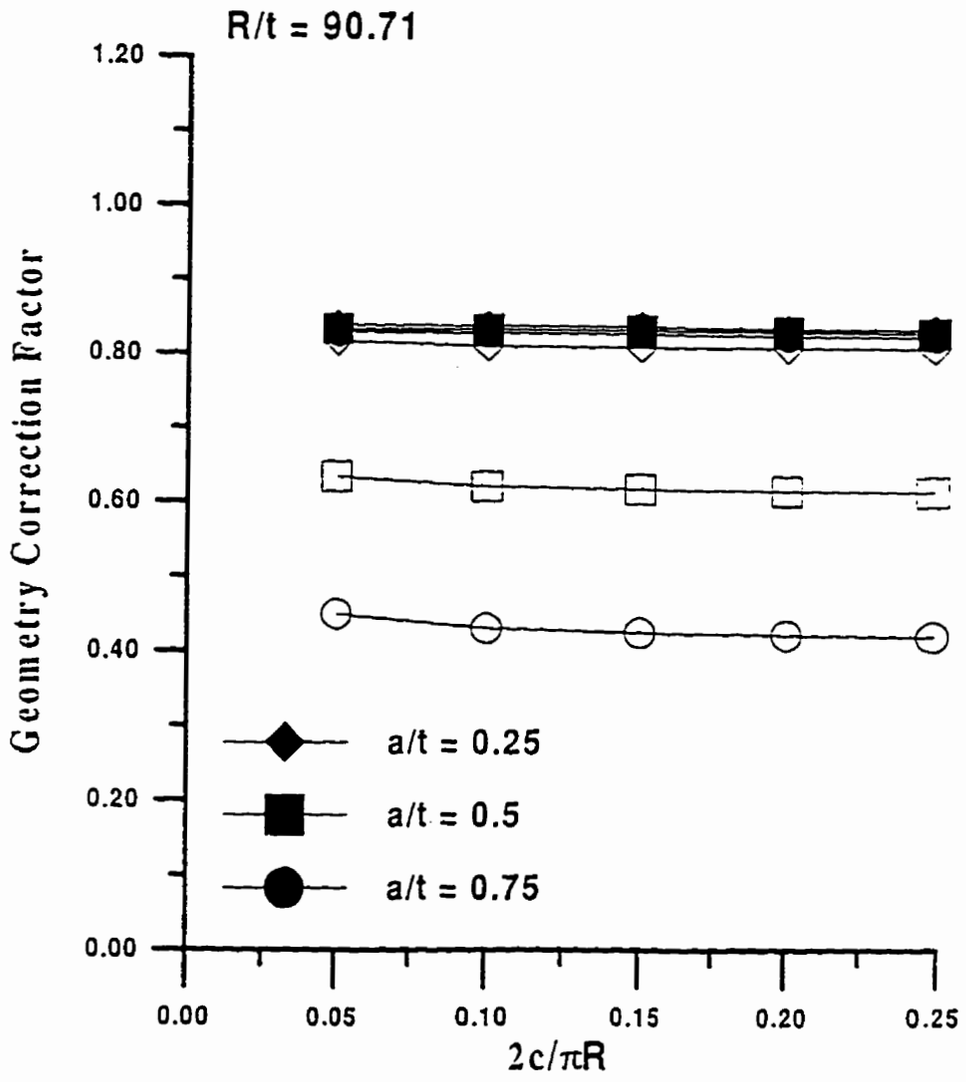

Figure 6.15 The geometry correction factors for R/t = 90.71.

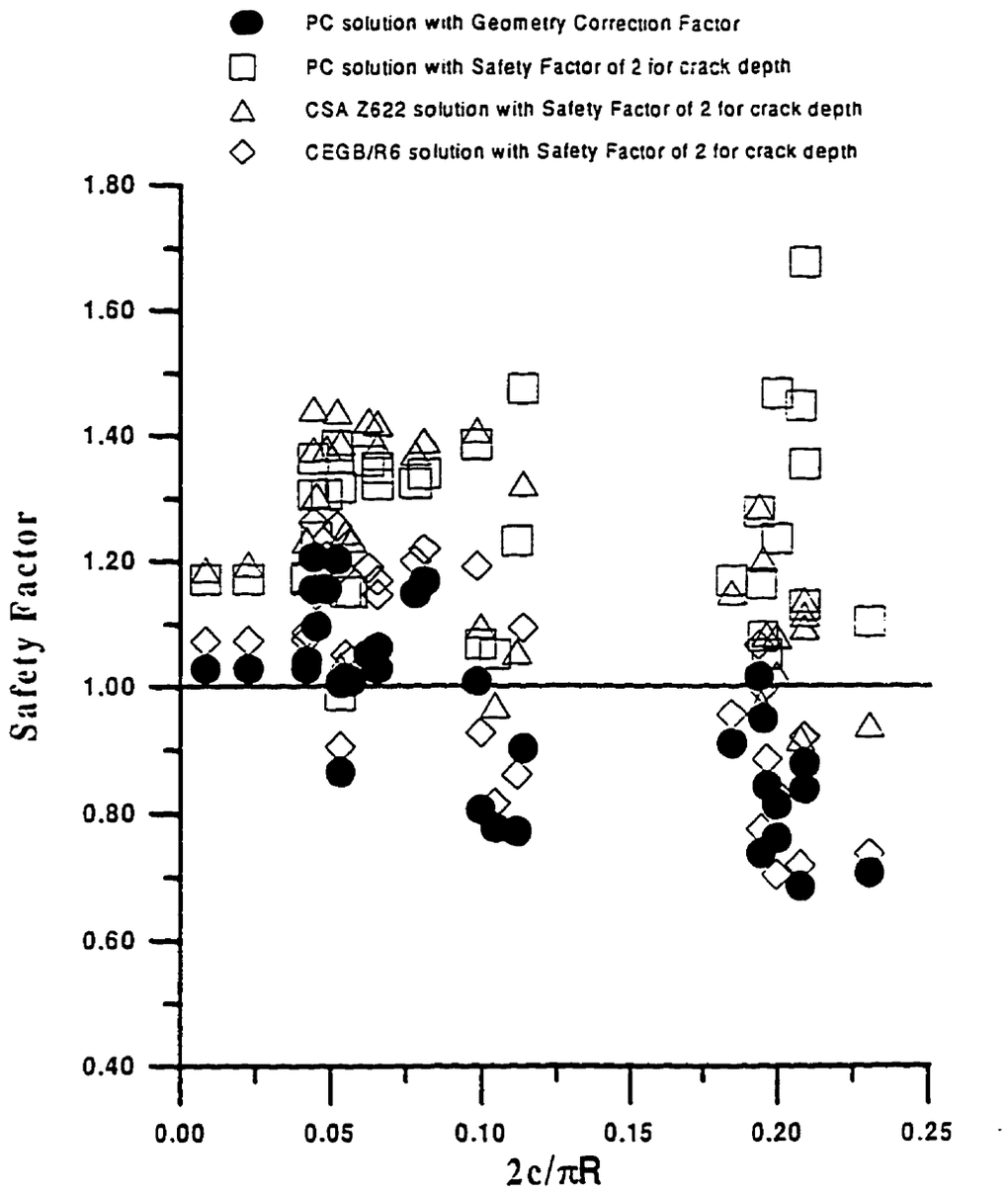

Figure 6.16 Safety factors obtained from the present plastic collapse solution.

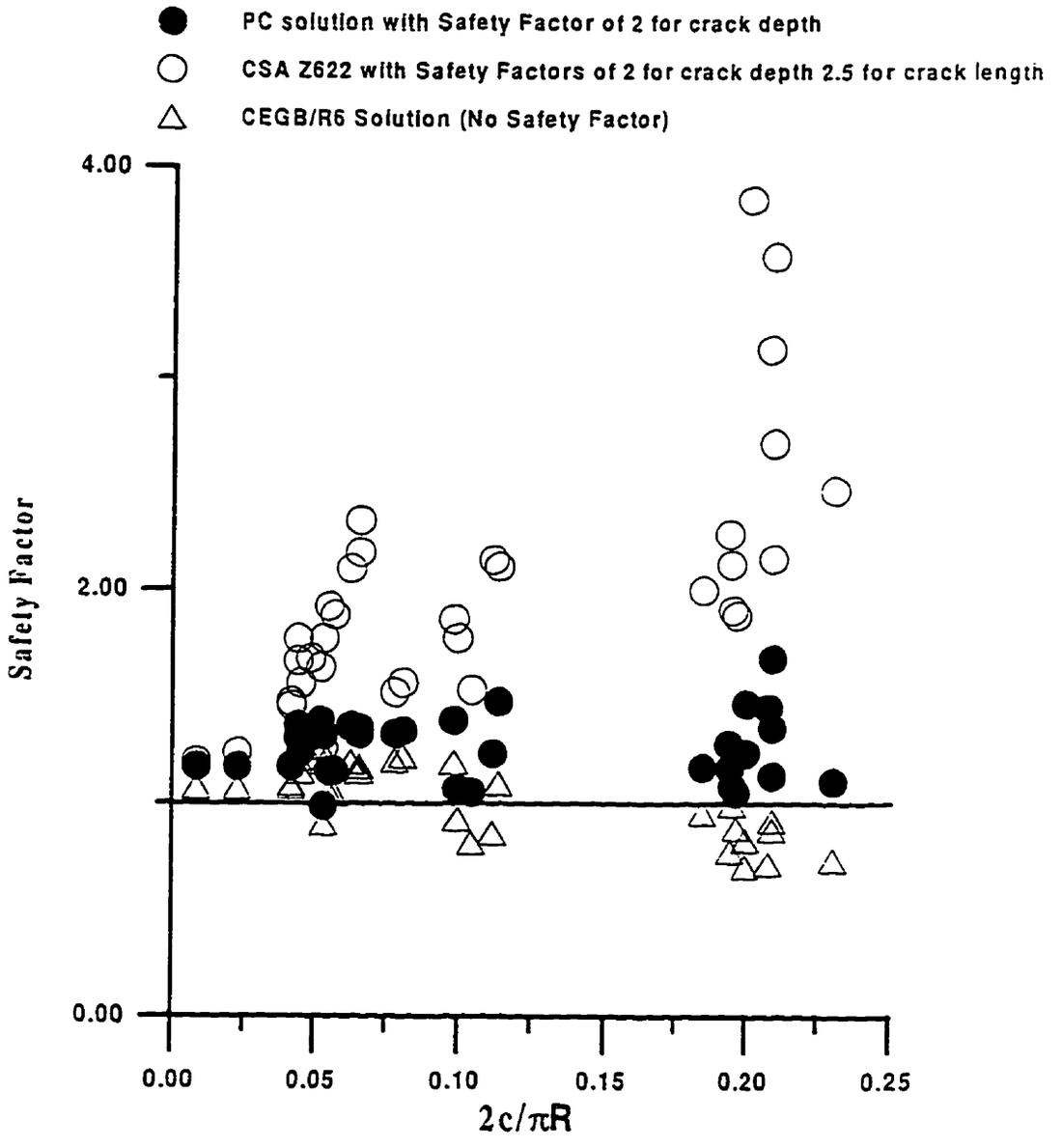

Figure 6.17 Safety factors obtained from the present plastic collapse solution for pipeline girth weld defects.